THE EFFECT OF MUTUAL COUPLING ON THE SIDE LOBE PERFORMANCE OF CHEBYSHEV ARRAYS, VOL. 1

THESIS

ROBERT A. GIERARD
Captain, USAF

AFIT/GE/ENG/89M-4

DEPARTMENT OF THE AIR FORCE
AIR UNIVERSITY
AIR FORCE INSTITUTE OF TECHNOLOGY
Wright-Patterson Air Force Base, Ohio

AFIT/GE/ENG/89M-4

THE EFFECT OF MUTUAL COUPLING ON THE SIDE LOBE PERFORMANCE OF CHEBYSHEV ARRAYS, VOL. 1

THESIS

ROBERT A. GIERARD
Captain, USAF

AFIT/GE/ENG/89M-4

APPROVED FOR PUBLIC RELEASE; DISTRIBUTION UNLIMITED

AFIT/GE/ENG/89M-4

THE EFFECT OF MUTUAL COUPLING ON THE SIDE LOBE PERFORMANCE OF CHEBYSHEV ARRAYS, VOL. 1

THESIS

Presented to the Faculty of the School of Engineering

of the Air Force Institute of Technology

Air University

In Partial Fulfillment of the

Requirements for the Degree of

Master of Science in Electrical Engineering

ROBERT A. GIERARD

Captain, USAF

March 1989

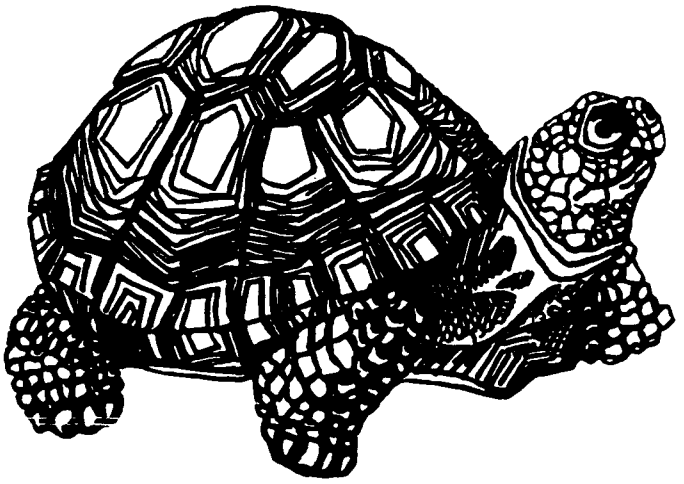

Slow and steady wins the race.

Easop

PREFACE

The primary purpose of this study was to develop a computer model of mutual coupling in linear arrays of parallel dipoles, and assess the impact of this coupling on the side lobe performance of low side lobe array distributions (like Chebyshev amplitude tapers). The secondary purpose of this study was to investigate simple compensation schemes to account for coupling. A fortran computer program was written to model coupling for any geometry of parallel dipoles, and applied to a variety of array sizes using several Chebyshev amplitude tapers and linear phase tapers. Curves of side lobe degradation as a function of array size, scan condition and desired side lobe level were produced. Three simple compensation techniques were attempted.

In performing this computer analysis, I have benefited from the advice and support of many individuals over a long period of time. I sincerely thank my faculty advisor, Dr. A. J. Terzuoli, my committee members, Dr. V. P. Pyati and Major H. H. Barksdale, the department head, Dr. J. J. D'Azzo and the school for their considerable patience and assistance in getting this program back on track. I owe Dr. R. J. Mailloux many thanks, both for suggesting this topic area and for his helpful feedback and direction over the course of this study. A word of thanks goes to MSgt Valerie Enos, whose meticulous efforts in the preparation of this and other manuscripts were invaluable. I am deeply indebted to my supervisor, Mr. Patrick Sharp, who understands me best of all, and has enabled me, at considerable cost to the organization, to reach this professional milestone. Finally, and importantly, I thank my wife, Heidi, and daughters, Kelly and Lauren, who are only now enjoying their proper share of my attention.

Robert A. Gierard

TABLE OF CONTENTS

VOLUME I

TABLE OF CONTENTS (CON'T)

LIST OF FIGURES

LIST OF FIGURES (CON'T)

LIST OF FIGURES (CON'T)

LIST OF FIGURES (CON'T)

LIST OF TABLES

ABSTRACT

This computer analysis assessed the impact of mutual coupling on the side lobe performance of Chebyshev linear arrays as a function array size, scan condition, and the severity of Chebyshev taper. Array elements were horizontal parallel dipoles over a ground plane. Three simple compensation schemes to account for coupling were investigated.

A fortran computer program, based upon King-Middleton's modified, zero-order, two-term theory for cylindrical dipoles, was written to calculate the generalized impedance matrix for the linear array, dipole current distributions and the far-field H-plane pattern in the presence of coupling. It is sufficiently general to allow the user to specify, number of dipoles, dipole length and radius, dipole spacing, height above ground plane, frequency, and complex generator voltages driving the array. The results relate side lobe degradation (growth) to array size, scan condition, and desired Chebyshev side lobe level.

Additional programs were written to reverse the matrix solution, and solve for generator voltages, which after coupling, produce a base current distribution with a Chebyshev taper. Three simple compensation schemes then used approximations of the compensated (complex) voltages to drive the array. The effectiveness of these compensation schemes are discussed. The results of this study indicate that linear arrays greater than 20 elements can probably ignore mutual coupling for side lobe considerations, and amplitude only compensation schemes significantly improve side lobe performance under all but the severest scan condition (45 deg) and Chebyshev tapers (-40 db) considered.

THE EFFECT OF MUTUAL COUPLING ON THE SIDE LOBE

PERFORMANCE OF CHEBYSHEV ARRAYS,

VOL. -

INTRODUCTION

Array analyses that ignore mutual coupling are based upon pattern multiplication. That is, a common element pattern assumed to be applicable to all array elements, is multiplied by an array factor, which includes all complex element weights, and path length differences due to geometry (5, Chap 5)(9, Chap 4)(24, Chap 3). For arrays of dipoles, this assumption implies identical current distributions for all dipoles. This implication is not correct. Mutual coupling induces parasitic currents on surrounding dipoles due to to the excitation of any single dipole. The element pattern of a driven dipole is then the superposition of fields due to the driven current, and all parasitic currents. Since the physical and electrical environment changes across the array, and in particular near the edges, the parasitic currents and therefore the element pattern change as well (7). The element pattern cannot be factored out of a far-field expression. This study will investigate the impact of mutual coupling on the sidelobe performance of linear arrays. Parallel dipole elements will be used due to their simple geometry and significant coupling properties. The utility of this can be extended due to equivalences between cylindrical dipoles, strip dipole, vertical monopoles over a ground plane, as well as two-wire and waveguide fed slots (9, Chap 7).

The modelling of mutual coupling has progressed from analyses that use assumed current distributions, to analyses that solve for actual current distributions. The early work of Carter (3) used the induced EMF Method to calculate the coupling between an isolated dipole pair is an example of the former. He

assumed sinusoidal current distributions, and used the calculated coupling of the isolated dipole pair for any similarly spaced dipoles in an array. The analyses of coupling and electromagnetic fields for arrays by Hansen (11) and King (14, Chap 5 and 6), solved simultaneously for all coupling coefficients between array elements as a single boundary value problem. This method also assumed sinusoidal currents, and its accuracy is limited by the suitability of sinusoidal currents to the dipole geometries under investigation. Later work by Chang and King (4) presented rigorous and highly accurate solutions for dipole current distributions by solving for coefficients to a five term expansion of dipole current. This work accurately calculated coupling between dipole elements but proved entirely too cumbersome for application to array problems. Later work by King, et al (15) developed a much simpler two-term theory for current distibutions, and applied this theory to linear arrays of thin, parallel dipoles. This simpler theory achieved excellent agreement with Mack's precise measurements (18) of dipole impedances and current distributions.

Section 1 outlines fundamental electromagnetic equations for the cylindrical dipole antenna. Section 2 and Appendices A1 and A2 present King-Middleton's Modified, Zero-Order, Two-Term Theory. This theory is used, in Section 3, to model the coupling of parallel, horizontal dipoles over a ground plane. A variety of array sizes (10, 20, 30, and 40 elements) employing numerous Chebyshev amplitude (15, 20, 30, and 40 dB) and linear phase (0, 15, 30, and 45 degrees of scan) tapers. Section 4 discusses the impact of mutual coupling on the sidelobe performance of the Chebyshev tapers, as a function of array size and scan condition. Section 5 employs three simple compensation methods to correct for the coupling, and discusses their effectiveness. Appendices B and C contain model results, in the form of far-field plots and active, current weights, for uncompensated and compensated arrays respectively. Volume II of this report

contains the fortran code and sample input/output files that implemented the linear array model of Section 3 and the compensation methods of Section 5.

1.0 FUNDAMENTAL ELECTROMAGNETIC THEORY

The fundamental characteristics of cylindrical antennas, the electromagnetic fields and driving point impedances, are completely determined by the distribution of currents on the antenna. The first section of this report will review the pertinent electromagnetic equations for both isolated and coupled cylindrical antennas (5)(9)(15)(24). Impedance and far-field expressions will be derived, assuming an idealized "slice" generator.

Fields problems are usually expressed by linear integral equations derived from Maxwell's equations and specific boundary conditions. Maxwell's equations can be stated as follows for homogeneous mediums.

$$\nabla \times \bar{E} = -j\omega\mu\bar{H} \tag{1-2a}$$

$$\nabla \cdot \bar{E} = \rho/\varepsilon \tag{1-2b}$$

$$\nabla \times \bar{H} = j\omega\varepsilon\bar{E} + \bar{J} \tag{1-2c}$$

$$\nabla \cdot \bar{H} = 0 \tag{1-2d}$$

$\bar{J}$ is assumed to be conduction current, related to the electric field by the conductivity, σ . That is,

$$\bar{J} = \sigma\bar{E} \quad . \tag{1-3}$$

For good conductors, $\bar{J}$ is constrained to be surface currents, as interior electric fields are zero. The volumetric charge density, ρ , is also constrained to be surface charge for good conductors. The permeability and permitivity are μ and ε , respectively. All field properties ($\bar{E}$, $\bar{H}$, $\bar{J}$ and ρ) are infact both spatial (x, y and z) and temporal (t) functions. The time dependence, $e^{j\omega t}$, is assumed for all field properties and suppressed throughout this report.

1.1 HELMHOLTZ EQUATIONS

Since $\bar{E}$ and $\bar{H}$ are coupled in Maxwell's equations, the equations must be solved simultaneously to determine the fields from a given current distribution, $\bar{J}$. Therefore, we introduce scalar and vector potential functions, ϕ and $\bar{A}$, to decouple and simplify the solution for the fields (24:§ 1.3). To satisfy (1-2d), we define the magnetic field, H , as a curl of the magnetic vector potential function, $\bar{A}$. That is,

$$\bar{H} = \frac{1}{\mu} \left(\nabla \times \bar{A} \right) \quad . \tag{1-4a}$$

By integrating (1-2a), we can form

$$\bar{E} = -j\omega\bar{A} - \nabla\phi \tag{1-4b}$$

where the electric scalar potential function, ϕ , is yet to be fully determined. To fully determine ϕ , we impose the Lorentz condition upon $\bar{A}$ and ϕ , that is

$$\nabla \cdot \bar{A} = -j\omega\varepsilon\mu\phi \tag{1-4c}$$

substituting (1-4a and c) into (1-2c) we form the Helmholtz equation for vector potential (or the vector wave equation),

$$\nabla^2\bar{A} + \beta^2\bar{A} = -\mu\bar{J} \tag{1-5a}$$

where

$$\beta^2 \doteq \omega^2\mu\varepsilon \quad .$$

Likewise, substituting (1-4b) and (1-4c) into (1-2b), we form the Helmholtz equation for scalar potential (or scalar wave equation),

$$\nabla^2\phi + \beta^2\phi = -\rho/\varepsilon \quad . \tag{1-5b}$$

For good conductors, the distributions, $\bar{J}$ and ρ , become the surface distributions, $\bar{J}_s$ and ρ_s . The particular integrals for (1-5a and b) can now be expressed in terms of the given surface distributions and the free space Green's function for outwardly radiating spherical waves. That is,

$$\bar{A}(r) = \mu \iint_S \bar{J}_s(r') \frac{e^{-j\beta R}}{4\pi R} ds' \qquad (1\text{-}6a)$$

and

$$\phi(r) = \frac{1}{\varepsilon} \iint_S \rho_s(r') \frac{e^{-j\beta R}}{4\pi R} ds' \qquad (1\text{-}6b)$$

where

$$R \doteq |r - r'|$$

which is the distance between the field point and the source point. Lastly, the law of conservation of charge is imposed upon J and ρ . Namely,

$$\nabla \cdot \bar{J} = -j\omega\rho \quad . \qquad (1\text{-}6c)$$

At the interface between two media, regions 1 and 2, the following boundary conditions must be satisfied:

$$(\bar{E}_1 - \bar{E}_2) \times \hat{n} = 0 \qquad (1\text{-}7a)$$

$$\hat{n} \times (\bar{E}_1 - \bar{E}_2) = \rho_s/\varepsilon \qquad (1\text{-}7b)$$

$$\hat{n} \times (\bar{H}_1 - \bar{H}_2) = J_s \qquad (1\text{-}7c)$$

$$\hat{n} \times (\bar{H}_1 - \bar{H}_2) = 0 \qquad (1\text{-}7d)$$

where $\hat{n}$ is the unit normal vector to the surface, pointing from region 1 to region 2.

1.2 THIN-WIRE APPROXIMATIONS

Thin-wire approximations are not limited in application to thin-wire structures, as general computer codes have proven themselves useful for modelling arbitrary conducting surfaces with thin-wire grids (20:§ 2.7). If the wire radius, a , is small relative to wavelength and wire junction separations are long relative to radius, then current flow is axial and uniformly distributed around the wire circumference. Further, all currents and charges can then be approximated by equivalent line sources located along the wire axis. In other words,

$$I(l) = 2\pi a J_s(l) \tag{1-8a}$$

$$q(l) = 2\pi a \rho_s(l) \quad . \tag{1-8b}$$

From (1-6c), we can restate the law of conservation of charge,

$$q(l) = \frac{j}{\omega} \frac{\partial I(l)}{\partial l} \tag{1-8c}$$

Finally, the thin-wire solutions to the Helmholtz equations can be written in terms of line integrals,

$$\bar{A}(r) = \mu \int_{\text{wire}} \bar{I}(l') \frac{e^{-j\beta R}}{4\pi R} dl' \tag{1-8d}$$

$$\phi(r) = \frac{j}{\omega\varepsilon} \int_{\text{wire}} \left(\frac{\partial \hat{l}'}{\partial l'} \cdot \bar{I}(l') \right) \frac{e^{-j\beta R}}{4\pi R} dl' \tag{1-8e}$$

These integrals express the potential functions in terms of a known source (current distributions in this case). The boundary condition to be satisfied for thin-wires, from (1-7a), is

$$\hat{l} \cdot (\bar{E}_1 - \bar{E}_2) = 0 \qquad (1\text{-}8f)$$

where $\hat{l}$ is a unit vector along the wire axis. For perfect conductors, $\bar{E}_2 \equiv 0$, and $\bar{E}_1$ can be expressed as a sum of incident and scattered fields such that

$$\bar{E}_i(l') + \bar{E}_s(l') = 0 \qquad (1\text{-}8g)$$

1.3 ISOLATED DIPOLE

The simple, realizable transmitting system in Figure 1 will be replaced by the idealized linear antenna of Figure 2. In this analysis, it is useful and convenient to replace the actual transmitter and transmission line with a "slice" generator (described in equations 1-9a and b).

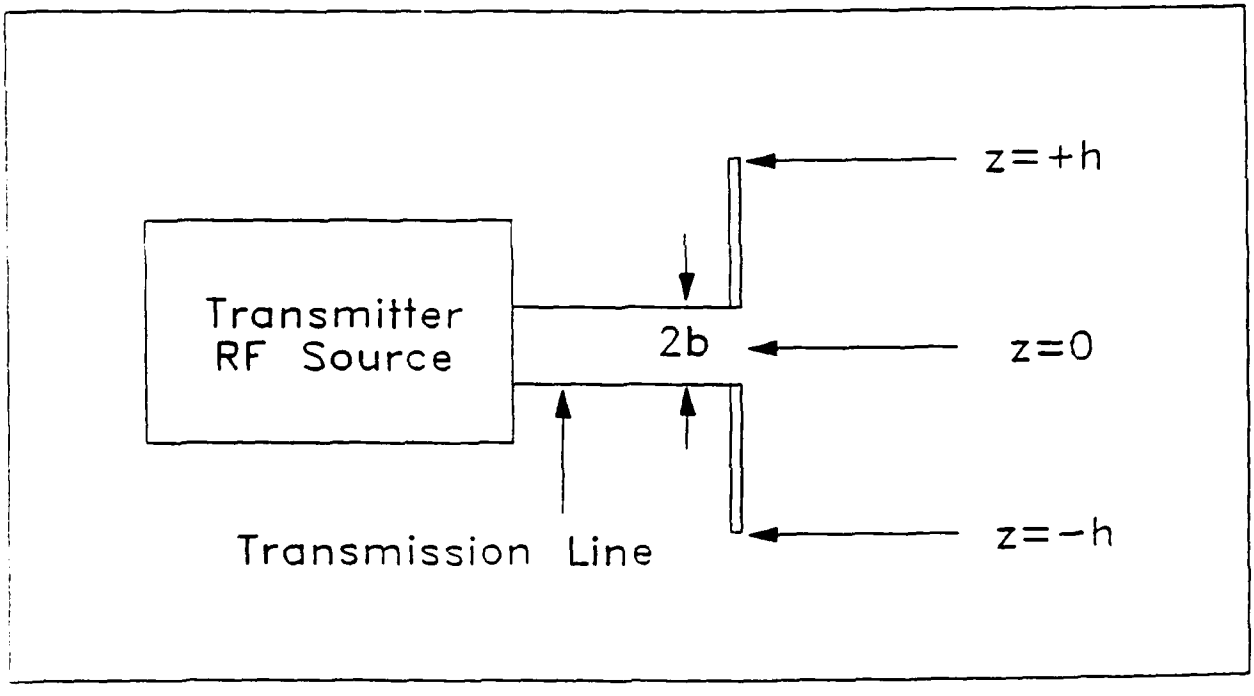

FIGURE 1. REALIZABLE LINEAR TRANSMITTER

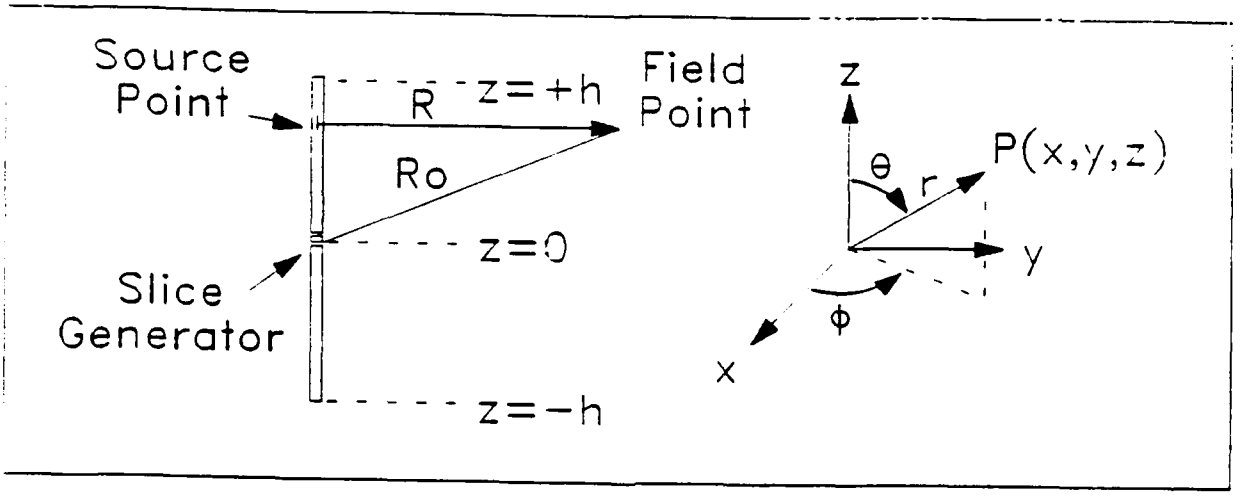

FIGURE 2. IDEALIZED LINEAR TRANSMITTER

Equations describing a "slice" voltage generator.

$$\delta(Z) = \begin{cases} 0, & \text{for } Z \neq 0 \\ 1, & \text{for } Z = 0 \end{cases} \qquad (1\text{-}9a)$$

$$\int_{-h}^{h} V(Z)\delta(Z)dz = V(o) = V_o \qquad (1\text{-}9b)$$

The idealized linear antenna (dipole) is made of a thin, perfectly conducting wire (or tube), of length 2h and radius a, with hemisherical end caps. This antenna is bisected by a "slice" voltage generator which maintains a uniform voltage step between the arms of the antenna. Both the density of current, J, and the volume density of charge, ρ, are exactly zero within a perfect

conductor. In general, the boundary conditions for normal and tangential electric ($\bar{E}$) and magnetic ($\bar{H}$) fields, at the interface between two regions (14:12-13), can be expressed

$$\hat{n}_1 \times \bar{E}_1 + \hat{n}_2 \times \bar{E}_2 = 0 \qquad (1\text{-}10a)$$

$$\hat{n}_1 \times \bar{H}_1 + \hat{n}_2 \times \bar{H}_2 = -(\bar{J}_{s1}+\bar{J}_{s2}) \qquad (1\text{-}10b)$$

$$\hat{n}_1 \cdot \bar{E}_1 + \hat{n}_2 \cdot \bar{E}_2 = -(\rho_{s1}+\rho_{s2})/\varepsilon_o \qquad (1\text{-}10c)$$

$$\hat{n}_1 \cdot \bar{H}_1 + \hat{n}_2 \cdot \bar{H}_2 = 0 \qquad (1\text{-}10d)$$

where $\hat{n}_1$ is the outward unit vector normal to the region 1, $\bar{J}_{si}$ is the density of surface current, and ρ_{si} is the density of surface charge at the interface. If region 1 is defined to be the antenna (perfect conductor), and region 2 is defined to be air, the boundary conditions reduce to,

$$\hat{n}_2 \times \bar{E}_2 = 0 \qquad (1\text{-}11a)$$

$$\hat{n}_2 \times \bar{H}_2 = -\bar{J}_{s1} \qquad (1\text{-}11b)$$

$$\hat{n}_2 \cdot \bar{E}_2 = -\rho_{s1}/\varepsilon_o \qquad (1\text{-}11c)$$

$$\hat{n}_2 \cdot \bar{H}_2 = 0 \quad . \qquad (1\text{-}11d)$$

Equation (1-11a) states that the tangential E-field at the surface of the antenna is continuous and zero. Equation (1-11b) states that the tangential H-field is discontinuous and proportional to the surface density of current on the antenna. Likewise, (1-11c) states that the normal E-field is discontinuous and proportional to the density of surface charge on the antenna. Equation (1-11d) states that the normal H-field is continuous and zero at the surface. For thin, Z-oriented, perfectly conducting, cylindrical antennas, where all vector potential is also Z-oriented, the Laplacians of (1-5a and b) reduce to,

$$(\partial^2/\partial z^2 + \beta_o^2)A_z = 0 \qquad (1\text{-}12a)$$

$$(\partial^2/\partial z^2 + \beta_o^2)\phi = 0 \quad . \qquad (1\text{-}12b)$$

The particular integrals of (1-12a and b) can be derived for Z-oriented antennas from (1-8d and e) and they are

$$A_z = \frac{\mu_o}{4\pi} \int_{-h}^{h} I_z(z') \frac{e^{-j\beta_o R}}{R} dz' \qquad (1\text{-}13a)$$

$$\phi = \frac{1}{4\pi\varepsilon_o} \int_{-h}^{h} q(z') \frac{e^{-j\beta_o R}}{R} dz' \qquad (1\text{-}13b)$$

where the total axial current is from (1-8a),

$$I_z(z) = 2\pi a J_z(z) \qquad (1\text{-}13c)$$

and

$\beta_o = 2\pi/\lambda_o$

$R^2 = (z-z')^2 + a^2$

$q(z)$ is the distribution of charge .

From (1-4a to c), we can totally determine the fields (E and H) from the vector potential, A_z. That is, for Z-oriented dipoles (in cylindrical coordinates),

$$H_\rho = \frac{1}{\mu_o \rho} \frac{\partial A_z}{\partial \phi}$$

$$H_\phi = \frac{-1}{\mu_o \rho} \frac{\partial A_z}{\partial \rho}$$

$$H_z = 0$$

and

$$E_\rho = \frac{-j\omega}{\beta_o^2}\left(\frac{\partial A_z}{\partial \rho \partial z}\right)$$

$$E_\phi = \frac{-j\omega}{\beta_o^2}\left(\frac{1}{\rho}\frac{\partial^2 A_z}{\partial \phi \partial z}\right)$$

$$E_z = \frac{-j\omega}{\beta_o^2}\left(\frac{\partial^2 A_z}{\partial z^2} + B_o^2 A_z\right) \quad .$$

For rotationally symmetric cylindrical antennas, all partial differentials with respect to ϕ vanish, therefore

$$H_\rho = H_z = 0 \qquad (1\text{-}14a)$$

$$H_\phi = \frac{-1}{\mu_o}\frac{\partial A_z}{\partial \rho} \qquad (1\text{-}14b)$$

and

$$E_\phi = 0 \qquad (1\text{-}14c)$$

$$E_\rho = \frac{-j\omega}{\beta_o^2}\left(\frac{\partial^2 A_z}{\partial \rho \partial z}\right) \qquad (1\text{-}14d)$$

$$E_z = \frac{-j\omega}{\beta_o^2}\left(\frac{\partial^2 A_z}{\partial z^2} + \beta_o^2 A_z\right) \quad . \qquad (1\text{-}14e)$$

Translating (1-14a through e) into spherical coordinates, we have

$$H_r = H_\theta = 0$$

$$H_\phi = \frac{-1}{\mu_o} \frac{\partial A_z}{\partial \rho} \tag{1-15a}$$

and

$$E_\phi = 0$$

$$E_r = E_z \cos\Theta + E\rho \sin\Theta$$

$$= \frac{-j\omega}{\beta_o^2} \left[\cos\Theta \left(\frac{\partial^2 A_z}{\partial z^2} + \beta_o^2 A_z \right) + \sin\Theta \left(\frac{\partial^2 A_z}{\partial \rho \partial z} \right) \right] \tag{1-15b}$$

$$E_\theta = - E_z \sin\Theta + E\rho \cos\Theta$$

$$= \frac{-j\omega}{\beta_o^2} \left[\cos\Theta \left(\frac{\partial^2 A_z}{\partial \rho \partial z} \right) - \sin\Theta \left(\frac{\partial^2 A_z}{\partial z^2} + \beta_o^2 A_z \right) \right] \quad . \tag{1-15c}$$

At large distances from the antenna ($r^2 \gg h^2$ & $(\beta_o r)^2 \gg 1$), the field equations reduce to the simpler radiation or far-field expressions (15:6-7), where uniform wave front approximations result in only transverse (but orthogonal) **E** and **H** fields. That is

$$\overline{H}^r = \hat{\phi} H_\phi^r = \hat{\phi} E_\theta^r / C \tag{1-16a}$$

$$\overline{E}^r = \hat{\Theta} E_\theta^r = \frac{j\omega\mu_o}{4\pi} \sin\Theta \int_{-h}^{h} I_z(z') \frac{e^{-j\beta_o R}}{R} dz' \quad . \tag{1-16b}$$

From Figure 3, the distance R, can be expressed via the cosine law

$$R^2 = r^2 + (z')^2 - 2rz'\cos\Theta \quad . \tag{1-17}$$

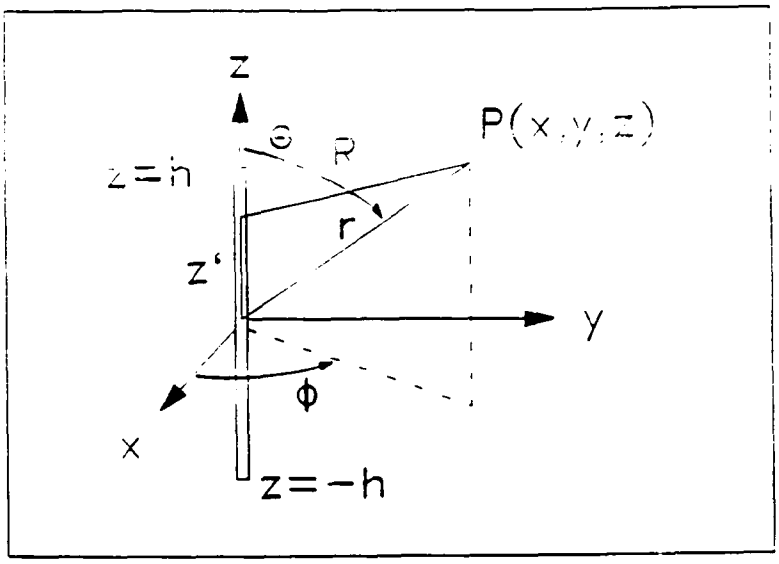

FIGURE 3. FAR-FIELD APPROXIMATION FOR R ($r^2 >> (z')^2$)

In the far-field, where $r^2 \rangle\rangle (z')^2$, the linear terms (in z') of a binomial expansion of (1-17) are sufficiently accurate. Therefore,

$$R \simeq r - z' \cos\Theta \quad . \tag{1-18}$$

This approximation has the useful property of separating the slowly varying amplitude dependence (in r), from the phase dependence in (1-16b). That is,

$$E_\theta^{\,r} = \frac{j\eta_o}{2\pi}\left(\frac{e^{-j\beta_o r}}{r}\right) F_o\,(\Theta,\beta_o h) \tag{1-19a}$$

where

$$F_o(\Theta,\beta_o h) = \frac{\beta_o \sin\Theta}{2}\int_{-h}^{h} I_z(z')e^{j\beta_o z'\cos\Theta}\,dz' \quad . \tag{1-19b}$$

The "field factor", $F_o(\Theta,\beta_o h)$, embodies all directional characteristics of the electric field of a Z-oriented dipole of length 2h. Likewise, the magnetic field, in the radiation zone, is at right angles but proportional to the electric field. From (1-16a) we see that the H-field shares the same directional characteristics, or

$$B_\phi = \frac{j}{2\pi}\left(\frac{e^{-j\beta_o r}}{r}\right) F_o(\Theta,\beta_o h) \quad . \tag{1-19c}$$

To formulate expressions for driving point impedances, we must use the concept of the complex Poynting vector, and the EMF method (15:9-11). The complex Poynting vector is defined as follows,

$$\bar{S} \triangleq \frac{\bar{E} \times \bar{B}^*}{2\mu_o} \equiv \frac{\bar{E} \times \bar{H}^*}{2} \quad . \tag{1-20a}$$

It is convenient to think of S as a vector field indicating the direction and magnitude of power flow. Now the EMF method solves for time average power transmitted by an antenna (more properly by a transmitting system), by taking the real part of the integral of the normal component of S, over a surface that completely encloses a transmitting system (usually a great sphere).

$$P = \mathrm{Re}\left\{\oint_{\Sigma_\tau} \hat{n} \cdot \bar{S}\, d\Sigma\right\} \tag{1-20b}$$

where

$\hat{n}$ is an outwardly pointing unit vector of the surface

Σ_τ is a surface that completely encloses the transmitting system.

If the maximum current value, Im (@ z=0 for h < $\lambda/4$ or @ z = h-$\lambda/4$ for h $\geq \lambda/4$, given sinusoidal currents), is related to the total power radiated through the surface of a great sphere, the concept of radiation resistance, R_m^e, can be defined

$$P \equiv \frac{1}{2} \left| \text{Im} \right|^2 R_m^e \quad . \tag{1-21}$$

The value of R_m^e is not, in general, the same as the driving point resistance, R_o. Only under the conditions of a sufficiently thin ($a/\lambda < 10^{-5}$), resonant dipole ($\beta_o h \rightarrow \pi/2$) does the radiation resistance approximate some of the driving point circuit properties on the antenna (15:14-16).

It is more common, when computing the circuit properties of linear antennas, to integrate S over the cylindrical surface of the antenna (15:22-23). That is for a Z-oriented dipole,

$$P = 2\pi a \int_{-h}^{h} S_\rho \, dz = -\pi a \int_{-h}^{h} E_z H_\phi^* \, dz \tag{1-22}$$

where

S_ρ is the $\hat{\rho}$ directed component of S

E_z is the E-field on the surface of the conductor

H_ϕ^* is the conjugate of the H-field on the surface of the conductor.

Setting (1-22) equal to common circuit equations for the "slice" voltage generator terminals.

$$1/2\ |I_o^2|Z_o \equiv 1/2\ V_o I_o^* = -\pi a \int_{-h}^{h} E_z H_\phi^*\ dz \quad . \tag{1-23a}$$

Solving for the driving point impedance, Z_o, we have

$$Z_o = \frac{-2\pi a}{|I_o|^2} \int_{-h}^{h} E_z H_\phi^*\ dz \quad . \tag{1-23b}$$

The H-field on the cylindrical surface of the conductor can be expressed by plugging (1-13c, 1-14a and b) into 1-11b and solving for H_ϕ^*,

$$H_\phi^* = \frac{-I_z^*}{2\pi a} \tag{1-23c}$$

therefore

$$Z_o = \frac{1}{|I_o|^2} \int_{-h}^{h} E_z I_z^* dz \quad .$$

This approach to the driving point impedance has ignored the boundary condition stated in (1-8f) (15:25-29), which states the tangential E-field vanishes at the surface of a perfect conductor. Since (1-8f) must be satisfied, some impressed E-field, E_z^e, supported by some continuous distribution of voltage generators is also implied. The impressed E-field exactly cancels the E-field in (1-14e), such that

$$E_z + E_z^e \equiv 0 \quad \therefore \quad E_z^e \equiv -E_z$$

Such a continuous distribution of generators is not conducive to the derivation of driving point properties, as there is no unique driving point. The center driven antenna with vanishing tangential E-fields (except in the gap) is therefore fundamentally different from an antenna with tangential E-fields expressed by (1-14e and 1-13a) due to assumed sinusoidal currents. The currents and fields are not generally the same, however under certain circumstances, some properties are comparable. For resonant dipoles, the current amplitude and phase distributions, of the sinusoidal current model, have proven (via measurement) to be reasonably accurate. Characteristics that depend wholely upon the current distribution (I_o, Z_o, & H_ϕ) must also be reasonably accurate. Since the E-field in the radiation zone is proportional to the magnetic field, it is comparable as well. This cannot be said for the full wavelength (antiresonant) dipole.

For near resonant dipoles, even though currents, near zone B-fields and all far zone fields are reasonably approximated by sinusoidal currents, measured charge distributions are very disimilar [15:27], at the center and ends of the antenna, from the cosinusoidal charge distribution required by the condition of conservation of charge. Since the radial E-field, E_ρ, is proportional to the charge per unit length along the antenna, near zone E-fields will not be comparable.

1.4 COUPLED DIPOLES

If it were not for the coupling between antennas, the driving point properties of coupled antennas would be identical to the isolated antenna, and the far-fields would be a straight forward superposition of the fields from each antenna taken separately. Unfortunately, the antennas do couple, so the cur-

rents on one antenna are dependent on the excitation of all antennas (to some degree), and therefore the fields cannot be formulated from the superposition of isolated antennas.

To compute the self and mutual impedances of the coupled dipoles, the EMF method is again employed. This time however, the Z-oriented E-field at the surface of one antenna, is the sum of fields from that antenna's own currents, and the currents of all other antennas. Consider the case of two coupled dipoles, in Figure 4.

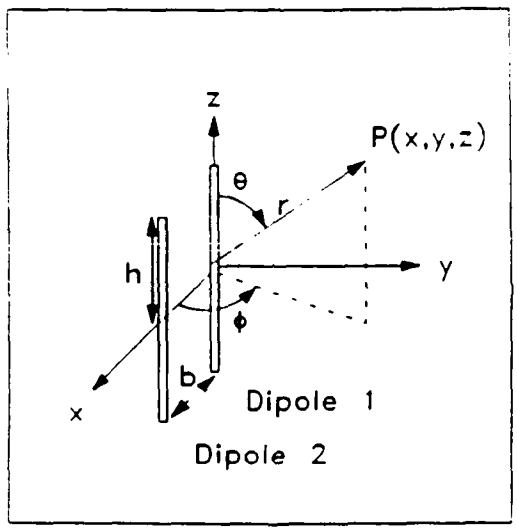

FIGURE 4. COUPLED DIPOLES

For the coupled, Z-oriented dipoles in Figure 4, (1-22) would become the sum,

$$P_k = 2\pi a \int_{-h}^{h} \sum_i \left(S_{\rho ki}\right) d\Sigma \qquad (1\text{-}24a)$$

where

$$S_{pki} = \frac{-E_{zki} H^{*}_{\phi ki}}{2} \qquad (1\text{-}24b)$$

and

P_K is the total, time averaged power crossing though the surface of the Kth dipole

S_ρ is the radially directed Poynting vector

E_{zki} is the E-field at the surface of the Kth dipole due to currents on the ith dipole

$H_{\phi ki}$ is the H-field at the surface of the Kth dipole due to currents on the ith dipole.

Note that the only H-field encircling the Kth dipole is due to currents on the Kth dipole (15:29) (see 1-23c), (1-24a) simplifies to

$$P_k = \frac{1}{2} \int_{-h}^{h} \sum_i \left(E_{zki} I^{*}_{zk} \right) dz \quad . \qquad (1\text{-}24c)$$

Equating (1-24c) to the power expression for the driving point,

$$P_k = \frac{1}{2} |I_{ok}|^2 Z_{ok} = \frac{1}{2} \sum_i \left(I_i I^{*}_k Z_{ik} \right) \qquad (1\text{-}25a)$$

where

$$Z_{ik} \triangleq \left(\frac{1}{I_i I^{*}_k} \right) \int_{-h}^{h} E_{zki} I^{*}_{zk} \, dz \qquad (1\text{-}25b)$$

and

Z_{ok} is the driving point impedance of the Kth dipole

Z_{kk} is the self impedance of the Kth dipole

Z_{ki} is the mutual impedance between the ith and Kth dipoles

I_{ok} is the complex, driving point current amplitude of the Kth dipole

I_k is the complex current amplitude of the Kth dipole due to the excitation on the Kth dipole .

Just as in the isolated dipole case, the sum of all E-fields (E_{zki}) must vanish on the surface of all dipoles, except in the gap region. Note again, however, that the charge distributions, and the radial components of the near zone E-fields, are not well approximated even for near resonant dipoles. This has somewhat greater impact on coupled antennas (15:44-45), because near zone fields become important in determining parasitic (coupled) currents. The far-field is a superposition of far-field from all currents (base driven and parasitic). King-Middleton's two and three-term theories address this problem in particular, in that they solve for the currents on each dipole (allowing those currents to vary across the coupled elements) and then derive the driving point and far-field properties from these more accurate currents.

Even though the assumed sinusoidal currents enable the approximation of driving point self and mutual impedances (from 1-27), they are more central to the computation of far-fields in conventional array theory. Apply (1-16b) to the coupled dipole case in Figure 4. The far-field is now a sum of integrals (one over each element's current distribution).

$$E_\theta = \frac{j\omega\mu_0}{4\pi} \sin\theta \left\{ \int_{-h}^{h} I_{1z}(z') \frac{e^{-j\beta_0 R_1}}{R_1} dz' + \int_{-h}^{h} I_{2z}(z') \frac{e^{-j\beta_0 R_2}}{R_2} dz' \right\} \quad (1\text{-}26)$$

where (see Figure 5)

$$\left.\begin{aligned} R_1 &\approx r - z'\cos\theta \\ R_2 &\approx r - z'\cos\theta - b\cos\phi \end{aligned}\right\} \text{ in the exponential term}$$

$$R_1 = R_2 \approx r \quad \text{in the denominators} \quad .$$

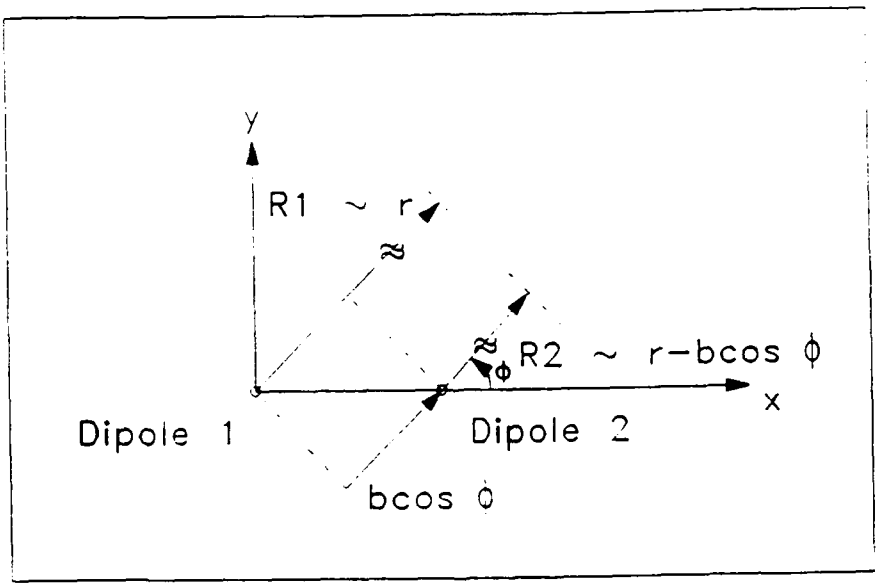

FIGURE 5. FAR-FIELD APPROXIMATION FOR R_1 & R_2

Let each element current include an arbitrary, complex amplitude (current weight), such that

$$I_{iz}(z') = I_{io}\, e^{j\delta_i}\, I_{iz}(z') \quad .$$

Then (1-26) could be rewritten,

$$E_{\Theta}^{r} = \frac{j\omega\mu_{o}}{4\pi} \text{SIN}\Theta \left[\int_{-h}^{h} I_{1_o} e^{j\delta_1} I_{1z}(z') \frac{e^{-j\beta_o(r-z'\text{COS}\Theta)}}{r} dz' \right.$$

$$\left. + \int_{-h}^{h} I_{2_o} e^{j\delta_2} I_{2z}(z') \frac{e^{-j\beta_o(r-z'\text{COS}\Theta-b\text{COS}\phi)}}{r} dz' \right] \quad . \tag{1-27}$$

By assuming all current distributions, $I_{iz}(z')$, are identical, we can separate E_{Θ}^{r} into a field factor, $F_m(\Theta,\beta_o h)$, which embodies all directional properties attributable to the current distribution (assumed to be applicable to all elements), and an array factor, $A(\Theta,\phi)$, which accounts for all time delays (or equivalently phasing) due to geometric placement of each element ($e^{j\beta_o b\text{COS}\phi}$) and the complex current weights ($I_{i_o} e^{j\delta i}$) (see equation 1-28a).

$$E_{\Theta}^{r} \propto \left(\frac{e^{-j\beta_o r}}{r} \right) A(\Theta,\phi) F_m(\Theta,\beta_o h) \quad . \tag{1-28a}$$

$$F_m(\Theta,\beta_o h) \triangleq \frac{\beta_o \text{SIN}\Theta}{2} \int_{-h}^{h} I_z(z') e^{j\beta_o z'\text{COS}\Theta} dz' \tag{1-28b}$$

For a linear array of N elements, the array factor could be extended,

$$A(\Theta,\phi) = \sum_{i=1}^{N} \left(I_{i_o} e^{j(\delta_i+\beta_o(i-1)b\text{COS}\phi)} \right) \quad . \tag{1-29}$$

In actuality, the current distributions on coupled antennas vary with the geometric and electromagnetic environment in an array [14:72-73]. Once again,

King-Middleton's two and three-term expansions for cylindrical antennas will allow for more accurate far-field computations. This accuracy is gained at the expense of evaluating an integral in (1-27) for every coupled antenna.

1.5 RUMSEY REACTION INTEGRAL

The Rumsey Reaction Technique is an alternative physical interpretation, that is useful in this (and many other) electromagnetics analyses. Reaction is basically a measure of coupling between one source and another (20:§ 2.13)(24:§ 7.4). Consider a wire structure (Figure 6) enclosed by a surface S , in the impressed fields, $\bar{E}_i$ and $\bar{H}_i$, due to remote sources, $\bar{J}_i$ and $\bar{M}_i$.

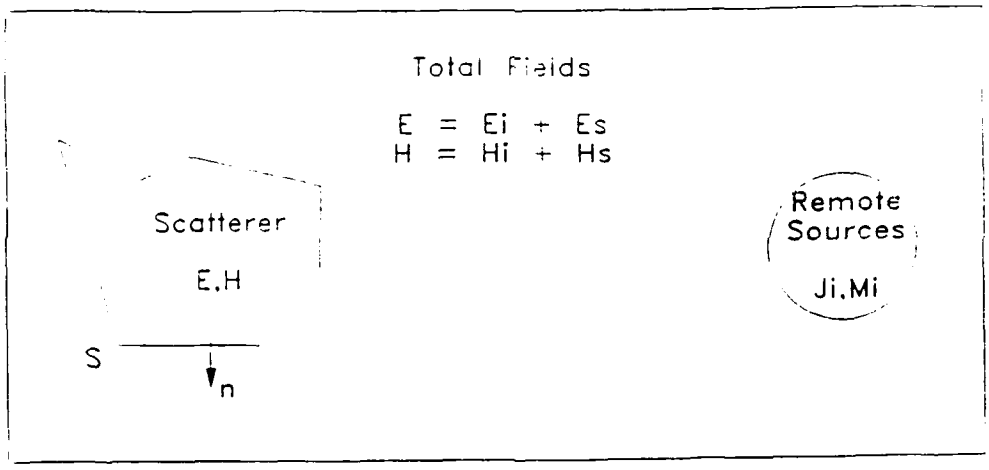

FIGURE 6. SCATTERER IN IMPRESSED FIELDS

The total fields are the sum of incident fields, and scattered fields due to the wire scatter. From Schelkunoff's surface equivalence theorem, the wire scatter can be replaced by equivalent surface sources, $\bar{J}_s$ and $\bar{M}_s$ (see Figure 7). The equivalent sources are defined by the curl expressions,

$$\bar{J}_s = \hat{n} \times \bar{H} \qquad (1\text{-}30a)$$

$$\bar{M}_s = \bar{E} \times \hat{n} \quad . \qquad (1\text{-}30b)$$

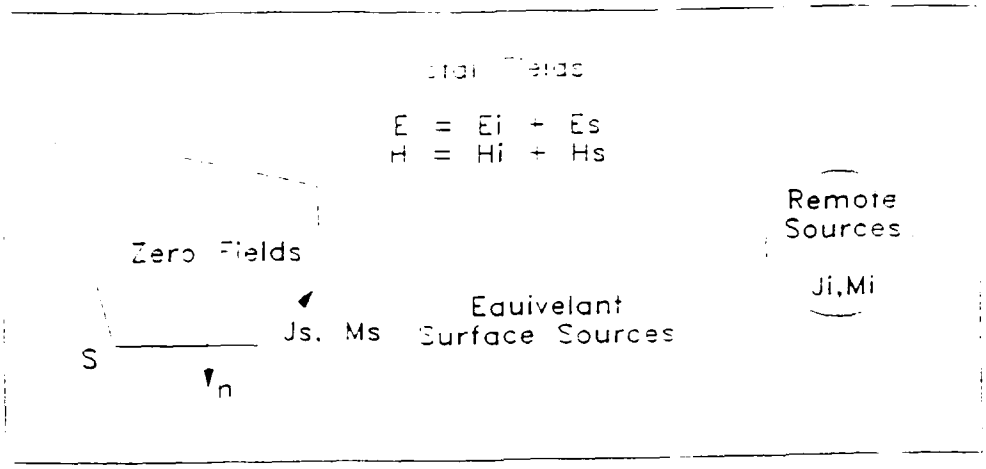

FIGURE 7. EQUIVALENT SURFACE SOURCES

Now add to this problem test sources, $\bar{J}_t$ and $\bar{M}_t$, that are located within S (see Figure 8). The total fields now include a term for the fields due to the test sources.

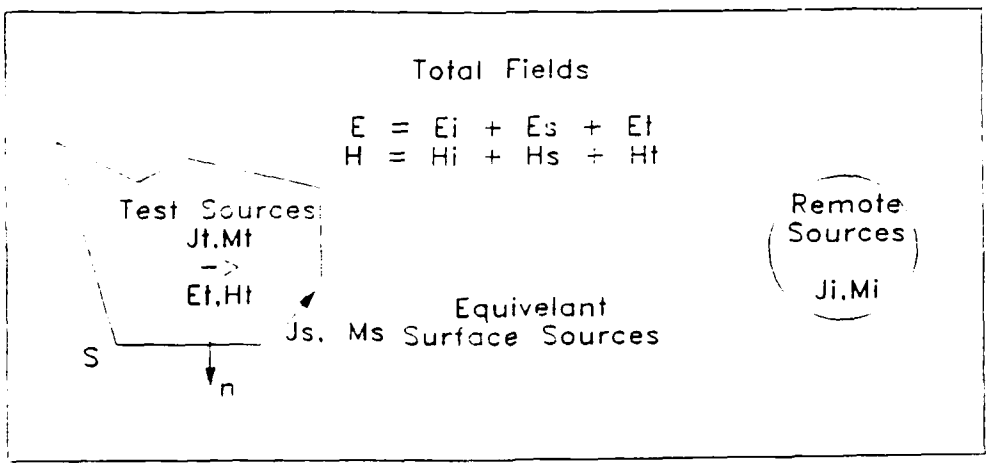

FIGURE 8. ADDITION OF TEST SOURCES

The reaction between the external sources, $\bar{J}_1$ $\bar{J}_2$ $\bar{M}_1$ and $\bar{M}_2$, and the test sources, $\bar{J}_t$ and $\bar{M}_t$, can be expressed in the manner of Rumsey,

$$\langle i+s,t\rangle = \iiint_V \left[\left(\bar{E}_i + \bar{E}_s \right) \cdot \bar{J}_t - \left(\bar{H}_i + \bar{H}_s \right) \cdot \bar{M}_t \right] d\tau = 0 \qquad (1\text{-}31a)$$

By reciprocity, we can also write

$$\langle i+s,t\rangle \equiv \langle t,i+s\rangle = \iiint_V \left[\bar{E}_t \cdot \left(\bar{J}_i + \bar{J}_s \right) - \bar{H}_t \cdot \left(\bar{M}_i + \bar{M}_s \right) \right] d\tau \qquad (1\text{-}31b)$$

For the purposes of this development, assume only electric test sources, only impressed electric sources and a perfectly conducting scatterer. Therefore,

$$\bar{M}_t = 0$$
$$\bar{M}_i = 0$$
$$\bar{M}_s = 0 \quad .$$

Equation (1-31b) reduces to,

$$\iiint_V \left[\bar{E}_t \cdot \left(\bar{J}_i + \bar{J}_s \right) \right] d\tau = 0 \quad . \qquad (1\text{-}32a)$$

Expanding (1-32a) by integrating over electric sources separately, we have

$$\iiint_i \left(\bar{E}_t \cdot \bar{J}_i \right) d\tau + \iint_s \left(\bar{E}_t \cdot \bar{J}_s \right) ds = 0 \quad . \qquad (1\text{-}32b)$$

Applying reciprocity to the integral over the impressed sources,

$$\iiint_t \left(\bar{E}_i \cdot \bar{J}_t \right) d\tau + \iint_s \left(\bar{E}_t \cdot \bar{J}_s \right) ds = 0 \quad . \qquad (1\text{-}32c)$$

For a perfectly conducting scatterers, the test sources, $\overline{J}_t$, will be constrained to the surface also, therefore,

$$\iint_t \left(\overline{E}_i \cdot \overline{J}_t \right) ds = - \iint_s \left(\overline{E}_t \cdot \overline{J}_s \right) ds \quad . \tag{1-32d}$$

Equation (1-32d) is the Rumsey integral equation, which can be solved for $\overline{J}_s$ in terms of known $\overline{E}_i$, and chosen $\overline{J}_t \rightarrow \overline{E}_t$. For thin-wire structures equation (1-32d) can be reduced to line integrals. The Rumsey Reaction Concept is discussed here because it is central to Richmond's Thin-Wire Method of Moments Code. That established code will be used later as a check this anthor's implementation of King-Middleton's Two-Term Theory in this study.

2.0 KING-MIDDLETON'S MODIFIED, ZERO-ORDER, TWO-TERM THEORY

King (14) , and King, Mack, and Sandler (15), after long and careful comparison of linear antenna analyses with measurements, proposed an iterative solution to Hallen's integral equation for currents on a cylindrical dipole. This solution assumed a three-term form for the dipole current distribution, and then solved a boundary value problem to determine the coefficients for each term. King, et al, demonstrated for near resonant isolated dipoles, and for linear arrays of parallel, near resonant dipoles, that a condensed two-term formulation, requiring a lumped capacitive correction to self admittances, is sufficiently accurate. This section presents the relevant two-term equations (derived in Appendix A1), for isolated and coupled dipoles. King-Middleton's Modified, Two-Term Theory (as implemented by this author) will be compared with J.H. Richmond's well known Thin-Wire Method of Moments Code, developed at Ohio State Universities Electroscience Laboratory (21)(22).

2.1 THE ISOLATED DIPOLE

Consider again the idealized dipole in Figure 9. The Hallen Integral Equation relates the magnetic vector potential due to currents along a dipole, to a general solution to the Helmholtz equation for magnetic vector potential.

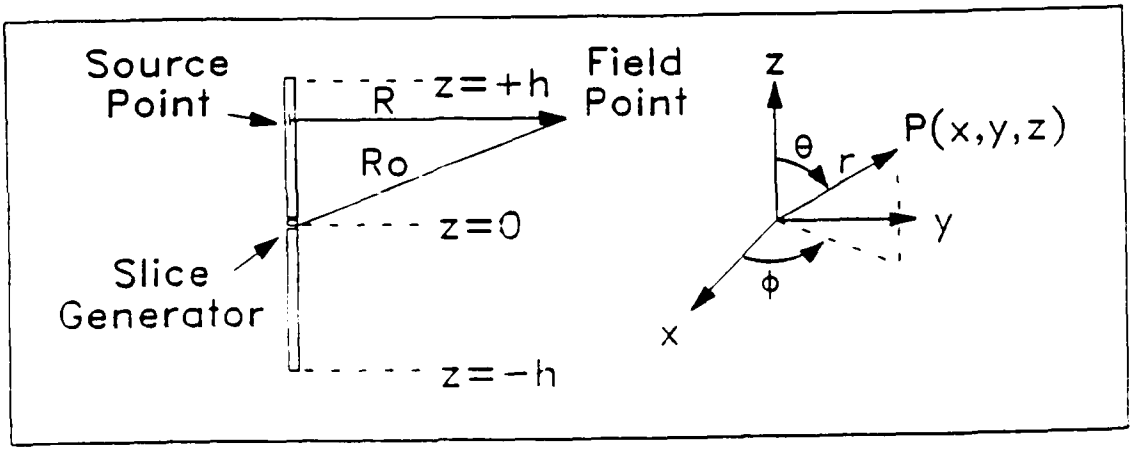

FIGURE 9. IDEALIZED DIPOLE

$$\int_{-h}^{h} I_z(z')K(z,z')dz' = \frac{-j4\pi}{\eta_o}\left(C\ COS\beta_o z + \frac{Vo}{2} SIN\beta_o |z| \right) \qquad (2\text{-}1)$$

where K(z,z') is the free space Green's function. In equation (2-1), C has yet to be determined. King-Middleton actually used a difference integral equation, that enabled them to solve for all coefficients.

$$\int_{-h}^{h} I_z(z')\Big[K(z,z')-K(h,z')\Big]dz' = \frac{-j4\pi}{\eta_o COS\beta_o h}\left(U\ F_{oz}(z) \frac{V_o}{2} M_{oz}(z) \right) \qquad (2\text{-}2a)$$

where V_o is the complex gap voltage, η_o is the intrinsic impedance of free space, and

$$U = \frac{-j\eta_o}{4\pi}\int_{-h}^{h} I_z(z')K(h,z')dz' \qquad (2\text{-}2b)$$

$$F_{oz}(z) = COS\beta_o z - COS\beta_o h \qquad (2\text{-}2c)$$

$$M_{oz}(z) = SIN\beta_o(h-|z|) \quad . \qquad (2\text{-}2d)$$

To reduce (2-2a) to an algebraic expression, King-Middleton expanded the integral into four integrals, over the real and imaginary parts of the Kernal, K(*,z'). Their study of the behavior of each integrand enabled them to approximate each integral by an algebraic term (involving an expansion coefficient). This analysis led King-Middleton to a three-term current form for isolated antennas, which collapsed to a two-term form for near resonant dipoles. By inserting this two-term form into (2-2a), and grouping coefficients of like terms, King-Middleton could solve for the coefficients of the two current terms.

They had thereby determined the current distribution along the dipole. Their two-term theory resulted in,

$$I_z(z) = -\frac{j\,2\pi\,V_o}{\eta_o\;\psi_{dR}}\left(G_{oz}(z) + T'\,F_{oz}(z)\right) \qquad (2\text{-}3a)$$

where

$$T' = \frac{(\psi_v - \psi_u\;\mathrm{SIN}\beta_o h)\;\mathrm{SEC}\;\beta_o h + \psi_{dU}\;\mathrm{SIN}\beta_o h - j\psi_{dI}}{\psi_u - \psi_{dU}\;\mathrm{COS}\beta_o h} \qquad (2\text{-}3b)$$

$$G_{oz}(z) = \mathrm{SIN}\beta_o|z| - \mathrm{SIN}\beta_o h \qquad (2\text{-}3c)$$

and ψ_{dR} , ψ_v , ψ_U , ψ_{dU} , and ψ_{dI} are defined in Appendix A1 (equations A-25a to h). Given the current distribution in (2-3a)(in terms of the dipole geometry and the gap voltage) one can solve directly for the driving point properties (at $z = 0$) , or integrate over the current to compute the farfields. The expression in (2-3a) includes some algebraic and trigonometric manipulation to remain determinate at $\beta_o h = \pi/2$ (see Appendix A1).

In Figure 10, the author'a two-term calculations are compared with King-Middleton's, two-term and three-term theories, as well as Mack's precise measurements, as a function of dipole length (in wavelengths) and a fixed dipole radius (a/λ) . The conductances are seen to agree very well, while the susceptances are seen to be somewhat in error. Figure 11 compares the author's two-term calculations with the output of Richmond's thin-wire code for the same dipole geometry. Richmond's Thin-Wire Code is derived from Rumsey Reaction Concepts applied to thin-wire structures. The test sources and remote sources are chosen to be overlapping sinusoidal dipoles and a generalized impedance

matrix is produced for all sources (21). This is equivalent to a Method of Moments procedure using sinusoidal basis functions and Galerkin's method (21)(12). Again, the author's two-term calculations compare favorably. King-Middleton modified their two-term theory with a lumped capacitive (subceptive) correction at the gap. King (15) supports this modification by discussing the inability of an ideal "slice" generator (infinitesimal discontinuity in scalar potential at the dipole center) to account for terminal zone effects of an actual dipole and driving circuitry. King has successfully matched measured 'apparent' admittances by a lumped subceptive correction. Their correction was chosen to match measurements for $\beta_o h = \pi$. This author chooses to correct his two-term implementation at $\beta_o h = 1.44$, for resonant dipoles which shall be used in later array analysis. Figure 12 shows that a lumped correction of -2.27 mMhos should be used.

By plotting the current in (2-3a) against Mack's measurements for a half wavelength dipole, we note good agreement (see Figure 13). We expect the far-fields from these similar currents to agree equally well.

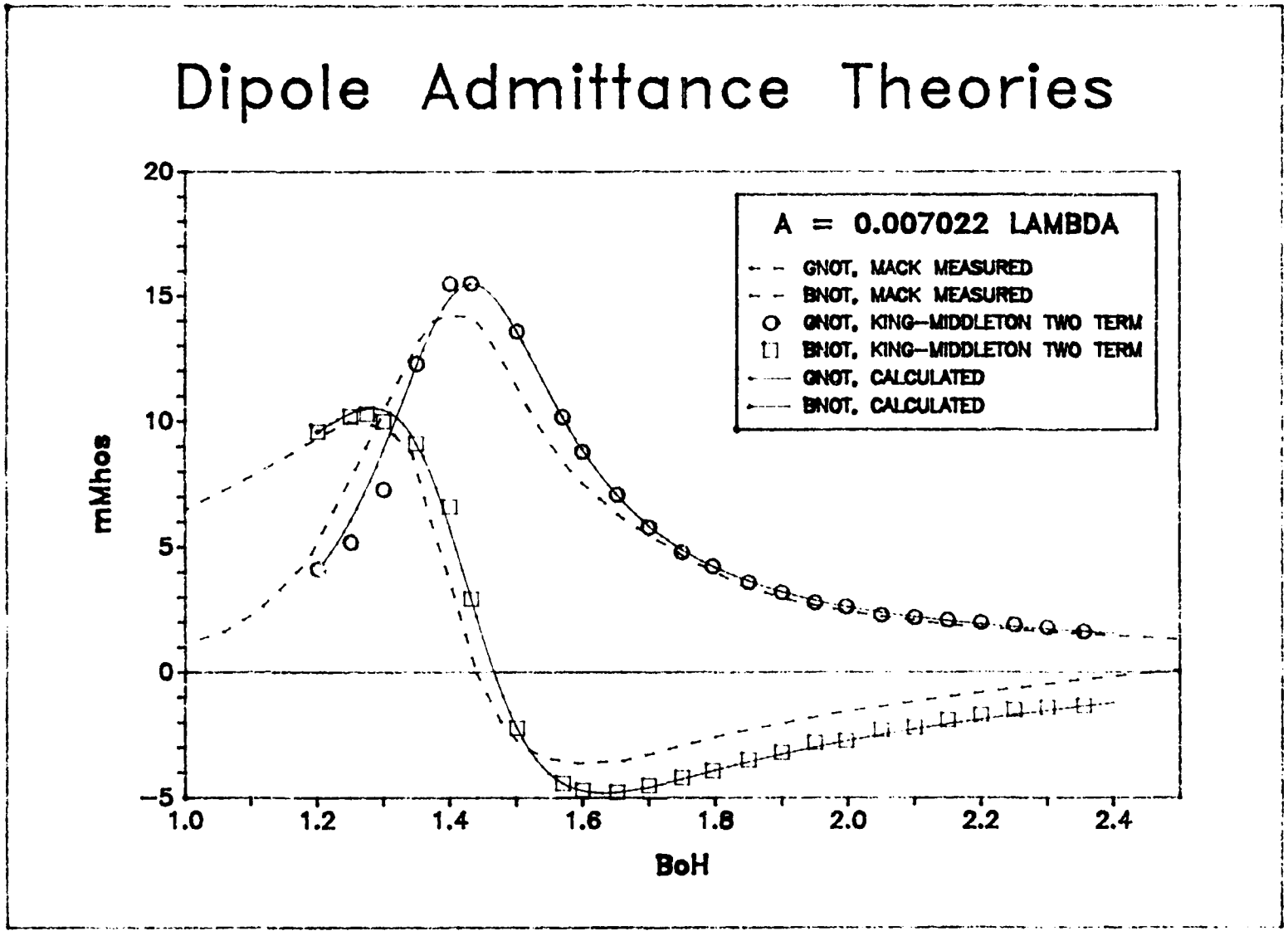

FIGURE 10. COMPARISON OF AUTHOR'S CALCULATED ADMITTANCES WITH KING-MIDDLETON THEORY AND MACK'S MEASUREMENTS

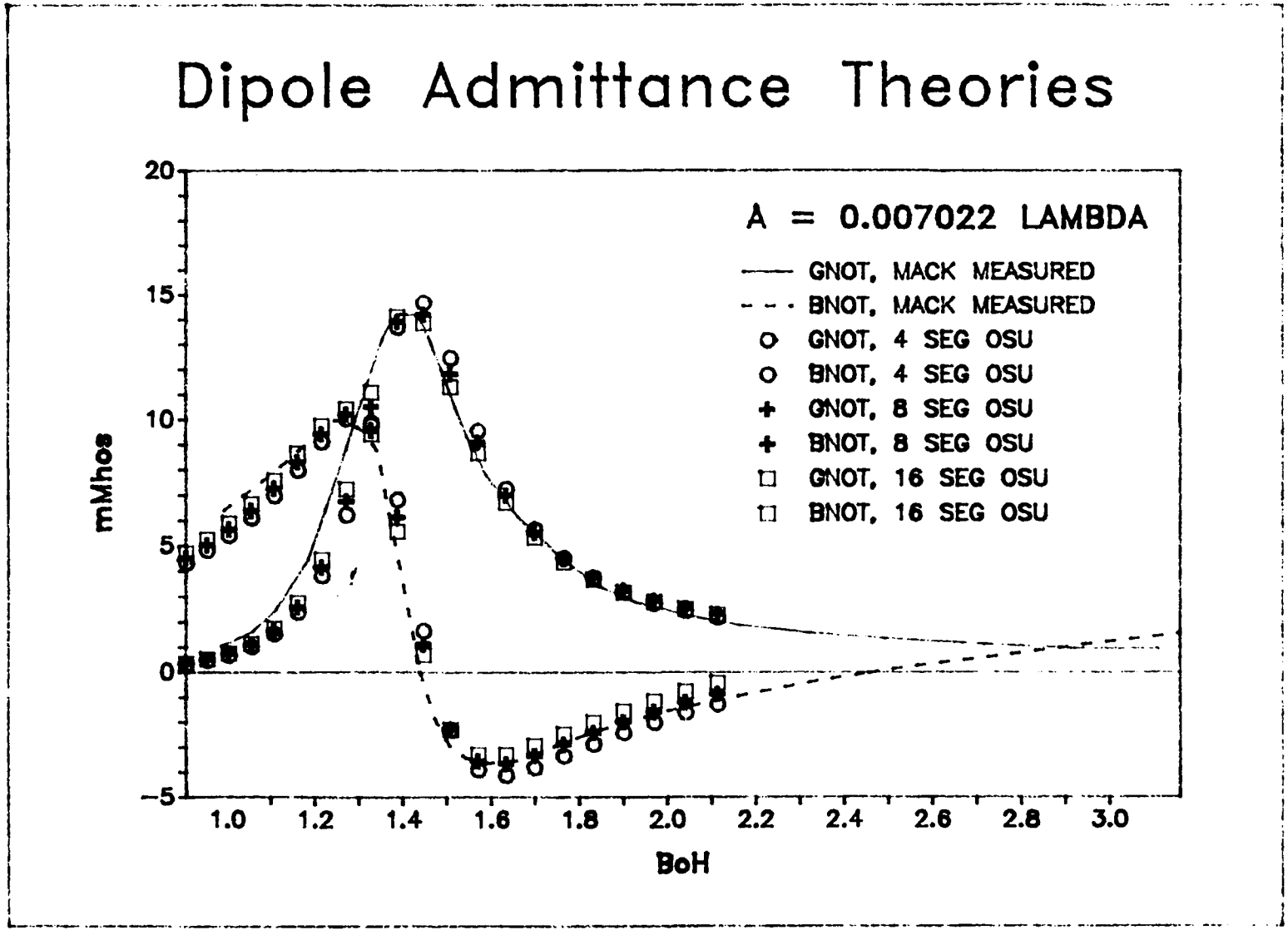

FIGURE 11. COMPARISON OF MACK'S MEASURED ADMITTANCES WITH RICHMOND'S THIN-WIRE CODE

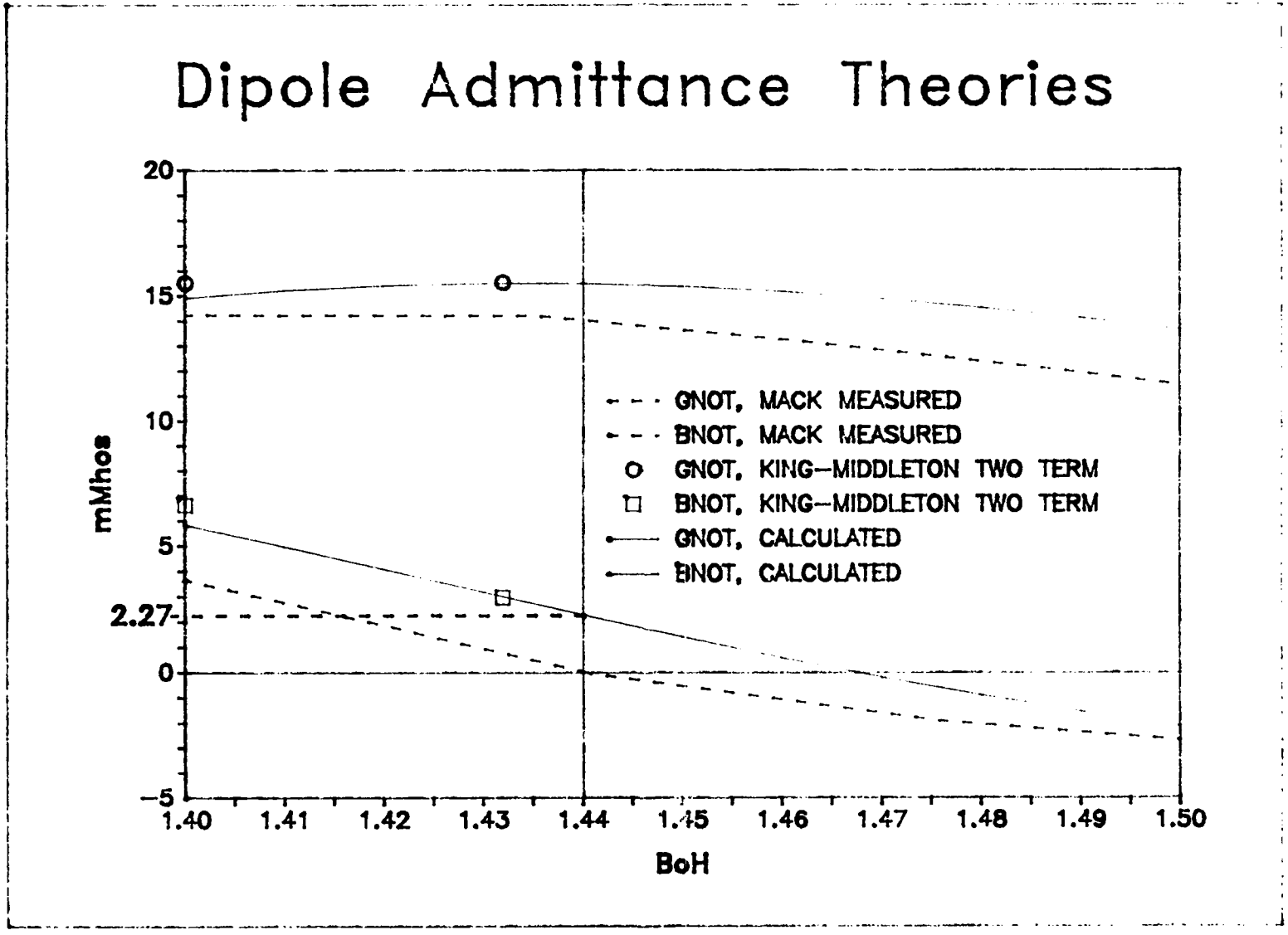

FIGURE 12. SUBCEPTIVE CORRECTION TO TWO-TERM THEORY FOR RESONANT DIPOLE, $\beta_o h = 1.44$

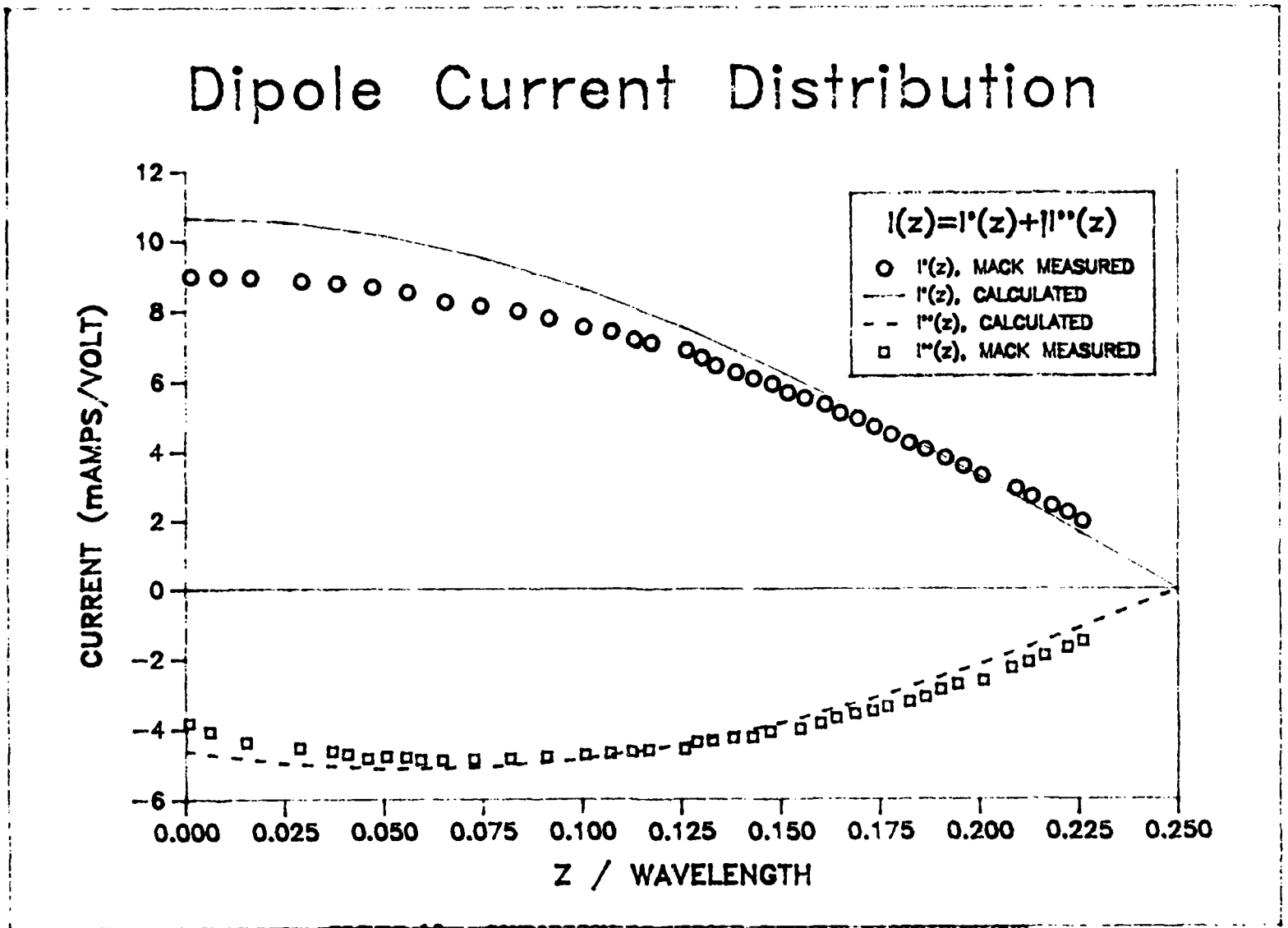

FIGURE 13. COMPARISON OF DIPOLE CURRENT DISTRIBUTIONS

2.2 THE COUPLE DIPOLE

Consider the coupled dipole pair in Figure 14. For coupled dipoles, the magnetic vector potential at the surface of one dipole is due to currents in all dipoles.

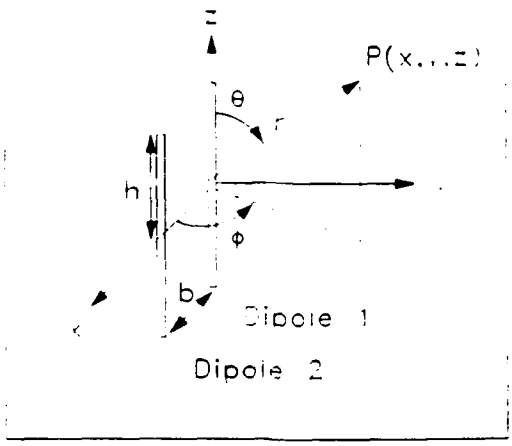

FIGURE 14. COUPLED DIPOLE PAIR

Therefore (2-2a) would be written for dipole 1,

$$\int_{-h}^{h} \left[I_{1z}(z') \left(K_{11}(z,z') - K_{11}(h,z') \right) + I_{2z}(z') \left(K_{12}(z,z') - K_{12}(h,z') \right) \right] dz'$$

$$= \frac{-j\,4\pi}{\eta_o \cos\beta_o h} \left(U_1 F_{oz}(z) + \frac{V_{o1}}{2} M_{oz}(z) \right) \qquad (2\text{-}4a)$$

and for dipole 2,

$$\int_{-h}^{h} \left[I_{2z}(z') \left(K_{22}(z,z') - K_{22}(h,z') \right) + I_{1z}(z') \left(K_{21}(z,z') - K_{21}(h,z') \right) \right] dz'$$

$$= \frac{-j\ 4\pi}{\eta_o \cos\beta_o h} \left(U_2 F_{oz}(z) + \frac{V_{o2}}{2} M_{oz}(z) \right) \qquad (2\text{-}4b)$$

where U_1 , U_2 , $K_{11}(z,z') \equiv K_{22}(z,z')$ and $K_{12}(z,z') \equiv K_{21}(z,z')$ are defined in Appendix A1. Assuming a two-term current form,

$$I_{iz}(z) = jA_i M_{oz}(z) + B_i F_{oz}(z) \qquad (2\text{-}5)$$

we can substitute into (2-4a and b) and apply the appropriate integral reduction rules from Appendix A1. Grouping coefficients of like terms we can solve for A_i's and B_i's. In matrix form we have,

$$\begin{bmatrix} A_1 \\ A_2 \end{bmatrix} = \frac{2\pi}{\eta_o\ \psi_{dR}\ \cos\beta_o h} \begin{bmatrix} V_{o1} \\ V_{o2} \end{bmatrix} \qquad (2\text{-}6a)$$

and

$$\begin{bmatrix} B_1 \\ B_2 \end{bmatrix} = \begin{bmatrix} \phi_u \end{bmatrix}^{-1} \begin{bmatrix} \phi_v \end{bmatrix} \begin{bmatrix} A_1 \\ A_2 \end{bmatrix} \qquad (2\text{-}6b)$$

where the matrices $[\ \phi_u\ ]$ and $[\ \phi_v\ ]$ are defined in Appendix A1. The matrix relationship between dipole base currents, $\mathbf{I}_o$, and gap voltages, $\mathbf{V}$, can be expressed in terms of a generalized admittance matrix, $[\ Y\ ]$. That is,

$$\bar{I}_o = [\ Y\ ]\ \bar{V} \qquad (2\text{-}7a)$$

where

$$\begin{bmatrix} Y \end{bmatrix} = \left(\begin{bmatrix} \phi_u \end{bmatrix}^{-1} \begin{bmatrix} \phi_v \end{bmatrix} F_{oz}(o) + \begin{bmatrix} I \end{bmatrix} M_{oz}(o) \right) \frac{2\pi}{\eta_o\ \psi_{dR}\ \cos\beta_o h} \qquad (2\text{-}7b)$$

and $[\ I\ ]$ is the identity matrix.

Equation (2-7b) is indeterminate at $\beta_o h = \pi/2$ (half wavelength dipoles). To avoid this difficulty a special form can be formulated, producing

$$\left[Y \right] = \left(\left[\phi'_u \right]^{-1} \left[\phi'_v \right] F_{oz}(o) + \left[I \right] G_{oz}(o) \right) \frac{2\pi}{\eta_o \ \psi_{dR}} \tag{2-8a}$$

where

$$\left[\phi'_u \right] = - \left[\phi_u \right] \cos\beta_o h \tag{2-8b}$$

$$\left[\phi'_v \right] = \left[\phi_v \right] + \left[\phi_u \right] \sin\beta_o h \quad . \tag{2-8c}$$

For this special form we can rewrite the two-term current for the ith dipole,

$$I_{iz}(z) = A'_i \ G_{oz}(z) + B'_i \ F_{oz}(z) \tag{2-9a}$$

where

$$A'_i = \frac{2\pi}{\eta_o \ \psi_{dR}} V_{oi} \tag{2-9b}$$

$$\bar{B}' = \left[\phi'_u \right]^{-1} \left[\phi'_v \right] \bar{A}' \quad . \tag{2-9c}$$

This matrix formulation is equally valid for any linear array of parallel dipoles. The diagonal elements of [Y] are self admittances and would be modified with the capacitive correction of Section 2.1. The off-diagonal elements are mutual admittances between dipoles. The inverse of [Y] would be the impedance matrix, [Z] .

To impedance match the ith voltage generator with the ith dipole, its internal impedance should be chosen as the conjugate of the ith dipoles self impedance. In actuality, the active impedance (driving point impedance for given driving voltages across the array, commonly uniform) should be matched. As active impedances vary with frequency and scan condition (7), that match is normally made for center frequency and broadside conditions (endfire condition for endfire arrays).

Figure 15 plots self and mutual admittances for King-Middleton modified, two-term theory, Richmond's thin-wire code, Mack's measurements, and the author's calculations for a pair of full wavelength dipoles, as a function of the dipole separation, b/λ . The self admittances, as in the isolated dipole case, include a capacitive correction to the self subceptance.

Table I compares the active (driven) admittances and impedances across a 10 element linear array of full wavelength dipoles, as computed by King-Middleton Two-Term Theory (unmodified) (16), OSU Thin-Wire Code (less King-Middleton Subceptive Correction) and the author's Two-Term calculations (unmodified). Table entries are in good agreement. The bar chart in Figure 16 compares the magnitude of the dipole active base currents (normalized to the center elements) for a uniformly illuminated 10 element array. Again all three methods agree very well.

To compute the far-fields of coupled dipoles one must superpose the contribution of each current term from each dipole. For the dipole pair $(N=2)$, we can write

$$E_\theta^r = \frac{j\omega\mu_o}{4\pi}\left(\frac{e^{-j\beta_u r}}{r}\right)\mathrm{SIN}\Theta \quad X$$

$$\sum_{i=1}^{N}\left[\left(A_i' G_m(\Theta,\beta_o h) + B_i' F_m(\Theta,\beta_o h)\right) e^{j\beta_u b_i \mathrm{COS}\Theta}\right] \qquad (2\text{-}10)$$

where $G_m(\Theta,\beta_o h)$ and $F_m(\Theta,\beta_o h)$ are as defined in Appendix A1. In this work, the coordinate system is referenced to the gap of dipole 1, so b_i is the separation between the gap of the ith dipole and the gap of dipole 1.

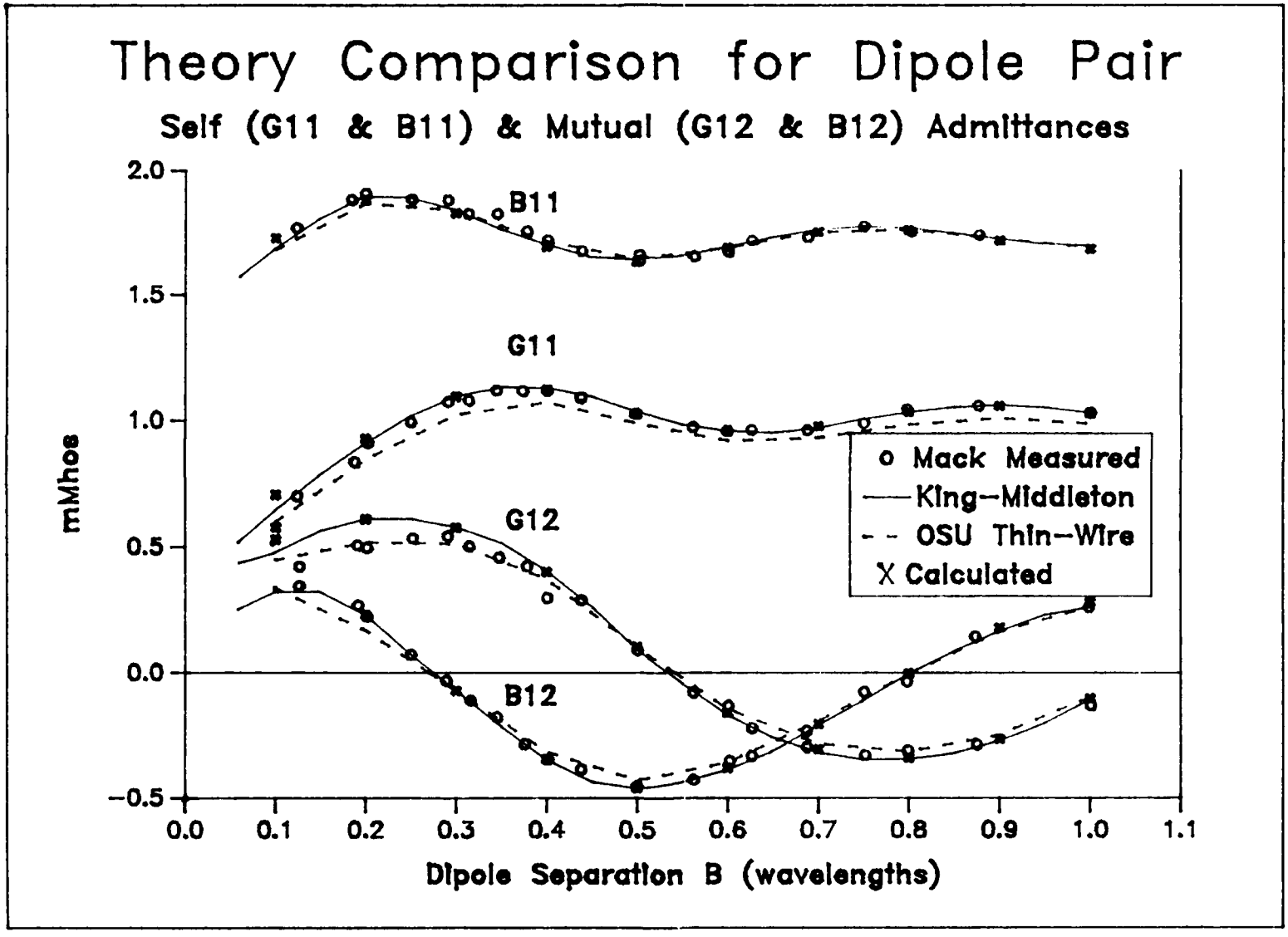

FIGURE 15. COMPARISON OF COUPLED DIPOLE ADMITTANCES

10 ELEMENT BROADSIDE ARRAY

$\beta_o h = \pi$ $\quad h/\lambda = .5$

$\beta_o b = \pi$ $\quad b/\lambda = .5$

$\Omega = 2 \ln (2h/a) = 10$ $\quad a/\lambda = .00673795$

KING-MIDDLETON		OSU THIN-WIRE		CALCULATED	
ADMITTANCE (mMhos)	IMPEDANCE (Ohms)	ADMITTANCE (mMhos)	IMPEDANCE (Ohms)	ADMITTANCE (mMhos)	IMPEDANCE (Ohms)
1.059 +j 0.600	714.585 -j 405.086	1.040 +j 0.568	740.507 -j 404.314	1.074 +j 0.566	728.689 -j 383.638
1.109 +j 0.198	873.705 -j 156.039	1.097 +j 0.187	885.608 -j 150.921	1.125 +j 0.157	871.727 -j 121.467
1.058 +j 0.363	845.679 -j 290.370	1.052 +j 0.341	860.146 -j 279.097	1.073 +j 0.325	853.783 -j 258.363
1.092 +j 0.285	857.310 -j 223.673	1.080 +j 0.267	872.306 -j 215.664	1.108 +j 0.245	860.391 -j 190.404
1.076 +j 0.317	855.336 -j 252.234	1.067 +j 0.298	869.361 -j 243.020	1.091 +j 0.278	860.567 -j 219.243
1.076 +j 0.317	855.336 -j 252.234	1.067 +j 0.298	869.361 -j 243.020	1.091 +j 0.278	860.567 -j 219.243
1.092 +j 0.285	857.310 -j 223.673	1.080 +j 0.267	872.306 -j 215.664	1.108 +j 0.245	860.391 -j 190.404
1.058 +j 0.363	845.679 -j 290.370	1.052 +j 0.341	860.146 -j 279.097	1.073 +j 0.325	853.783 -j 258.363
1.109 +j 0.198	873.705 -j 156.039	1.097 +j 0.187	885.608 -j 150.924	1.125 +j 0.157	871.727 -j 121.467
1.059 +j 0.600	714.585 -j 405.086	1.040 +j 0.568	740.507 -j 404.314	1.074 +j 0.566	728.689 -j 383.638

TABLE I. COMPARISON OF ACTIVE IMPEDANCES OF UNIFORMLY DRIVEN, 10 ELEMENT LINEAR ARRAY

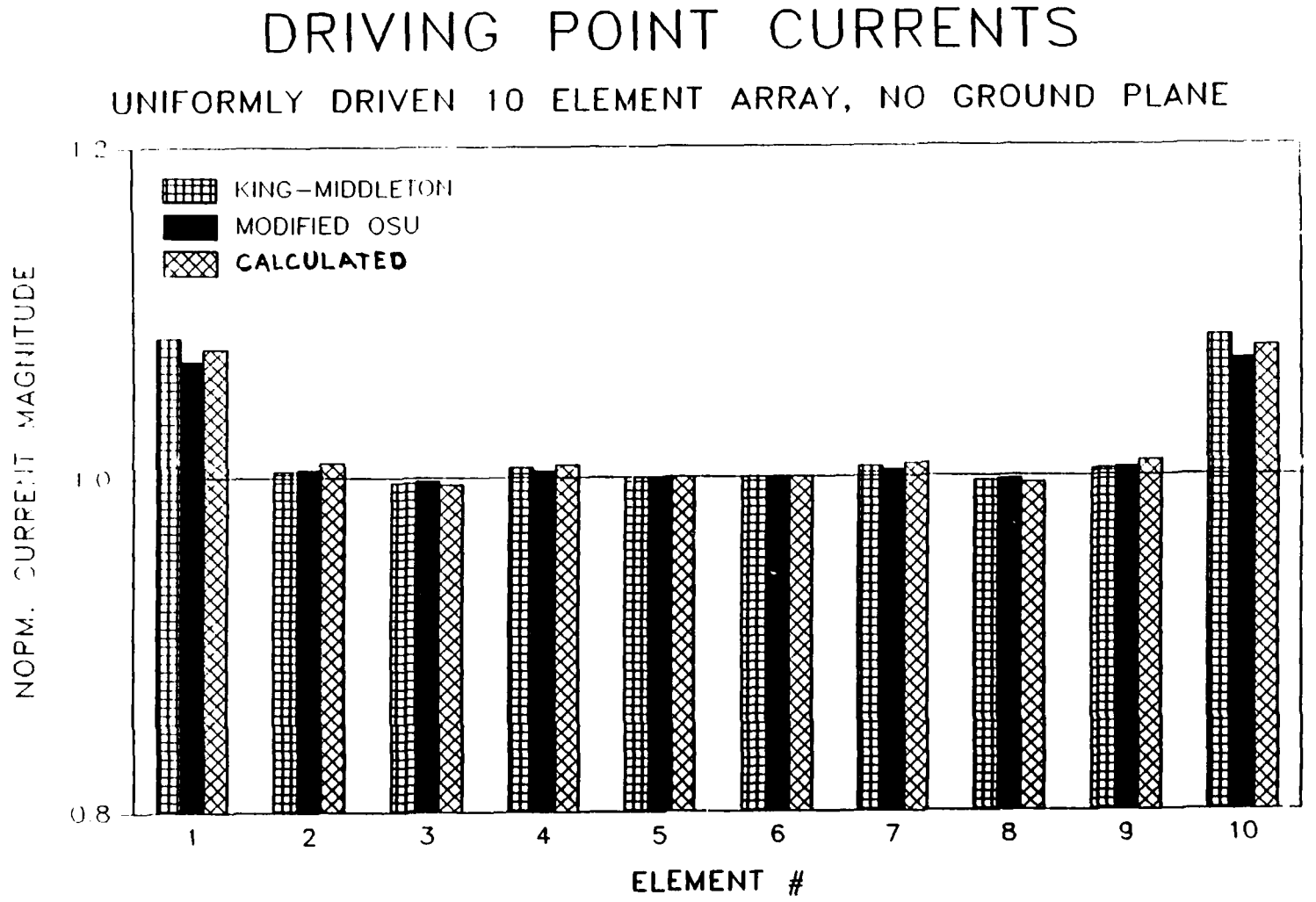

FIGURE 16. COMPARISON OF ACTIVE BASE CURRENT FOR UNIFORMLY DRIVEN, 10 ELEMENT LINEAR ARRAY

3.0 LINEAR ARRAY OF PARALLEL DIPOLES

To extend the theory of section two to the analysis of larger linear array geometries, one starts with a multi-port matrix model of an isolated array of tuned dipoles, then models a ground plane via image dipoles. The generalized admittance matrix is computed using King-Middleton's, modified two-term theory, for all dipoles real and imaginary. The array is element-by-element impedance matched, for the uniformly illuminated broadside condition, by choosing the voltage generator's internal impedance based upon each elements active impedance under broadside, uniformly driven conditions. Lastly various Dolph-Chebyshev amplitude tapers (for sidelobe control) and linear phase tapers (for scanning control) will be applied via the voltage generators. Array size, in conjunction with amplitude and phase tapers, will be varied to investigate coupling effects on low-side lobe array design.

3.1 LINEAR ARRAY MODEL

Figure 17 illustrates a geometry for a linear array of N parallel dipoles. Figure 18 illustrates the 2N port matrix model of this array. For this study, the array geometry will be

$$\beta_o h = 1.44 \rightarrow h/\lambda = 0.2291831 \qquad (3\text{-}1a)$$

$$a/\lambda = 0.007022 \qquad (3\text{-}1b)$$

$$d/\lambda = 0.5 \qquad (3\text{-}1c)$$

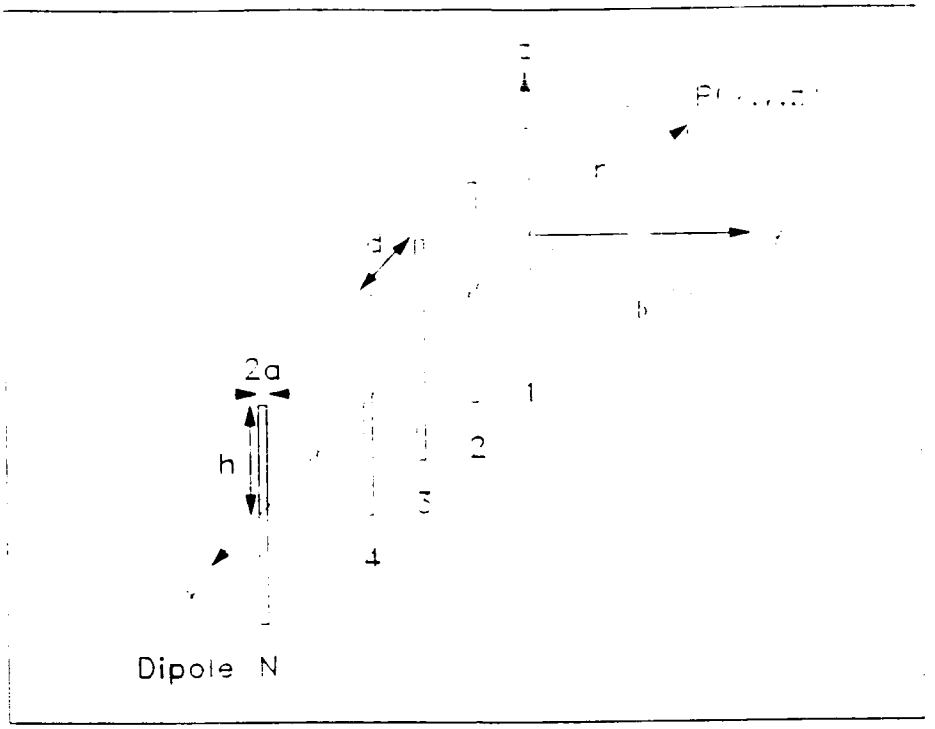

FIGURE 17. ISOLATED LINEAR ARRAY ON N PARALLEL DIPOLES

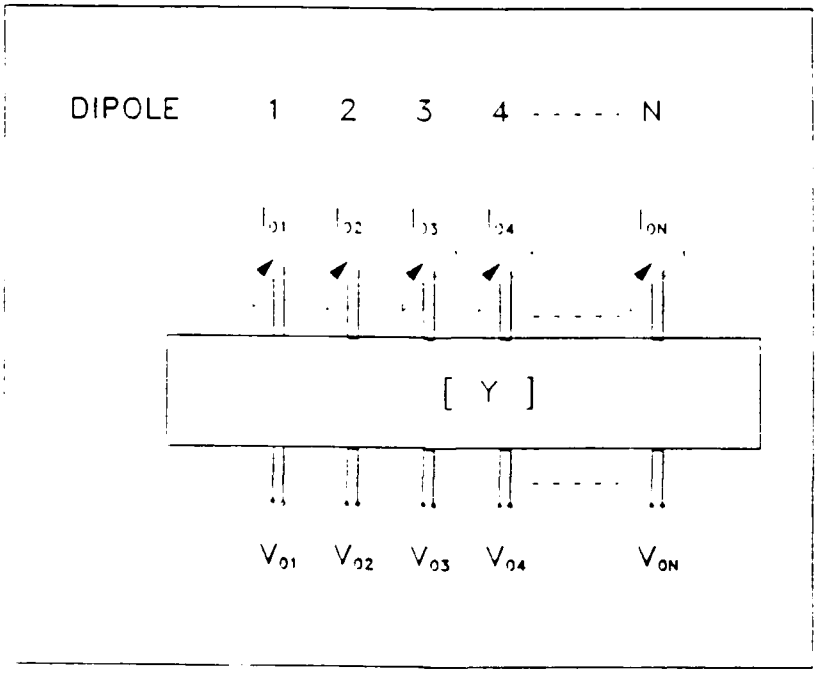

FIGURE 18. 2N PORT MATRIX MODEL OF LINEAR ARRAY IN FIGURE 17

The generalized admittance matrix, [Y] , would be computed using King-Middleton Theory. The addition of a ground plane, 1/4 wavelength behind the array ($s/\lambda = 0.5$) , is accomplished using image dipoles with inverted generator voltages (9:§ 2.5) (see Figures 19 and 20).

The voltages, V_{oi} , in Figure 20 imply ideal voltage generators with zero internal impedances. A constant power, voltage source, which includes an internal impedance, is more realistic. To include constant power sources in the array model, inspect Figure 21 for the equivalent circuit of the ith dipole and its voltage source. A common voltage divider relationship exists between the generator voltage, V_{oi} , and the gap voltage, V'_{oi} . This relationship can be expressed,

$$V'_{oi} = V_{oi} \left(\frac{Z_{ii}}{Z_{ii} + Z_{gi}} \right) \equiv V_{oi} \left(\frac{Y_{gi}}{Y_{gi} + Y_{ii}} \right) \quad . \tag{3-2}$$

The gap voltages from (3-2) can now be applied to the admittance matrix as in Figure 22.

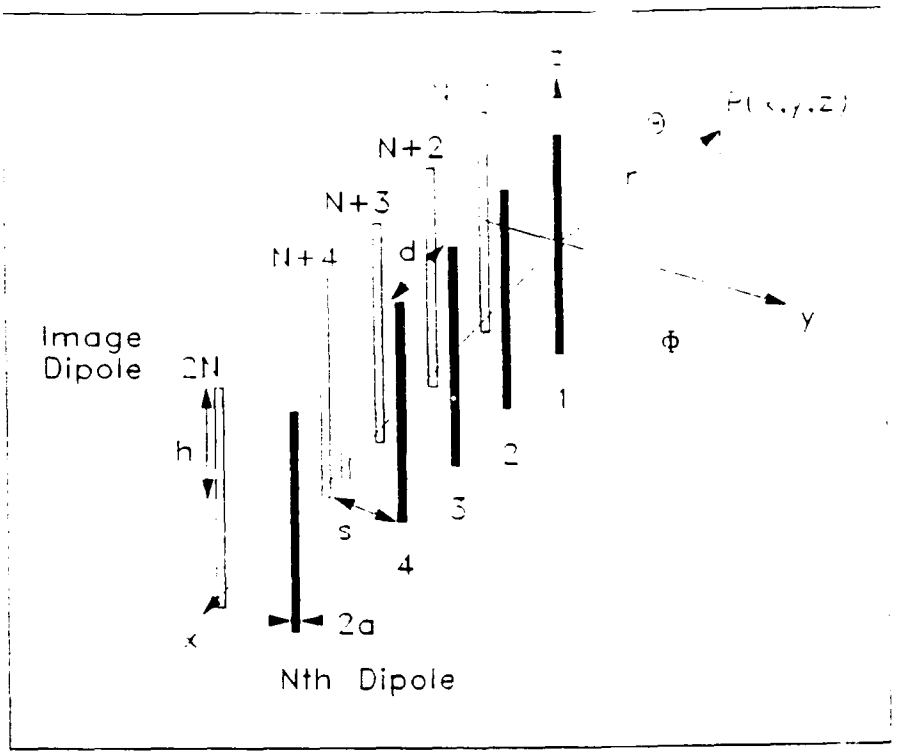

FIGURE 19. LINEAR ARRAY OF HORIZONTAL DIPOLES OVER A GROUND PLANE MODELLED BY IMAGE ARRAY (AT Y = -S)

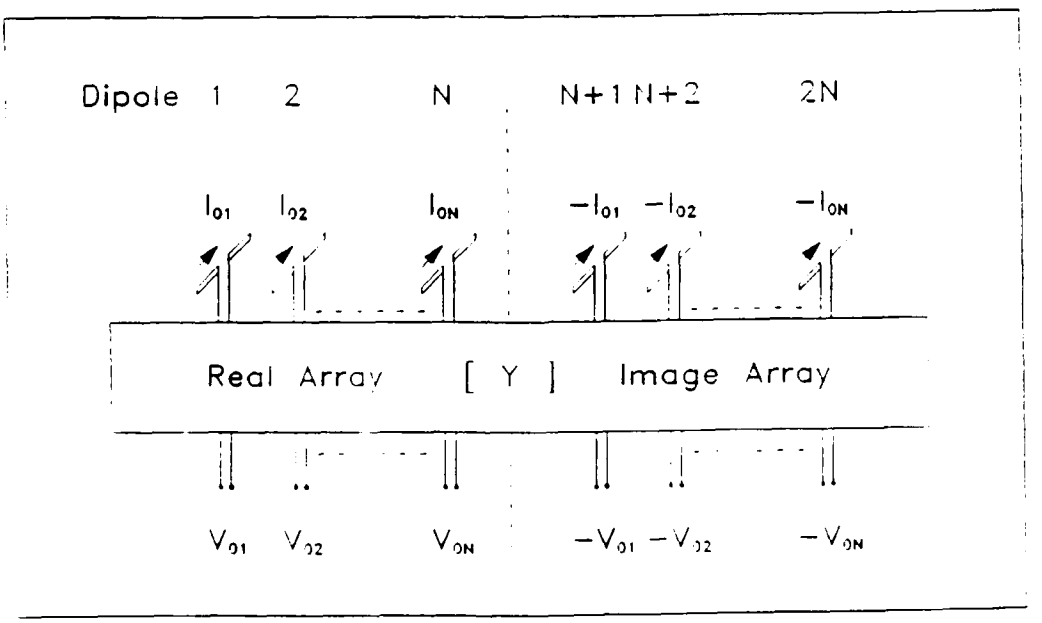

FIGURE 20. 4N PORT MATRIX MODEL OF LINEAR ARRAY OVER GROUND PLANE

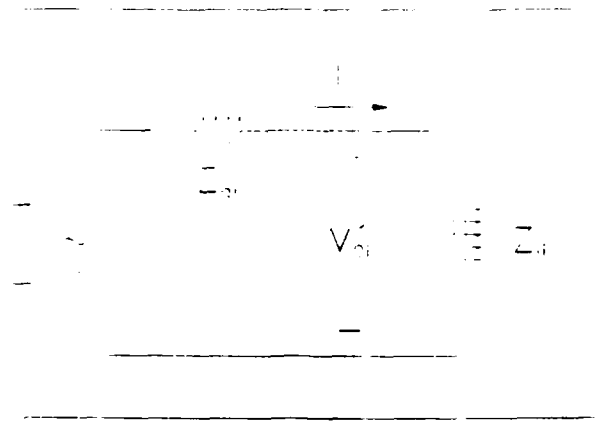

FIGURE 21. EQUIVALENT CIRCUIT FOR iTH DIPOLE AND CONSTANT POWER, VOLTAGE SOURCE

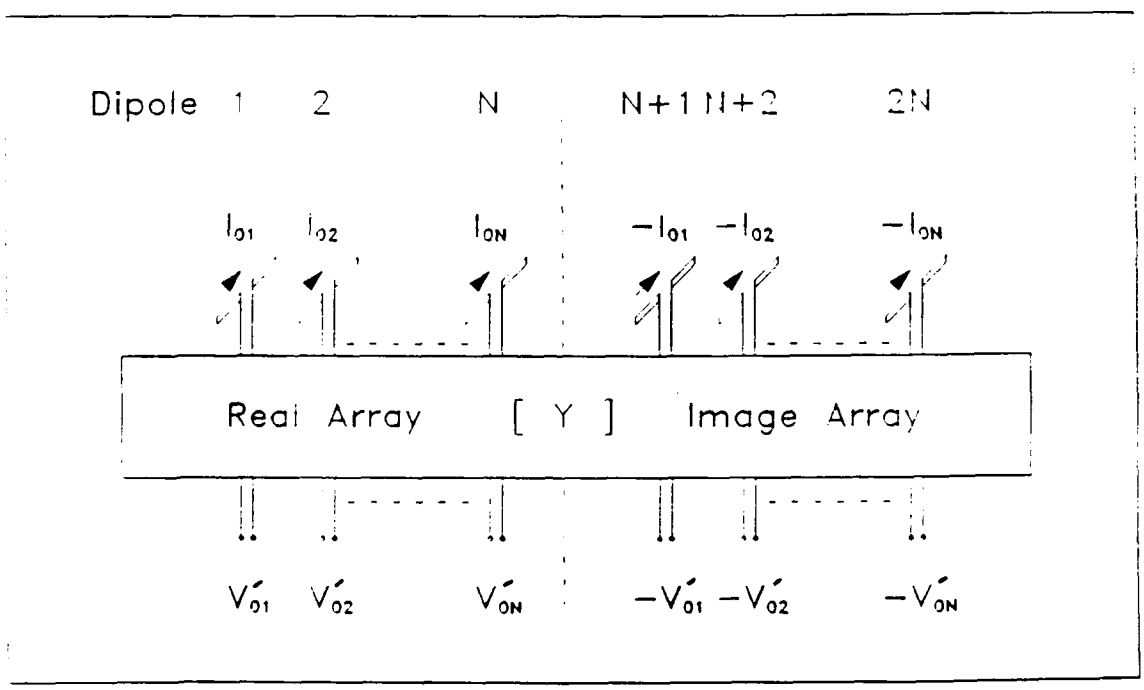

FIGURE 22. 4N PORT MATRIX MODEL OF LINEAR ARRAY IN FIGURE 19, APPLYING NEW GAP VOLTAGES TO IMPEDANCE TO MATRIX [Y]

3.2 IMPEDANCE MATCHING

Due to mutual coupling, currents are induced on a dipole by all voltage sources in the array. Impedance matching the ith voltage generator to the self

impedance of the ith dipole is therefore insufficient. Impedance matching to the "active" impedance of the ith dipole is better. Active impedances are commonly measured (or calculated) for uniform voltage distributions with no phase slope (no scanning). The active impedances can be calculated from (A-44b) as follows,

$$i_a = \left[Y \right] V_u \qquad (3\text{-}3a)$$

where

$$i_a \doteq \begin{bmatrix} i_{a1} \\ \cdot \\ \cdot \\ \cdot \\ \cdot \\ i_{a2u} \end{bmatrix} \quad \text{, active base currents} \qquad (3\text{-}3b)$$

$$[\ Y\ ] \doteq \text{generalized admittance matrix from (A-4b)} \qquad (3\text{-}3c)$$

$$V_u \doteq \begin{bmatrix} 1 \\ \cdot \\ \cdot \\ \cdot \\ 1 \\ \cdots \\ -1 \\ \cdot \\ \cdot \\ \cdot \\ -1 \end{bmatrix} = \text{uniform voltage distribution for real and image arrays} \qquad (3\text{-}3d)$$

and

$$Y_{ai} \doteq i_{ai}/V_{ui} = \text{active admittance} \qquad (3\text{-}4a)$$

$$Z_{ai} \doteq 1/Y_{ai} = \text{active impedance} \quad . \qquad (3\text{-}4b)$$

Choosing the ith voltage generator's internal impedance, Z_{gi}, to be the

conjugate of the ith dipole's active impedance, maximizes the power transferred to (radiated by) the dipole, and therefore impedance matches the voltage generator for uniformly illuminated, broadside conditions. Assuming the array will scan some volume about broadside, this is also a reasonable match over expected scan conditions. Note that both the currents and driving voltages for image dipoles are negative, therefore the active impedance of these dipoles and their images are equal. Substituting Y_{ai}^{*} for Y_{gi} in (3-2) incorporates an element-by-element active impedance match into the 4N port matrix model, illustrated in Figure 22.

3.3 CHEBYSHEV AMPLITUDE TAPER

The generator voltages, V_{oi}, in Figure 18, are complex array weights that can be varied to control features of the array's farfield pattern. Dolph-Chebyshev amplitude tapers are real (amplitude only) tapers developed by Dolph (8) and pursued by Brown and Sharpe (2) as a realizable manner to optimize either beamwidth given a sidelobe constraint, or sidelobe levels given a beamwidth constraint. The far-fields of Chebyshev line sources (and linear arrays) are characterized by uniform sidelobe levels and the narrowest possible beamwidth given that sidelobe level (see Figure 23).

There are approximate methods (10)(1) for synthesizing Chebyshev array weights, however the methods result in approximate Chebyshev patterns, having non-uniform sidelobe structure. To obtain true Chebyshev patterns, cumbersome perturbation techniques are applied to alter the zeroes of the approximate pattern. Sharpe and Brown (2) have already accomplished this procedure for a variety of array sizes and sidelobe levels. In this analysis, their tabulated array weights will be used as voltage generator weights (see Figure 24 to 27).

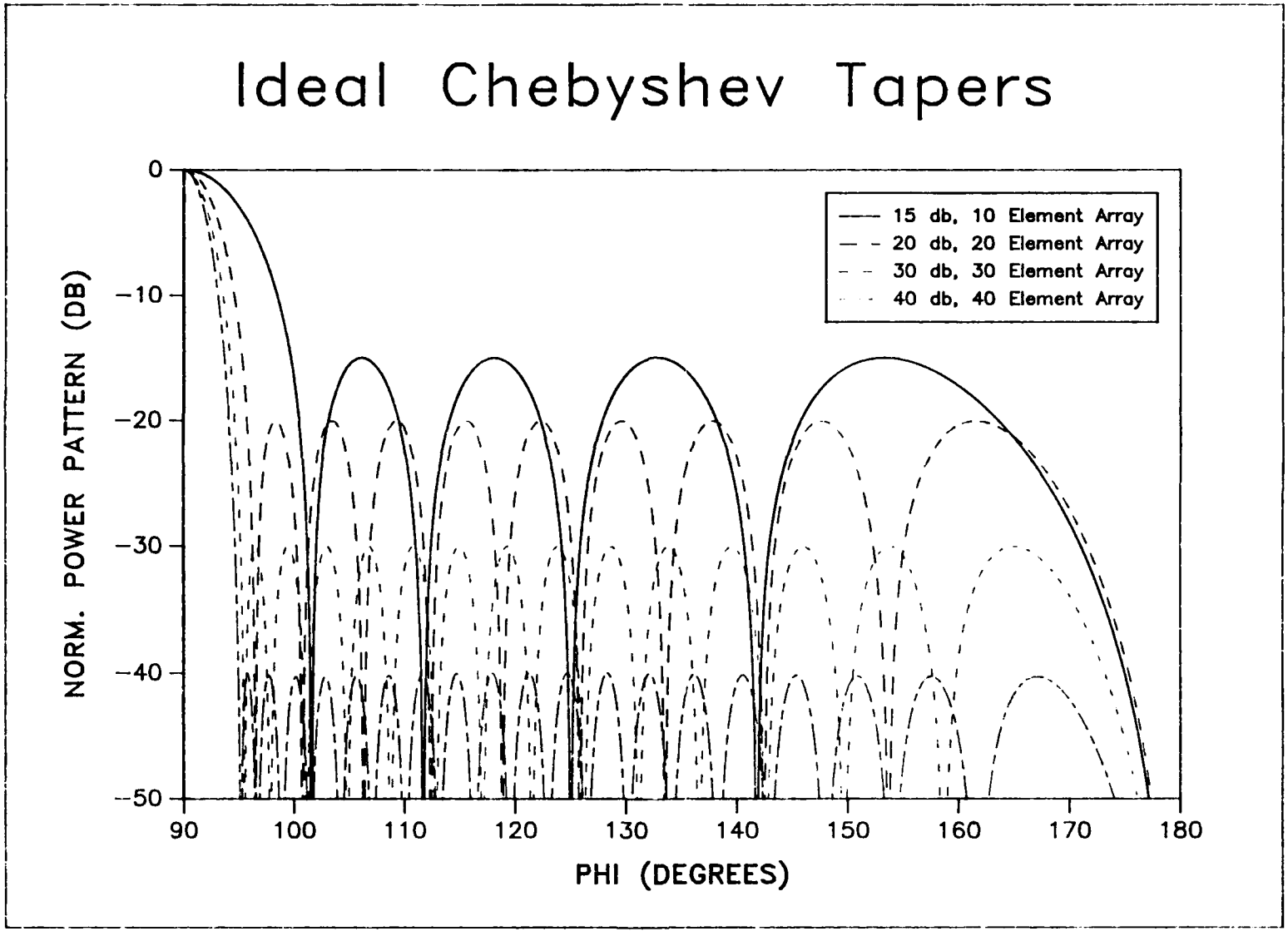

FIGURE 23. IDEAL CHEBYSHEV PATTERNS

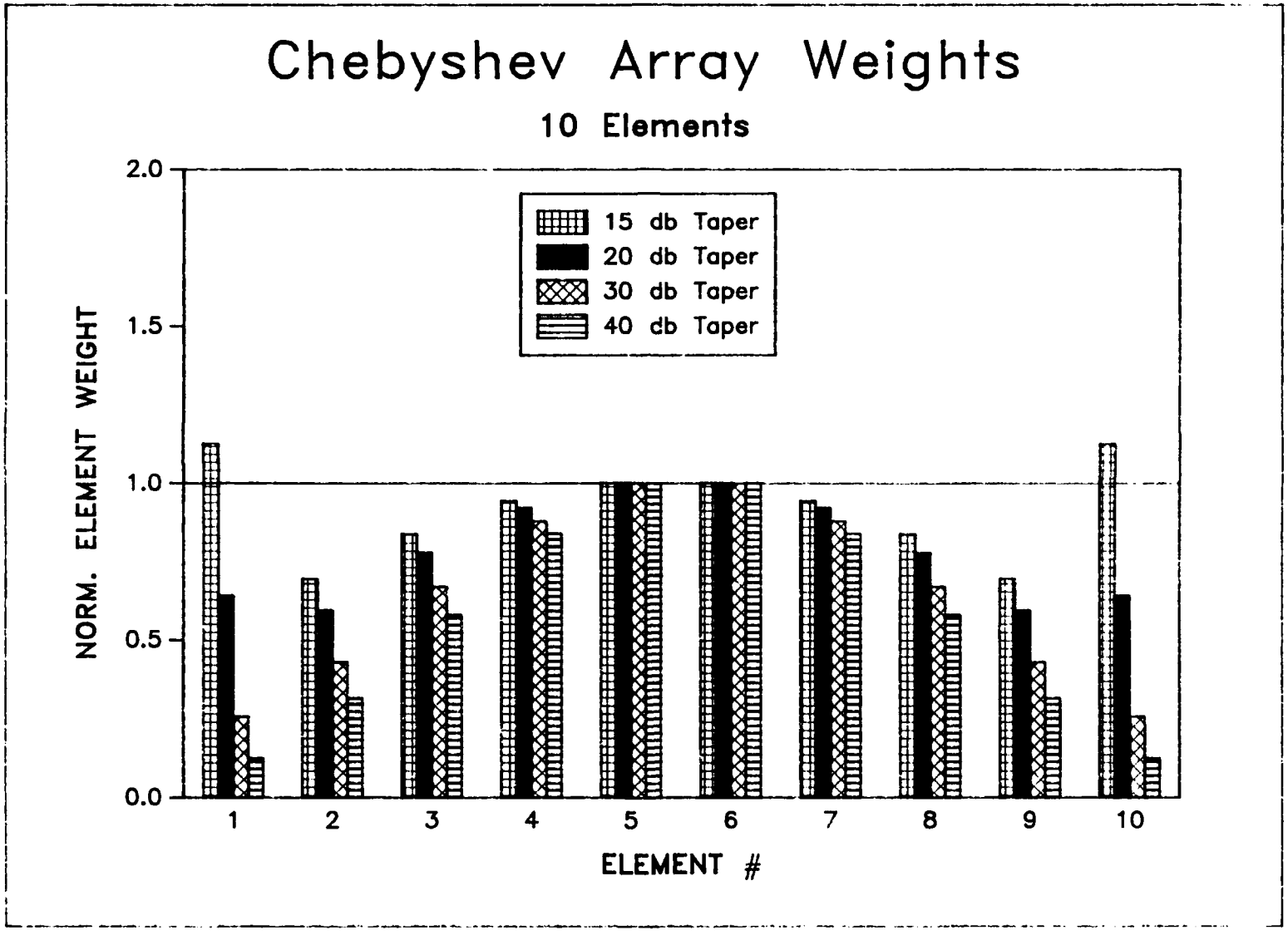

FIGURE 24. IDEAL CHEBYSHEV WEIGHTS, 10 ELEMENTS

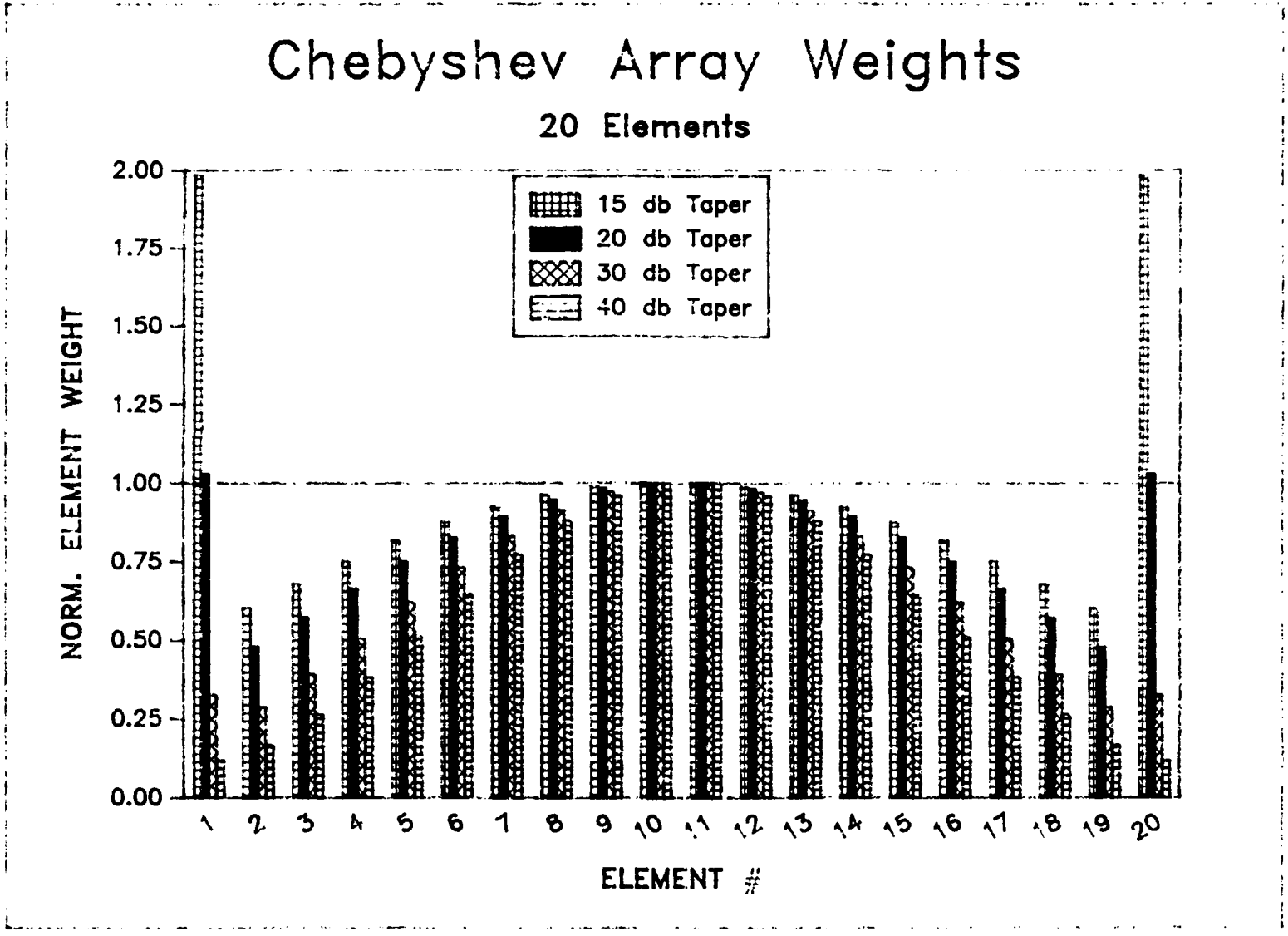

FIGURE 25. IDEAL CHEBYSHEV WEIGHTS, 20 ELEMENTS

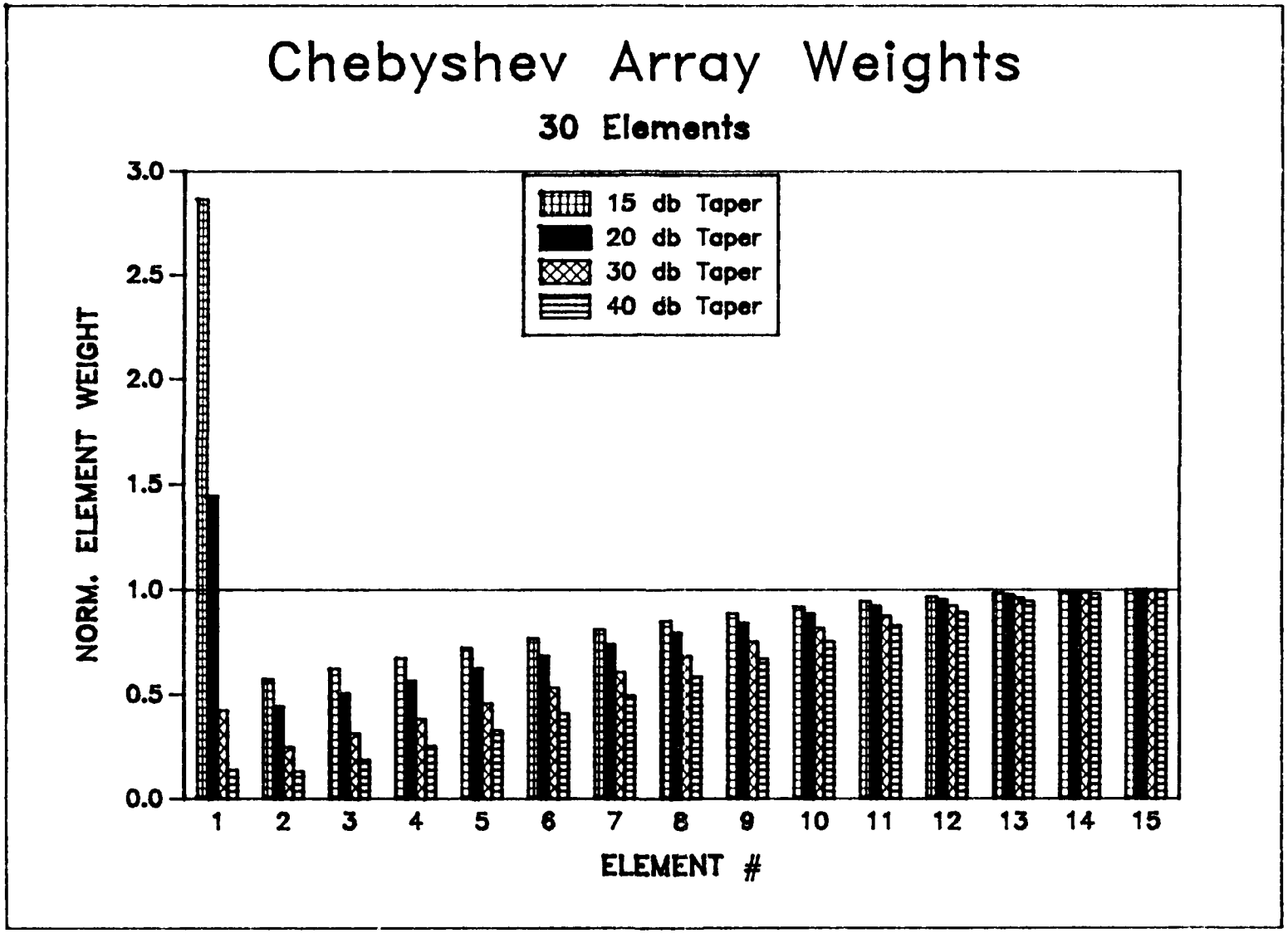

FIGURE 26. IDEAL CHEBYSHEV WEIGHTS, 30 ELEMENTS

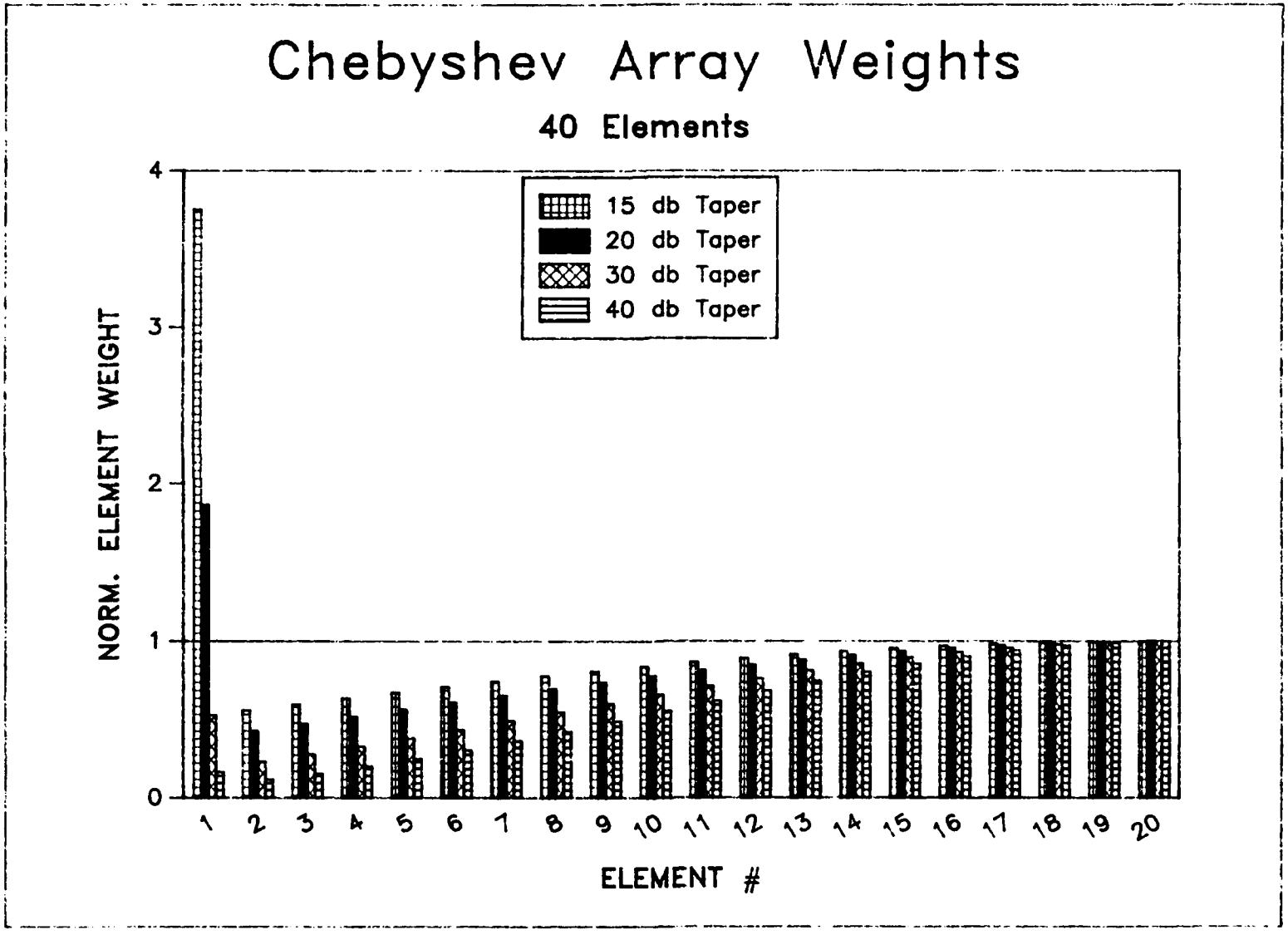

FIGURE 27. IDEAL CHEBYSHEV WEIGHTS, 40 ELEMENTS

3.4 LINEAR PHASE TAPER

The Chebyshev pattern, synthesized in Section 3.3, can be scanned in Φ by adding a linear phase slope (taper) across the array. Consider the geometry in Figure 28, in which the dipole elements are oriented perpendicular to the page. If the phasing of elements, δ_i , is advanced to the physical length (in wavelengths) between the plane wavefront (A-B) and the ith element, the array pattern would be scanned in the ϕ direction. For the ith element the phase advance required would be,

$$\text{COS}\phi = \frac{\delta^1}{(i-1)d} \tag{3-5a}$$

or

$$\delta_i = (i-1)d\ \text{COS}\phi \quad . \tag{3-5b}$$

To apply such a phase taper to a Chebyshev amplitude taper, we advance each element weight according to (3-5b), that is

$$V'_{oi} = \left(V_{oi} \Big|_{CHEBYSHEV} \right) e^{\delta_i}$$

$$= \left(V_{oi} \Big|_{CHEBYSHEV} \right) \left[\text{COS}\left((i-1)d\ \text{COS}\phi\right) + j\text{SIN}\left((i-1)d\ \text{COS}\phi\right) \right] \tag{3-6}$$

The weights in (3-6) will scan the Chebyshev pattern to the angle ϕ . In reality, the mutual coupling and the pattern will vary (distort) with scan. It is the challenge of the antenna designer to choose array geometries and tapers suitably, or to limit scan volume such that the resultant array patterns are

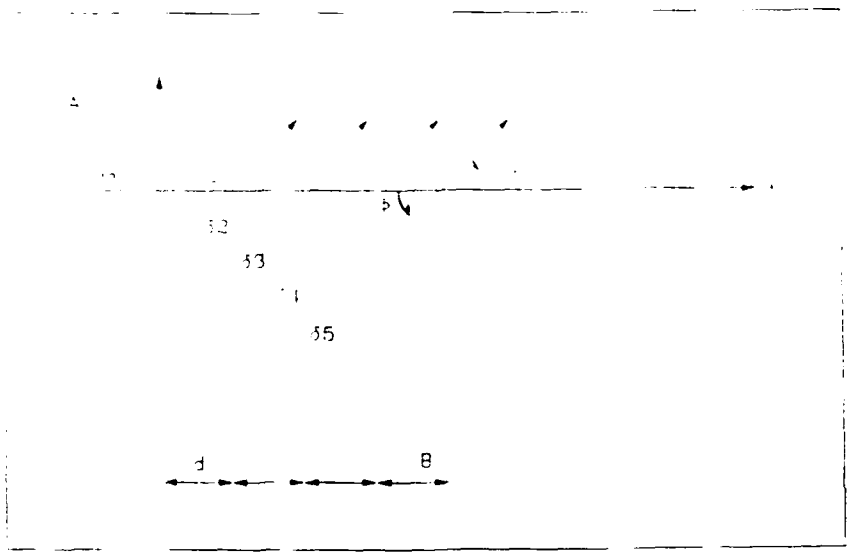

FIGURE 28. LINEAR PHASE SLOPE

still useful. In the analysis, the main beamwidth will be seen to increase and become asymmetric, but remain useful. See Figure 29 for example scanning of 40 db Chebyshev linear array of 40 isotropic sources. Of more interest in this work is the growth in sidelobe levels as scan angle increases.

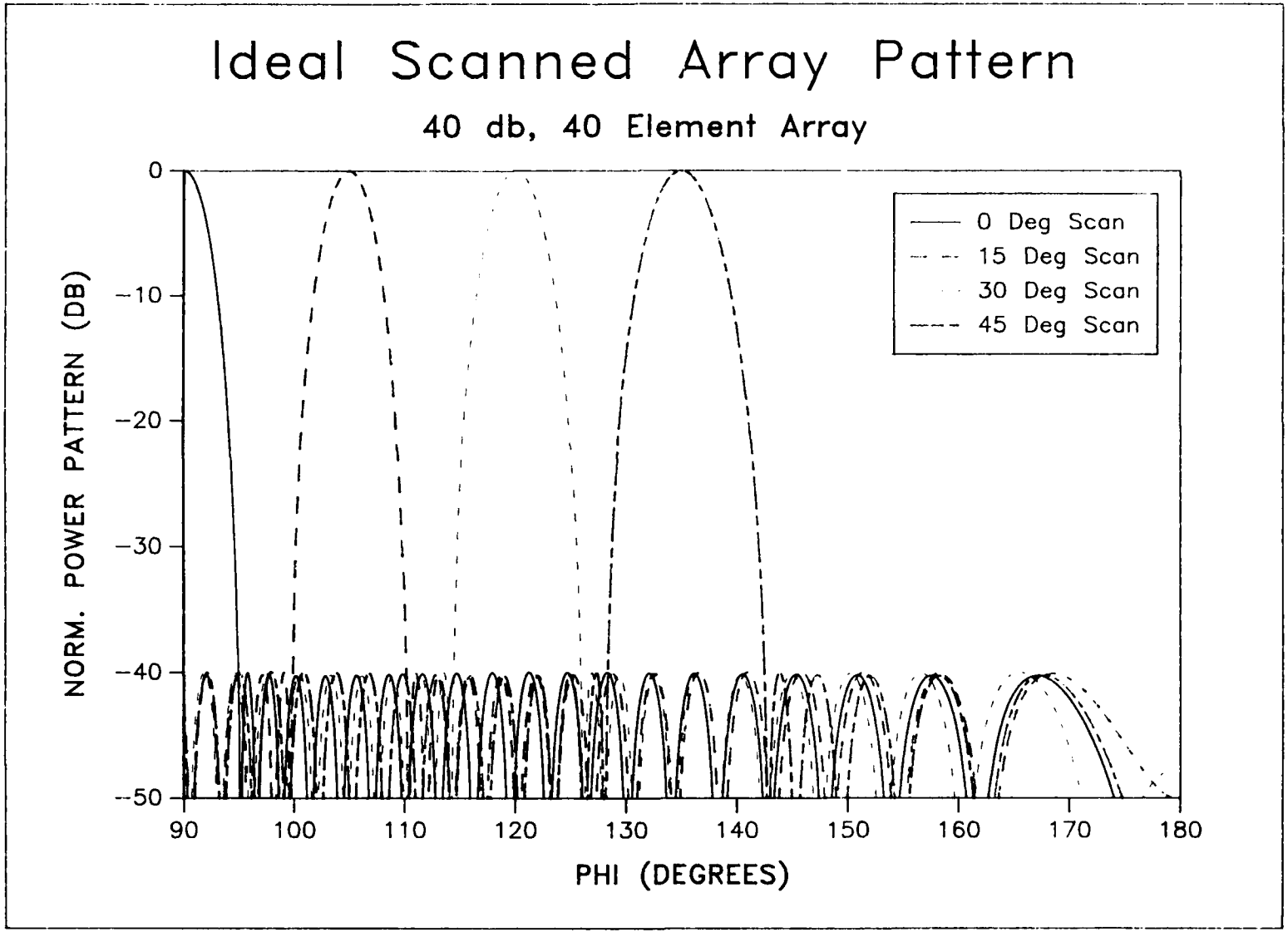

FIGURE 29. IDEAL SCANNING OF LINEAR ARRAY OF ISOTROPIC ELEMENTS (NO GROUND PLANE)

4.0 MODEL RESULTS

After running four linear array sizes (10, 20, 30, and 40 elements) through the coupling model applying four Chebyshev amplitude tapers (15, 20, 30, and 40 db) at four scan conditions (0, 15, 30, and 45 degrees) for each array, two expected trends are evident. First, the smaller the array the greater the impact of mutual coupling on the far-field patterns. Second, the greater the scan (steeper the linear phase taper) the more impact on sidelobe level. This is due in some portion to the ground planes impact on mainlobe field strength as it is scanned. However, that portion due to the ground plane is limited to ~ 1 db over a 45 degree scan angle (see Figures 30 and 31). These trends are illustrated in Figures 32 through 35. The X-axis is the desired (designed) Chebyshev taper applied to the array as real voltages. The Y-axis is the resultant, maximum sidelobe level minus the desired sidelobe level. The Y-axis is therefore a measure of sidelobe growth due to coupling. Each figure has four curves by array size. Figure 32 through 35 are for 0 to 45 degree scan conditions respectively.

The following general comments are based upon a fairly arbitrary 3 db growth standard. The sidelobe growth for 30 and 40 element arrays, due to mutual coupling, is minimal. The 20 element array has significant sidelobe growth only under the 45 degree scan condition, and then, only for the 40 db taper. The 10 element array has significant growth under all but broadside scan conditions, but normally only for 40 db Chebyshev tapers (both the 40 db and 30 db tapers at the 45 degree scan condition exceed the 3 db standard).

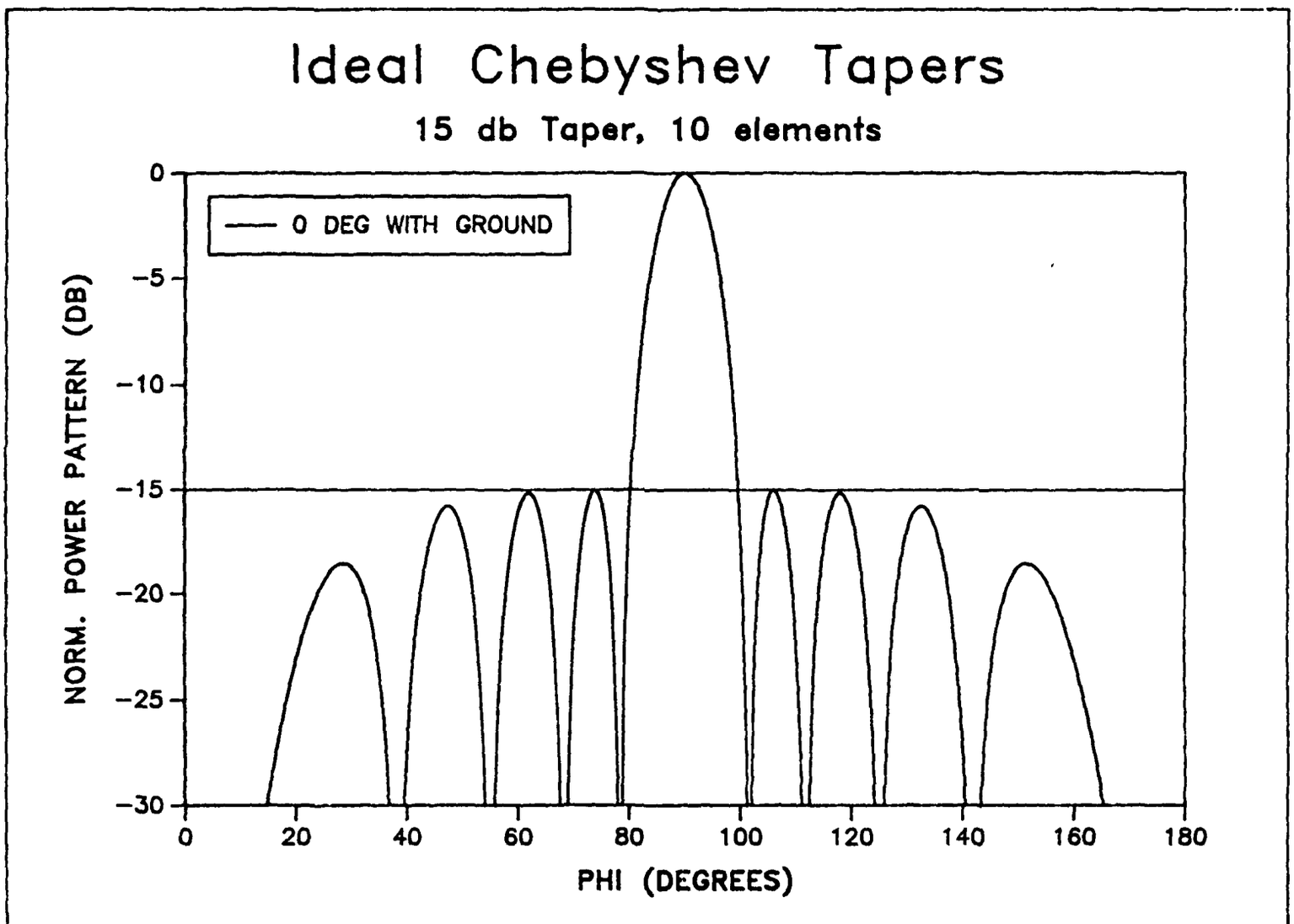

FIGURE 30. IDEAL CHEBYSHEV TAPERS (15 DB TAPER, 10 ELEMENTS, 0 DEGREE WITH GROUND)

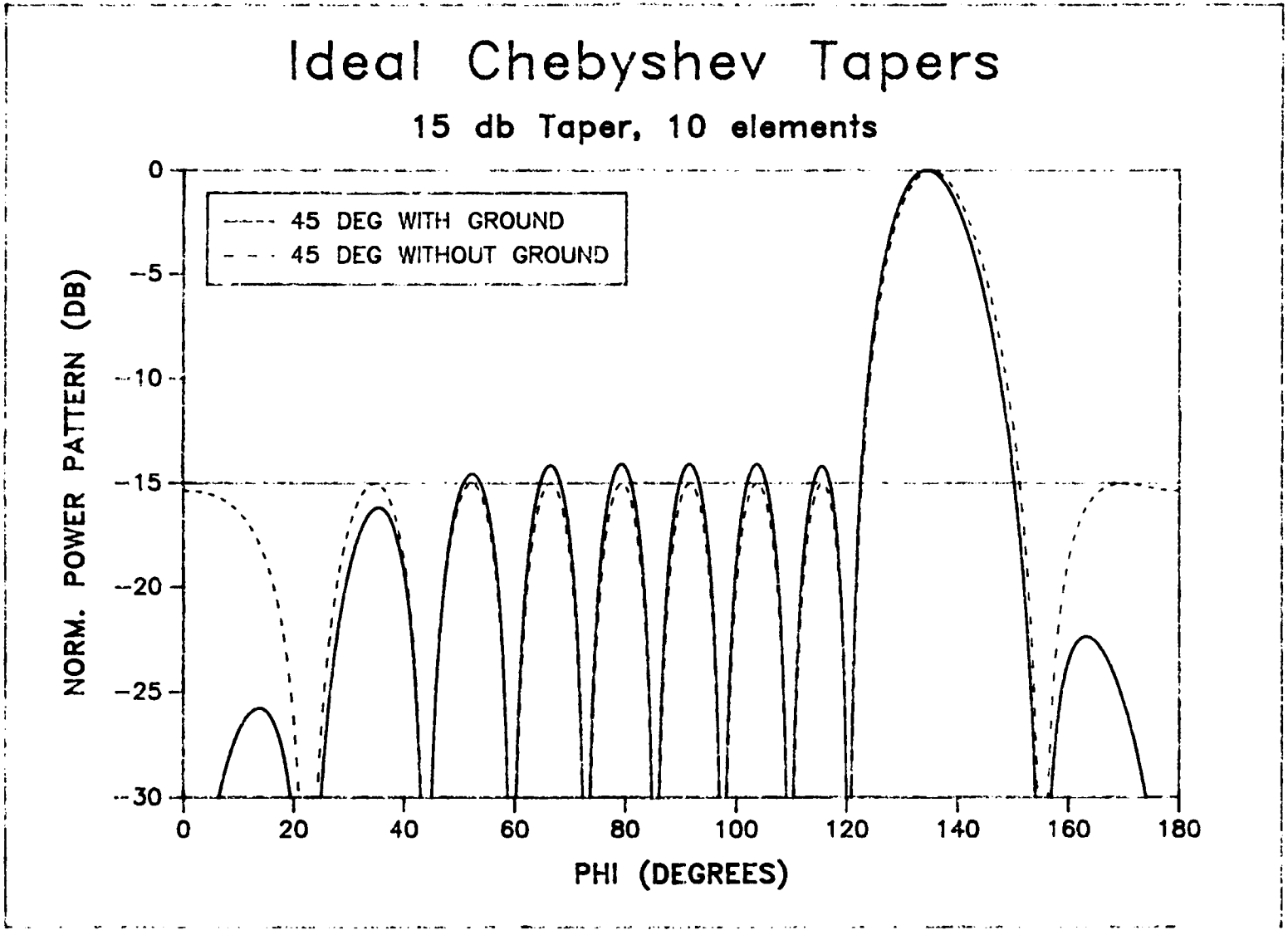

FIGURE 31. IDEAL CHEBYSHEV TAPERS (15 DB TAPER, 10 ELEMENTS, 45 DEG WITH/WITHOUT GROUND)

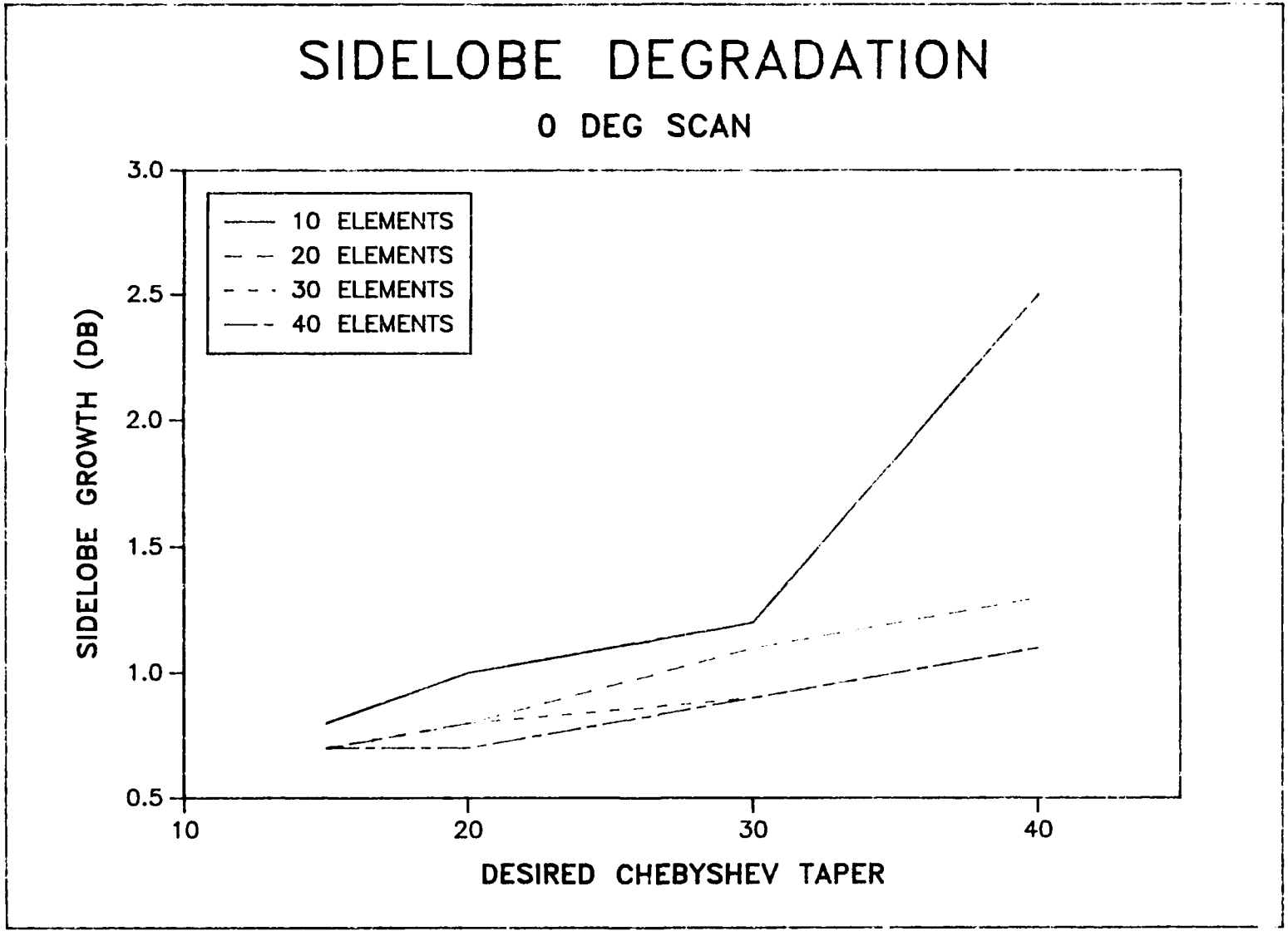

FIGURE 32. SIDELOBE DEGRADATION (0 DEGREE SCAN)

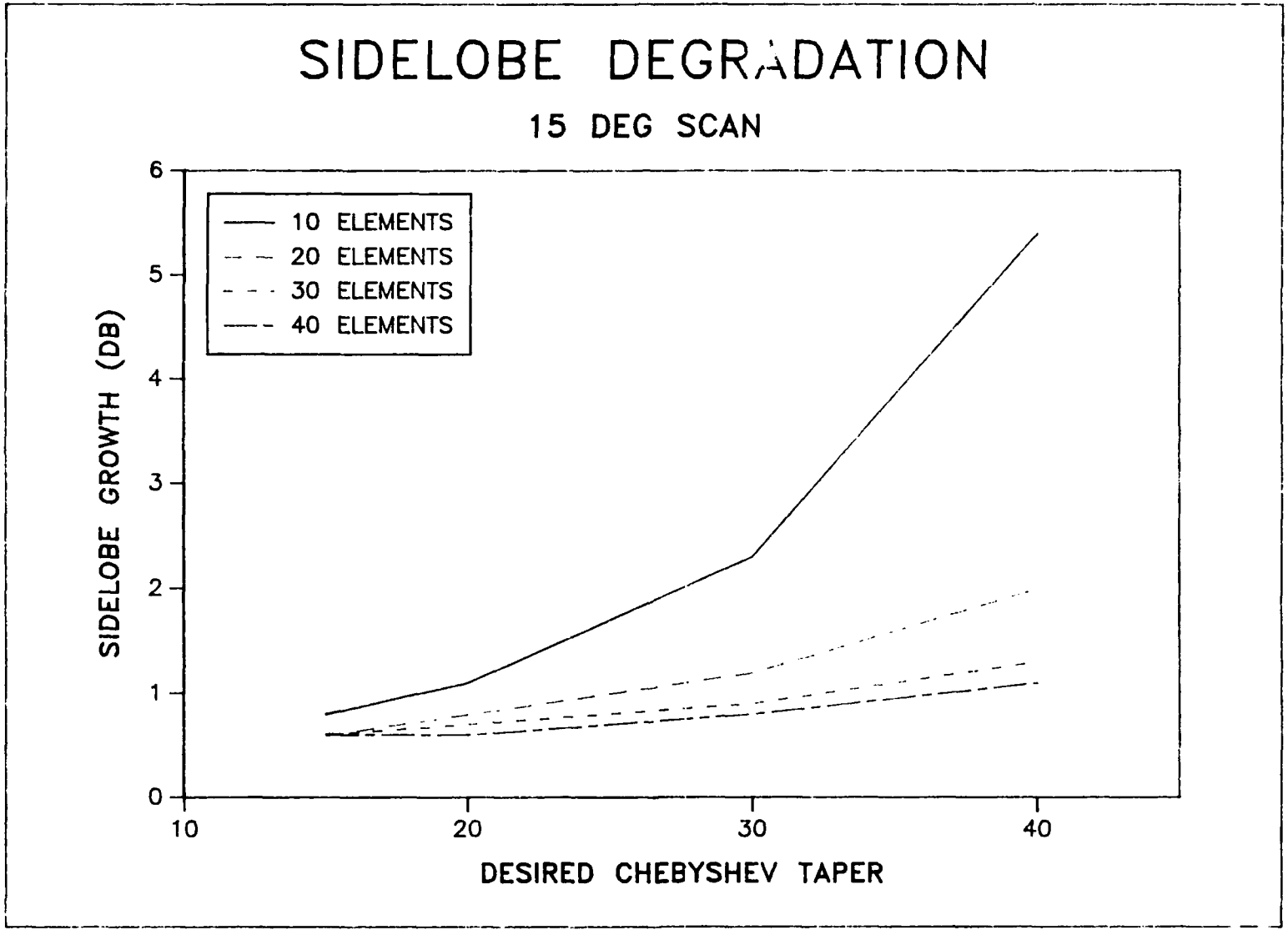

FIGURE 33. SIDELOBE DEGRADATION (15 DEGREE SCAN)

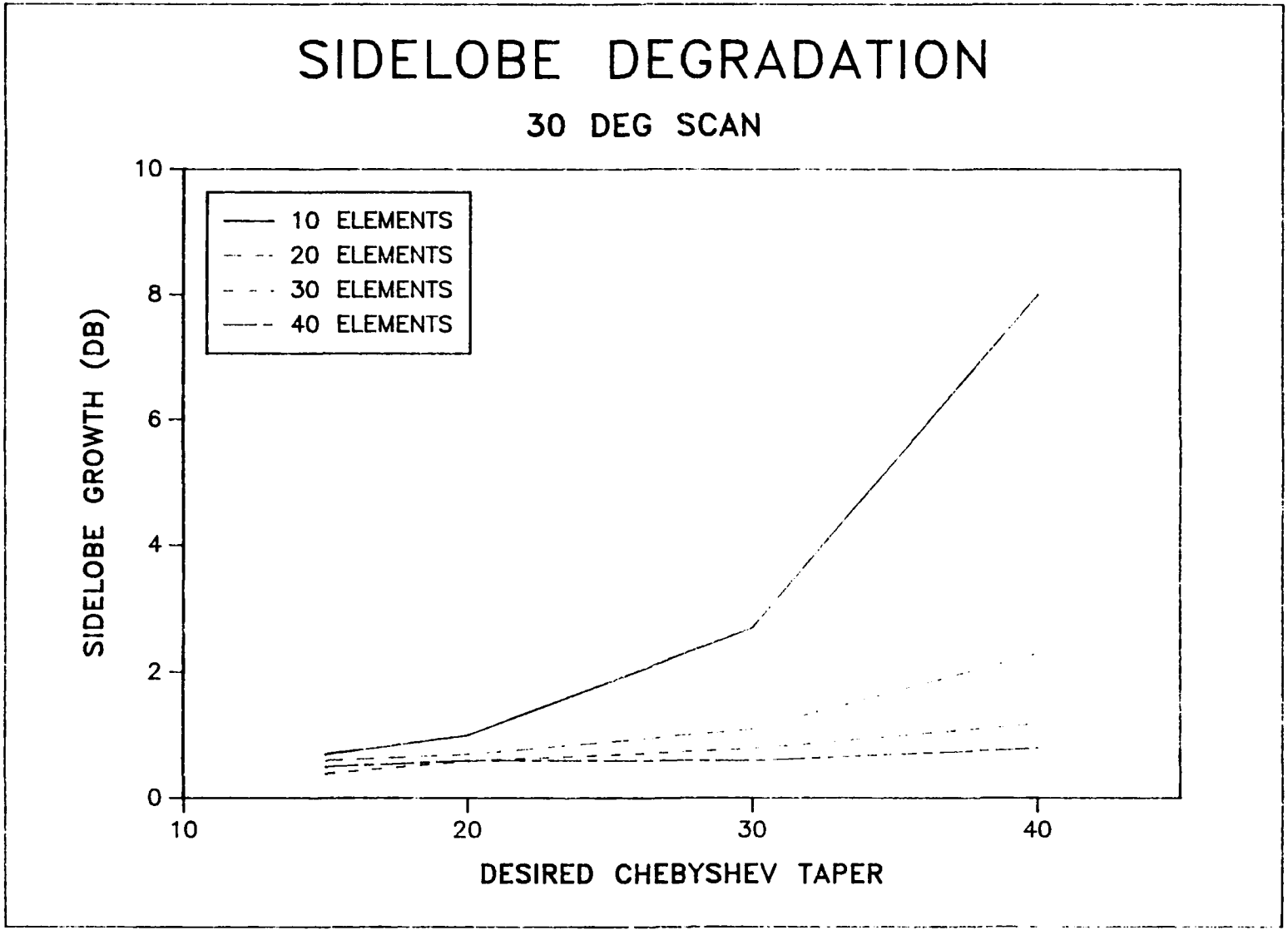

FIGURE 34. SIDELOBE DEGRADATION (30 DEGREE SCAN)

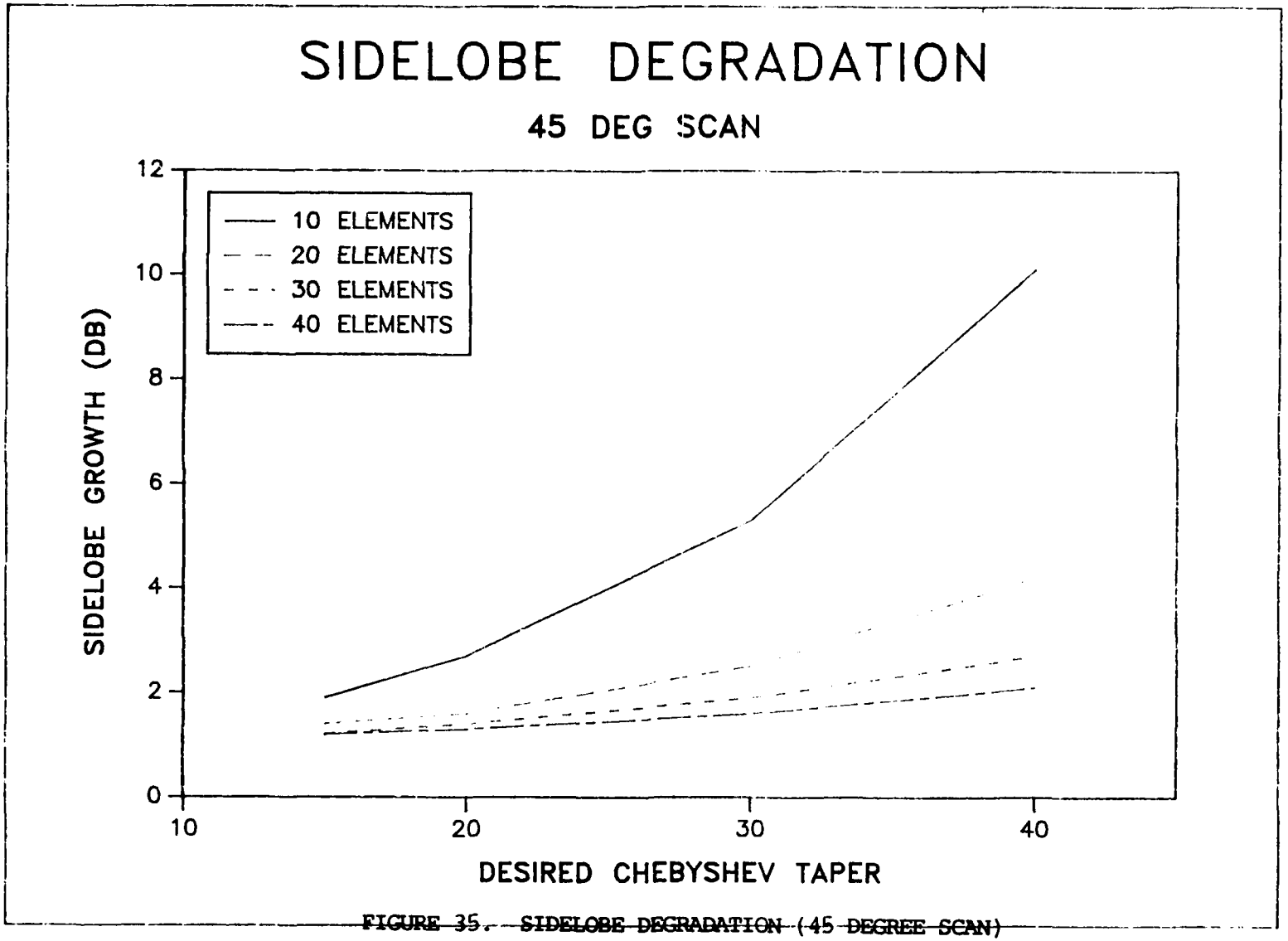

FIGURE 35. SIDELOBE DEGRADATION (45 DEGREE SCAN)

Figures 36 through 39 are bar charts of ideal Chebyshev voltage weights versus the magnitude of resultant current weights due to coupling. The impact of coupling manifests itself primarily in the 5 edge elements for severe tapers (30 and 40 db, see Figure 39). For less severe tapers (15 and 20 db, see Figure 38), eight edge elements are significantly impacted by coupling. The less severe Chebyshev tapers are characterized by radically large edge element weights, and are therefore more impacted by coupling.

Figures 40 through 47 demonstrate that nearly all far-field patterns are well behaved even accounting for coupling. The only notable exception is Figure 43. The 40 db Chebyshev taper for small arrays translates to a relatively large main beamwidth. At large scanning angles beam is further broadened and distorted and vestiges of this beam have been scanned out of visible space. This condition is contributing to the increased sidelobe growth evident in Figure 43. The significantly larger growth for 40 db tapers and small arrays (Figures 30 through 33, 10 element curve) far exceeds the growth evident for even the 45 degree scan condition for an idealized array of isotropic radiators over a ground (see Figure 30).

Figures 44 through 47 demonstrate that large array patterns are well behaved for all tapers and scan conditions investigated. This would indicate that mutual coupling maybe ignored, for sidelobe considerations, for the 30 and 40 element linear arrays.

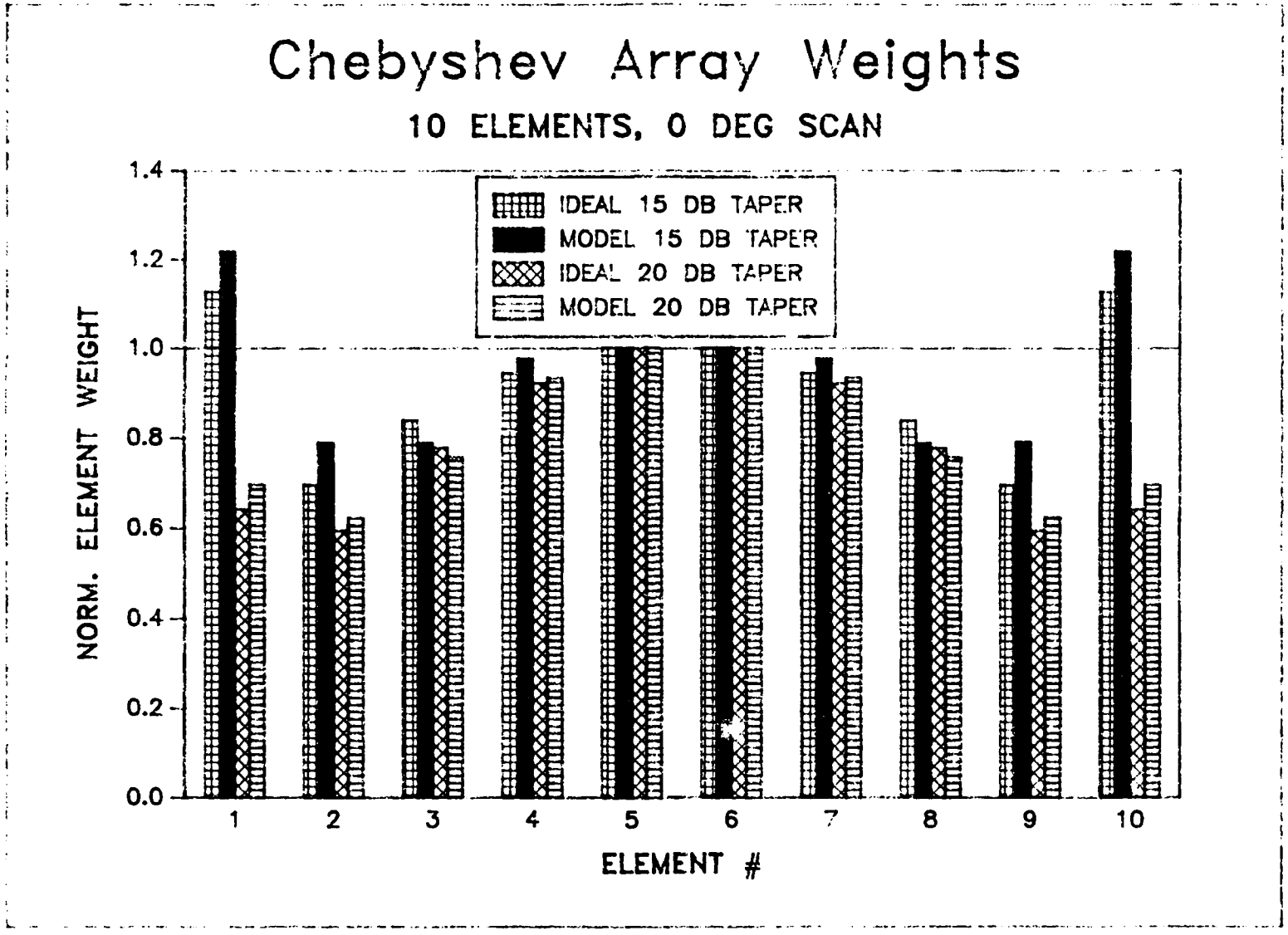

FIGURE 36. CHEBYSHEV ARRAY WEIGHTS (10 ELEMENTS, 0 DEGREE SCAN, 15 AND 20 DB TAPER)

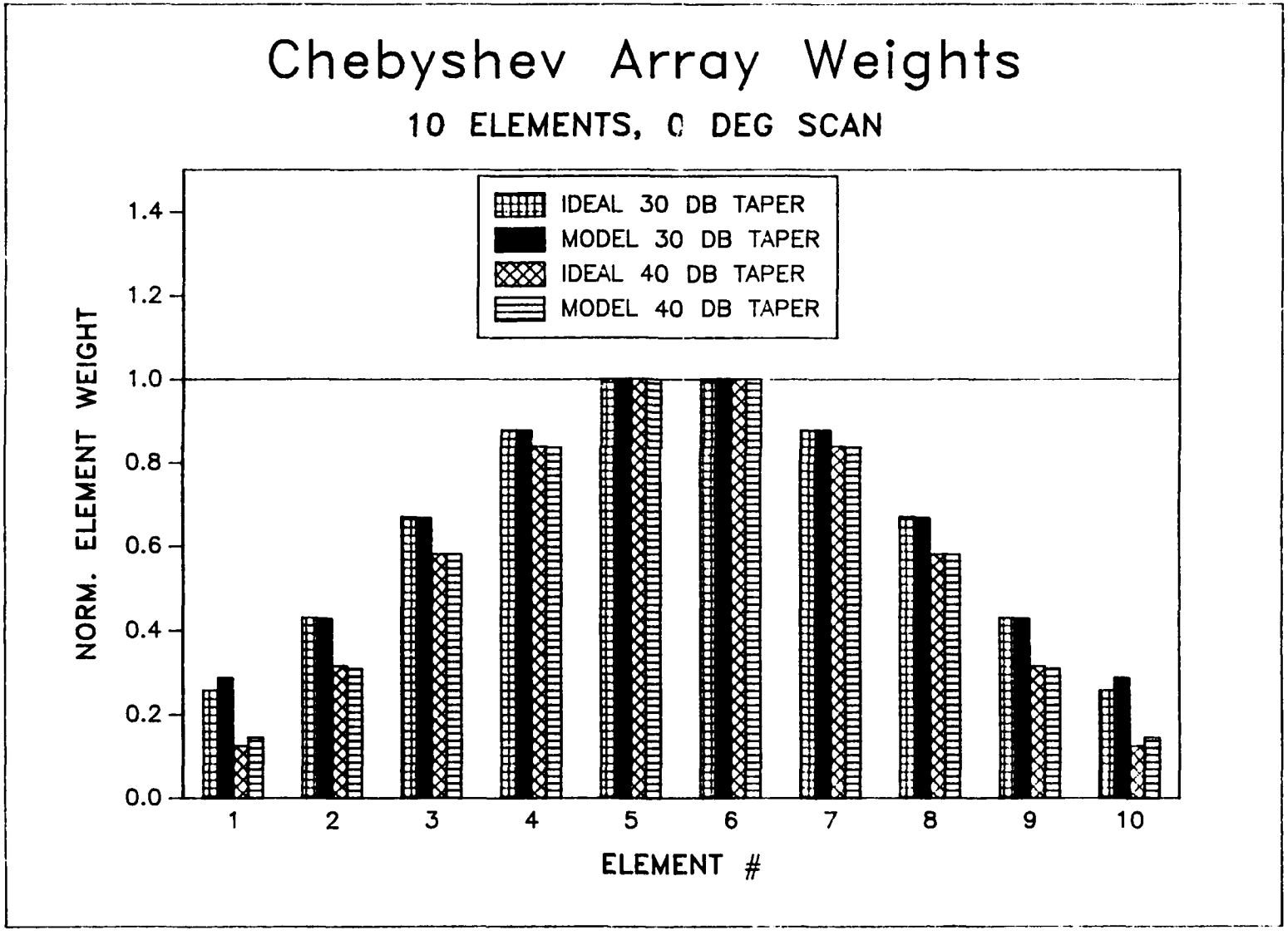

FIGURE 37. CHEBYSHEV ARRAY WEIGHTS (10 ELEMENTS, 0 DEGREE SCAN, 30 AND 40 DB TAPER

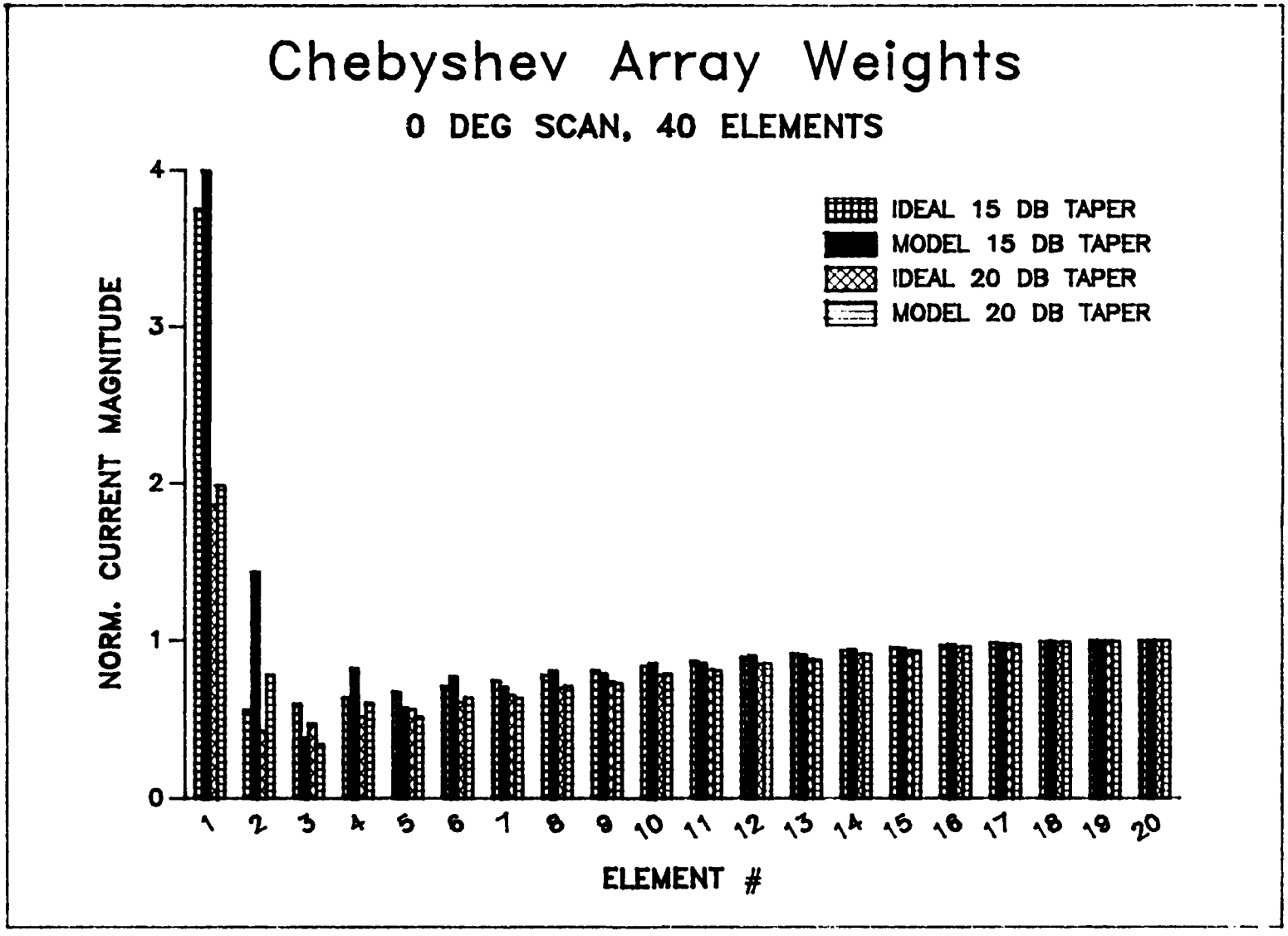

FIGURE 38. CHEBYSHEV ARRAY WEIGHTS (15 DB TAPER, 40 ELEMENTS, 15 AND 20 DB TAPER)

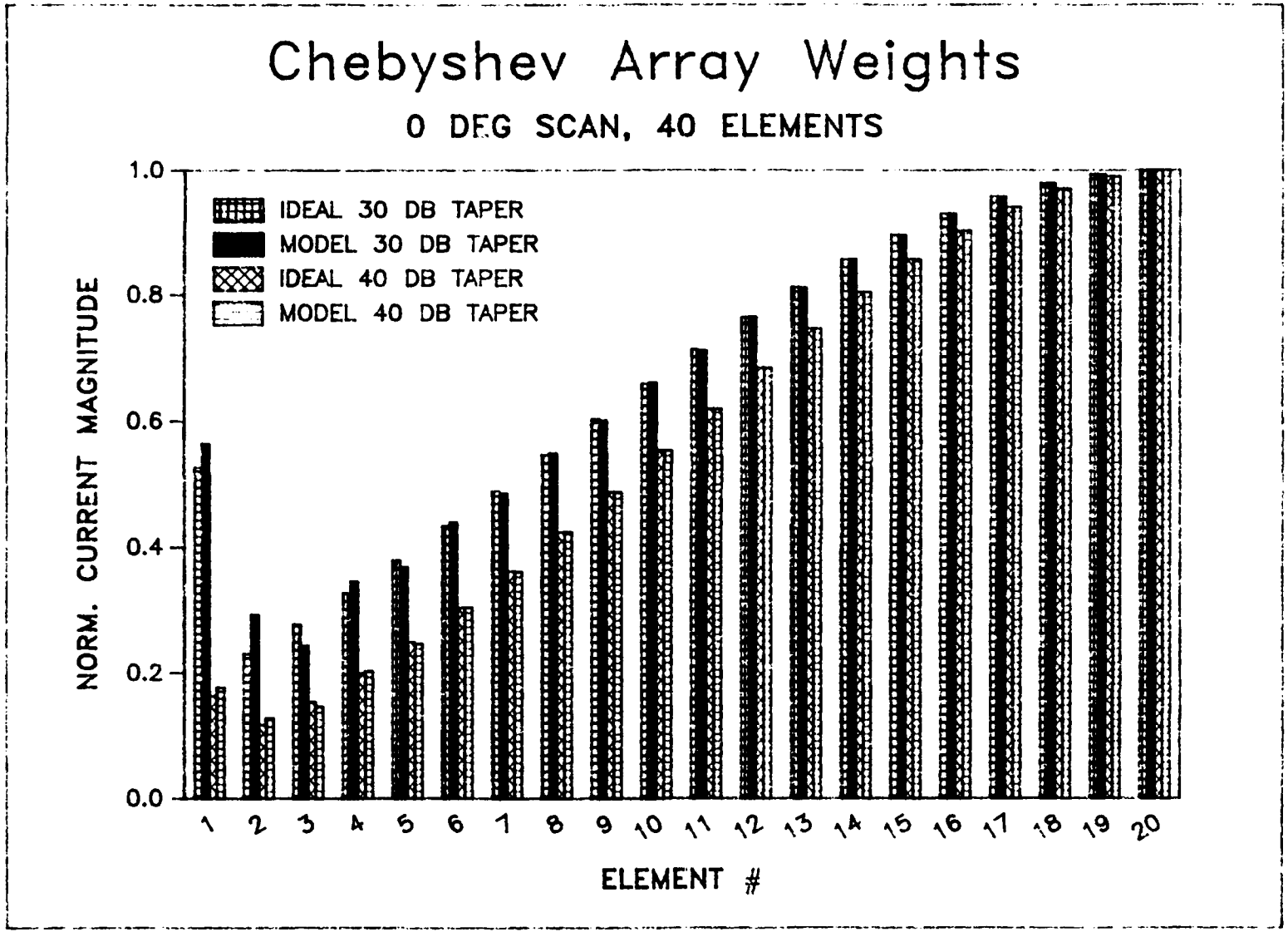

FIGURE 39. CHEBYSHEV ARRAY WEIGHTS (40 ELEMENTS, 0 DEGREE SCAN, 30 AND 40 DB TAPER)

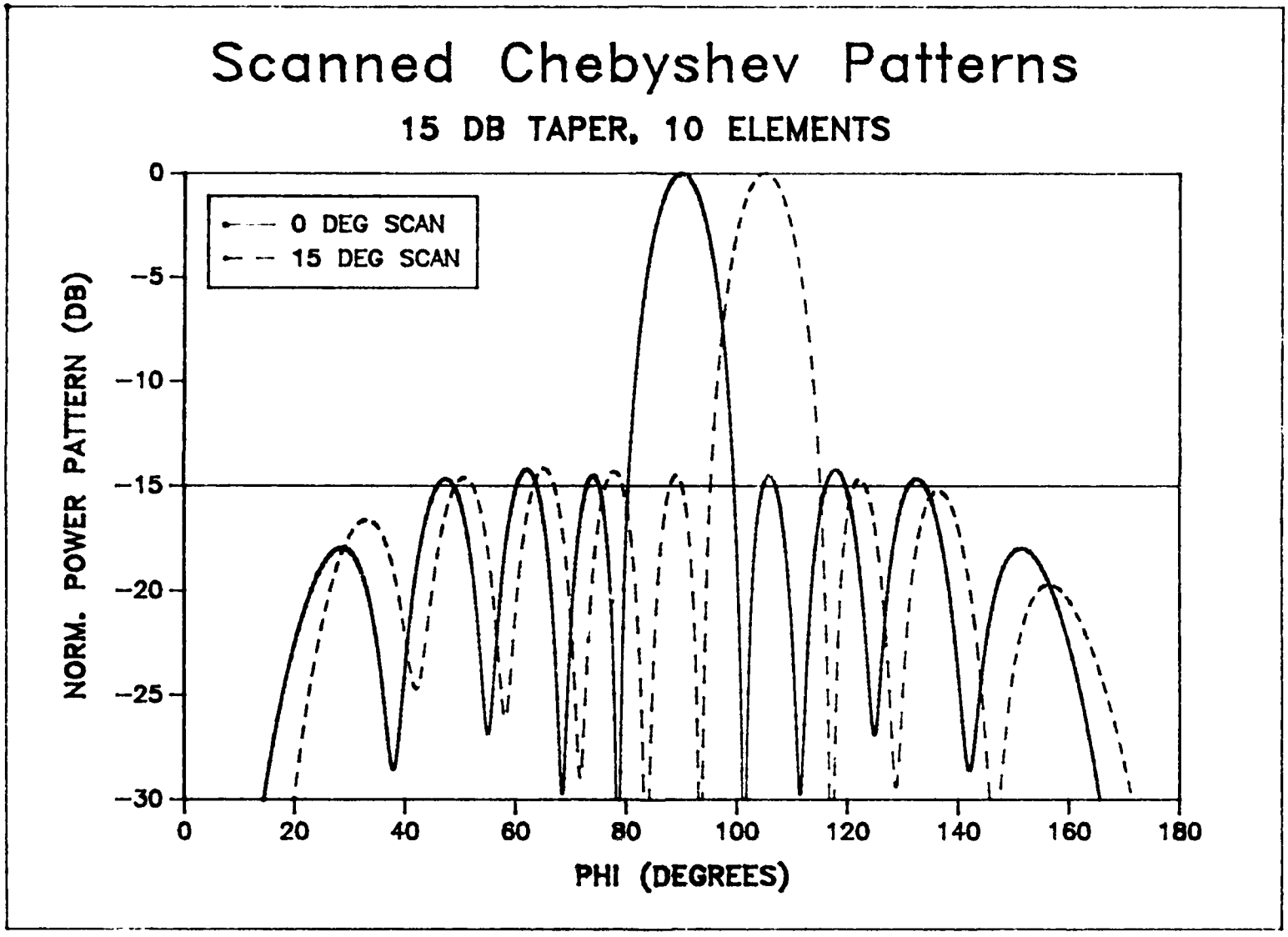

FIGURE 40. SCANNED CHEBYSHEV PATTERNS (15 DB TAPER, 10 ELEMENTS, 0 AND 15 DEGREE SCAN)

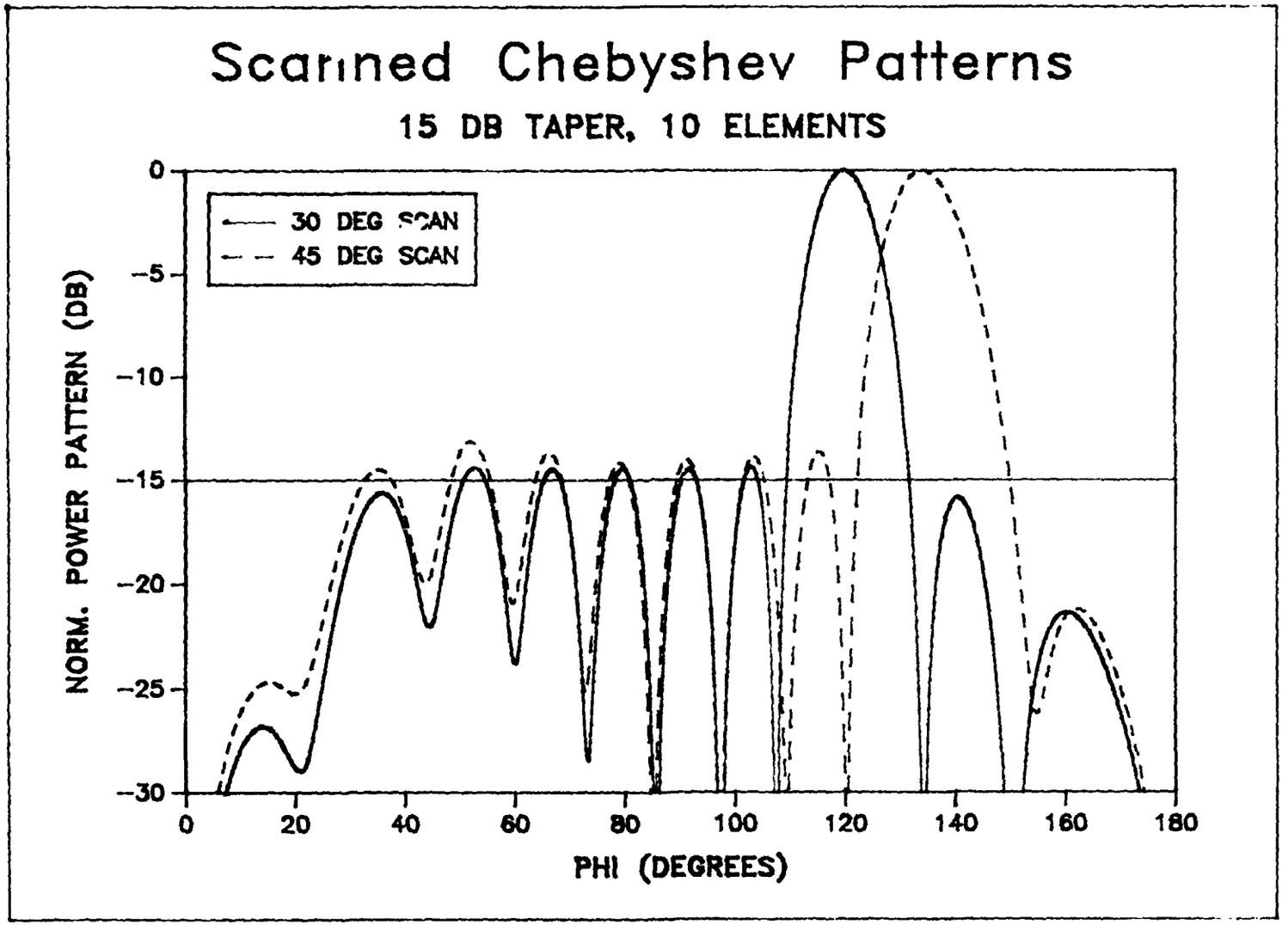

FIGURE 41. SCANNED CHEBYSHEV PATTERNS (15 DB TAPER, 10 ELEMENTS, 30 AND 45 DEGREE SCAN)

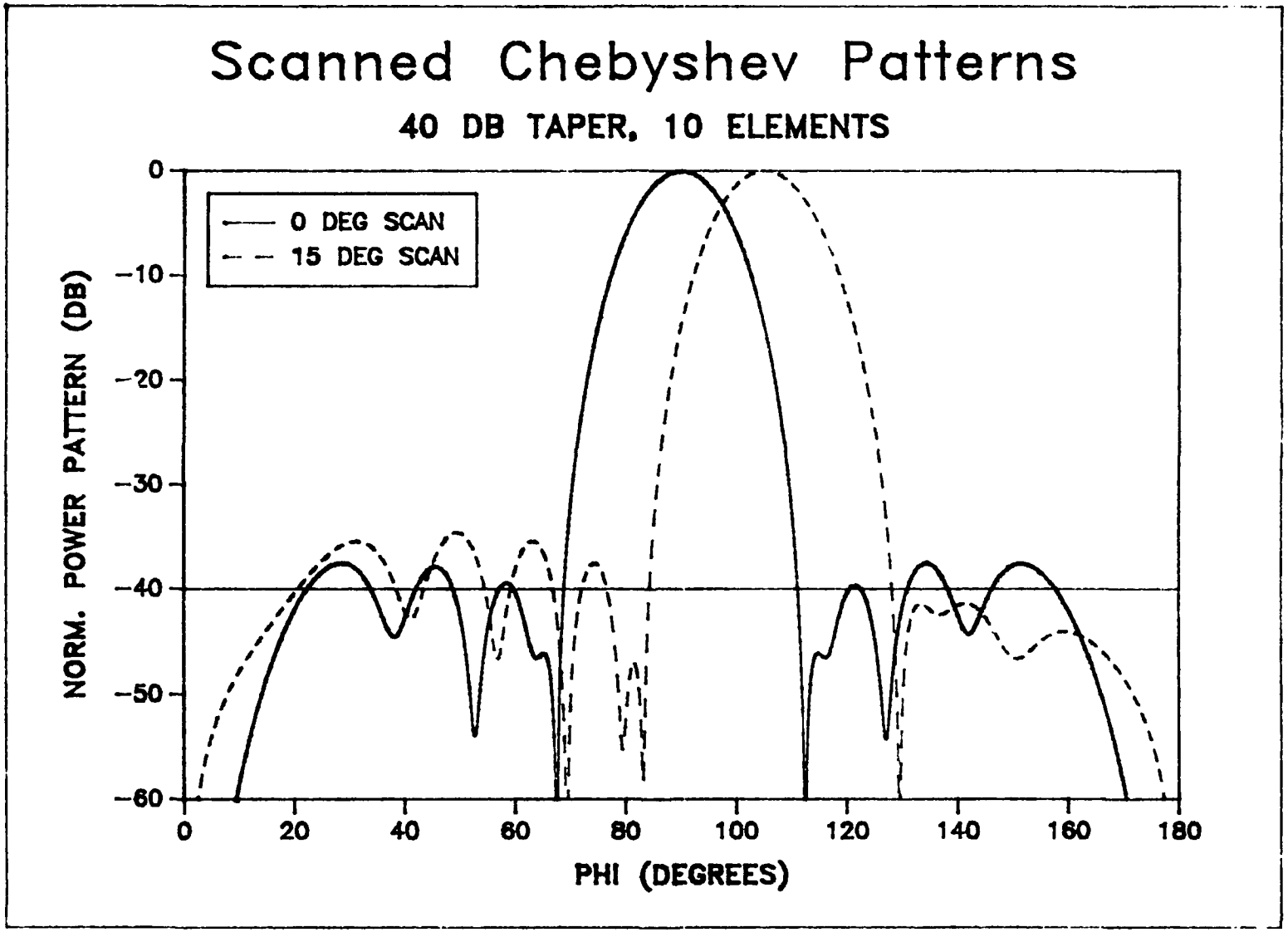

FIGURE 42. SCANNED CHEBYSHEV PATTERNS (40 DB TAPER, 10 ELEMENTS, 0 AND 15 DEGREE SCAN)

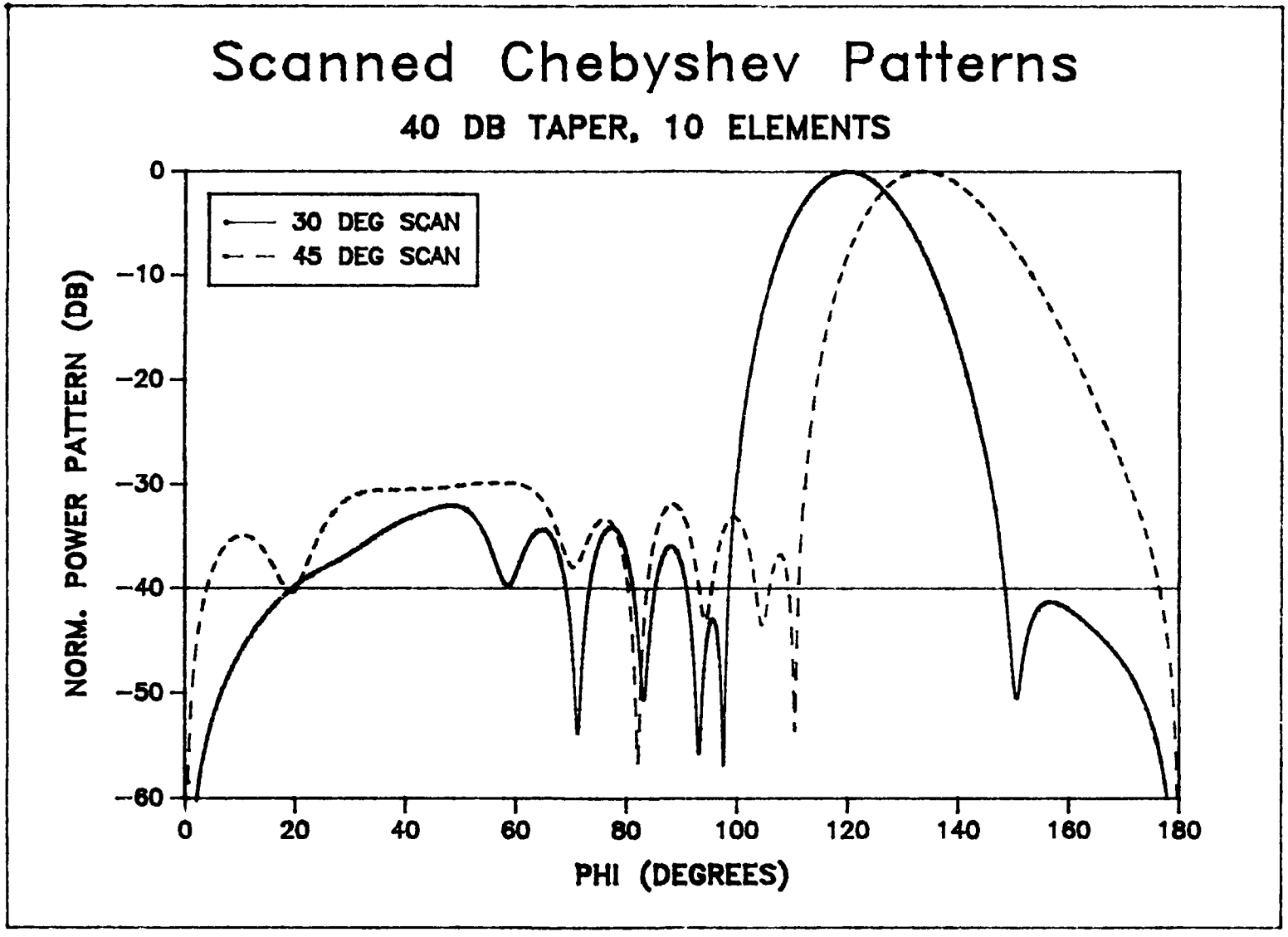

FIGURE 43. SCANNED CHEBYSHEV PATTERNS (40 DB TAPER, 10 ELEMENTS, 30 AND 45 DEGREE SCAN)

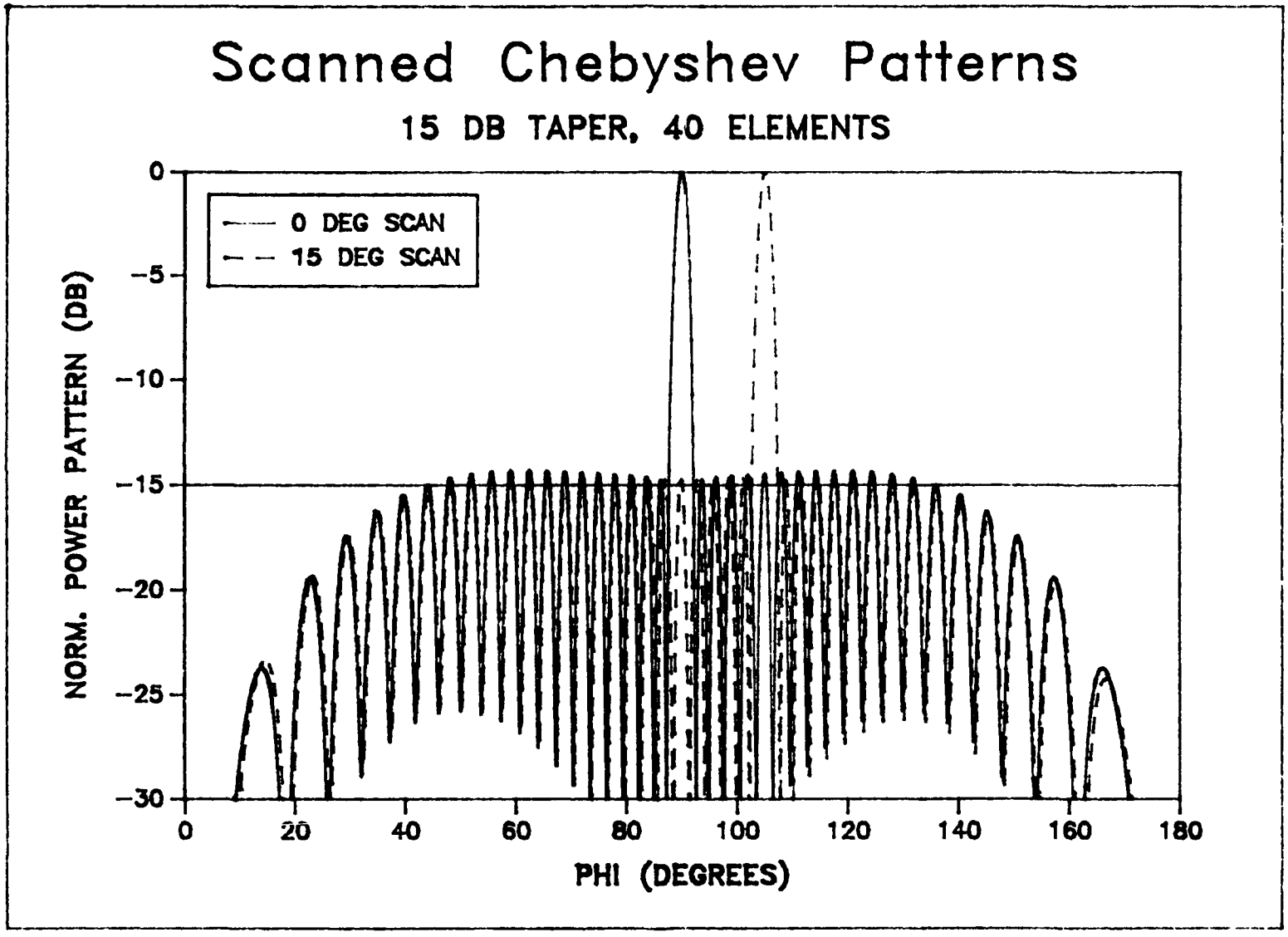

FIGURE 44. SCANNED CHEBYSHEV PATTERNS (15 DB TAPER, 40 ELEMENTS, 0 AND 15 DEGREE SCAN)

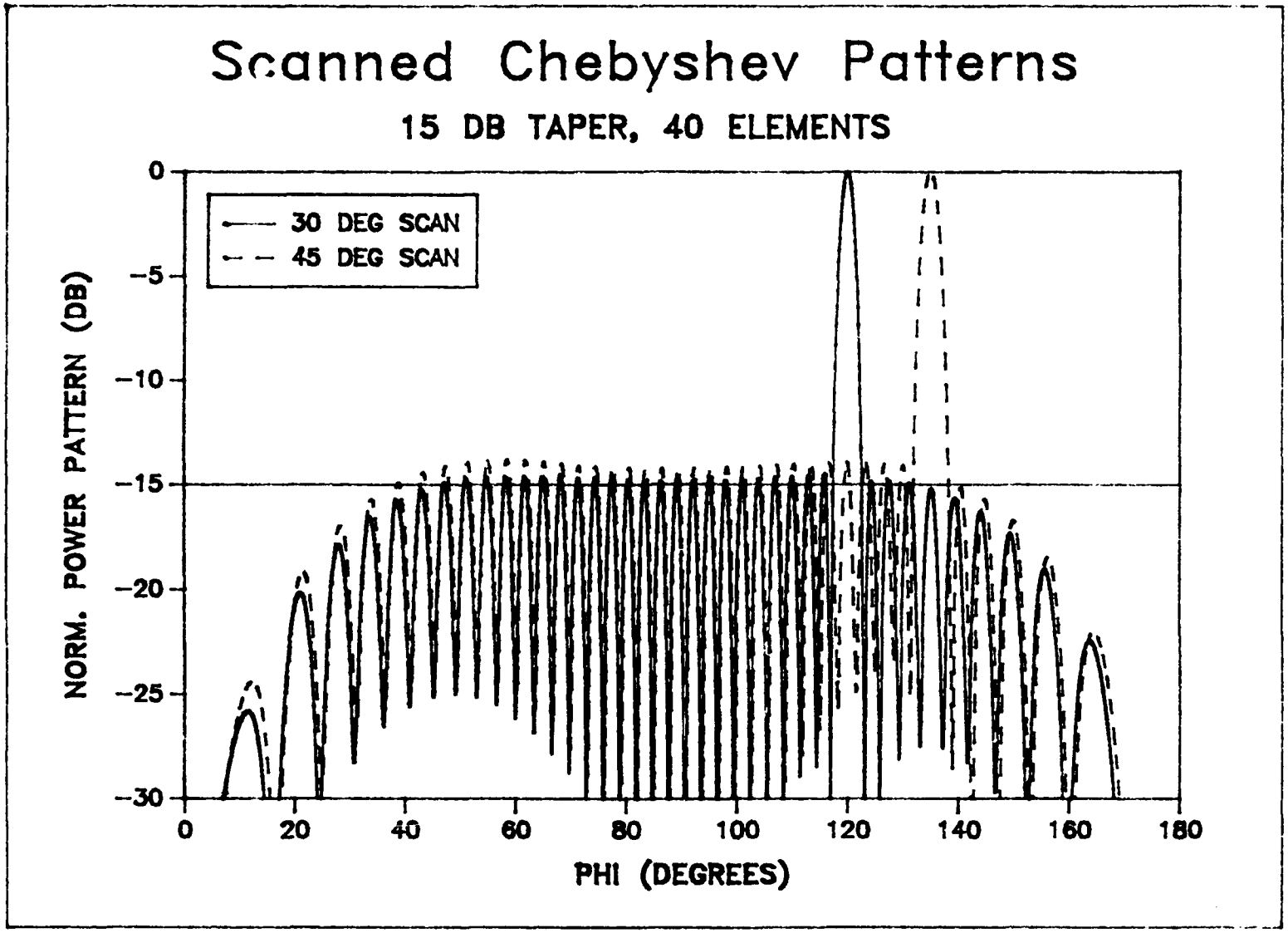

FIGURE 45. SCANNED CHEBYSHEV PATTERNS (15 DB TAPER, 40 ELEMENTS, 30 AND 45 DEGREE SCAN)

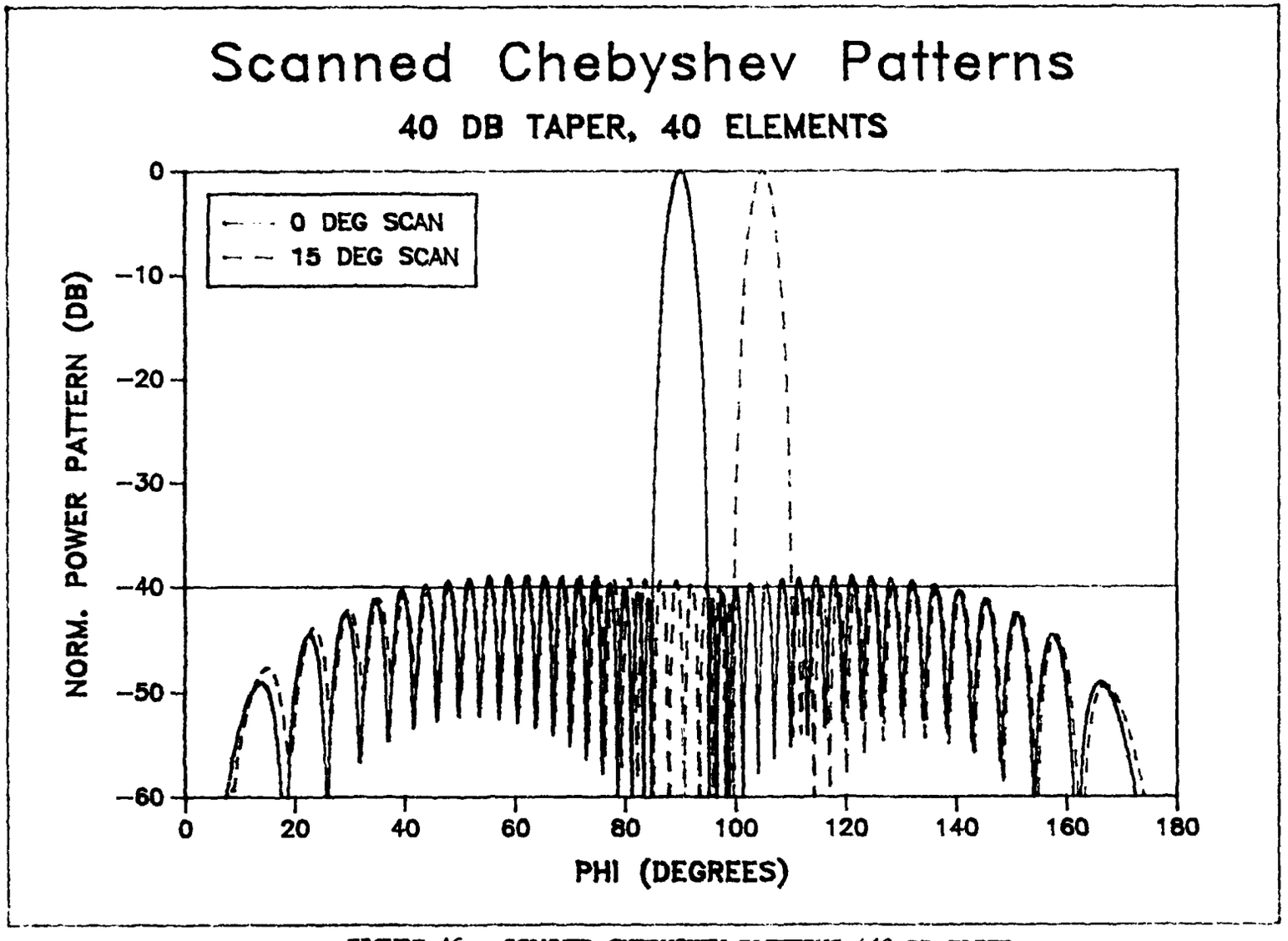

FIGURE 46. SCANNED CHEBYSHEV PATTERNS (40 DB TAPER, 40 ELEMENTS, 0 AND 15 DEGREE SCAN)

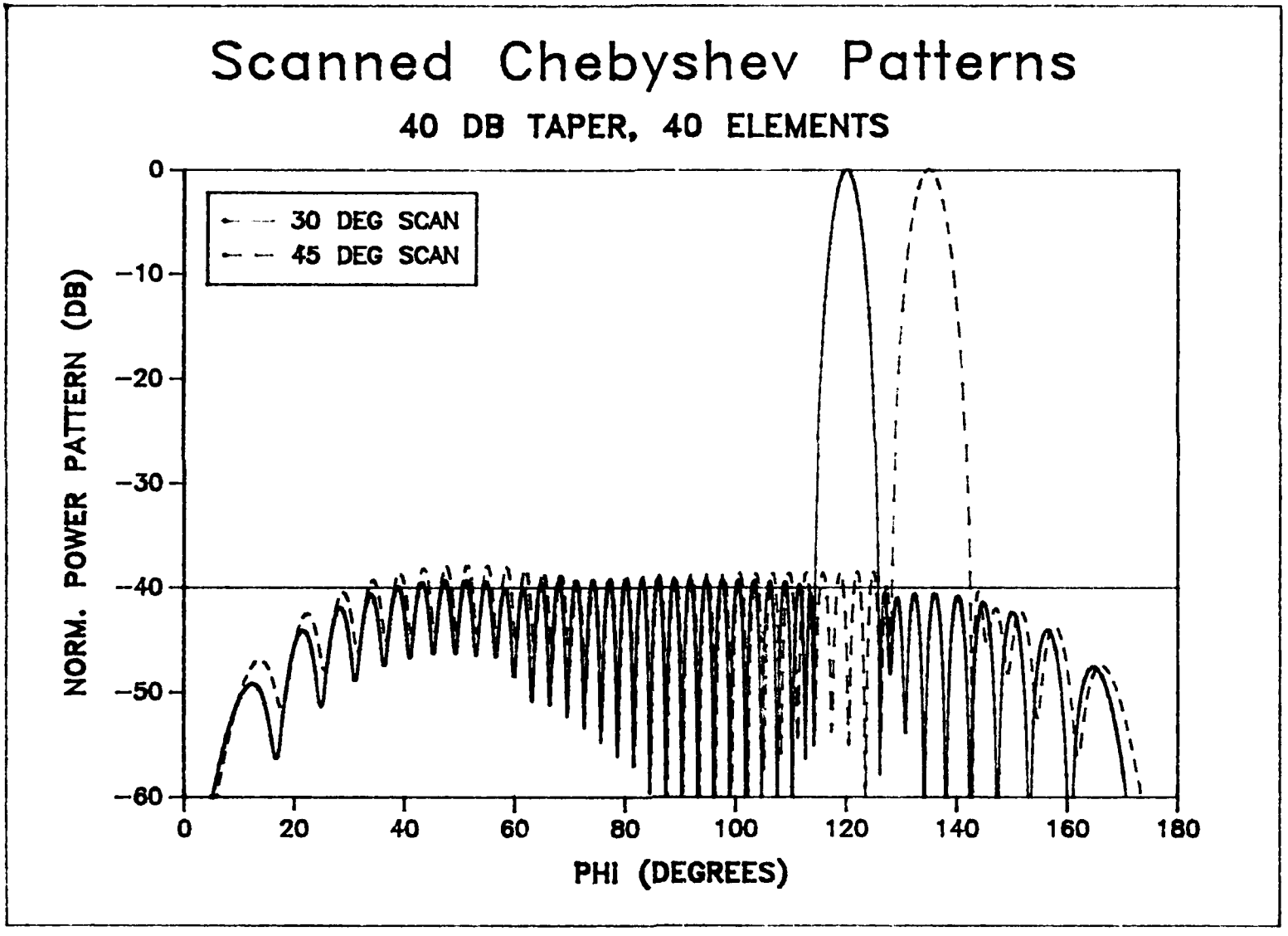

FIGURE 47. SCANNED CHEBYSHEV PATTERNS (40 DB TAPER, 40 ELEMENTS, 30 AND 45 DEGREE SCAN)

5.0 COMPENSATION METHODS AND RESULTS

The impact of mutual coupling, evident in Figures 32-35, may preclude the design of low side lobe arrays for given array size, scan condition and bandwidth specifications (6)(17)(23). The Chebyshev voltage distributions driving the linear arrays in Section 4.0, do not translate into Chebyshev base current distributions due to mutual coupling. This section will discuss three simple compensation schemes to correct for mutual coupling, and then apply these schemes to the linear arrays under investigation.

5.1 COMPENSATION SCHEMES

All three compensation schemes revolve around equations 3-3a through d. That is, having modelled coupling in the formulation of the generalized admittance matrix, [Y] (see equation 2-8a), one can simply reverse the matrix problem (13)(23) to solve for the complex generator voltages, V'_{oi}, required to achieve a known Chebyshev base current distribution, I_{oi} . One must solve the matrix equation

$$\mathbf{V}'_o = [\ Y\ ]^{-1}\ I_o \quad . \tag{5-1}$$

The resultant generator voltages, V'_{oi} , are as previously stated, complex. Such an excitation may not be realizable. To alleviate this concern, three simple compensation schemes, that approximate the excitation, V'_{oi} , will be used in this study. The first scheme, 'amplitude only', uses only the magnitude of the complex voltages, V'_{oi} . The second scheme, '5 deg phase', adds some phase control by using both magnitude and phase of V'_{oi} , however phase is 'discretized' to the nearest multiple of 5 degrees. The third scheme, '2.5 deg phase', merely increases the resolution of the phase increment to 2.5 degrees. In all three

schemes, the approximate compensated generator voltages, V'_{o_1} , are used as driving voltages for the arrays of interest.

5.2 COMPENSATION RESULTS

The need for compensation schemes is inversely proportional to array size, and proportional to scan angle and Chebyshev taper (see Figures 32-35). The effectiveness of the simple compensation schemes presented here is just the opposite (see Figures 48, 53-55, 60, 63 and 66). These simple schemes are particularly effective at broadside, regardless of array size and taper (see Figures 48-52, 60-62, 67 and 68). This trend agrees with Herd's experimental work with even smaller linear arrays of dipoles (13).

Based on the cases modelled in this study, linear arrays of 20 dipoles and larger do not benefit enough from these compensation schemes (Figures 60, 63 and 66) to justify the design effort. Large scan angles for the 20 element array (Figure 63) are an exception. The smaller 10 element array benefited considerably from these schemes, however (see Figures 48-60) amplitude only compensation is sufficient. In general, the 5 degree phase compensation proved considerably less effective than the amplitude only scheme. This is dramatically true for severe Chebyshev tapers. For the severe tapers on small arrays, the 2.5 degree phase compensation was required to achieve the desired side lobe levels. In general, the 2.5 degree phase compensation did no better (and often a little worse) than amplitude only. Small arrays with large scan angles and severe tapers were not helped significantly by any of these compensation schemes (see Figures 58 and 59). This is more probably due to scanning some vestige of a large mainbeam out of visible space.

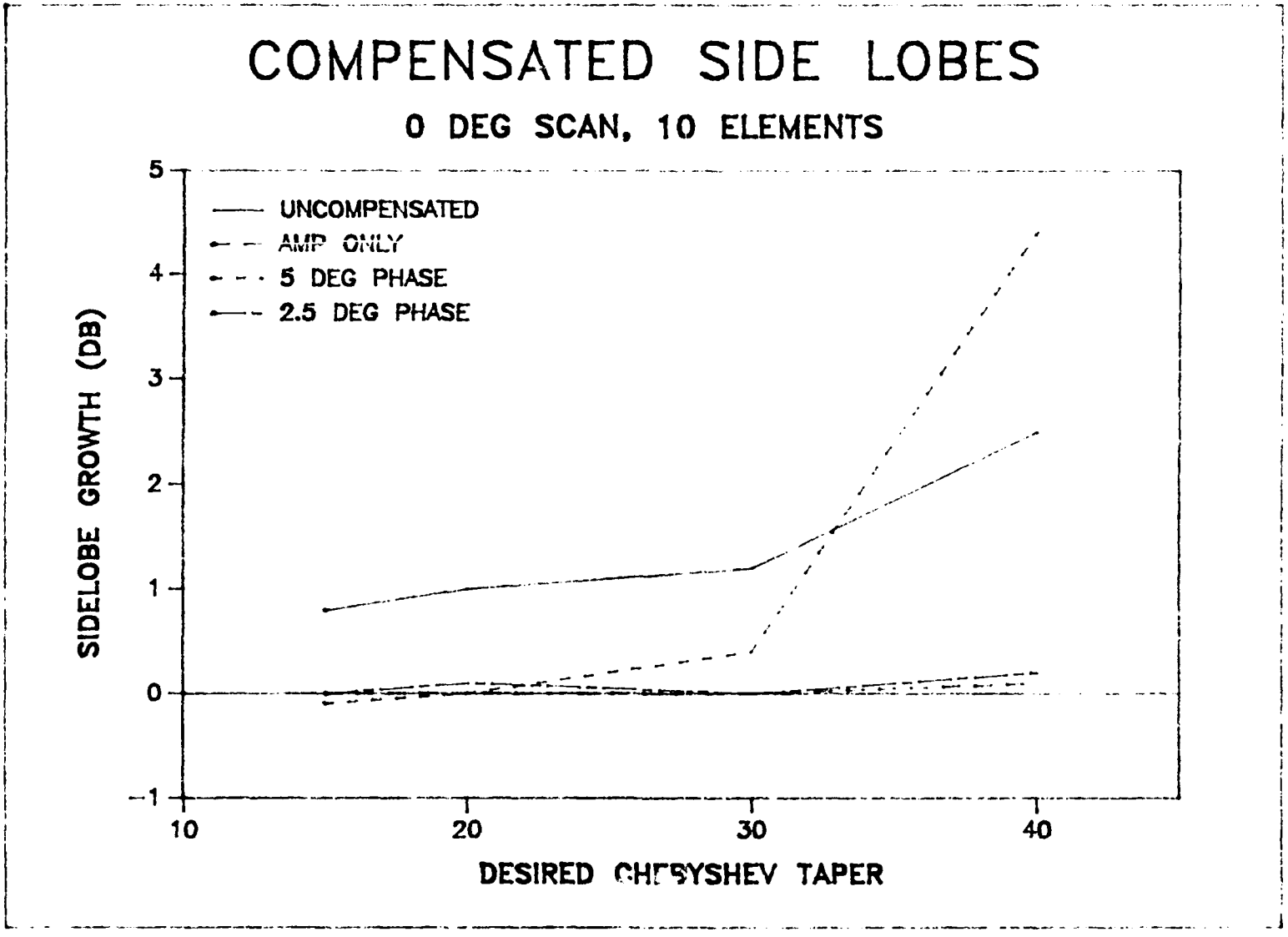

FIGURE 48. COMPENSATED SIDE LOBES (0 DEG SCAN, 10 ELEMENTS)

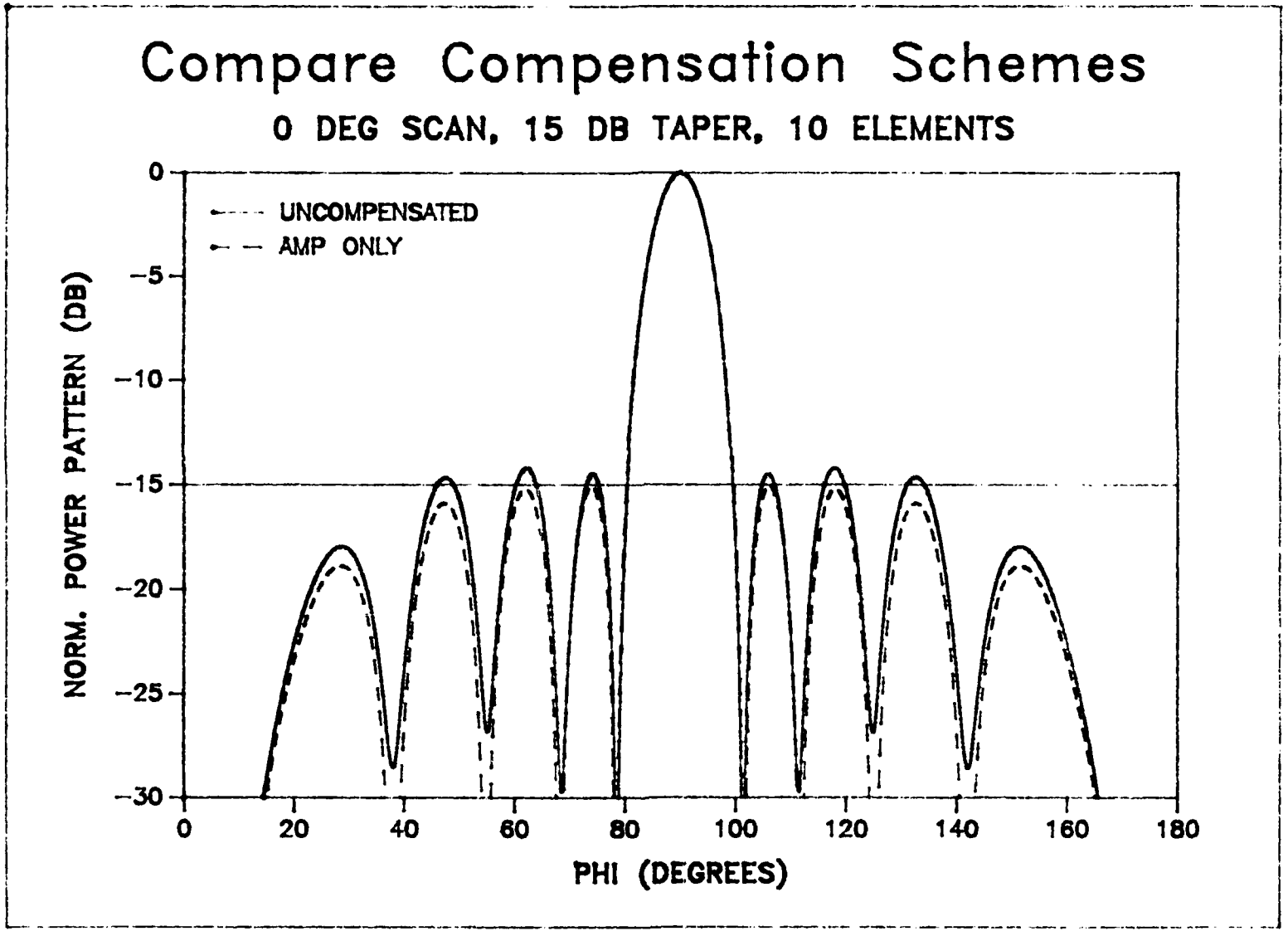

FIGURE 49. COMPARE UNCOMPENSATED AND AMPLITUDE ONLY COMPENSATION; 0 DEG SCAN, 15 DB TAPER, 10 ELEMENTS

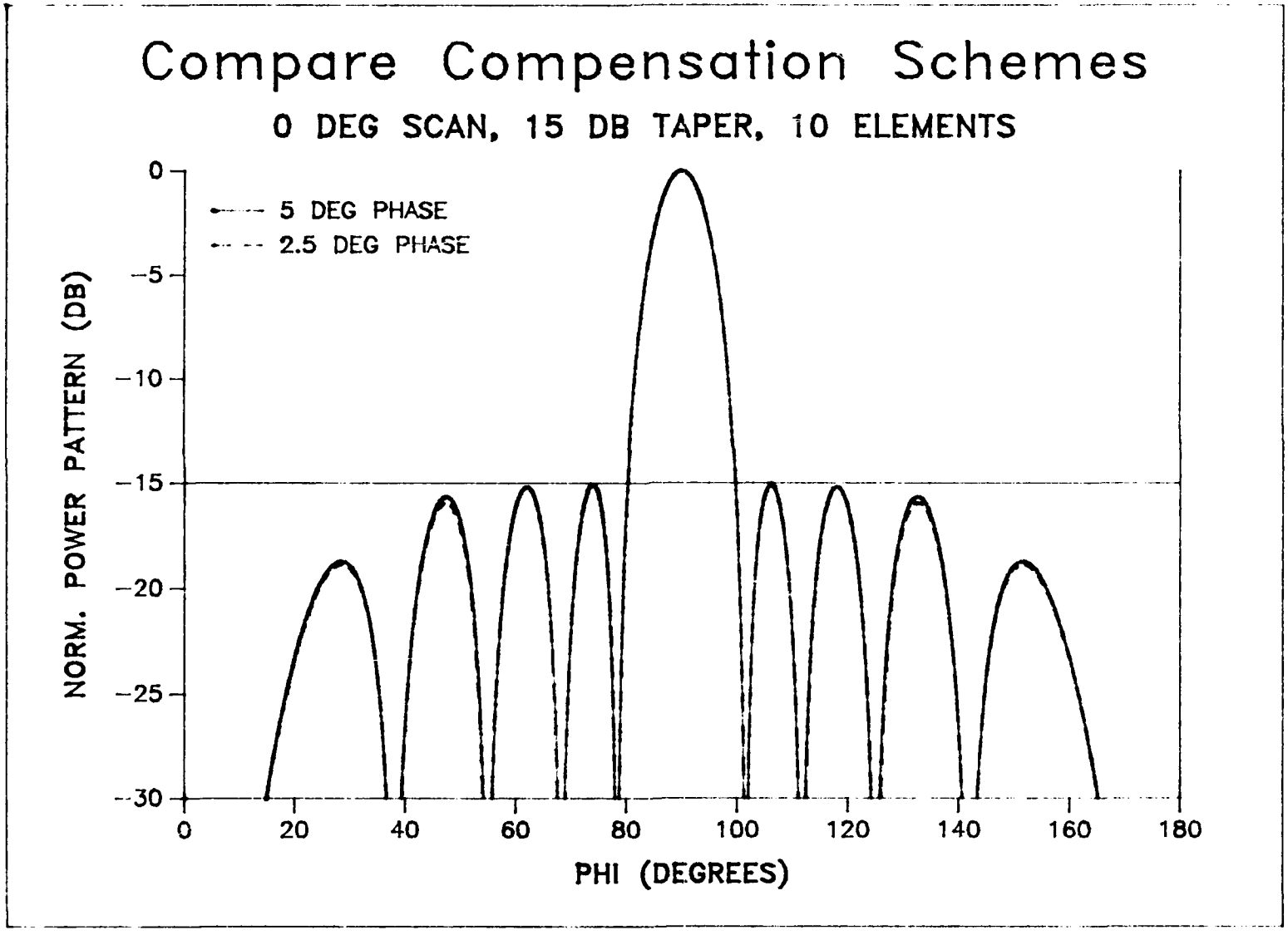

FIGURE 50. COMPARE 5 DEG & 2.5 DEG COMPENSATION SCHEMES;
0 DEG SCAN, 15 DB TAPER, 10 ELEMENTS

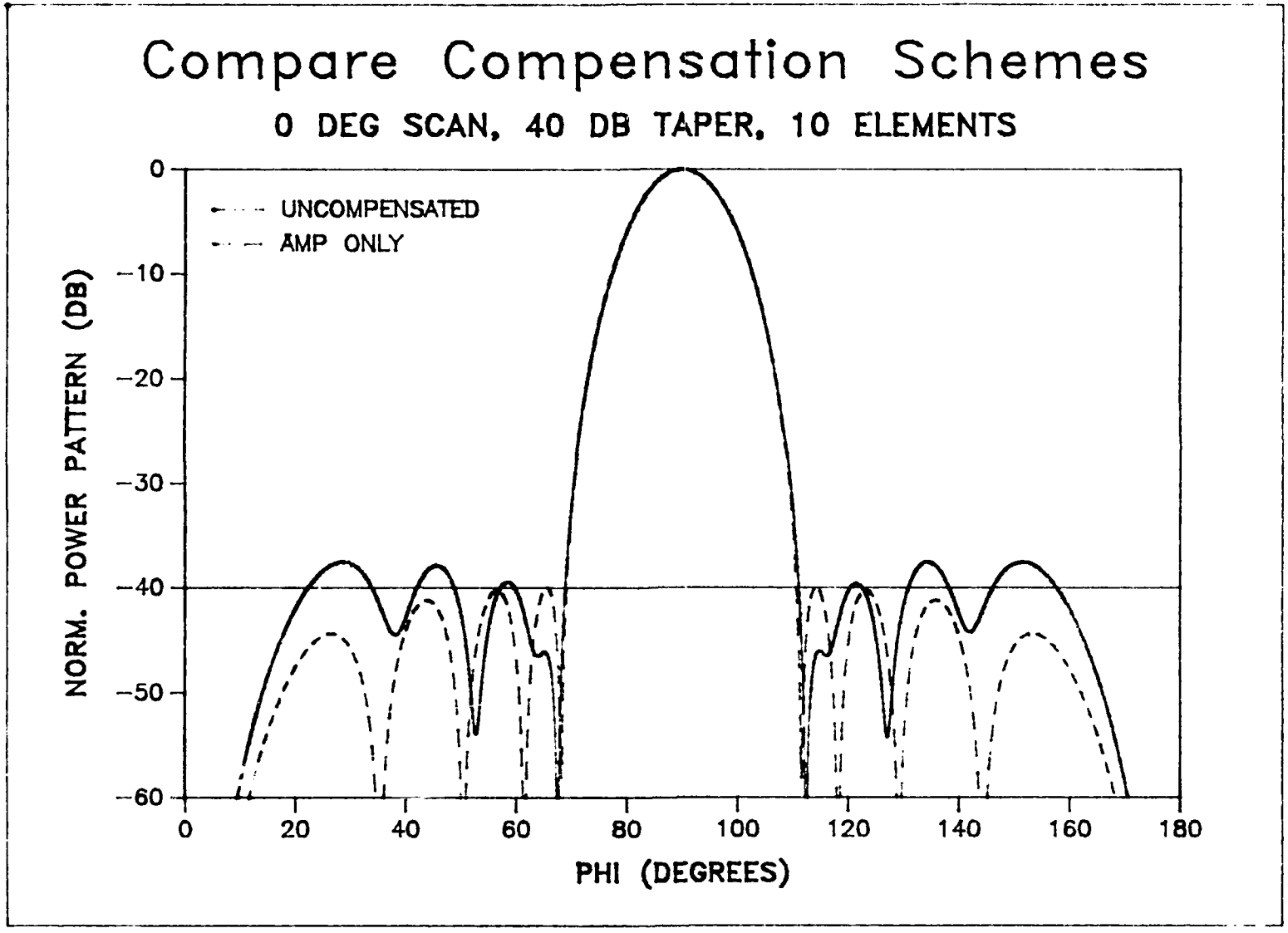

FIGURE 51. COMPARE UNCOMPENSATED AND AMPLITUDE ONLY COMPENSATION; 0 DEG SCAN, 40 DB TAPER, 10 ELEMENTS

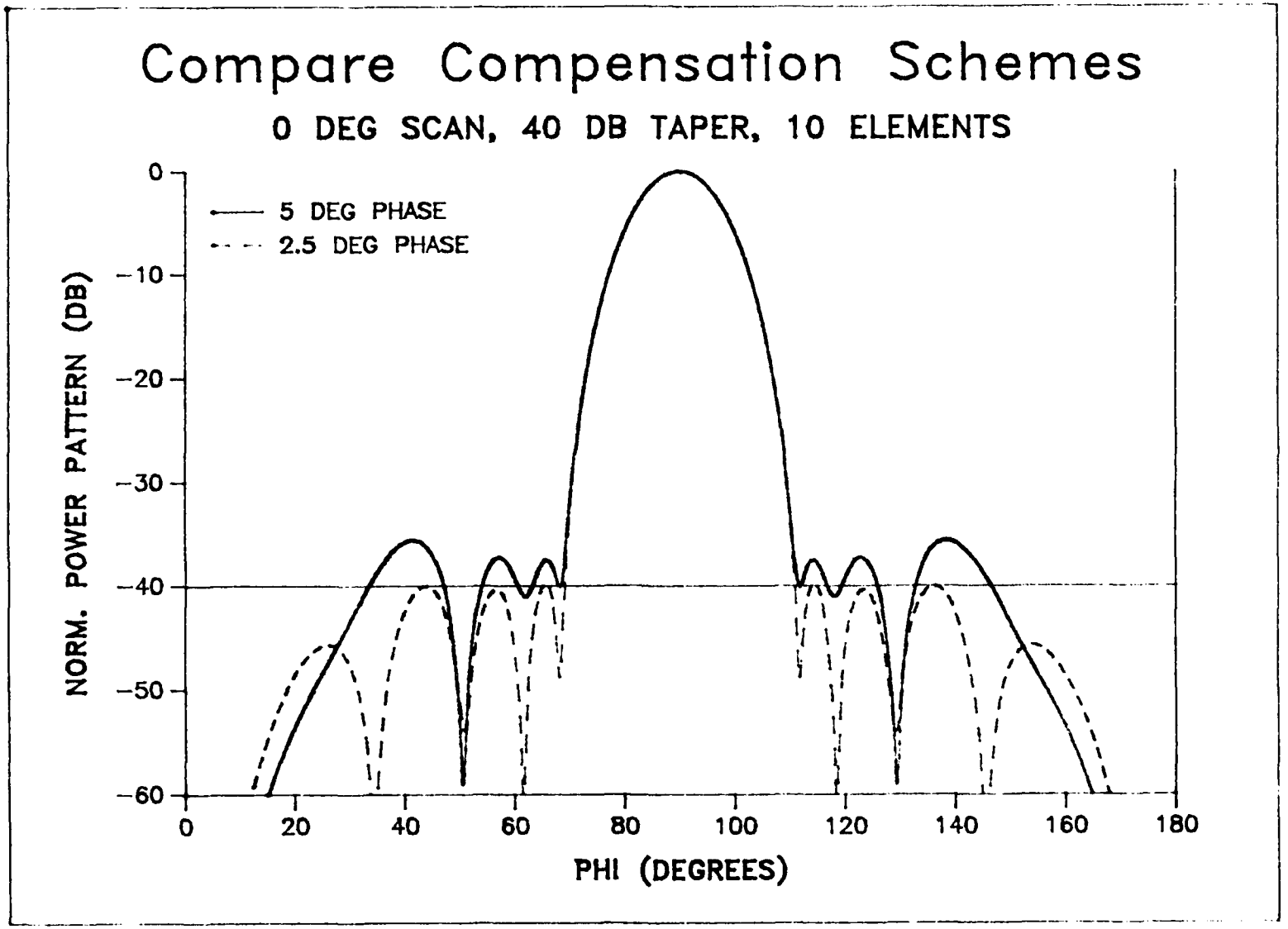

FIGURE 52. COMPARE 5 DEG & 2.5 DEG COMPENSATION SCHEMES;
0 DEG SCAN, 40 DB TAPER, 10 ELEMENTS

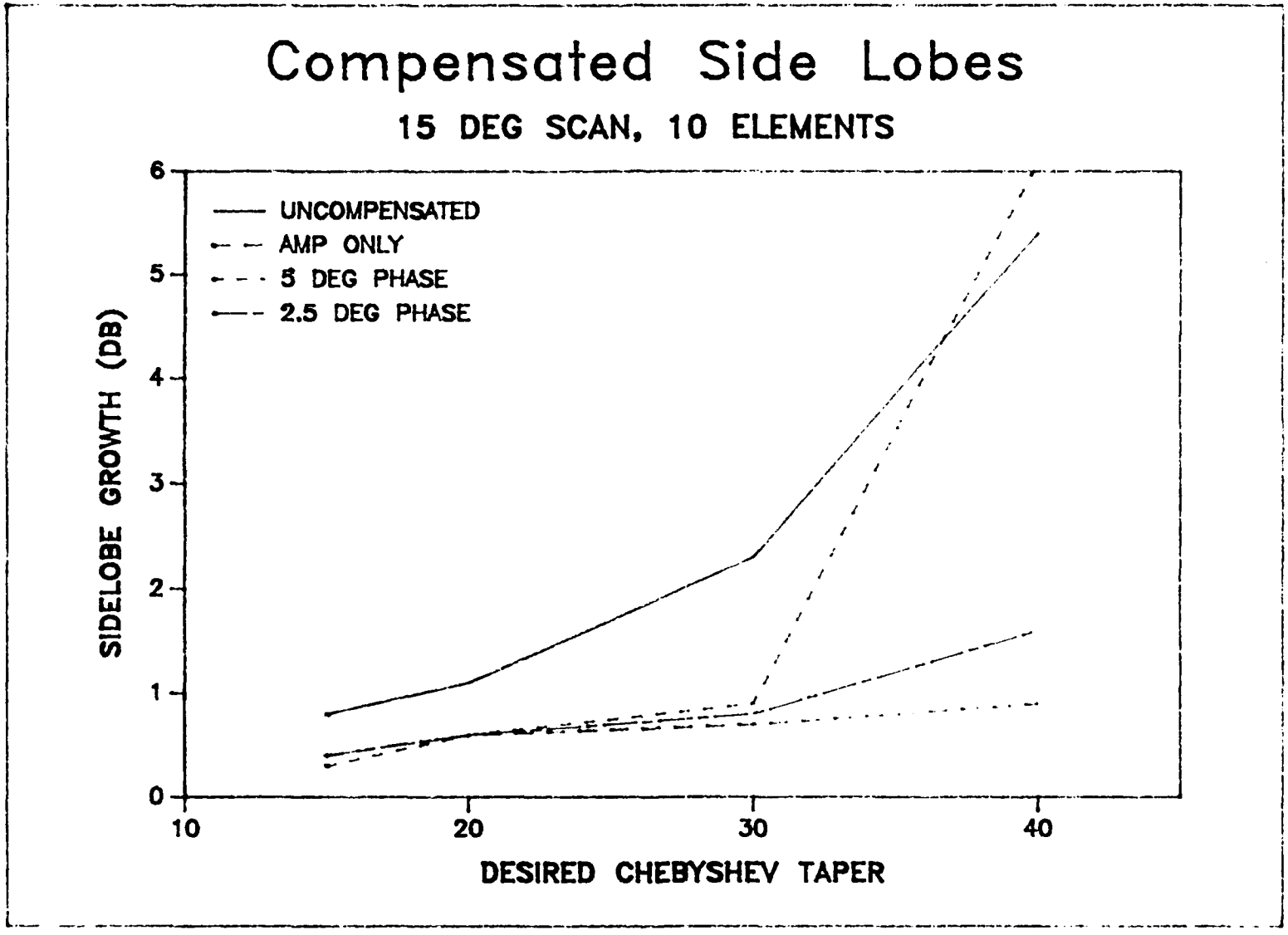

FIGURE 53. COMPENSATED SIDE LOBES (15 DEG SCAN, 10 ELEMENTS)

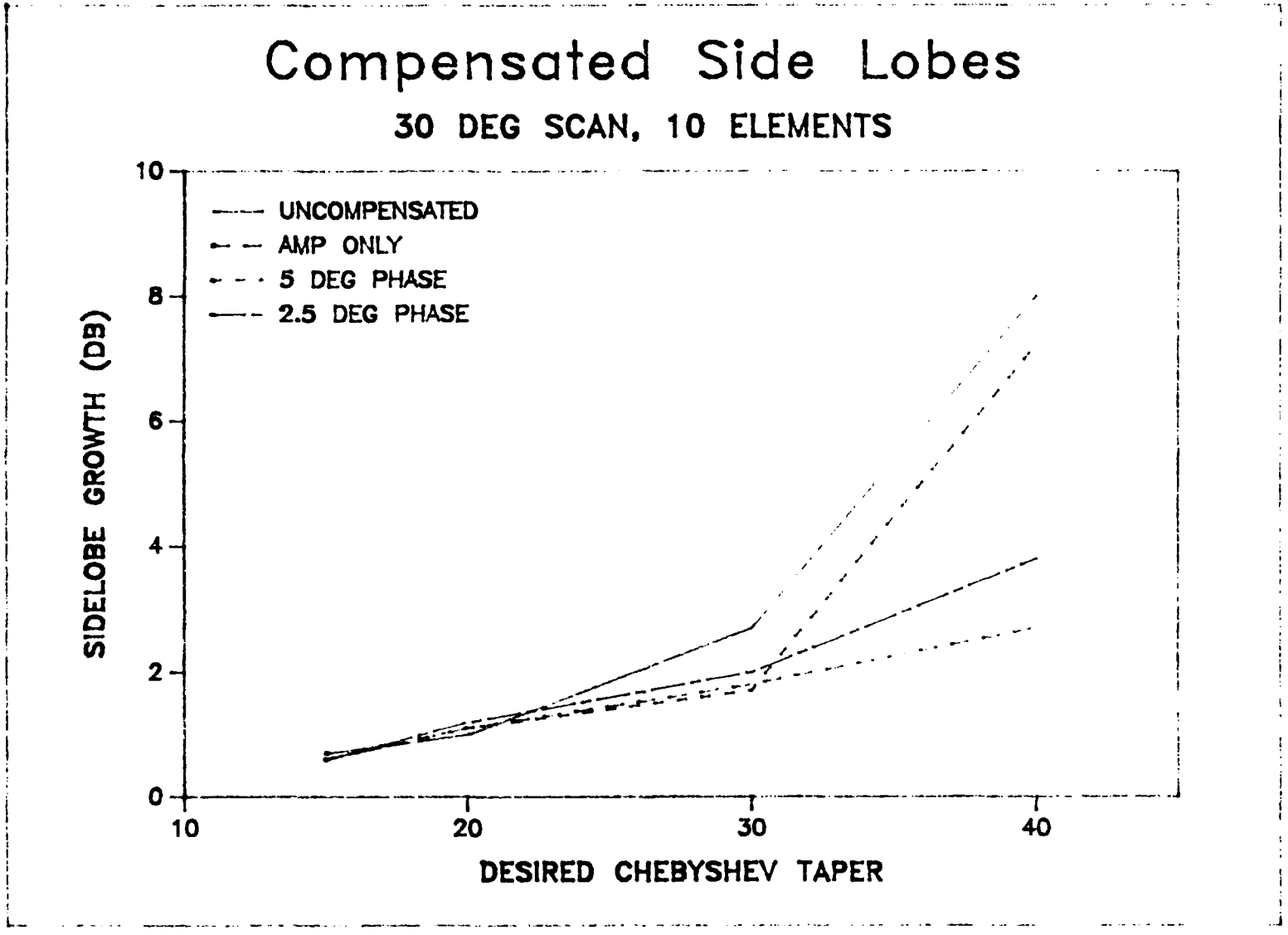

FIGURE 54. COMPENSATED SIDE LOBES (30 DEG SCAN, 10 ELEMENTS)

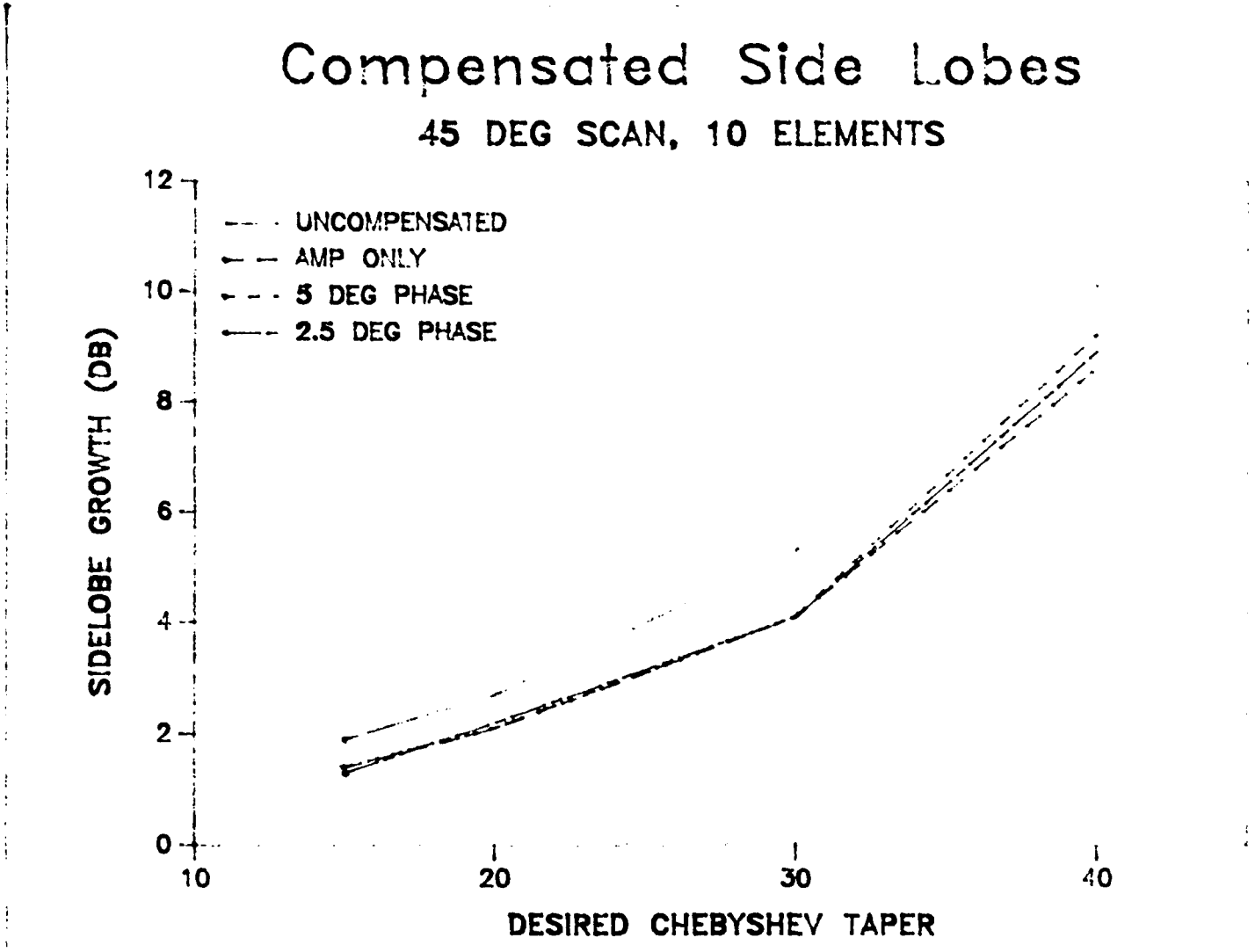

FIGURE 55. COMPENSATED SIDE LOBES (45 DEG SCAN, 10 ELEMENTS)

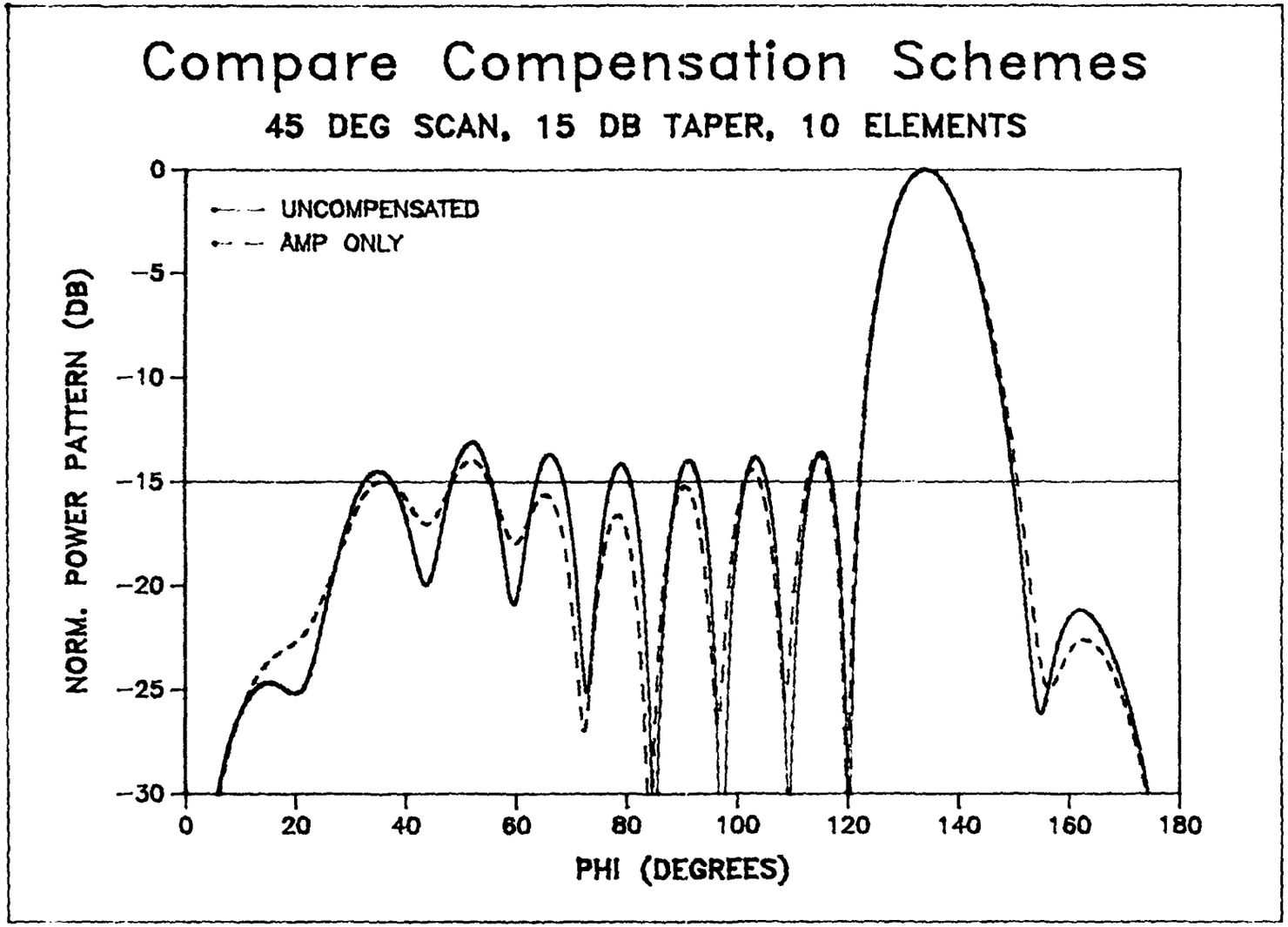

FIGURE 56. COMPARE UNCOMPENSATED AND AMPLITUDE ONLY COMPENSATION; 45 DEG SCAN, 15 DB TAPER, 10 ELEMENTS

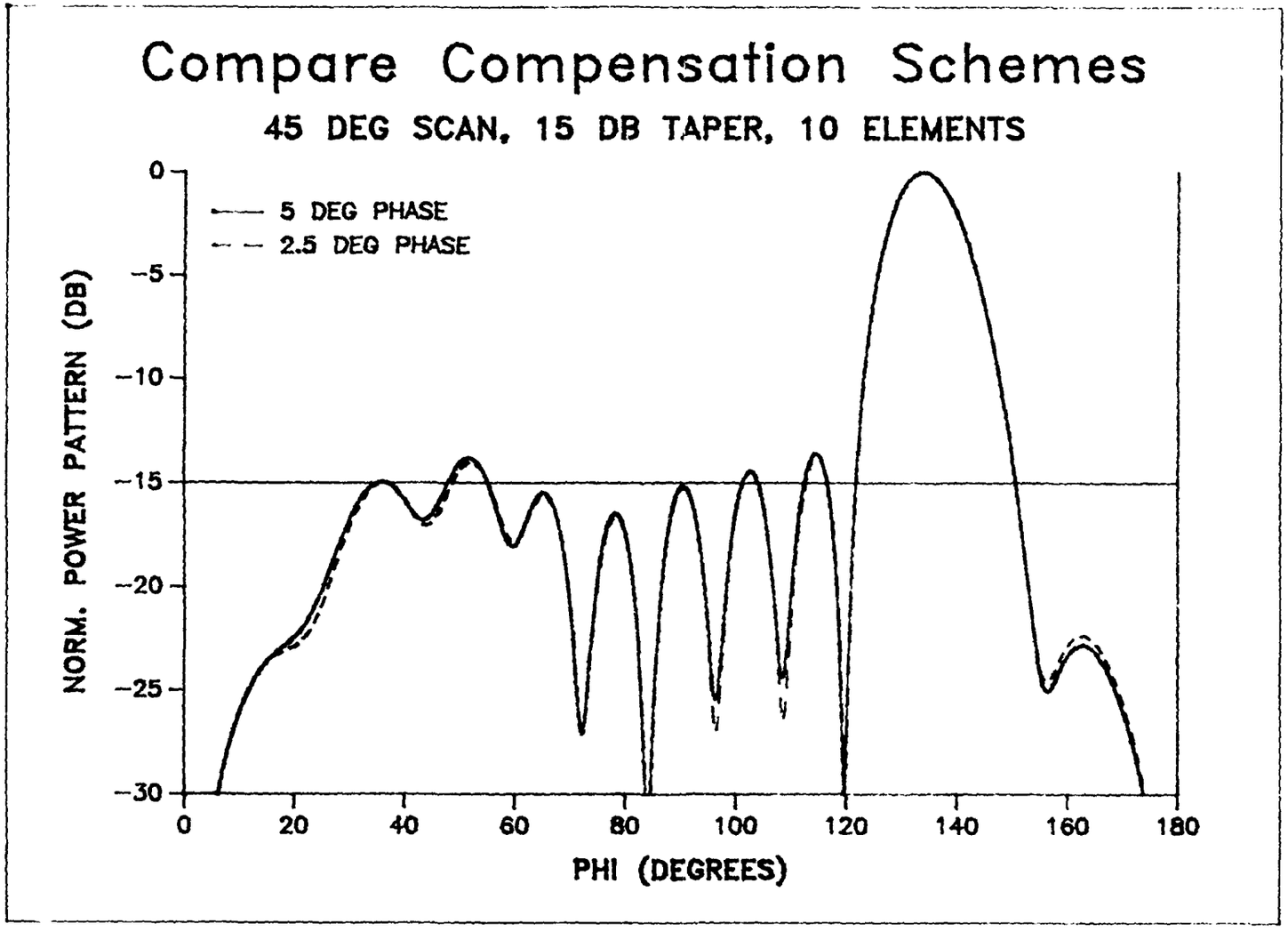

FIGURE 57. COMPARE 5 DEG & 2.5 DEG COMPENSATION SCHEMES;
45 DEG SCAN, 15 DB TAPER, 10 ELEMENTS

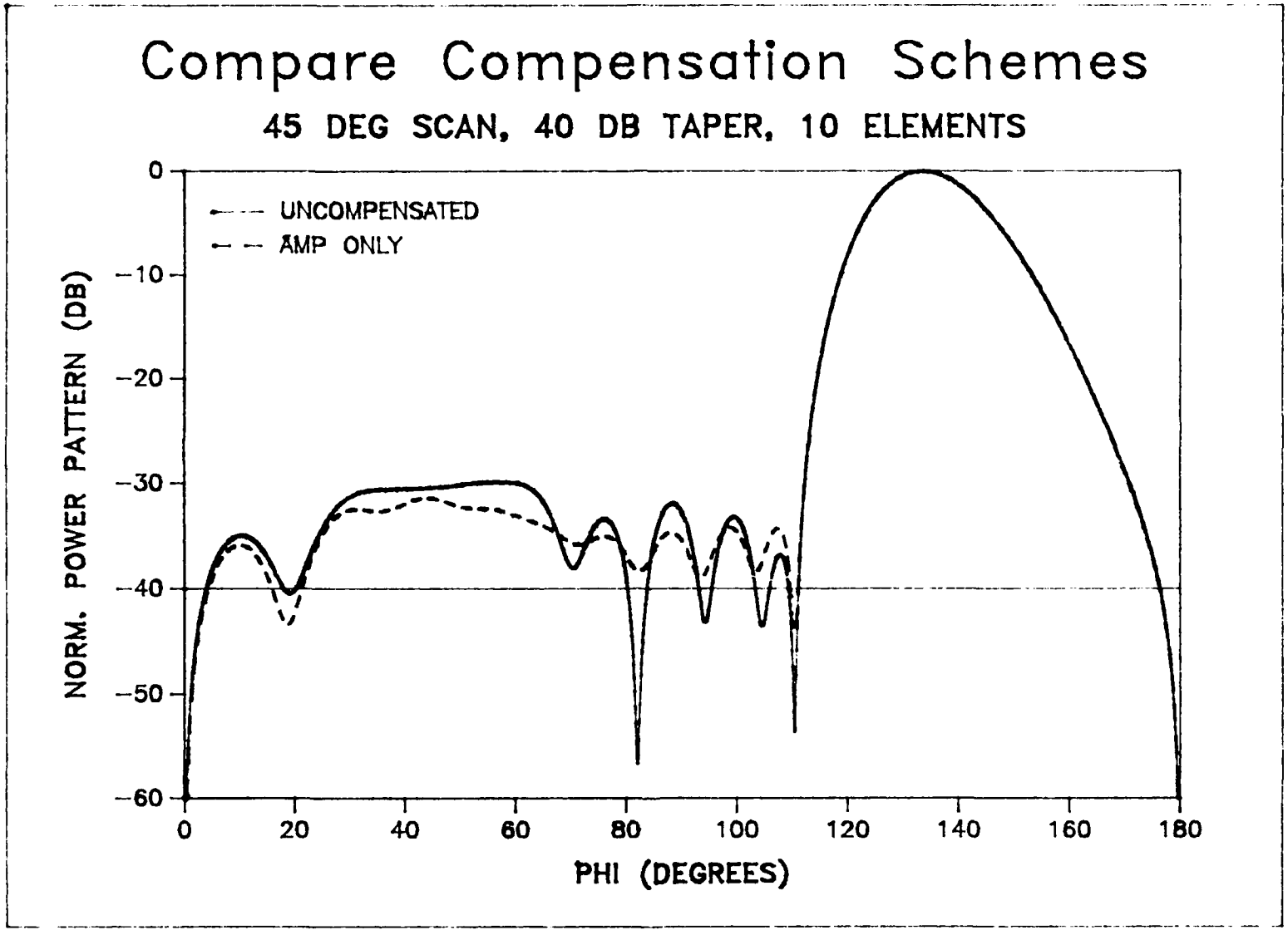

FIGURE 58. COMPARE UNCOMPENSATED AND AMPLITUDE ONLY COMPENSATION; 45 DEG SCAN, 40 DB TAPER, 10 ELEMENTS

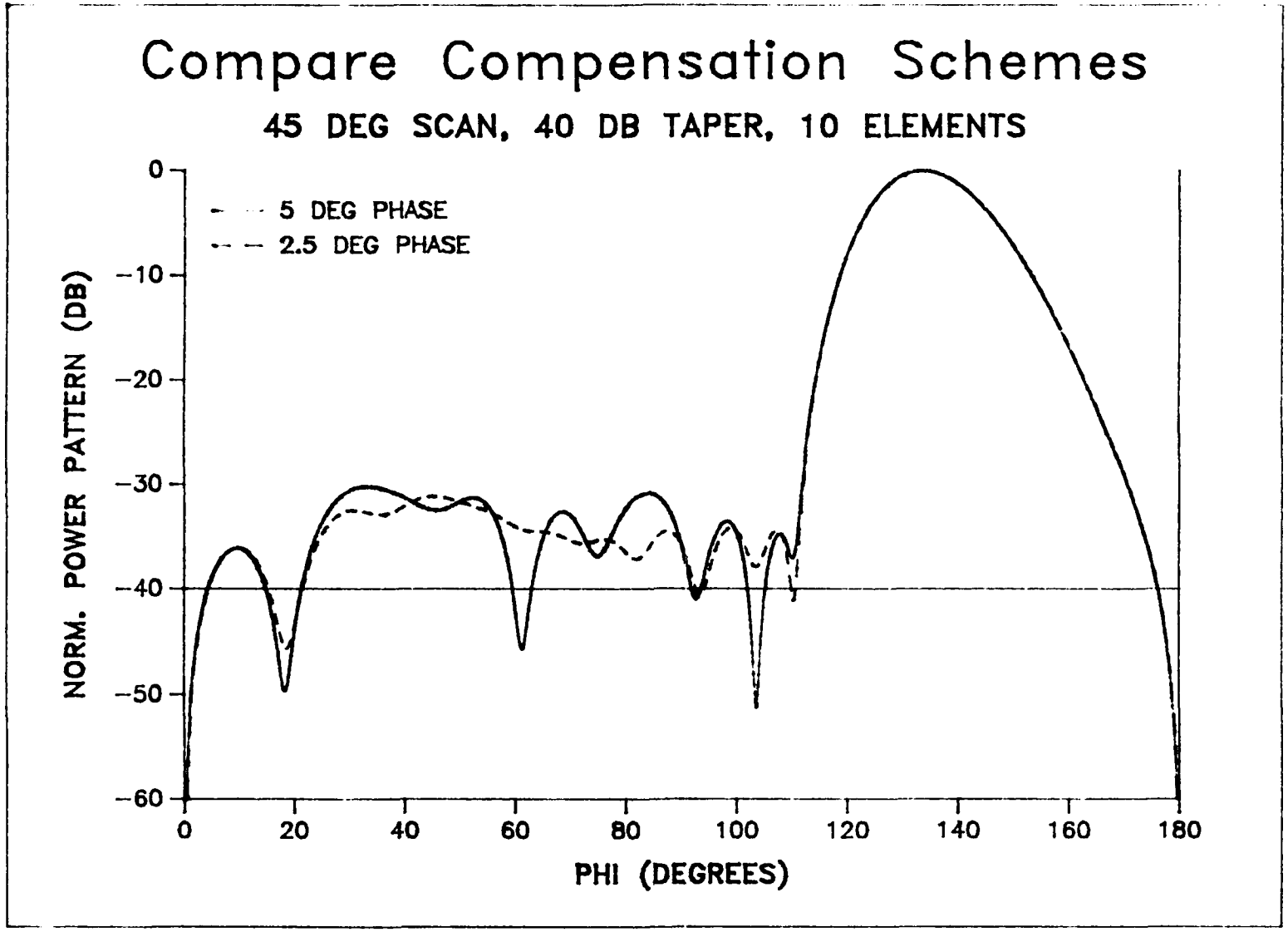

FIGURE 59. COMPARE 5 DEG & 2.5 DEG COMPENSATION SCHEMES;
45 DEG SCAN, 40 DB TAPER, 10 ELEMENTS

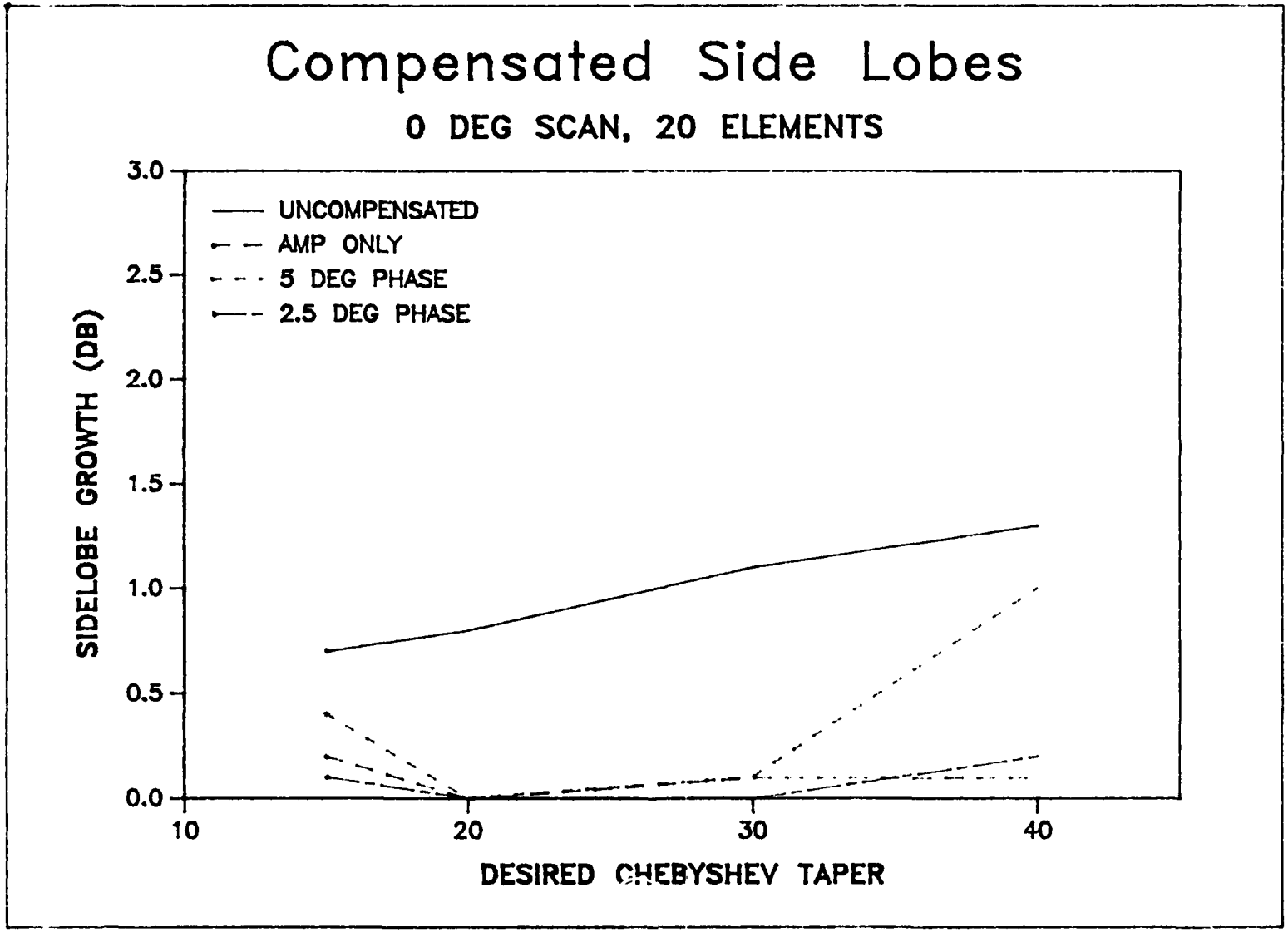

FIGURE 60. COMPENSATED SIDE LOBES (0 DEG SCAN, 20 ELEMENTS)

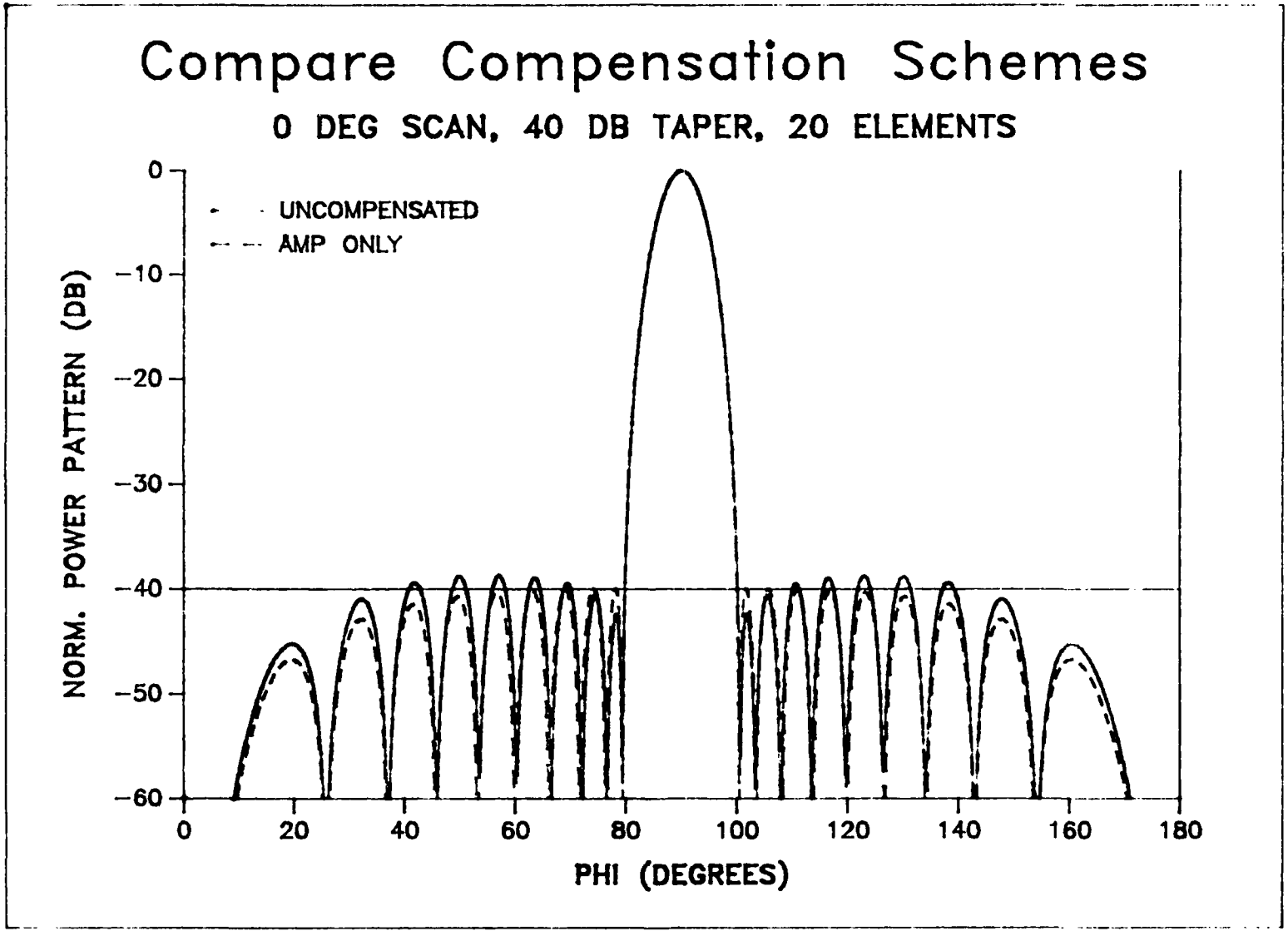

FIGURE 61. COMPARE UNCOMPENSATED AND AMPLITUDE ONLY COMPENSATION; 0 DEG SCAN, 40 DB TAPER, 20 ELEMENTS

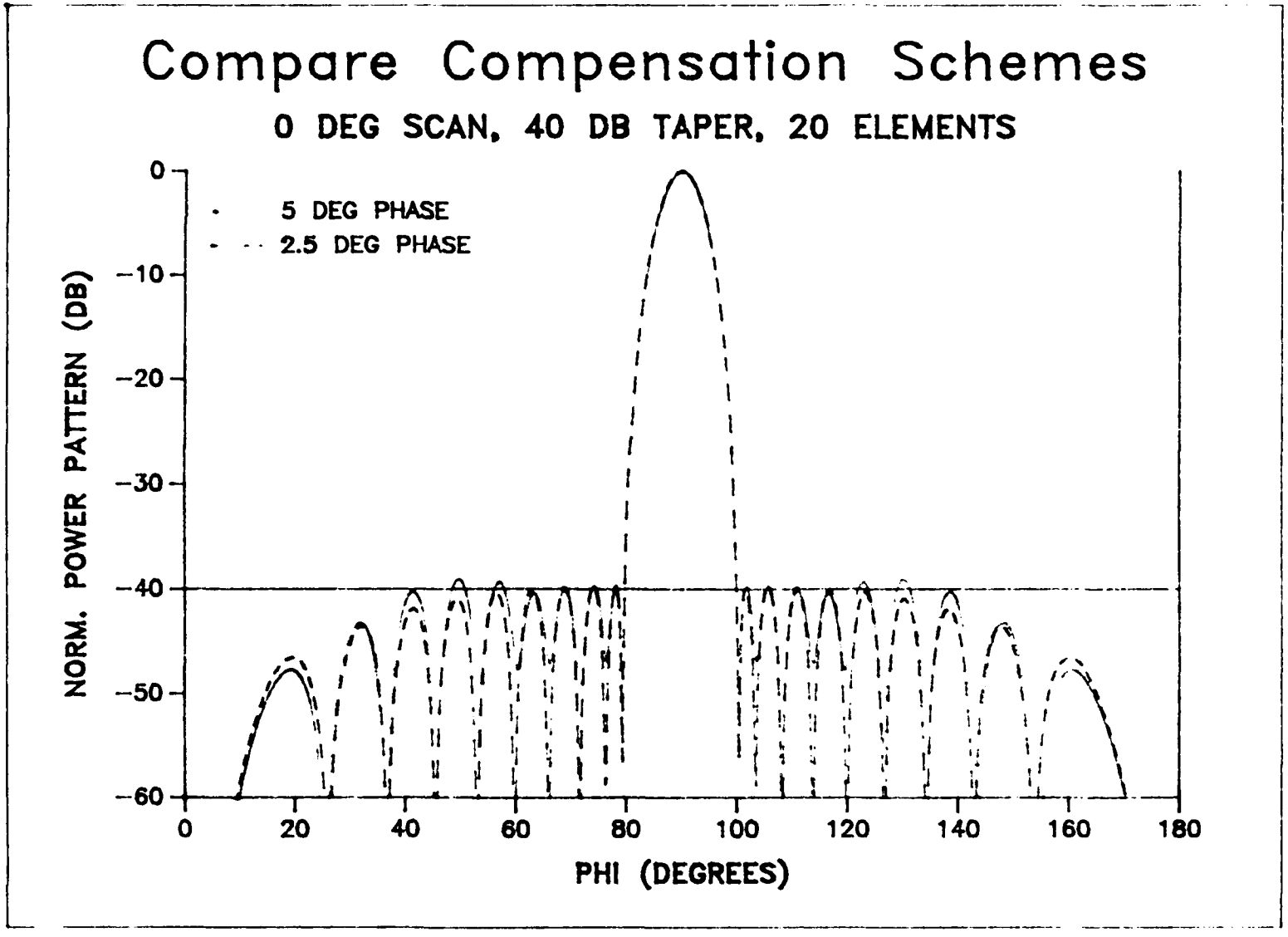

FIGURE 62. COMPARE 5 DEG & 2.5 DEG COMPENSATION SCHEMES;
0 DEG SCAN, 40 DB TAPE, 20 ELEMENTS

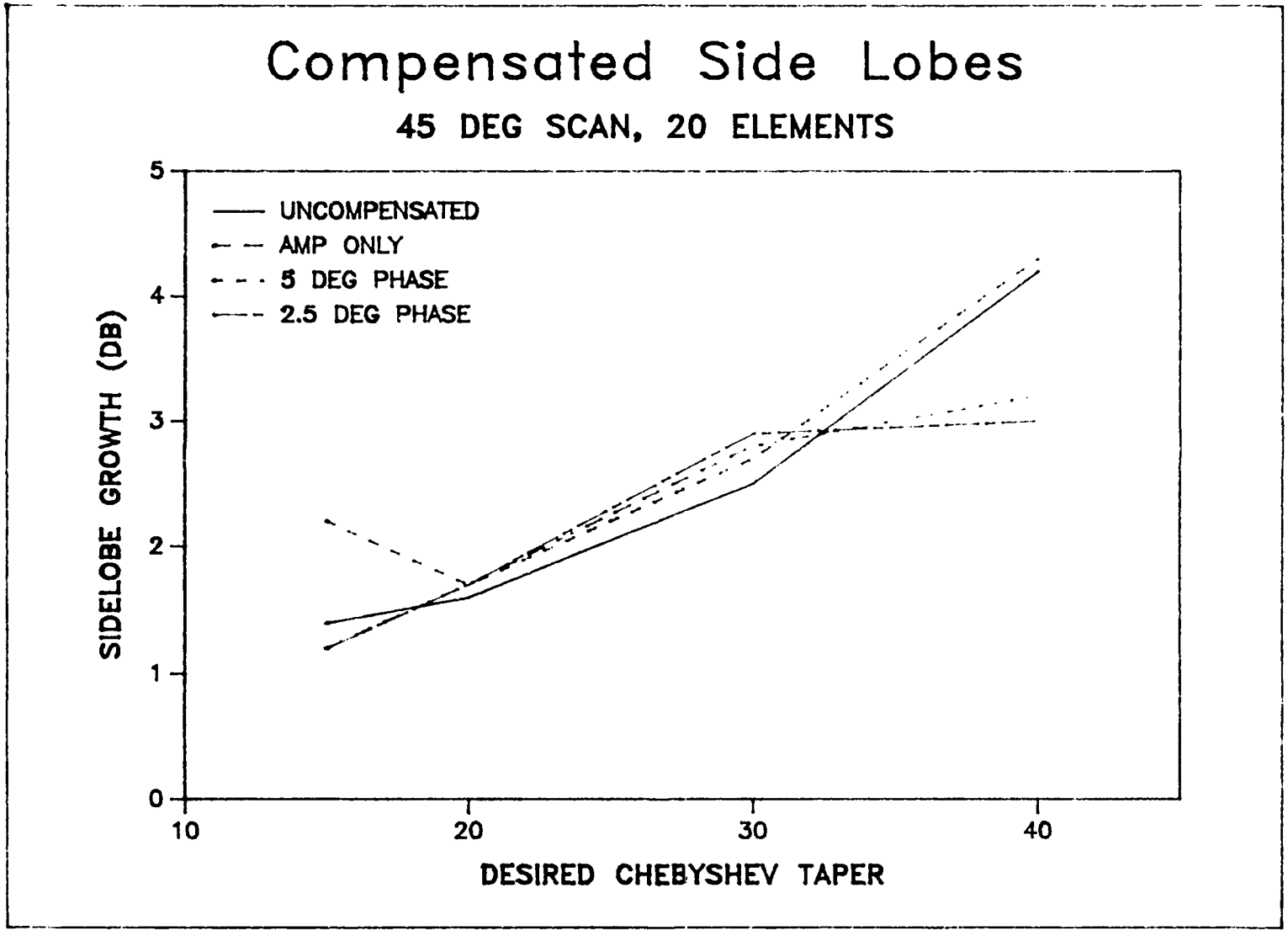

FIGURE 63. COMPENSATED SIDE LOBES (45 DEG SCAN, 20 ELEMENTS)

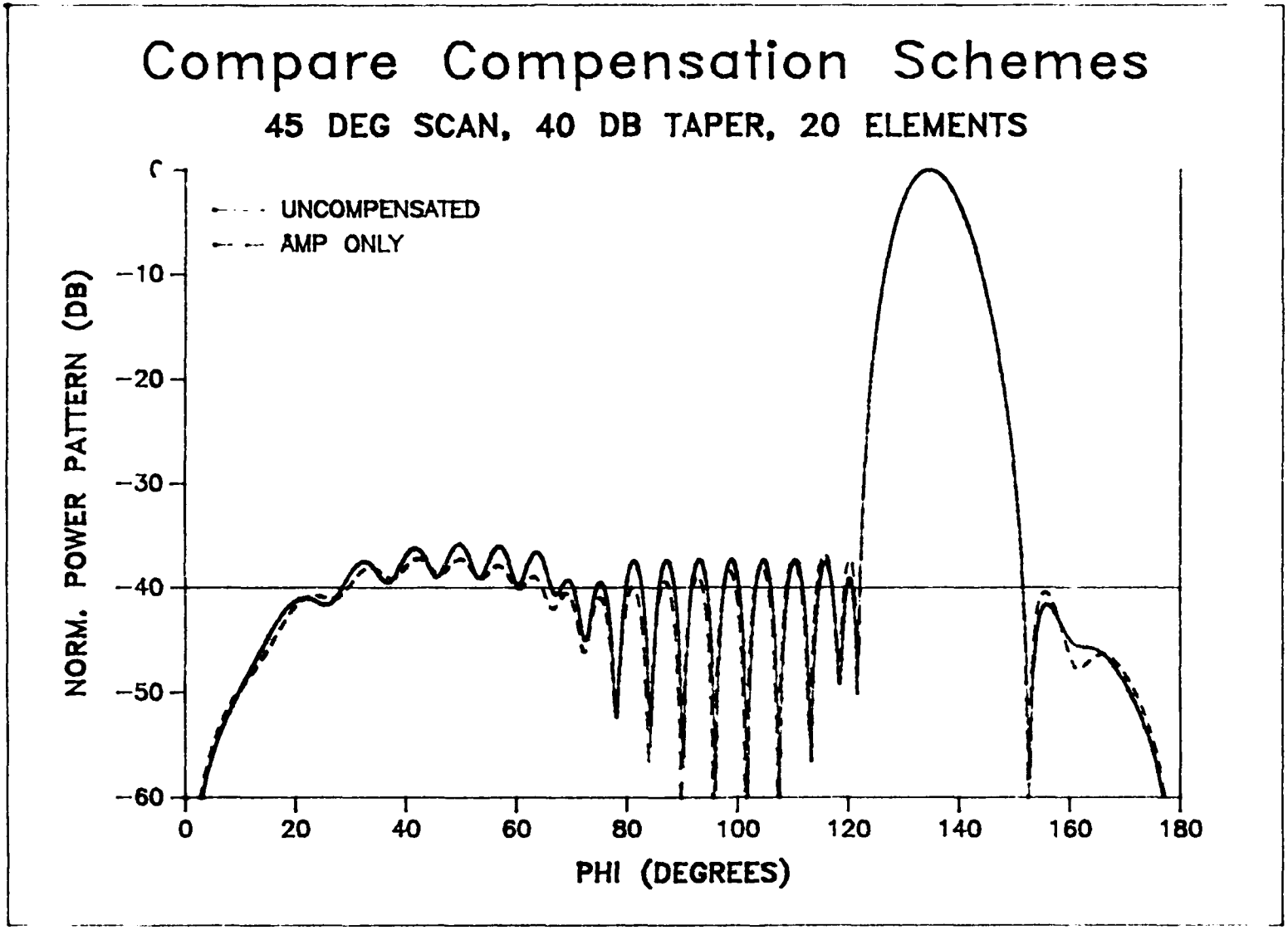

FIGURE 64. COMPARE UNCOMPENSATED AND AMPLITUDE ONLY COMPENSATION; 45 DEG SCAN, 40 DB TAPER, 20 ELEMENTS

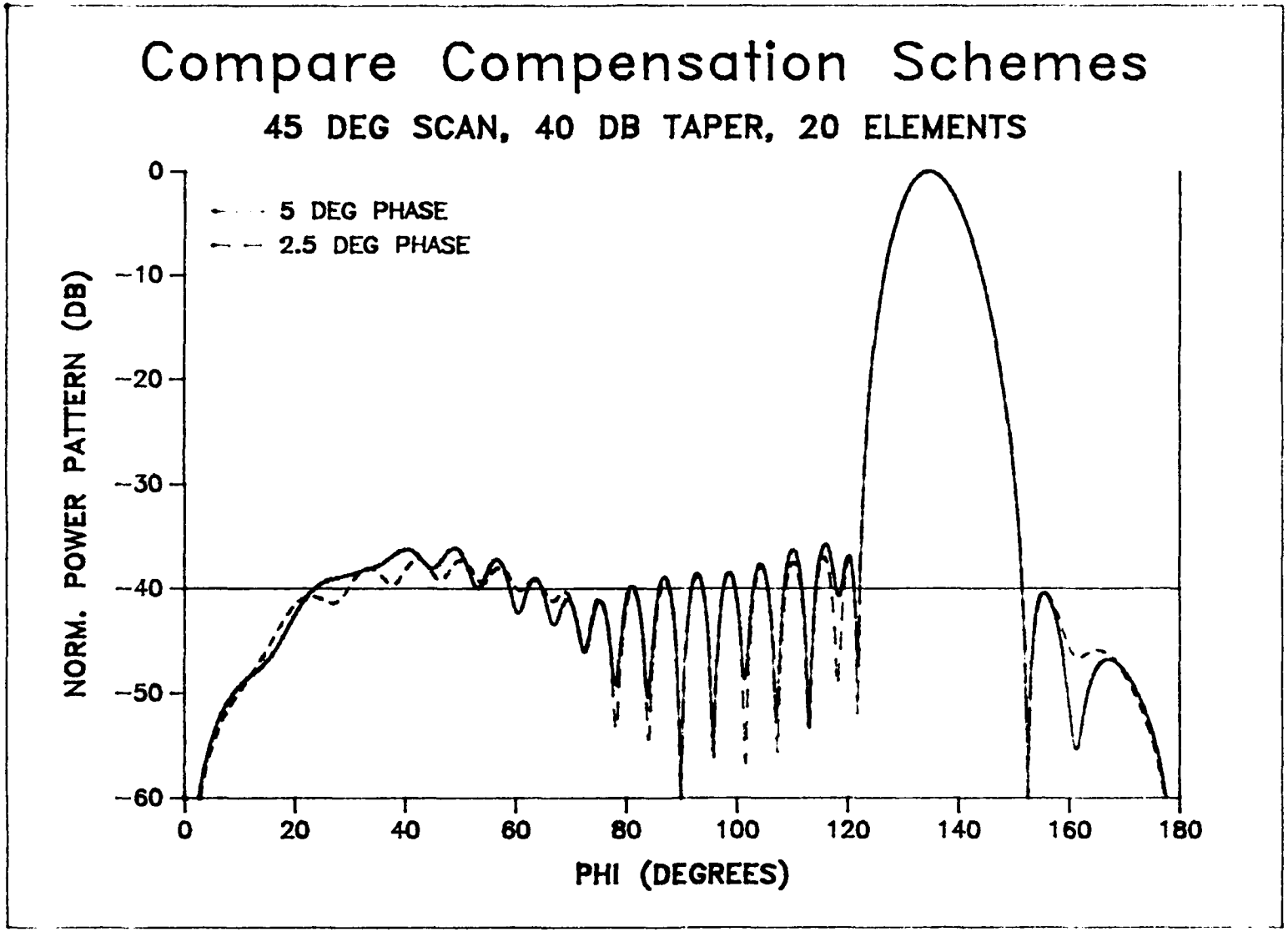

FIGURE 65. COMPARE 5 DEG & 2.5 DEG COMPENSATION SCHEMES;
45 DEG SCAN, 40 DB TAPER, 20 ELEMENTS

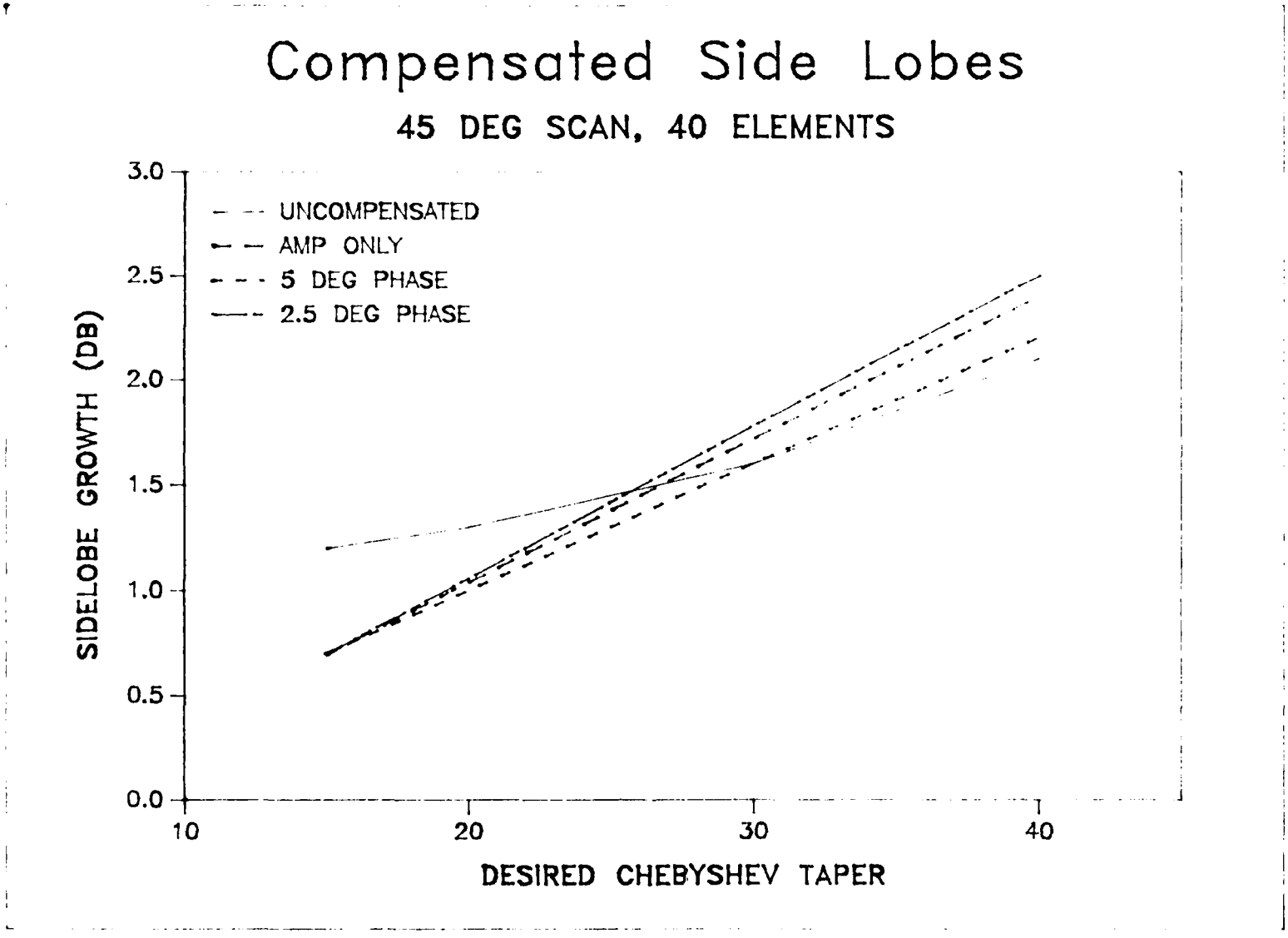

FIGURE 66. COMPENSATED SIDE LOBES (45 DEG SCAN, 40 ELEMENTS)

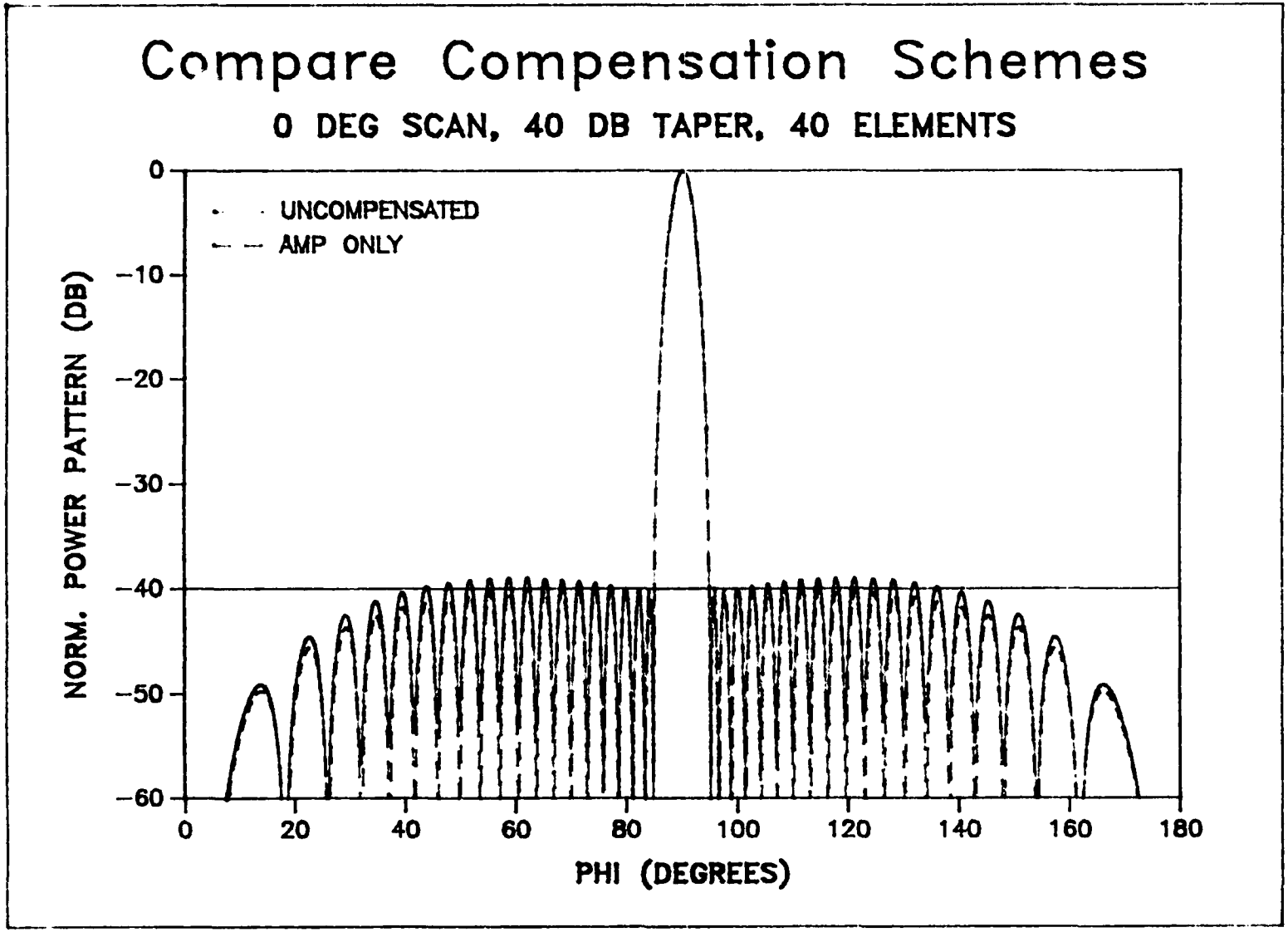

FIGURE 67. COMPARE UNCOMPENSATED AND AMPLITUDE ONLY COMPENSATION; 0 DEG SCAN, 40 DB TAPER, 40 ELEMENTS

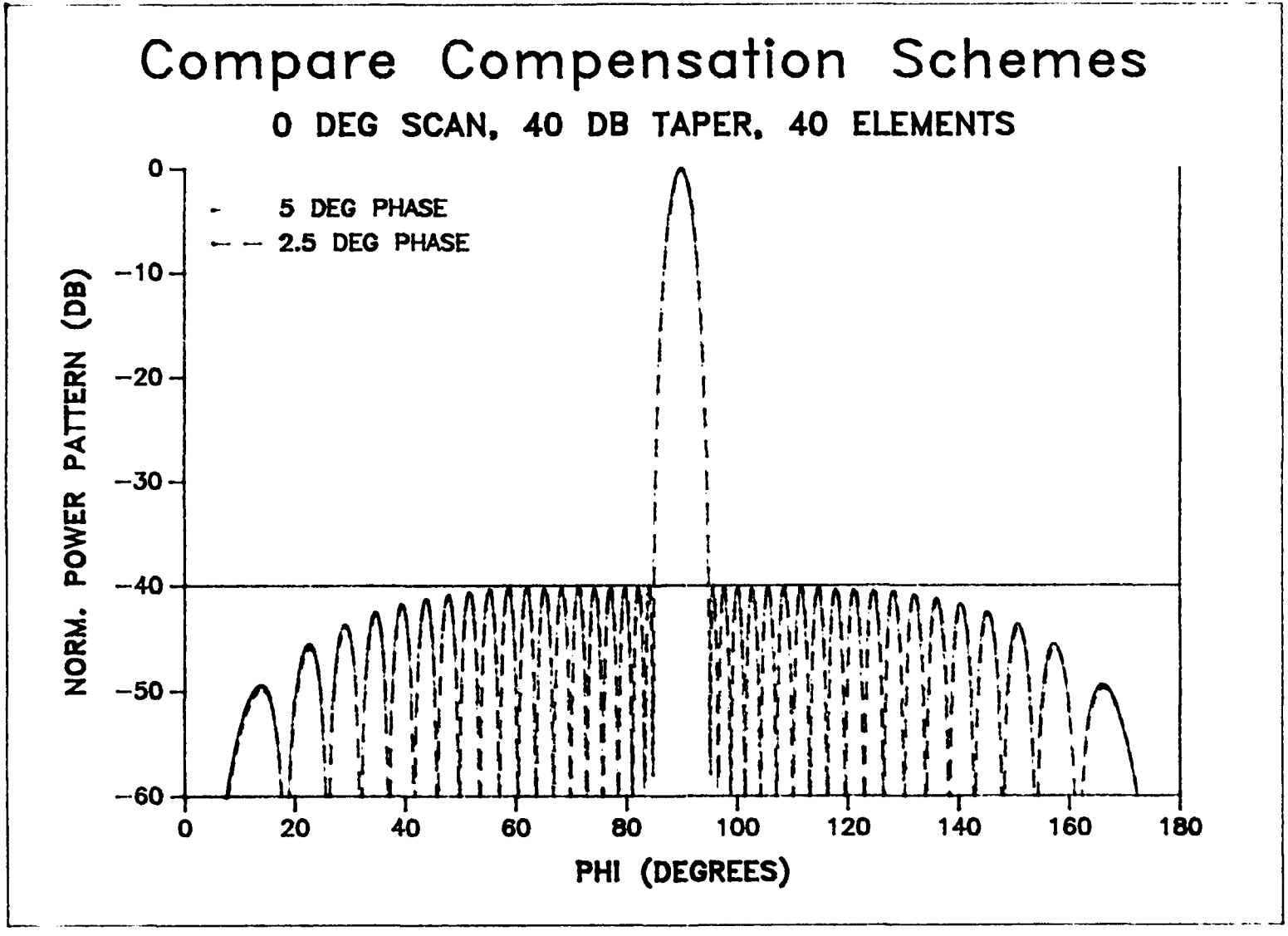

FIGURE 68. COMPARE 5 DEG & 2.5 DEG COMPENSATION SCHEMES;
0 DEG SCAN, 40 DB TAPER, 40 ELEMENTS

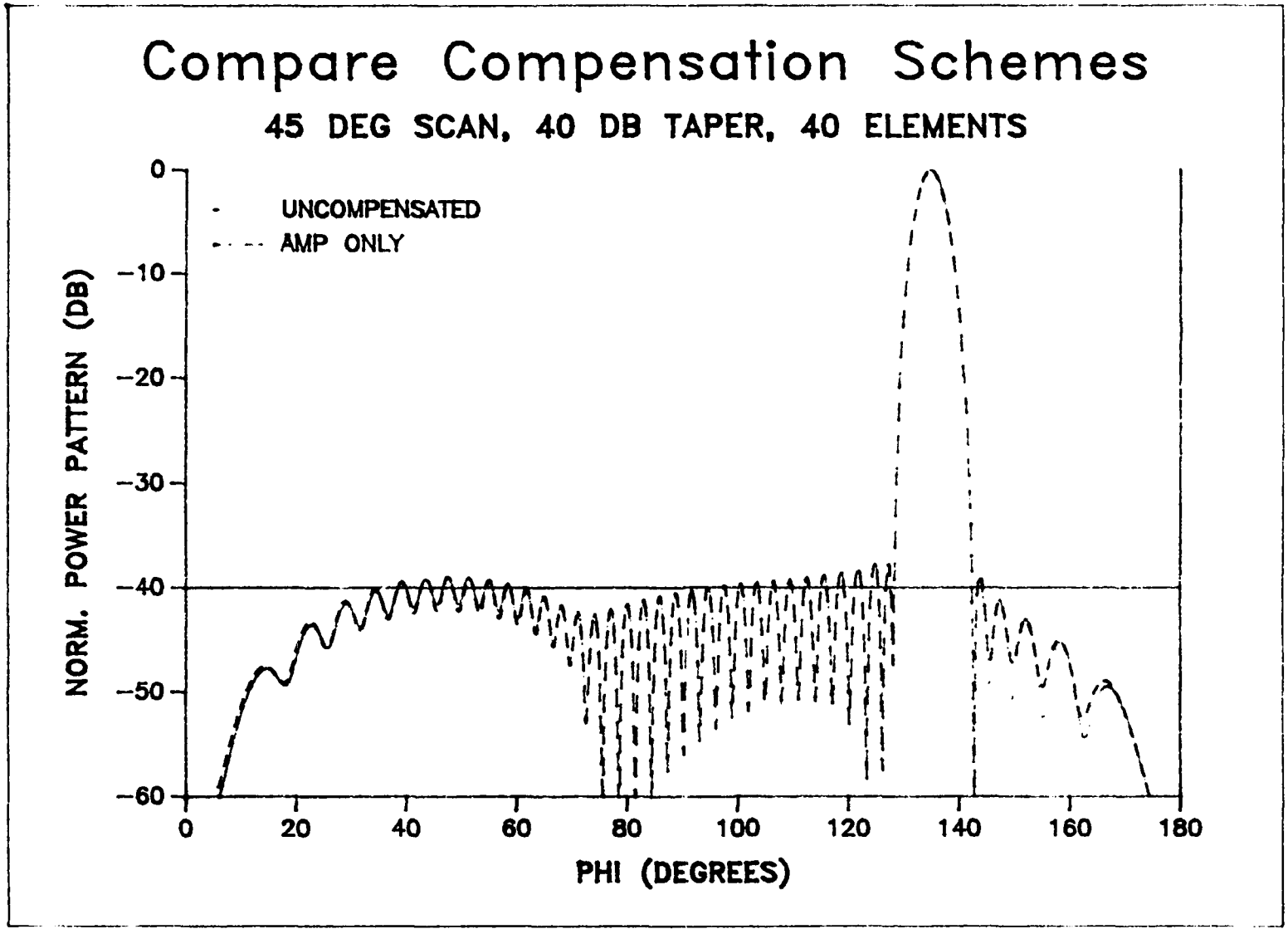

FIGURE 69. COMPARE COMPENSATED AND AMPLITUDE ONLY COMPENSATION; 45 DEG SCAN, 40 DB TAPER, 40 ELEMENTS

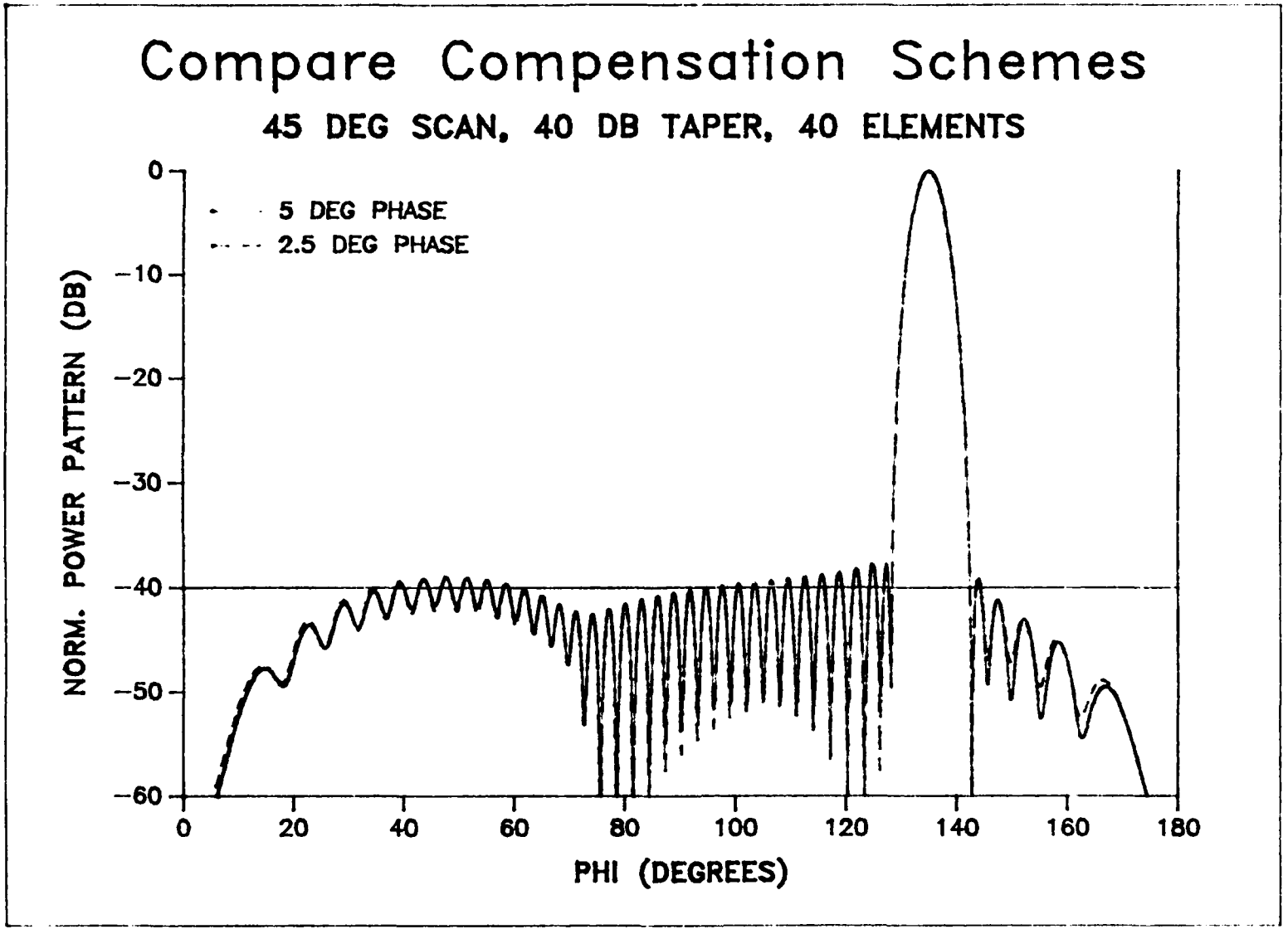

FIGURE 70. COMPARE 5 DEG & 2.5 DEG COMPENSATION SCHEMES;
45 DEG SCAN, 40 DB TAPER, 40 ELEMENTS

6.0 CONCLUSIONS AND RECOMMENDATIONS

Several expected relationships were evident in this study. Namely, smaller arrays are dominated by edge effects and are therefore significantly impacted by mutual coupling. Severe amplitude tapers and resulting low side lobe patterns are difficult to achieve. And lastly, scanning compounds these effects. From a design point of view, the following guidelines may prove useful.

For 30 and 40 element arrays, mutual coupling may be ignored for side lobe considerations. Since the far-field patterns are so well behaved, the inevitable side lobe growth at large scan angles, can be easily dealt with by specifying side lobe performance 3 to 5 db lower than necessary at broadside.

The 20 element array just crosses the arbitrary 3 db growth standard at large scan angles, and severe tapers. The compensation techniques provide some measurable improvement up to 30 db Chebyshev tapers, however near 40 db (-35 to -38) tapers are achievable without resorting to coupling analyses and compensation techniques.

The 10 element arrays are dominated by coupling, however 30 db tapers can be achieved using amplitude only compensation for moderate scan volumes $\leq 30°$. The 40 db tapers can be achieved near broadside, but are not achievable for 45 deg scan angles using any of the compensation schemes in this report.

It is interesting to note that the amplitude plus 5 degree phase compensation scheme was less effective than the amplitude only scheme. The 2.5 degree scheme was approximately the same as the amplitude only scheme, therefore phase compensation techniques provided no additional side lobe performance to justify their use over the amplitude only technique (for the array geometries and excitations studied in the report). This may not hold true for greater than 40 db Chebyshev tapers.

Areas of further study could either extend the fortran codes in this study to model linear arrays of strip dipoles with specific corporate feed structures, or focus on the impact of coupling on more complex shaped pattern design problems. Comparisons of amplitude versus phase only tapers, as well as the sensitivity of unequally spaced or sparse linear arrays to coupling, could easily be added to this code. If planar arrays are of interest, the King-Middleton Five-Term theory would be required, which would entail considerable modification of the author's programs. Existing method of moments codes may be easier to apply, in many instances, than the King-Middleton Theory, at some additional computational cost. If this code is extended, available symmetries should be exploited to reduce the required computer resources.

APPENDIX A1

DERIVATION OF KING-MIDDLETON'S ZERO-ORDER, TWO-TERM THEORY FOR DIPOLE ANTENNA

A1.1 ISOLATED DIPOLE

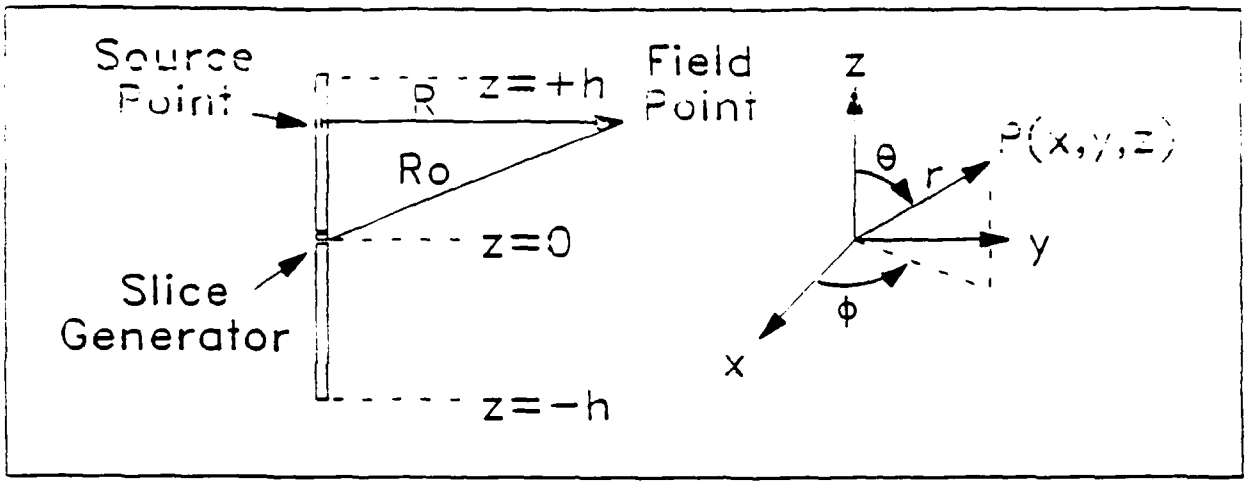

FIGURE A.1. DIPOLE GEOMETRY

Consider the antenna geometry shown in Figure A.1. The following conditions are imposed upon this dipole:

$$h >> a \qquad \text{(A-1a)}$$

$$\beta_o a << 1 \qquad \text{(A-1b)}$$

$$I_z(z) = I_z(-z) \qquad \text{(A-2a)}$$

$$A_z(z) = A_z(-z) \qquad \text{(A-2b)}$$

$$\phi(z) = -\phi(-z) \qquad \text{(A-2c)}$$

$$q(z) = -q(-z) \qquad \text{(A-2d)}$$

$$I_z(\pm h) = 0 \qquad \text{(A-3a)}$$

$$z_i \equiv 0 \quad . \qquad \text{(A-3b)}$$

Equations (A-1a & b) establishes, in a general sense, what is sufficiently thin. Equations (A-2a-d) state the symmetry conditions that apply to cylindrical

dipole antennas. Equation (A-3a) states currents vanish at the end of the antenna (which can be achieved in practice by using hemispherical end caps), and (A-3b) which states that the internal impedance of a perfect conductor is exactly zero.

Given (A-3b), the vector potential must satisfy the homogeneous Helmholtz for a Z-aligned dipole (1-12a), restated here

$$\left(\frac{\partial^2}{\partial z^2} + \beta_o^{\,2}\right) A_z = 0 \quad . \tag{A-4}$$

The homogeneous solution to (A-4) can be written (15:48)

$$A_z = \begin{cases} \dfrac{-j}{\nu_o}\left(C_1 \ \mathrm{COS}\ \beta_o\ z + C_2\ \mathrm{SIN}\beta_o z\right)\Big|_{\rho=a} & , \ \delta \le z \le h \\ \dfrac{-j}{\nu_o}\left(C_1 \ \mathrm{COS}\ \beta_o\ z - C_2\ \mathrm{SIN}\beta_o z\right)\Big|_{\rho=a} & , \ -\delta \ge z \ge -h \quad . \end{cases} \tag{A-5}$$

Substituting (A-5) into the Lorentz condition equation (1-4c), and equating the gap voltage, V_o, to the scalar potential difference, $\phi(\delta) - \phi(-\delta)$, one can solve for the C_2 coefficient. Equation (A.5) can be reformulated for a "slice" generator ($\delta \to 0$).

$$A_z(z) = \frac{-j}{\nu_o}\left(C_1\ \mathrm{COS}\beta_o z + \frac{Vo}{2}\ \mathrm{SIN}\beta_o |z|\right)\Big|_{\rho=a} \quad , \ -h \le z \le h \quad . \tag{A-6}$$

From retarded potential theory, the vector potential on the surface of a cylindrical antenna can be related to an integral over all currents within that

cylinder (14:76). Further, all currents within that cylinder can be treated as an axial current. That is

$$A_z(z)\Big|_{\rho=a} = \frac{\mu_o}{4\pi}\int_{-h}^{h} I_z(z')\,K(z,z')\,dz' \qquad \text{(A-7a)}$$

where

$$K(z,z') = \frac{e^{-j\beta_o R}}{R} \qquad \text{(A-7b)}$$

$$R^2 = (z-z')^2 + a^2 \quad . \qquad \text{(A-7c)}$$

$K(z,z')$ is the free space Green's function, and $I_z(z')$ is the axial distribution of current, and z' is the coordinate of source points, and z is the coordinate of field points. By equating (A-7a) with the general solution of the vector Helmholtz equation (A-6), we can form the Hallen integral equation (15:52-54).

$$\int_{-h}^{h} I_z(z')K(z,z')dz' = \frac{-j4\pi}{\eta_o}\left(C_1\ \cos\beta_o z + \frac{V_o}{2}\ \sin\beta_o |z|\right),\ -h \le z \le h \qquad \text{(A-8)}$$

Since no closed form solution to (A-8) exists, King's solution to the Hallen integral equation is based on a careful choice of current distribution, and expansion functions (15:51), such that

$$\int_{-h}^{h} I_z(z')K(z,z')\,dz' = J(z)\psi(z) \quad . \qquad \text{(A-9)}$$

Thus reducing the integral equation to an algebraic equation. For example, if we let

$$J(z) \triangleq I_a F(z) \tag{A-10a}$$

be an assumed distribution, and the actual distribution can be expressed

$$I(z') = I_o H(z') \quad . \tag{A-10b}$$

We could express $I(z')$ in terms of $J(z)$ by dividing (A-10b) by (A-10a) and solving for $I(z)$ or

$$I(z') = J(z) \left(\frac{I_o H(z')}{I_a F(z)}\right) \triangleq J(z)g(z,z') \quad . \tag{A-10c}$$

The function $g(z,z')$ is an expansion function relating actual and assumed distributions. Define

$$\psi(z) \triangleq \int_{-h}^{h} g(z,z')K(z,z')dz' \quad . \tag{A-10d}$$

Since $H(z')$ is not known, choosing $g(z,z')$ exactly is not likely, therefore (A-10d) can be used in the left hand side of (A-8).

$$\int_{-h}^{h} I(z')K(z,z')dz' = J(z)\psi(z) + \int_{-h}^{h} \left(I(z')-J(z)g(z,z')\right)K(z,z')dz' \tag{A-11}$$

The difference integral on the right side of (A-11) reintegrates the lost current distribution in the first term. If $g(z,z')$ is chosen accurately enough, the first term can be called the dominating term, and the difference integral will be a negligable correction. The equation (A-11) can be solved approximately for the expansion function

$$\psi(z) = \frac{1}{J(z)} \int_{-h}^{h} I_z(z')\, K(z,z')\, dz' \equiv \frac{4\pi}{\mu_o J(z)} \left[A_z(z)\right]\Big|_{\rho=a} \quad . \tag{A-12a}$$

Due to the R in the denominator of the integrand (see (A-7b)), we can claim that the vector potential (on the surface) is governed mainly by the currents near or at $z'=z$ (14:15-17). Therefore $\psi_z(z)$ is mostly real and constant over the antenna. Therefore

$$\psi(z) \approx \psi(z_r) \tag{A-12b}$$

where

$\psi(z_r)$ is the ratio of vector potential-to-axial current at a reference point, z_r .

Therefore the expansion function of (A-12a) becomes an expansion coefficient.

$$\psi \triangleq \psi(z_r) = \frac{1}{J(z_r)} \int_{-h}^{h} I_z(z')\, K(z_r,z')\, dz' \tag{A-12c}$$

The reference point chosen by King was the point of maximum current in $J(z)$.

King actually starts with a Hallen difference integral equation (which vanishes at $z=\pm h$ by definition) (14:81-86).

$$A_z(z)-A_z(h)\Big|_{z=\pm h} \equiv 0 \tag{A-13}$$

Therefore

$$\int_{-h}^{h} I_z(z')K_d(z,z')dz' = \frac{-j4\pi}{\eta_o}\left(C_1 \ \mathrm{COS}\beta_o z + \frac{V_o}{2}\ \mathrm{SIN}\beta_o |z| + U\right) \tag{A-14a}$$

and

$$U \triangleq \frac{-4\pi}{\mu_o} A_z(h) = \frac{-j\eta_o}{4\pi}\int_{-h}^{h} I_z(z')K(h,z')dz' \tag{A-14b}$$

$$K_d(z,z') \triangleq K(z,z') - K(h,z') \quad . \tag{A-14c}$$

Applying the boundary condition of (A-13), the C_1 coefficient can be determined,

$$C_1 = -\left(\frac{U + (V_o/2)\ \mathrm{SIN}\beta_o h}{\mathrm{COS}\beta_o h}\right) \tag{A-15}$$

and (A-11a) can be re-written

$$\int_{-h}^{h} I_z(z')K_d(z,z')dz' = \frac{-j4\pi}{\eta_o \mathrm{COS}\beta_o h}\left(U(\mathrm{COS}\beta_o z-\mathrm{COS}\beta_o h) + \frac{V_o}{2}\ \mathrm{SIN}\beta_o (h-|z|)\right). \tag{A-16}$$

To choose the form of the current distribution, break the left side of (A-14a) into the four integrals.

$$\int_{-h}^{h} I_z(z')K_d(z,z')dz' = \int_{-h}^{h} I_z(z')\left(\frac{\cos\beta_o R}{R}\right)dz' + j\int_{-h}^{h} I_z(z')\left(\frac{\sin\beta_o R}{R}\right)dz'$$

$$- \int_{-h}^{h} I_z(z')\left(\frac{\cos\beta_o R_h}{R_h}\right)dz' - j\int_{-h}^{h} I_z(z')\left(\frac{\sin\beta_o R_h}{R_h}\right)dz' \qquad \text{(A-17)}$$

where

$$R_h^2 \doteq (h-z')^2 + a^2 \quad .$$

Reducing each integral according to the behavior of the Kernal (see Figure A.2), that is

$$\frac{\cos\beta_o R}{R} \simeq \psi\delta(z-z'), \ \psi \text{ is a constant} \qquad \text{(A-18a)}$$

$$\frac{\sin\beta_o R}{\beta_o R} \simeq \cos\left(\frac{\beta_o R}{2}\right) \quad . \qquad \text{(A-18b)}$$

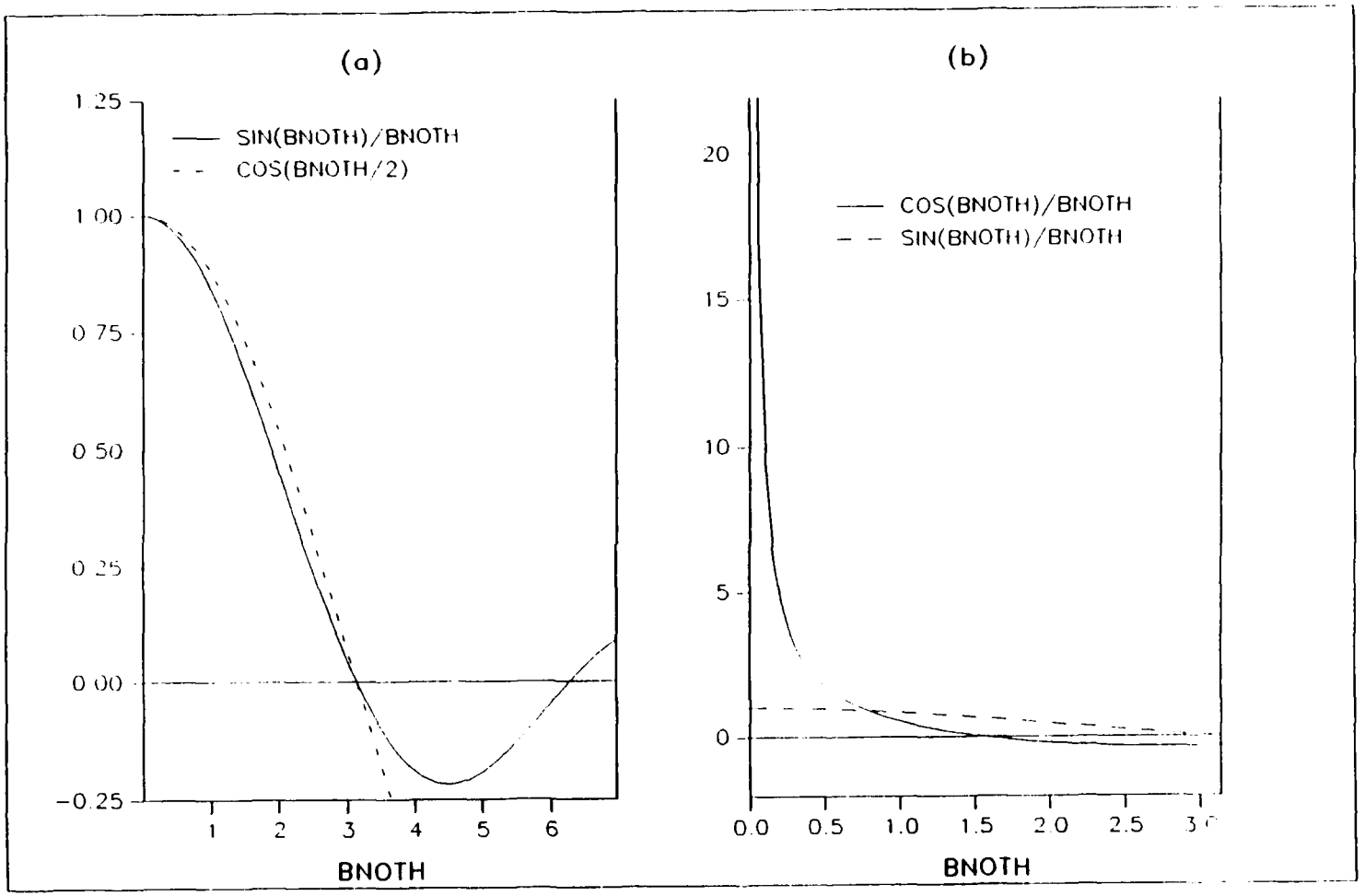

FIGURE A.2. FUNCTIONAL APPROXIMATION OF KERNALS

Plugging (A-18a & b) into (A-17), we can reduce to

$$\int_{-h}^{h} I_z(z')K_d(z,z')dz' \simeq I_z(z)\psi_1 - (\text{COS } 1/2\beta_o z - \text{COS } 1/2\beta_o h)\psi_2 \qquad \text{(A-19a)}$$

and

$$\psi_2 = j\beta_o 2\int_o^h I_z(z')\text{COS } 1/2\beta_o z'dz' \quad . \qquad \text{(A-19b)}$$

Inserting (A-19a & b) into (A-16) we can write

$$I_z(z)\psi_1 - (\text{COS } 1/2\beta_o z - \text{COS } 1/2\beta_o h)\psi_2 = \frac{-j4\pi}{\eta_o \text{COS}\beta_o h}\left(U(\text{COS}\beta_o h - \text{COS}\beta_o z) + \frac{V_o}{2}\text{SIN}\beta_o(h-|z|)\right) \quad . \qquad \text{(A-20)}$$

Solving (A-17) for $I_z(z)$, we obtain King's three-term current distribution (15:63-65) of the form

$$I_z(z) = I_v(M_{oz} + T_U F_{oz} + T_D H_{oz}) \qquad \text{(A-21a)}$$

where I_v, T_U and T_D are complex coefficients and the current distribution includes the shifted sinusoidal, shifted cosinusdal, and shifted half-angle cosinusoidal terms.

$$M_{oz} \triangleq \text{SIN}\beta_o(h-|z|) \qquad \text{(A-21b)}$$

$$F_{oz} \triangleq (\text{COS}\beta_o z - \text{COS}\beta_o h) \qquad \text{(A-21c)}$$

$$H_{oz} \triangleq (\text{COS } 1/2\beta_o z - \text{COS } 1/2\beta_o h) \qquad \text{(A-21d)}$$

Now, inserting this three-term form in (A-21a through d) into (A-16), we have

$$\int_{-h}^{h} I_v(M_{oz} + T_U F_{oz} + T_D H_{oz})K_d(z,z')dz' =$$

$$K\left[\left(\frac{-j\eta_o}{4\pi}\int_{-h}^{h} I_v(M_{oz} + T_U F_{oz} + T_D H_{oz})K(h,z')dz'\right)F_{oz} + \frac{V_o}{2}M_{oz}\right] \qquad \text{(A-22a)}$$

where

$$K \triangleq \frac{j4\pi}{\eta_o \cos\beta_o h} \quad . \qquad \text{(A-22b)}$$

Restating the form of the integral reduction rules in (A-19a),

$$\int_{-h}^{h} I_z(z')K_d(z-z')dz' \simeq I_z(z')\psi_1 - H_{oz}\psi_2 \quad . \qquad \text{(A-23)}$$

Equation (A-22a) reduces to

$$\left(I_v\psi_{dR}M_{oz} + jI_v\psi_{dI}H_{oz}\right) + \left(I_v T_U\psi_{dUR}F_{oz} + jI_v T_U\psi_{dUI}H_{oz}\right)$$

$$+ \left(I_v T_D\psi_{dDR}H_{oz} + jI_v T_D\psi_{dDIhoz}\right) = K\left[\left(\frac{-j\eta_o I_v}{4\pi}\left(\psi_v+T_U\psi_u+T_D\psi_D\right)F_{oz} + \frac{V_o}{2}M_{oz}\right]\right. \quad . \qquad \text{(A-24)}$$

The many expansion functions are defined as follows,

$$\psi_v = \int_{-h}^{h} M_{oz}(z')K(h,z')dz' \qquad \text{(A-25a)}$$

$$\psi_U = \int_{-h}^{h} F_{oz}(z')K(h,z')dz' \qquad \text{(A-25b)}$$

$$\psi_D = \int_{-h}^{h} H_{oz}(z')K(h,z')dz' \qquad \text{(A-25c)}$$

$$\psi_{dR} = \left(\frac{1}{M_{oz}(z_r)}\right)\int_{-h}^{h} M_{oz}(z')\left(K_R(z_r,z')-K_R(h,z')\right)dz'\Bigg|_{z_r=\begin{cases}0 & ,\ \beta_o h \le \pi/2\\ h-\lambda/4, & \beta_o h > \pi/2\end{cases}} \qquad \text{(A-25d)}$$

$$\psi_{dI} = \left(\frac{1}{H_{oz}(z_r)}\right)\int_{-h}^{h} M_{oz}(z')\left(K_I(z_r,z') - K_I(h,z')\right)dz'\Bigg|_{z_r=0} \qquad \text{(A-25e)}$$

$$\psi_{dUR} = \left(\frac{1}{F_{oz}(z_r)}\right)\int_{-h}^{h} F_{oz}(z')\left(K_R(z_r,z') - K_R(h,z')\right)dz'\Bigg|_{z_r=0} \qquad \text{(A-25f)}$$

$$\psi_{dUI} = \left(\frac{1}{H_{oz}(z_r)}\right)\int_{-h}^{h} F_{oz}(z')\left(K_I(z_r,z') - K_I(h,z')\right)dz'\Bigg|_{z_r=0} \qquad \text{(A-25g)}$$

$$\psi_{dD} = \left(\frac{1}{H_{oz}(z_r)}\right)\left[\int_{-h}^{h} H_{oz}(z')\left[K(z_r,z') - K(h,z')\right]dz'\right]_{z_r=0} . \qquad \text{(A-25h)}$$

Grouping all terms in (A-24) by current distribution, and equating the coefficients to zero, we form three equations in three unknowns; I_v, T_D and T_U.

$$I_v\psi_{dR} - \frac{KV_o}{2} = 0 \qquad \text{(A-26a)}$$

$$T_U\psi_{dUR} - \left(\frac{1}{\cos\beta_o h}\right)(\psi_v + T_U\psi_u + T_D\psi_D) = 0 \qquad \text{(A-26b)}$$

$$T_D\psi_{dDR} + j(\psi_{dI} + T_U\psi_{dUI} + T_D\psi_{dDI}) = 0 \qquad \text{(A-26c)}$$

Solving (A-26a through c) for I_v, T_D and T_U,

$$I_v = \frac{KV_o}{2\psi_{dR}} = \frac{j2\pi V_o}{\eta_o\psi_{dR}\cos\beta_o h} \qquad \text{(A-27a)}$$

$$T_D = -j\left(\frac{\psi_{dI}(\psi_{dUR}\cos\beta_o h - \psi_u) + \psi_v\psi_{dUI}}{\psi_{dD}(\psi_{dUR}\cos\beta_o h - \psi_u) + j\psi_D\psi_{dUI}}\right) \qquad \text{(A-27b)}$$

$$T_u = \left(\frac{\psi_v\psi_{dD} - j\psi_D\psi_{dI}}{\psi_{dD}(\psi_{dUR}\cos\beta_o h - \psi_u) + j\psi_D\psi_{dUI}}\right) . \qquad \text{(A-27c)}$$

Having determined these unknown coefficients, we have solved for the currents on a thin, gap driven dipole. This form, as expressed in (A-21a) is King-Middleton's zero-order, three-term theory. To obtain even greater accuracy

in the formulation of dipole current distributions, plug the zero-order current expression (A-21a) into (A-11), for both I(z') and J(z) in the difference integral (15:63-65). The difference integral can be evaluated to formulate a correction current distribution which, when added to the zero-order solution creates a first order solution. Likewise a second order solution can be formulated by plugging the first order solution into the difference integral term of (A-11) and deriving a second correction current distribution. The second order current distribution is just the sum of the zero-order solution and both correction distributions. King and Middleton demonstrated excellent agreement between their second order theory, and the precise impedance measurements of R.B. Mack (see Figure A-3). The second order theory is excessively cumbersome when applied to numerous, coupled elements, therefore it has not been developed with any rigor here. As King has shown, lower order, two-term theories, when properly corrected with lumped constants, are adequate for many array environments of interest (14:63-65).

A1.2 TWO-TERM THEORY

For the isolated dipole, the three-term theory is particularly needed for antennas near antiresonance (or $\beta_o h = N\pi$). However,this report will focus on resonant antennas (that is $\beta_o h \rightarrow \pi/2$) for which King has demonstrated that a modified, zero-order, two-term theory is sufficiently accurate. To formulate this simpler theory for resonant antennas, first note that current form in (A-21a) is indeterminate at resonance ($\beta_o h \pi/2$). From inspection of (A-27a), we see that $\cos\beta_o h$ approaches zero at resonance, and so I_v and $I_z(z)$ are indeterminate. A special form can be derived, which is determinate at resonance, by rearranging (A-21a) (15:63-65). The M_{oz} current term can be expanded (via the trigonometric identity, $\sin(X \pm Y) = \sin X \cos Y \pm \cos X \sin Y$) , and the $\cos\beta_o h$

factor can be recombined with T_U and T_D such that

$$I_z(z) = \frac{-j2\pi V}{\eta_o \psi_{dR}} \left[G_{oz} - T_U' F_{oz} - T_D' H_{oz} \right] \qquad \text{(A-28a)}$$

where

$$G_{oz}(z) = \text{SIN}\beta_o |z| - \text{SIN}\beta_o h \qquad \text{(A-28b)}$$

$$T_U' = - \left(\frac{T_U + \text{SIN}\beta_o h}{\text{COS}\beta_o h} \right) \qquad \text{(A-28c)}$$

$$T_D' = T_D / \text{COS}\beta_o h \quad . \qquad \text{(A-28d)}$$

The equations (A-28a through d) are determinate at resonance. Notice that current term M_{oz} has been replaced by G_{oz}. As previously stated, a two-term formulation is sufficiently accurate for far-field and driving point impedance considerations. To achieve this, set

$$H_{oz} = F_{oz}$$
$$\psi_{dD} = \psi_{dU}$$
$$\psi_D = \psi_u$$
$$T = T_U + T_D$$

in (A-21a). The resulting two-term theory can be expressed

$$I_z(z) = \frac{-j2\pi V_o}{\eta_o \psi_{dR}} \left| G_{oz} + T' F_{oz} \right| \qquad \text{(A-29a)}$$

and

$$T' = \left(\frac{(\psi_u - \psi_{du}\,\mathrm{SIN}\beta_o h)\mathrm{SEC}\beta_o h + \psi_{du}\,\mathrm{SIN}\beta_o h - j\psi_{dR}}{\psi_u - \psi_{du}\,\mathrm{COS}\beta_o h} \right) \qquad \text{(A-29b)}$$

A1.3 TWO-TERM IMPEDANCE FORMULAS

To formulate the admittance of the isolated dipole, apply Ohm's Law to the gap, and evaluate the base current by setting Z=0 in (A-29a & b). That is the admittance can be expressed

$$Y \triangleq \frac{I_z(0)}{V_o} = \frac{-j2\pi}{\eta_o \psi_{dR}} \left(G_{oz} + T'F \right) \Bigg|_{z=0}$$

or

$$Y = \frac{-j2\pi}{\eta_o \psi_{dR}} \left(-\mathrm{SIN}\beta_o h + T'(1-\mathrm{COS}\beta_o h) \right) \qquad \text{(A-30)}$$

Figure A.3 compares the admittance of (A-30) with Mack's measured values. The conductance, G, is the real part of the admittance, Y, and the subceptance, B, is the imaginary part.

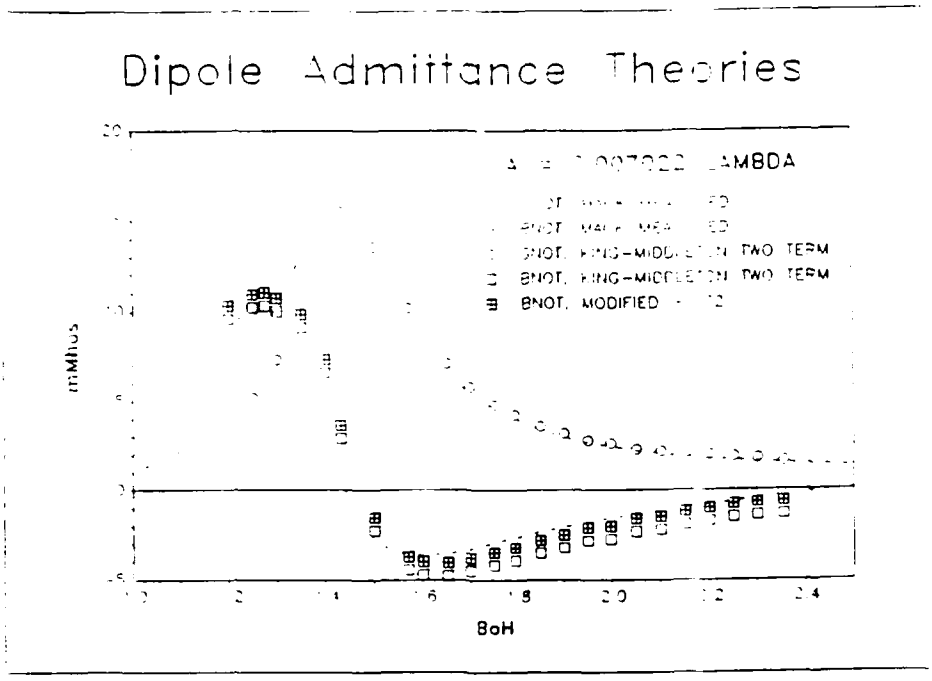

FIGURE A.3. COMPARISON OF KING-MIDDLETON 2ND ORDER, & ZERO-ORDER THEORIES WITH MEASURED DATA

A1.4 TWO-TERM, FAR-FIELD FORMULAS

The far-fields of the isolated dipole can be formed by superposing the far-field of each current term. By substituting (A-39) into (1-19 and b), we get

$$E_\vartheta^r = \frac{j\omega\mu_o}{4\pi} \sin\Theta \left(\frac{e^{-j\beta_o r}}{r}\right) \int_{-h}^{h} \left[\frac{j2\pi V_o}{\eta_o \Psi_{dR}} \left(G_{oz}(z') - T' F_{oz}(z')\right) e^{j\beta_o z' \cos\Theta}\right] dz'$$

or

$$E_\Theta^r = \frac{-V_o}{\Psi_{dR}} \left(\frac{e^{-j\beta_o R}}{r}\right) f(\Theta, \beta_o h) \qquad \text{(A-31a)}$$

and

$$f(\Theta, \beta_o h) = \left[H_{o\vartheta}(\Theta, \beta_o h) - T' G_{o\vartheta}(\Theta, \beta_o h)\right] \qquad \text{(A-31b)}$$

$$H_m(\Theta,\beta_o h) = \frac{\beta_o \mathrm{SIN}\Theta}{2}\int_{-h}^{h}(\mathrm{SIN}\beta_o|z'| - \mathrm{SIN}\beta oh)e^{-j\beta_o z'\mathrm{COS}\Theta}\,dz'$$

$$= \frac{\left(1-\mathrm{COS}\beta_o h\mathrm{COS}(\beta_o h\mathrm{COS}\Theta)\right)\mathrm{COS}\Theta-\mathrm{SIN}\beta_o h\ \mathrm{SIN}(\beta_o h\mathrm{COS}\Theta)}{\mathrm{SIN}\Theta\ \mathrm{COS}\Theta} \qquad \text{(A-31c)}$$

$$G_m(\Theta,\beta_o h) = \frac{\beta_o \mathrm{SIN}\Theta}{2}\int_{-h}^{h}(\mathrm{COS}\beta_o z'-\mathrm{COS}\beta_o h)e^{j\beta_o z'\mathrm{COS}\Theta}\,dz'$$

$$= \frac{\mathrm{SIN}\beta_o h\ \mathrm{COS}(\beta_o h\mathrm{COS}\Theta)\mathrm{COS}\Theta - \mathrm{COS}\beta_o h\ \mathrm{SIN}(\beta_o h\mathrm{COS}\Theta)}{\mathrm{SIN}\Theta\ \mathrm{COS}\Theta} \qquad \text{(A-31d)}$$

A1.5 DIPOLE PAIR

Consider now the geometry of Figure A.4.

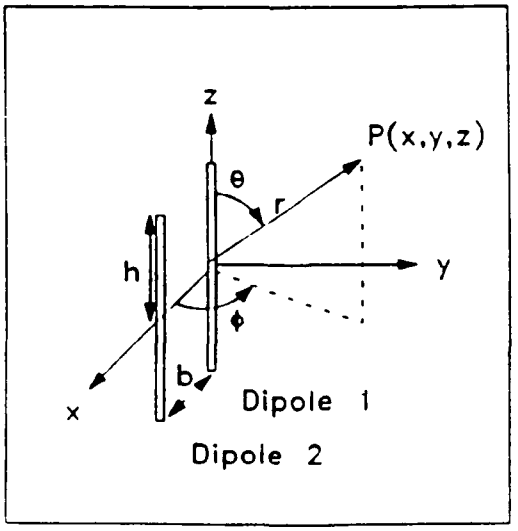

FIGURE A.4. COUPLED DIPOLE GEOMETRY

The same symmetry conditions and boundary conditions imposed in section A.1 (A-1 to A-3) are imposed on both dipoles here. If we form the Hallen difference integral (A-14a) for coupled dipoles, we get for dipole 1

$$\int_{-h}^{h} \left(I_{z1}(z')K_{11d}(z,z') + I_{z2}(z')K_{12d}(z,z')\right)dz'$$

$$= K\left(\frac{V_1}{2}\,\mathrm{SIN}\beta_o(h-|z|) + U_1(\mathrm{COS}\beta_o z - \mathrm{COS}\beta_o h)\right) \qquad \text{(A-32a)}$$

and for dipole 2

$$\int_{-h}^{h} \left(I_{z1}(z')K_{21d}(z,z') + I_{z2}(z')K_{22d}(z,z')\right)dz'$$

$$= K\left(\frac{V_2}{2}\,\mathrm{SIN}\beta_o(h-|z|) + U_2(\mathrm{COS}\beta_o z - \mathrm{COS}\beta_o h)\right) \qquad \text{(A-32b)}$$

where

$$K_{11d}(z,z') \triangleq K_{11}(z,z') - K_{11}(h,z') = \frac{e^{-j\beta_o R_{11}}}{R_{11}} - \frac{e^{-j\beta_o R_{11h}}}{R_{11h}} \qquad \text{(A-32c)}$$

$$K_{12d}(z,z') \triangleq K_{12}(z,z') - K_{12}(h,z') = \frac{e^{-j\beta_o R_{12}}}{R_{12}} - \frac{e^{-j\beta_o R_{12h}}}{R_{12h}} \qquad \text{(A-32d)}$$

$K_{22d}(z,z') \equiv K_{11d}(z,z')$

$K_{21d}(z,z') \equiv K_{12d}(z,z')$

$$R_{11}^2 = (z,z')^2 + a^2 \qquad R_{11h}^2 = (h-z')^2 + a^2 \tag{A-32e}$$

$$R_{12}^2 = (z-z')^2 + b^2 \qquad R_{12h}^2 = (h-z')^2 + b^2 \tag{A-32f}$$

$$K = \frac{j4\pi}{\eta_o \cos\beta_o h} \tag{A-32g}$$

and

$$U_1 = \frac{-j\eta_o}{4\pi} \int_{-h}^{h} \left[I_{z1}(z')K_{11}(h,z') + I_{z2}(z')K_{12}(h,z') \right] dz' \tag{A-32h}$$

$$U_2 = \frac{-j\eta_o}{4\pi} \int_{-h}^{h} \left[I_{z1}(z')K_{21}(h,z') + I_{z2}(z')K_{22}(h,z') \right] dz' \quad . \tag{A-32i}$$

In (A-32a & b), we have two simultaneous integral equations to solve for the current distributions on each dipole, in the presence of the other. For N coupled elements, (A-32a & b) would increase to N simultaneous integral equations, and the lefthand side of each equation would integrate over N current distributions, $I_{zi}(z')$. This report will later develop a matrix formulation for an N element linear array of parallel dipoles. At this point, still focusing on the two coupled antennas of this section, King would substitute his two or three -term current expansion into (A-32a-i), depending upon the actual element geometry (14:96-97, 133, 188, 207, 237-238, 272-280).

Let us restate the two-term current, for the ith dipole as follows

$$I_{zi}(z) \triangleq I_{ui}(z) + I_{vi}(z) = jA_i H_{zz} - B_i F_{zz} \tag{A-33}$$

and $M_{oz}(z)$ & $F_{oz}(z)$ are defined in (A-21b) and (A-21c) respectively. Substituting (A-33) into (A-32a-i), numerous integral terms over $I_{ui}(z)$ and $I_{vi}(z)$ must be reduced to algebraic equations. The integral reduction rules vary now with the spacing ,b, between the coupled elements. In general, for $\beta_o b \geq 1$

$$\left.\begin{aligned} \int_{-h}^{h} I_{ui}(z')K_{Kid}(z,z')dz' &\simeq \left(\frac{B_i}{B_k}\right)\psi_{Kidu}\ I_{uk}(z) \qquad \text{(A-34a)} \\ \int_{-h}^{h} I_{vi}(z')K_{Kid}(z,z')dz' &\simeq \left(\frac{jA_i}{B_k}\right)\psi_{Kidv}\ I_{vk}(z) \qquad \text{(A-34b)} \end{aligned}\right\} \beta_o b \geq 1$$

and for $\beta_o b < 1$, the reduction rules are

$$\left.\begin{aligned} \int_{-h}^{h} I_{ui}(z')K_{Kid}(z,z')dz' &\simeq \left(\frac{B_i}{B_k}\right)\psi_{Kidu}\ I_{uk}(z) \qquad \text{(A-34c)} \\ \int_{-h}^{h} I_{vi}(z')K_{KidR}(z,z')dz' &\simeq \left(\frac{A_i}{A_k}\right)\psi_{KidR}\ I_{vk}(z) \qquad \text{(A-34d)} \\ \int_{-h}^{h} I_{vi}(z')K_{KidI}(z,z')dz' &\simeq \left(\frac{jA_i}{B_k}\right)\psi_{KidI}\ I_{uk}(z) \qquad \text{(A-34e)} \end{aligned}\right\} \beta_o b < 1 \quad .$$

Additional reduction rules needed to evaluate U_1 and U_2 in (A-32h & i) are,

$$\int_{-h}^{h} I_{ui}(z')K_{xi}(h,z')dz' \simeq B_i \psi_{kiu} \qquad \text{(A-34f)}$$

$$\int_{-h}^{h} I_{vi}(z')K_{ki}(h,z')dz' \simeq jA_i \psi_{kiv} \quad . \qquad \text{(A-34g)}$$

Commonly, $\beta_o b < 1$ is only true for i=k, therefore $\beta_o b \triangleq \beta_{o_a} << 1$. This is not generally true, but element spacings will be chosen to meet this condition through out this report.

For dipole 1, (A-32a) becomes

$$\int_{-h}^{h} \left[\left(I_{u1}(z') + I_{v1}(z') \right) K_{11d}(z,z') + \left(I_{u2}(z') + I_{v2}(z') \right) K_{12d}(z,z') \right] dz'$$

$$= \frac{KV_1}{2} M_{oz} + KU_1 F_{oz} \quad . \qquad \text{(A-35a)}$$

After reducing integral terms, we have

$$\left(\frac{B_1}{B_1}\right)\psi_{11du} I_{u1}(z) + \left(\frac{A_1}{A_1}\right)\psi_{11dR} I_{v1}(z) + \left(\frac{jA_1}{B_1}\right)\psi_{11dI} I_{u1}(z)$$

$$- \left(\frac{B_2}{A_1}\right)\psi_{12du} I_{u1}(z) - \left(\frac{jA_2}{B_1}\right)\psi_{12dv} I_{v1}(z)$$

$$= \frac{KV_1}{2} M_{oz} + KU_1 F_{oz} \quad . \tag{A-35b}$$

Grouping terms for dipole 1, we can write

$$\left[\left(\frac{B_1}{B_1}\right)\psi_{11du} + \left(\frac{jA_1}{B_1}\right)\psi_{11dI} + \left(\frac{B_2}{B_1}\right)\psi_{12du} + \left(\frac{jA_2}{B_1}\right)\psi_{12dv}\right] I_{u1}(z) = KU_1 F_{oz} \tag{A-36a}$$

and

$$\left(\frac{A_1}{A_1}\right)\psi_{11dR} I_{v1}(z) = \frac{KV_1}{2} M_{oz} \quad . \tag{A-36b}$$

Likewise for dipole 2, equations like (A-36a and b) can be written

$$\left[\left(\frac{B_1}{B_2}\right)\psi_{21dR} + \left(\frac{jA_1}{B_2}\right)\psi_{21dv} + \left(\frac{B_2}{B_2}\right)\psi_{22du} + \left(\frac{jA_2}{B_2}\right)\psi_{22dI}\right] I_{u2}(z) = KU_2 Foz \tag{A-36c}$$

$$\left(\frac{A_2}{A_2}\right)\psi_{22dR} I_{v2}(z) = \frac{KV_2}{2} M_{oz} \quad . \tag{A-36d}$$

In (A-36a through d), we have four equations in four unknowns, A_1, A_2, B_1, and B_2. We can then write for the Kth dipole

$$I_{vk}(z) = \frac{KV_k}{2\psi_{kkdR}} M_{oz} \tag{A-37a}$$

and

$$\sum_{i=1}^{2} \left[\left(\frac{B_i}{B_k}\right)\psi_{kidu} + \left(\frac{jA_i}{B_k}\right)\left(\psi_{kidv}(1-\delta_{ik}) + \psi_{kidI}\right)\right] I_{uk}(z)$$

$$= K\left(\frac{-j\eta_o}{4\pi}\sum_{i=1}^{2}\left(jA_i\psi_{kiv} + B_i\psi_{kiu}\right)\right)F_{oz} \qquad \text{(A-37b)}$$

where

$$\delta_{ik} \triangleq \begin{cases} 0, & \text{for } i \neq K \\ 1, & \text{for } i = K \end{cases} .$$

By cancelling out the current distribution on either side of (A-37b), and grouping terms by coefficients, A_i & B_i, we can write

$$\sum_{i=1}^{2} B_i\left(\psi_{kidu}\cos\beta_o h - \psi_{kiu}\right)$$

$$= j\sum_{i=1}^{2}\left[\psi_{kiv} - \left(\psi_{kidv}(1-\delta_{ik}) + j\,\psi_{kidI}\,\delta_{ik}\right)\cos\beta_o h\right]. \qquad \text{(A-37c)}$$

From (A-37a) we can note that the A_i's, and therefore the shifted sinusoidal distribution term, is determined entirely from the gap voltage, and the dipole dimensions (embodied in ψ_{kkdR}). In (A-37c), we have a set of two linear algebraic equations that can be solved for two unknowns, B_1 and B_2, in terms of A_1 and A_2. Upon solving these linear equations, we have determined the currents on both dipoles, and can compute self, mutual and driving point impedances, in the manner presented in Section one (1-24 and 1-25). The far-fields from these coupled dipoles can be determined in a similar manner to the isolated dipole. For coupled dipoles, one must superpose the fields of each current distribution (see equations A-31a through d) from each element (see equations 1-26 and 1-27) given arbitrary, complex voltage weights (part of B_i). We can compute the far-field

$$E_\Theta^r = \frac{j\omega\mu_o}{4\pi} \text{SIN}\Theta \sum_{i=1}^{2} \left[\int_{-h}^{h} I_{iz}(z') \frac{e^{-j\beta_o(r-z'\text{COS}\Theta)}}{r} dz' \right] \quad . \qquad \text{(A-38a)}$$

Substituting (A-33), and separating the amplitude and phase dependent portions of the Kernal, we have

$$E_\Theta^r = \frac{j\omega\mu_o}{4\pi} \left(\frac{e^{-j\beta_o r}}{r} \right) \text{SIN}\Theta \sum_{i=1}^{2} \left[\int_{-h}^{h} \left(jA_i M_{oz} + B_i F_{oz} \right) e^{j\beta_o(z'\text{COS}\Theta + b_i \text{COS}\phi)} dz' \right] \qquad \text{(A-38b)}$$

or

$$E_\Theta^r = \frac{j\omega\mu_o}{4\pi} \left(\frac{e^{-j\beta_o r}}{r} \right) \sum_{i=1}^{2} \left[\left(jA_i F_m(\Theta, \beta_o h) + B_i G_m(\Theta, \beta_o h) \right) e^{j\beta_o b_i \text{COS}\phi} \right] \qquad \text{(A-38c)}$$

where $F_m(\Theta, \beta_o h)$ is defined by (1-28b) and $G_m(\Theta, \beta_o h)$ is defined by (A-31d). Notice that (A-38c) cannot be separated into an array factor and a unique field factor as in (1-28a).

APPENDIX A2

EQUATIONS FOR KING-MIDDLETON'S ZERO-ORDER, TWO-TERM THEORY FOR LINEAR ARRAYS OF DIPOLES

Equation (A-37c) could easily be extended to a set of N linear algebraic equations, for N coupled dipoles. As N increases, matrix notation becomes more efficient. Assuming the two-term current form of (A-33), we can express the gap driving voltages (which are complex) in vector form,

$$\bar{V} \triangleq \begin{bmatrix} V_1 \\ \cdot \\ \cdot \\ \cdot \\ V_N \end{bmatrix} \tag{A-39}$$

The A_i coefficients can be determined from the vector multiplication

$$\bar{A} \equiv \begin{bmatrix} A_i \\ \cdot \\ \cdot \\ \cdot \\ A_N \end{bmatrix} = -jK'\bar{V} \tag{A-40a}$$

$$K' = \left(\frac{KV_k}{2\psi_{dR}}\right) \tag{A-40b}$$

where K is defined by (A-22b). The vector of B_i coefficients

$$\bar{B} \equiv \begin{bmatrix} B_i \\ \cdot \\ \cdot \\ \cdot \\ B_N \end{bmatrix}$$

is related to the A_i vector by a set of linear equations like (A-37c). For N elements, these equations can be represented in matrix form

$$\begin{bmatrix} \phi_u \end{bmatrix}\bar{B} = \begin{bmatrix} \phi_{,} \end{bmatrix}\bar{A} \tag{A-41}$$

or by matrix inversion

$$\bar{B} = \left[\phi_u \right]^{-1} \left[\phi_v \right] \bar{A} \qquad \text{(A-42)}$$

where

$$\left[\phi_u \right] = \begin{bmatrix} \phi_{11u} & & \\ & \ddots & \\ & & \phi_{NNu} \end{bmatrix} \quad \& \quad \left[\phi_v \right] = \begin{bmatrix} \phi_{11v} & & \\ & \ddots & \\ & & \phi_{NNv} \end{bmatrix}$$

and

$$\phi_{kiu} \triangleq \psi_{kidu} \cos\beta_o h - \psi_{kiu} \qquad \text{(A-43a)}$$

$$\phi_{KIv} \triangleq \psi_{KIv} - \psi_{KIDv} \cos\beta_o H(1-\delta_{IK}) - J\, \psi_{KIDI} \cos\beta_o H\, \delta_{IK} \; . \qquad \text{(A-43b)}$$

The admittance matrix of self and mutual admittances of the N elements can also be expressed in matrix notation. Starting with a vector of current distributions, that is

$$\bar{I}_z(z) = \begin{bmatrix} I_1(z) \\ \vdots \\ I_N(z) \end{bmatrix} = \left[\phi_u \right]^{-1} \left[\phi_v \right] j\bar{A}F_{oz} + j\bar{A}M_{oz} \; . \qquad \text{(A-44a)}$$

By substituting (A-40a) into (A-44a), we get

$$\bar{I}_z(z) = \left(\left[\phi_u \right]^{-1} \left[\phi_v \right] K'F_{oz} + K' \left[I \right] M_{oz} \right) \bar{V} \; . \qquad \text{(A-44b)}$$

To evaluate driving point properties, evaluate (A-44b) for z=0, or

$$\bar{I}_o = \left(\left[\phi_u \right]^{-1} \left[\phi_v \right] K' F_{oz}(0) + K' \left[I \right] M_{oz}(0) \right) \bar{V} \qquad \text{(A-44c)}$$

where

$\bar{I}_o$ is a vector of base currents

[I] is a NXN identity matrix.

The admittance matrix is then derived by the matrix expression inside the outer brackets.

$$\left[Y \right] = \left(\left[\phi_u \right]^{-1} \left[\phi_v \right] K' F_{oz}(0) + K' \left[I \right] M_{oz}(0) \right) \qquad \text{(A-45)}$$

The impedance matrix is just the inverse of the admittance matrix.

$$\left[Z \right] = \left[Y \right]^{-1} \qquad \text{(A-46)}$$

It is interesting to notice that the admittance matrix is solely a function of array geometry and the current distributions. The driving point characteristics of an antenna are determined by the driving voltage (and resultant currents) of all antennas.

APPENDIX B

UNCOMPENSATED MODEL RESULTS: 10 ELEMENT ARRAY

20 ELEMENT ARRAY

30 ELEMENT ARRAY

40 ELEMENT ARRAY

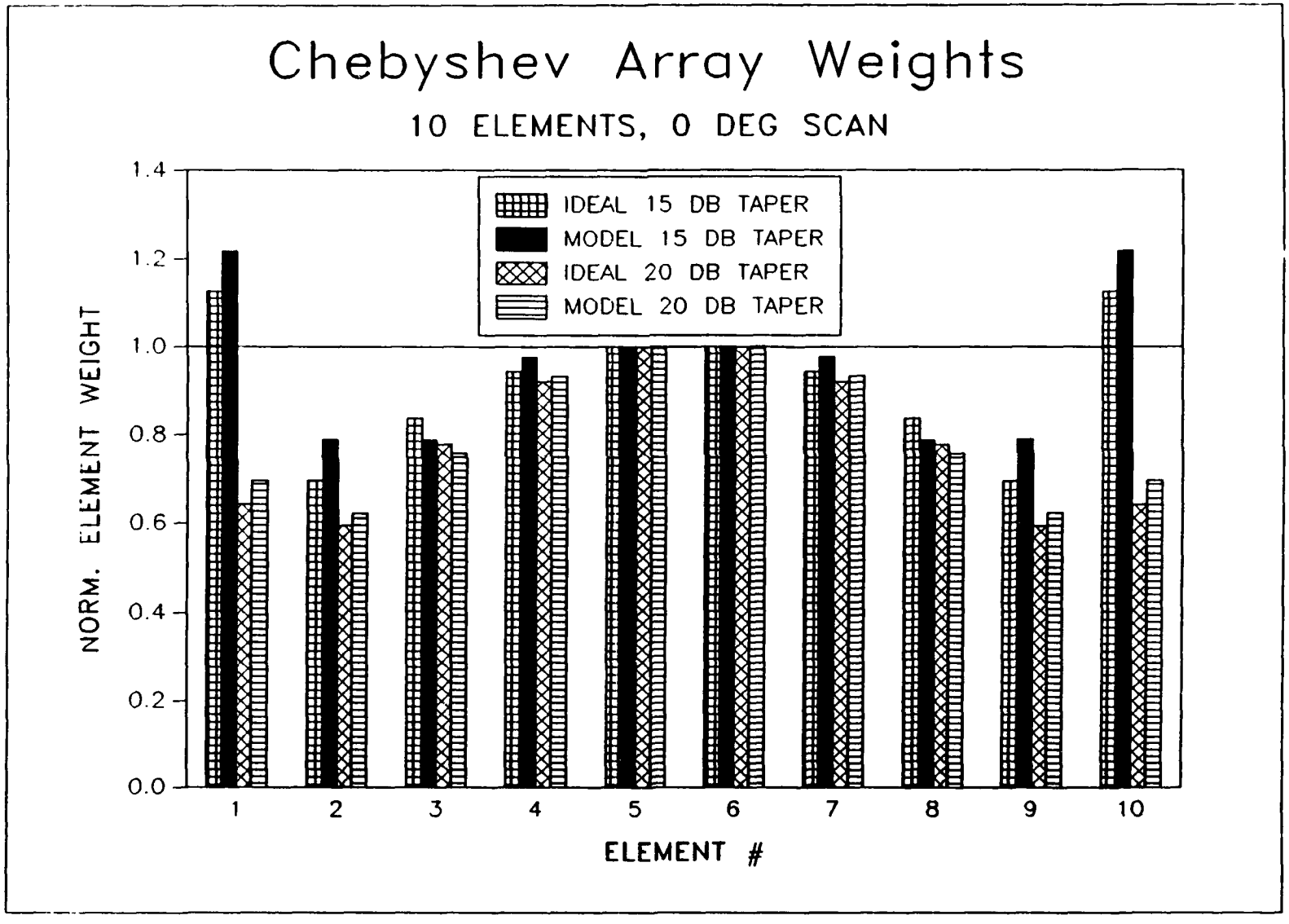
Chebyshev Array Weights
10 ELEMENTS, 0 DEG SCAN
IDEAL 15 DB TAPER
MODEL 15 DB TAPER
IDEAL 20 DB TAPER
MODEL 20 DB TAPER
NORM. ELEMENT WEIGHT
1.4
1.2
1.0
0.8
0.6
0.4
0.2
0.0
1
2
3
4
5
6
7
8
9
10
ELEMENT #

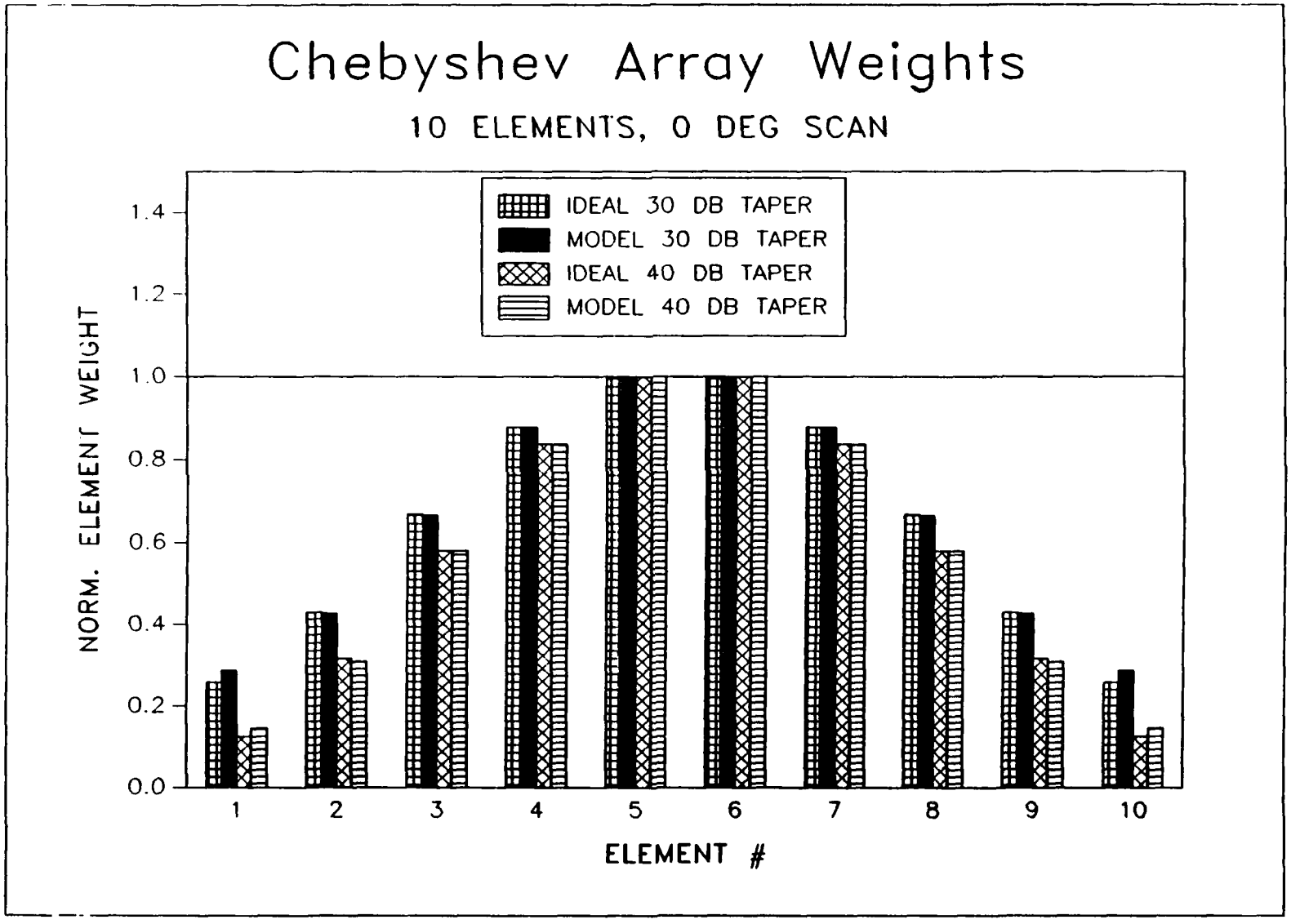
Chebyshev Array Weights
10 ELEMENTS, 0 DEG SCAN
IDEAL 30 DB TAPER
MODEL 30 DB TAPER
IDEAL 40 DB TAPER
MODEL 40 DB TAPER
NORM. ELEMENT WEIGHT
1.4
1.2
1.0
0.8
0.6
0.4
0.2
0.0
1
2
3
4
5
6
7
8
9
10
ELEMENT #

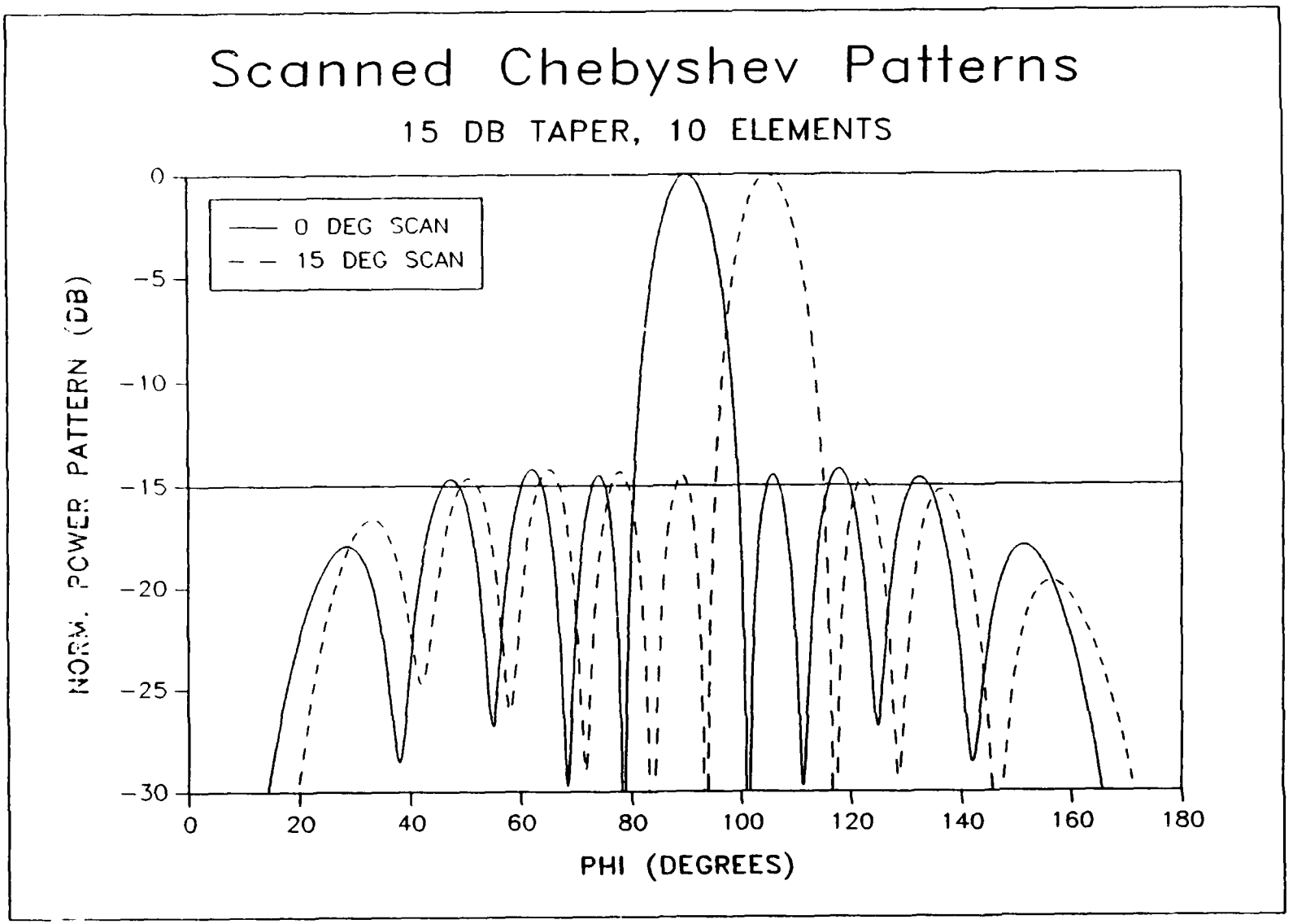
Scanned Chebyshev Patterns
15 DB TAPER, 10 ELEMENTS
0 DEG SCAN
15 DEG SCAN
NORM. POWER PATTERN (DB)
0
-5
-10
-15
-20
-25
-30
0
20
40
60
80
100
120
140
160
180
PHI (DEGREES)

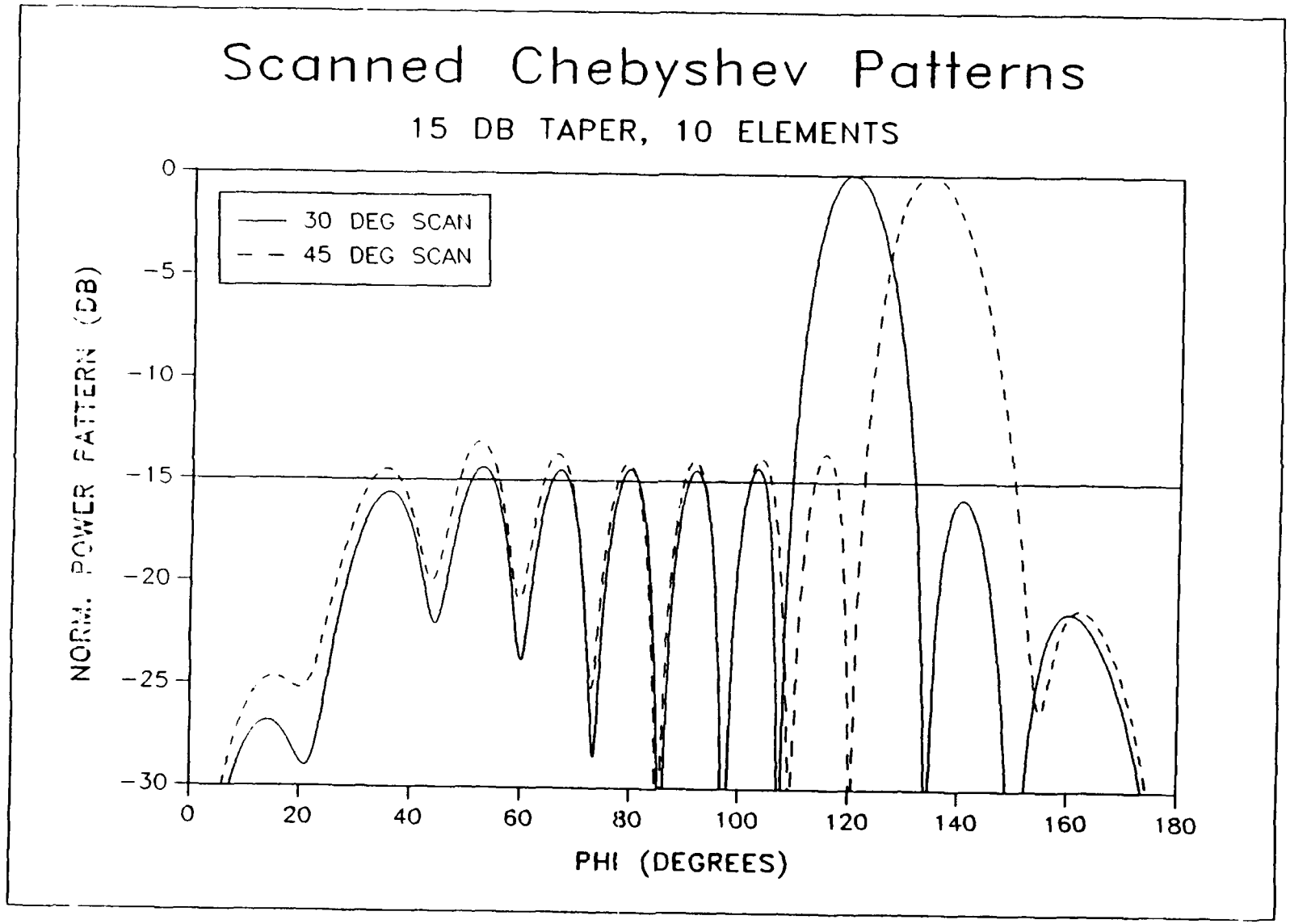
Scanned Chebyshev Patterns
15 DB TAPER, 10 ELEMENTS
30 DEG SCAN
45 DEG SCAN
NORM. POWER PATTERN (DB)
0
-5
-10
-15
-20
-25
-30
0
20
40
60
80
100
120
140
160
180
PHI (DEGREES)

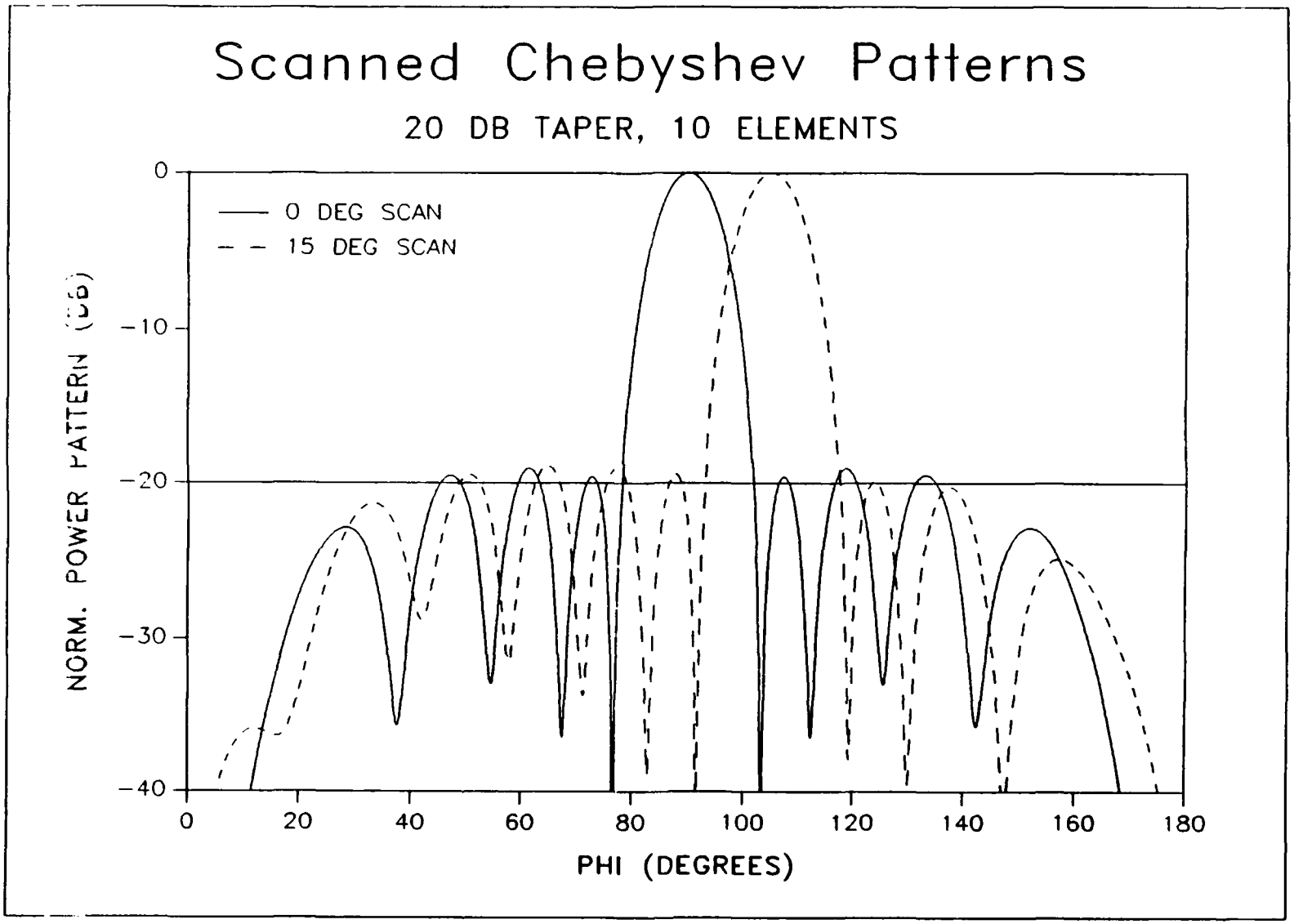
Scanned Chebyshev Patterns
20 DB TAPER, 10 ELEMENTS
0 DEG SCAN
15 DEG SCAN
NORM. POWER PATTERN (DB)
0
-10
-20
-30
-40
0
20
40
60
80
100
120
140
160
180
PHI (DEGREES)

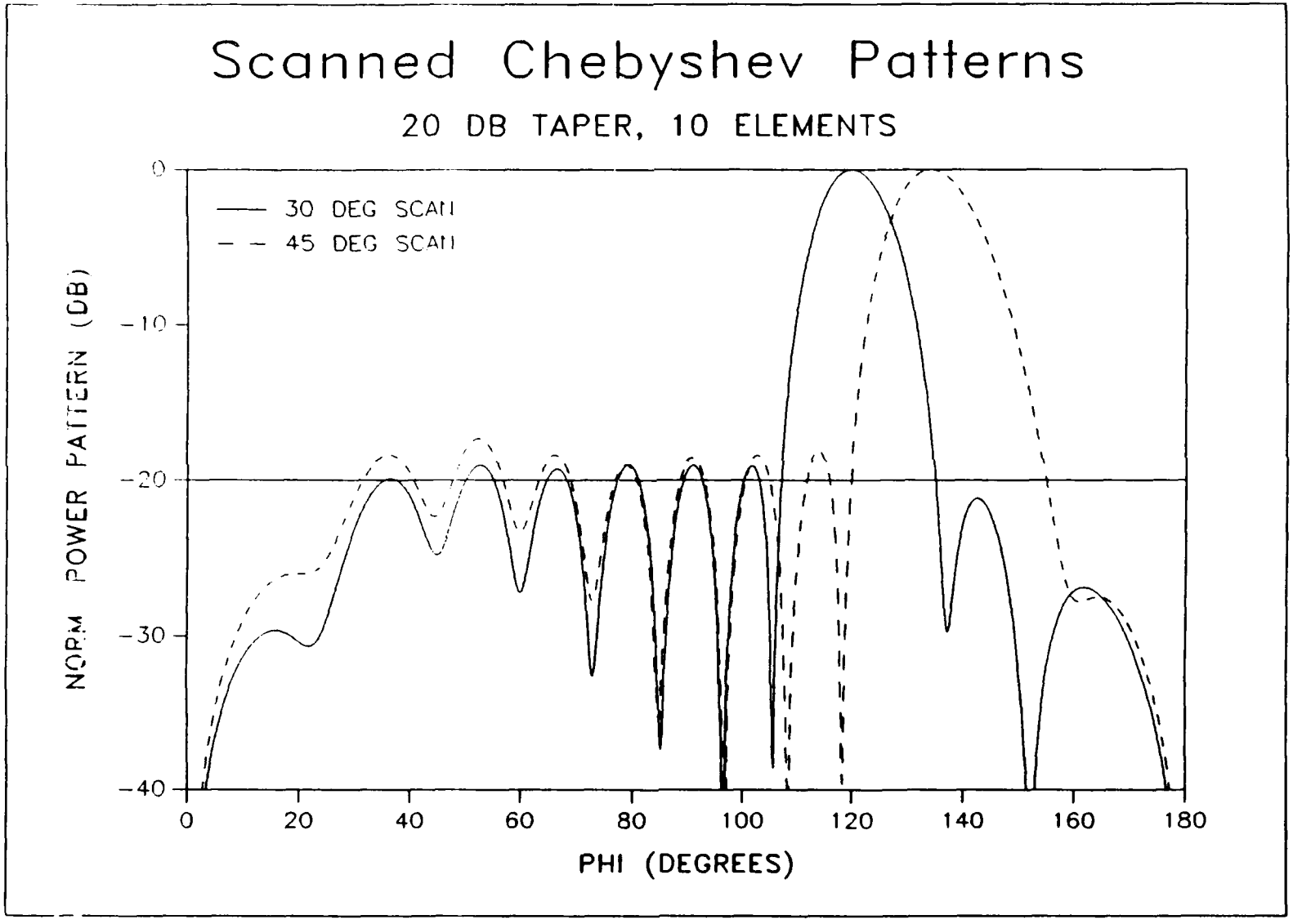
Scanned Chebyshev Patterns
20 DB TAPER, 10 ELEMENTS
30 DEG SCAN
45 DEG SCAN
NORM POWER PATTERN (DB)
0
-10
-20
-30
-40
0
20
40
60
80
100
120
140
160
180
PHI (DEGREES)

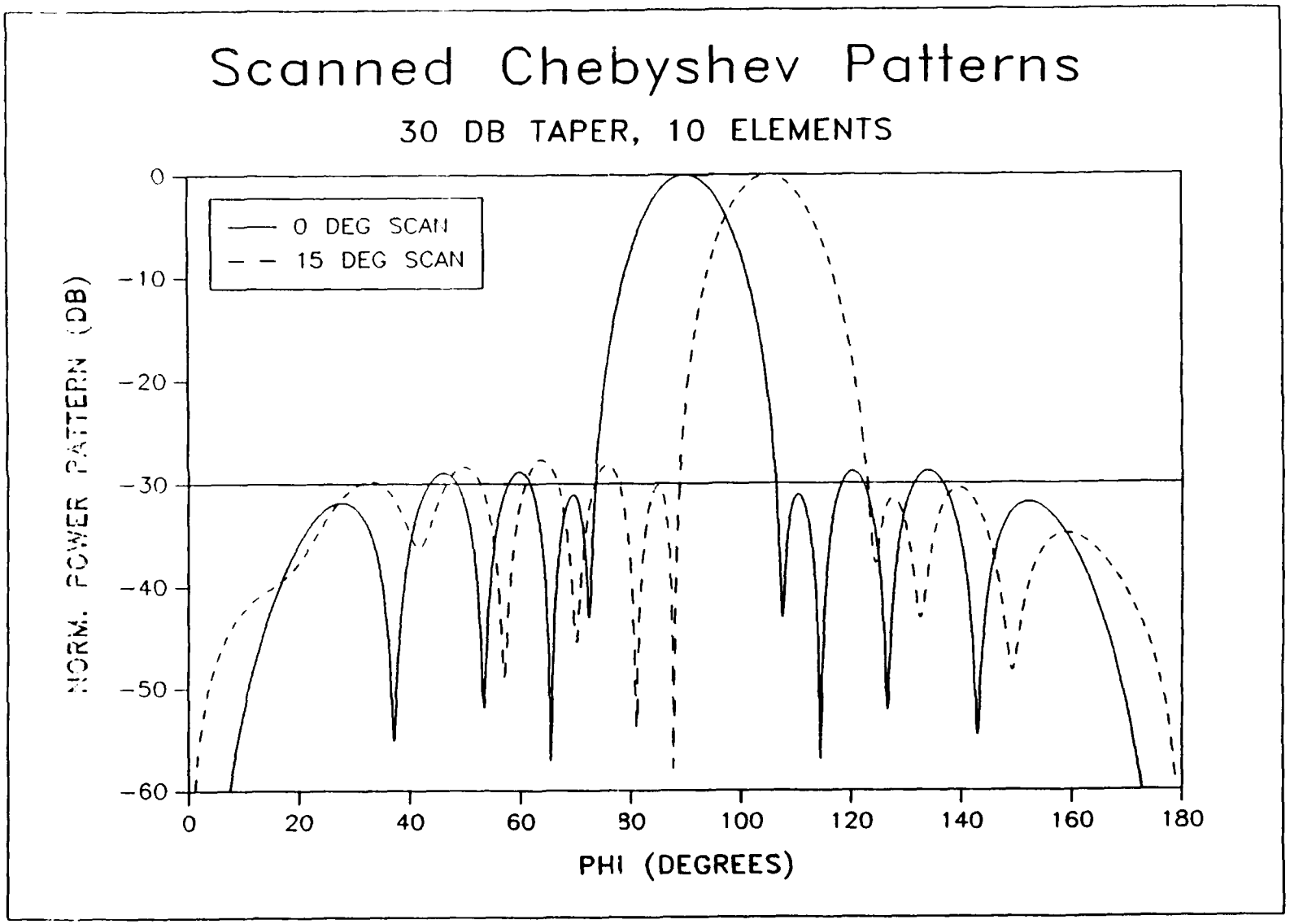
Scanned Chebyshev Patterns
30 DB TAPER, 10 ELEMENTS
0 DEG SCAN
15 DEG SCAN
NORM. POWER PATTERN (DB)
0
-10
-20
-30
-40
-50
-60
0
20
40
60
80
100
120
140
160
180
PHI (DEGREES)

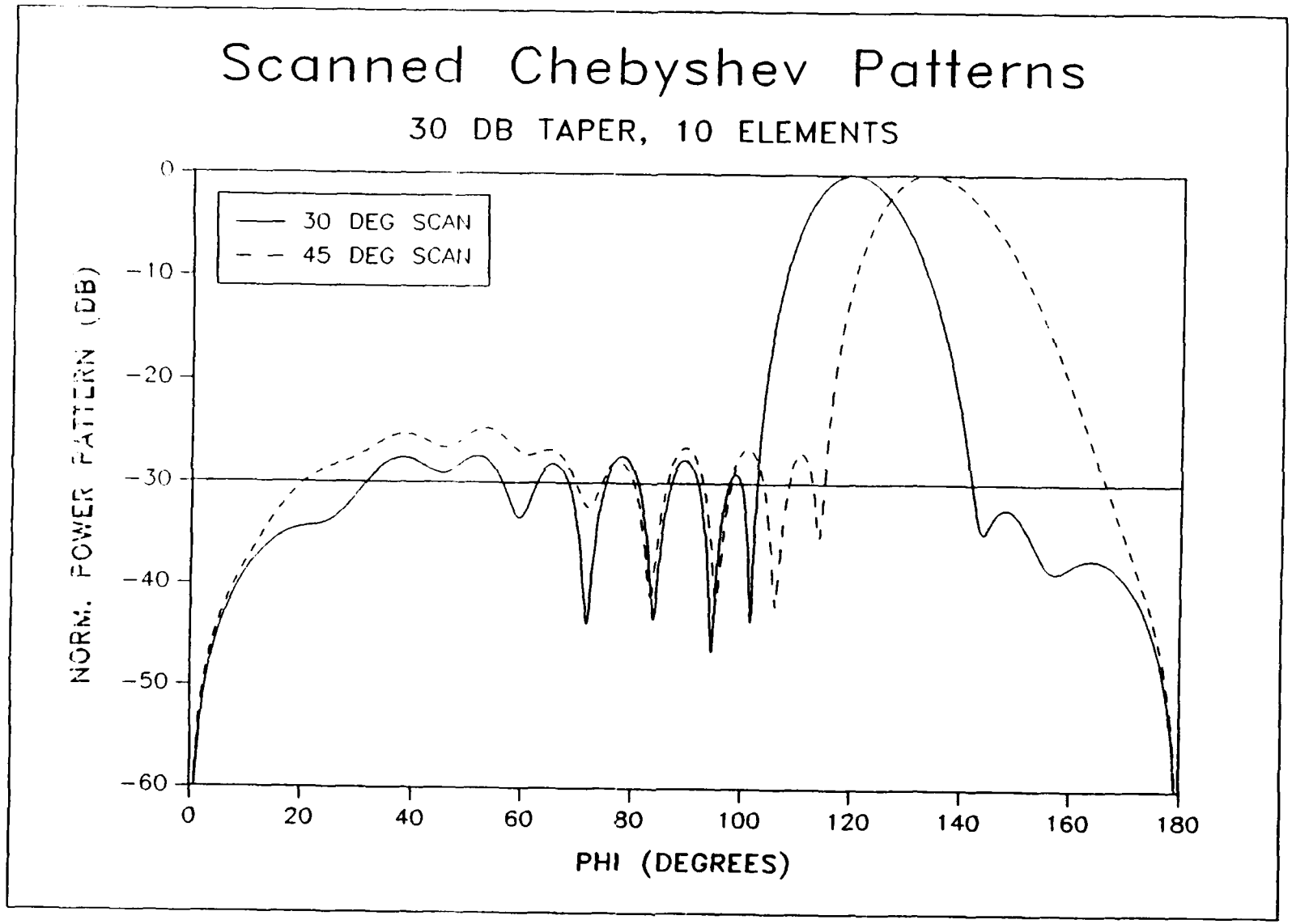
Scanned Chebyshev Patterns
30 DB TAPER, 10 ELEMENTS
30 DEG SCAN
45 DEG SCAN
NORM. POWER PATTERN (DB)
0
-10
-20
-30
-40
-50
-60
0
20
40
60
80
100
120
140
160
180
PHI (DEGREES)

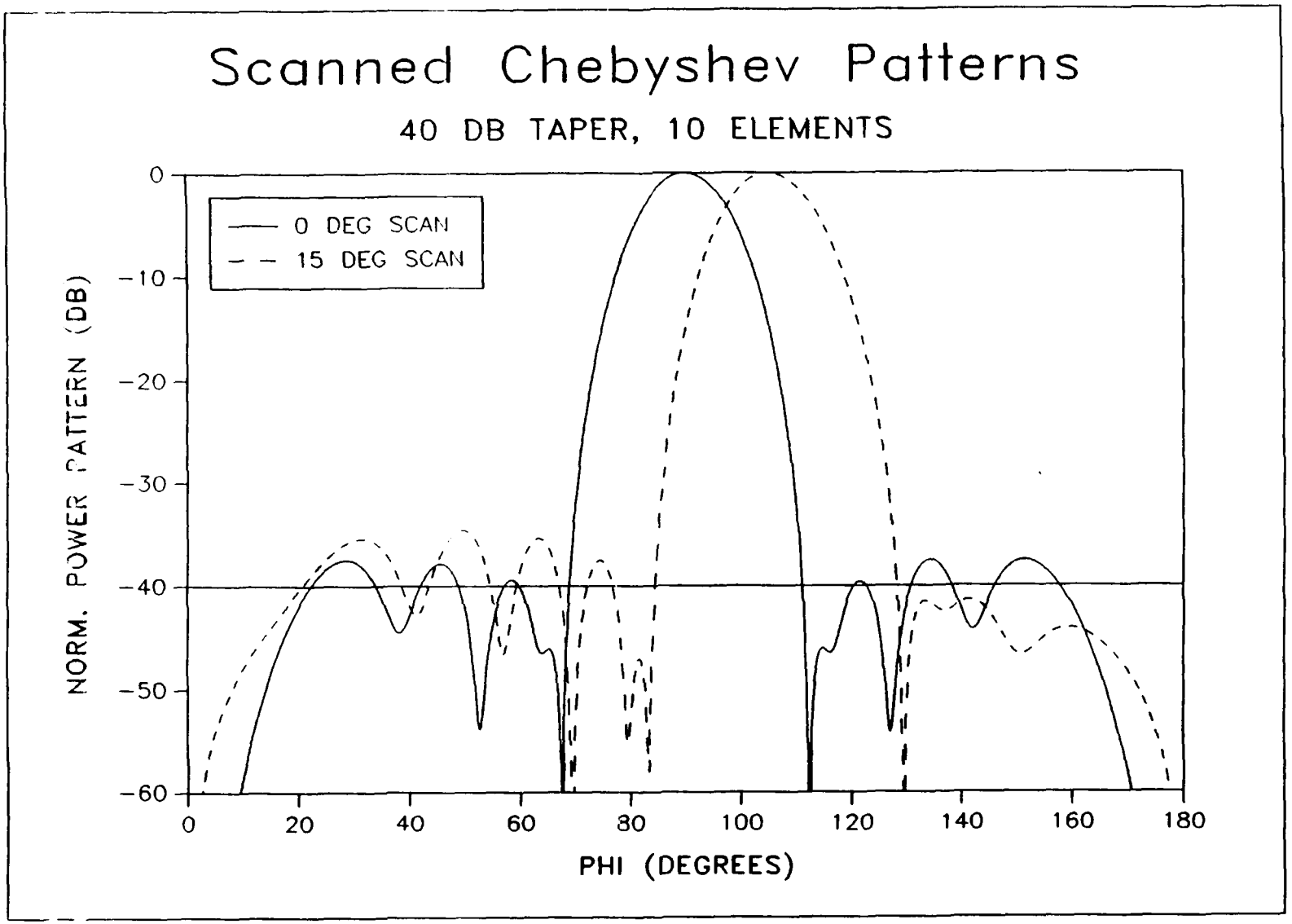
Scanned Chebyshev Patterns
40 DB TAPER, 10 ELEMENTS
0 DEG SCAN
15 DEG SCAN
NORM. POWER PATTERN (DB)
0
-10
-20
-30
-40
-50
-60
0
20
40
60
80
100
120
140
160
180
PHI (DEGREES)

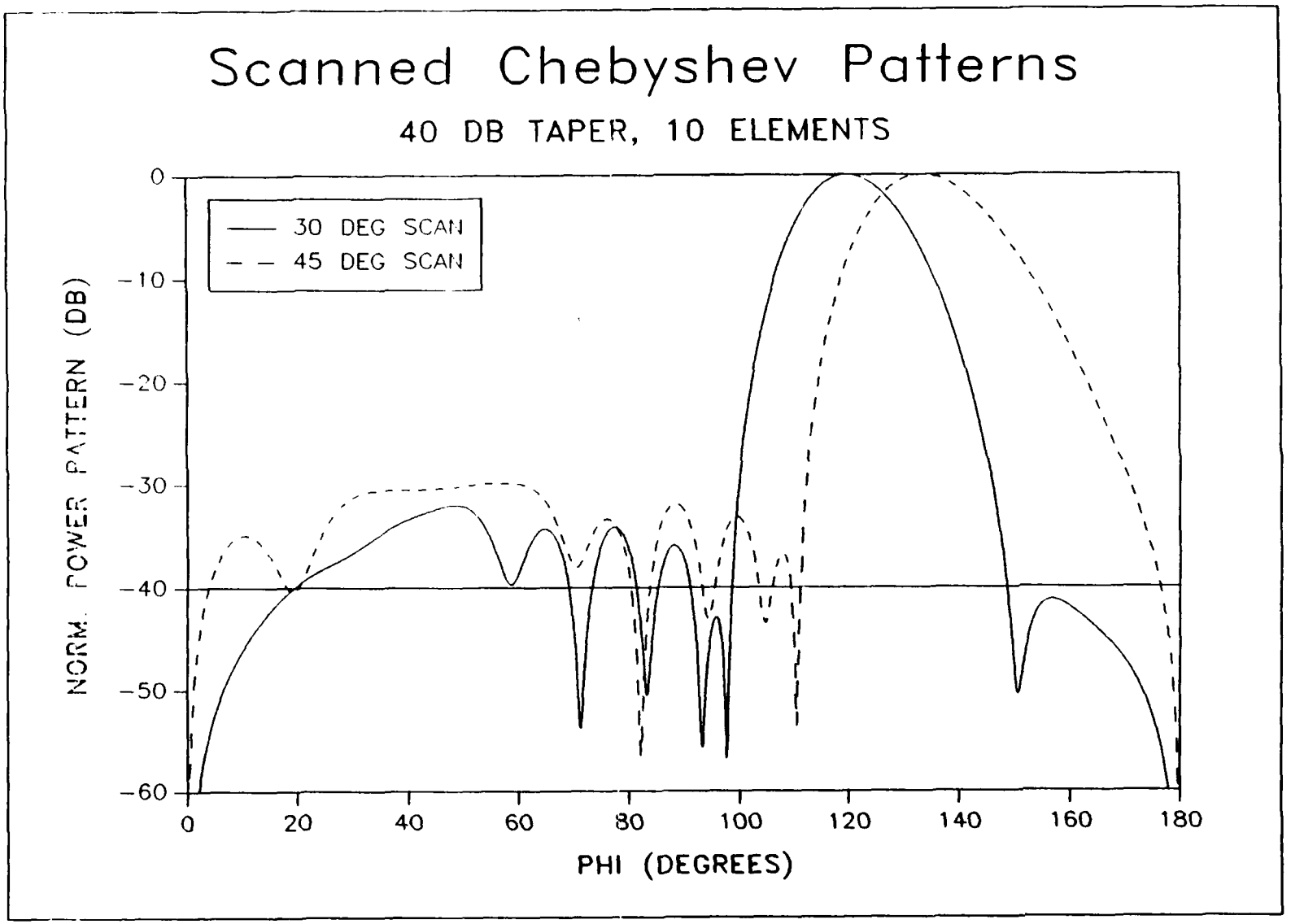
Scanned Chebyshev Patterns
40 DB TAPER, 10 ELEMENTS
30 DEG SCAN
45 DEG SCAN
NORM. POWER PATTERN (DB)
0
-10
-20
-30
-40
-50
-60
0
20
40
60
80
100
120
140
160
180
PHI (DEGREES)

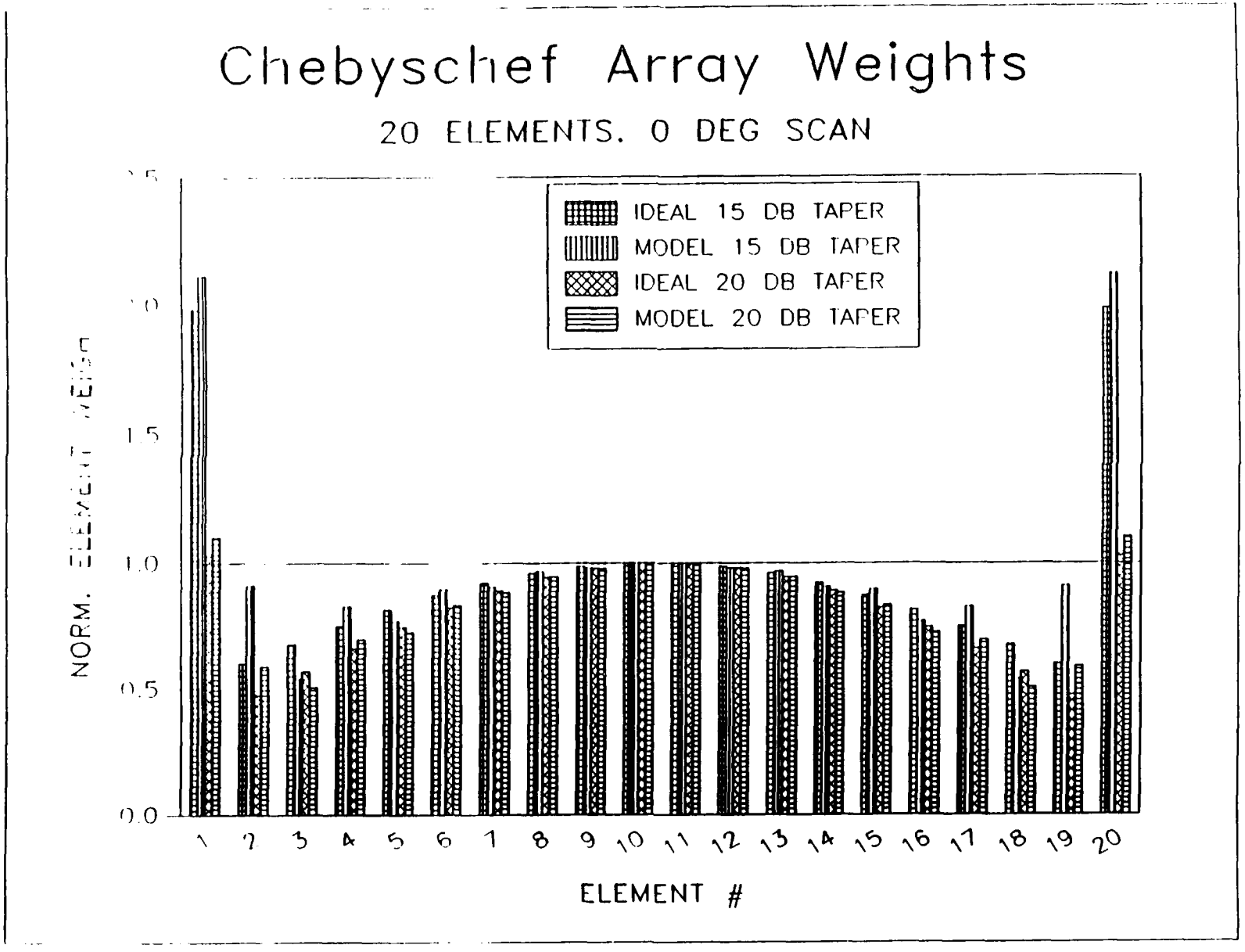
Chebyschef Array Weights
20 ELEMENTS. 0 DEG SCAN
IDEAL 15 DB TAPER
MODEL 15 DB TAPER
IDEAL 20 DB TAPER
MODEL 20 DB TAPER
NORM. ELEMENT WEIGHT
0.0
0.5
1.0
1.5
1 2 3 4 5 6 7 8 9 10 11 12 13 14 15 16 17 18 19 20
ELEMENT #

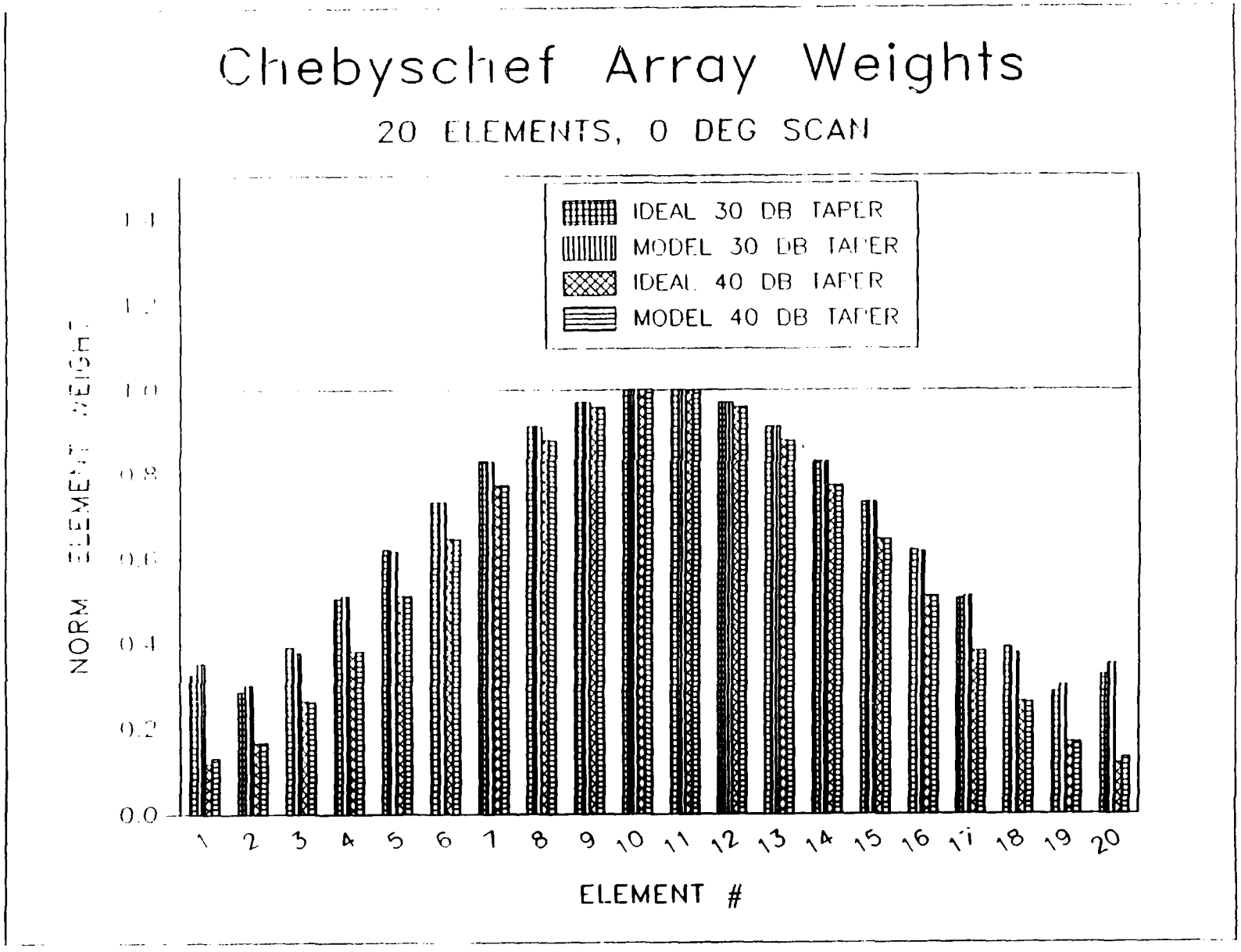
Chebyschef Array Weights
20 ELEMENTS, 0 DEG SCAN
IDEAL 30 DB TAPER
MODEL 30 DB TAPER
IDEAL 40 DB TAPER
MODEL 40 DB TAPER
NORM ELEMENT WEIGHT
0.0
0.2
0.4
1 2 3 4 5 6 7 8 9 10 11 12 13 14 15 16 17 18 19 20
ELEMENT #

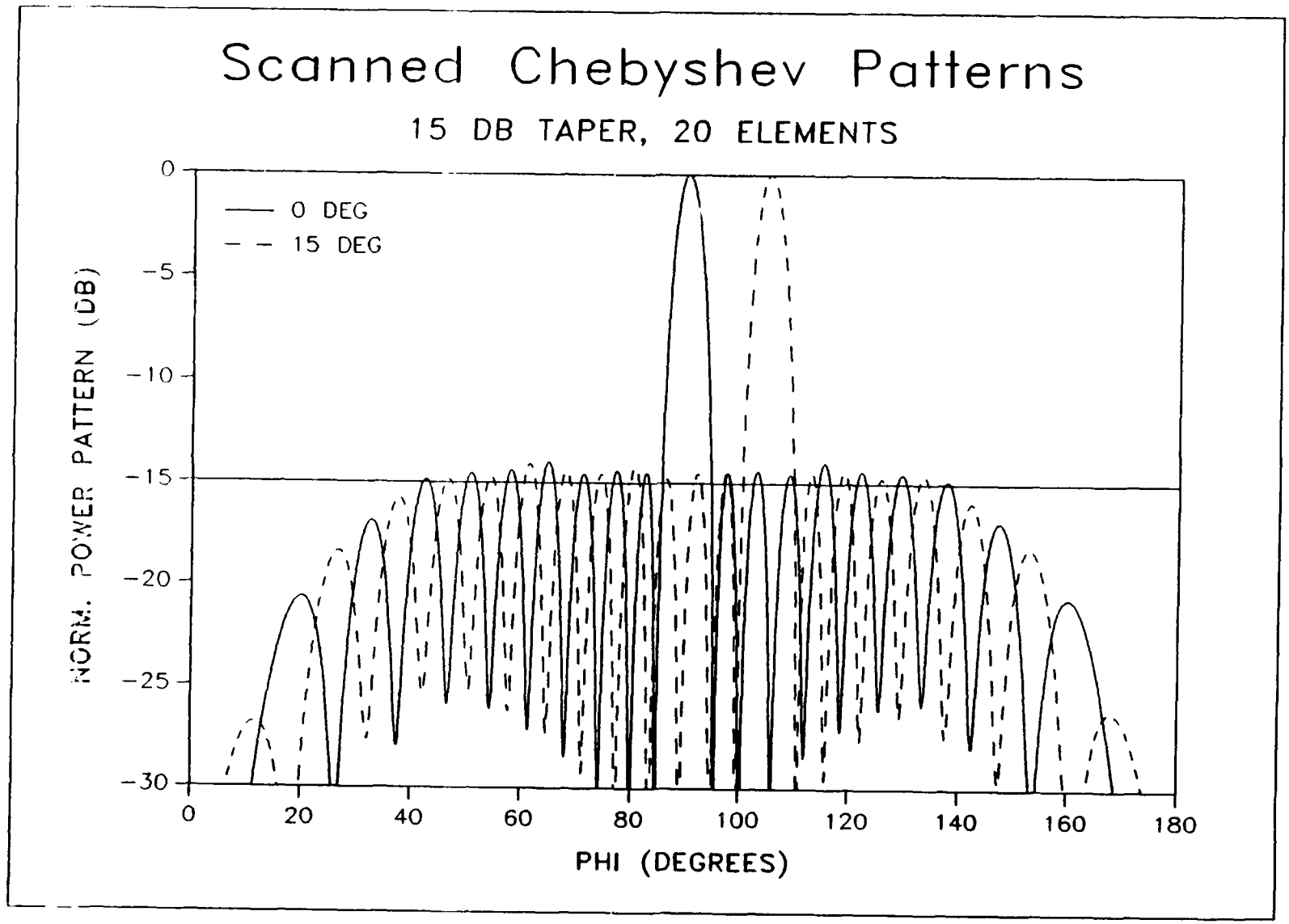
Scanned Chebyshev Patterns
15 DB TAPER, 20 ELEMENTS
0 DEG
15 DEG
NORM. POWER PATTERN (DB)
0
-5
-10
-15
-20
-25
-30
0
20
40
60
80
100
120
140
160
180
PHI (DEGREES)

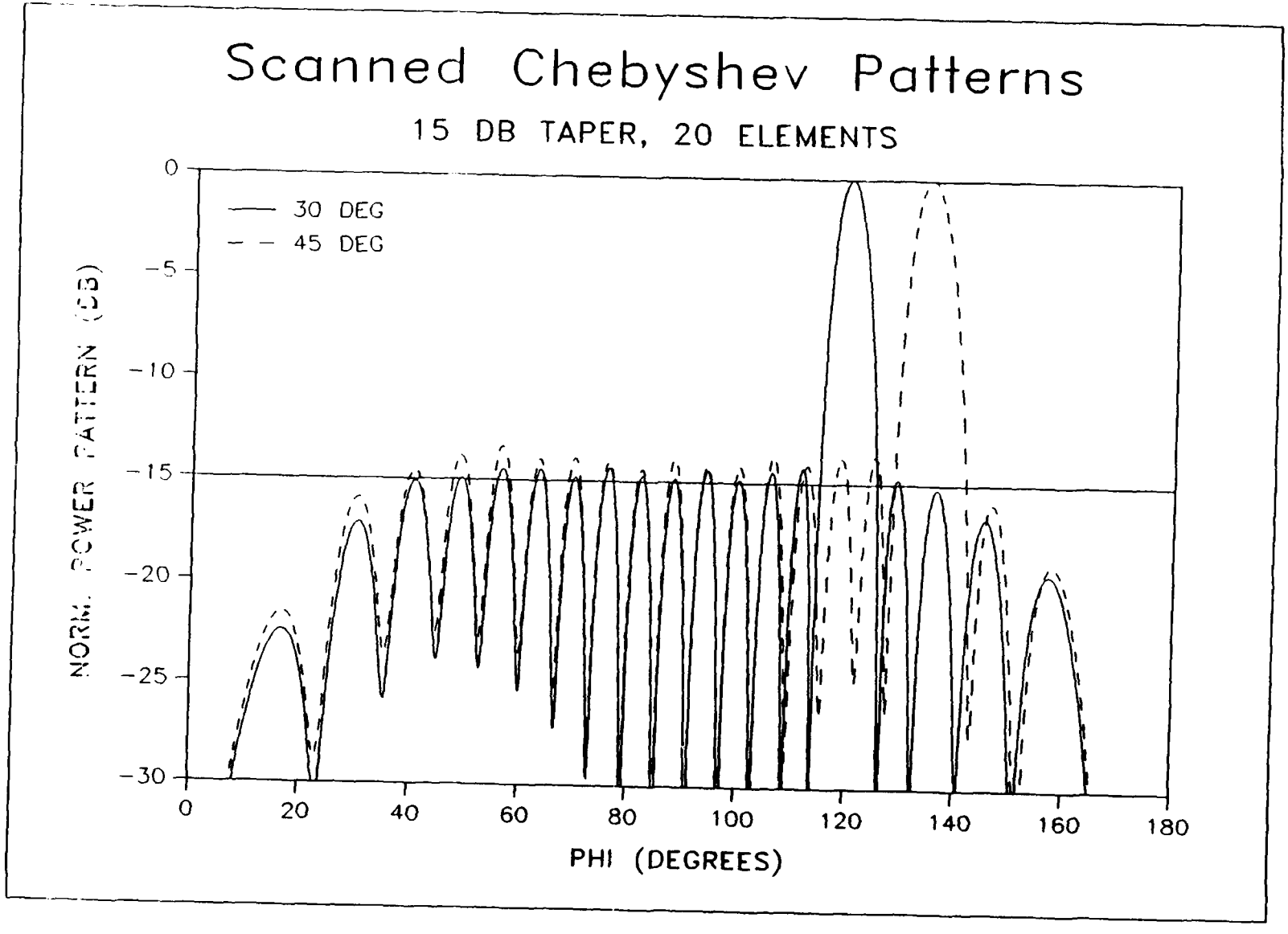
Scanned Chebyshev Patterns
15 DB TAPER, 20 ELEMENTS
30 DEG
45 DEG
NORM. POWER PATTERN (DB)
0
-5
-10
-15
-20
-25
-30
0
20
40
60
80
100
120
140
160
180
PHI (DEGREES)

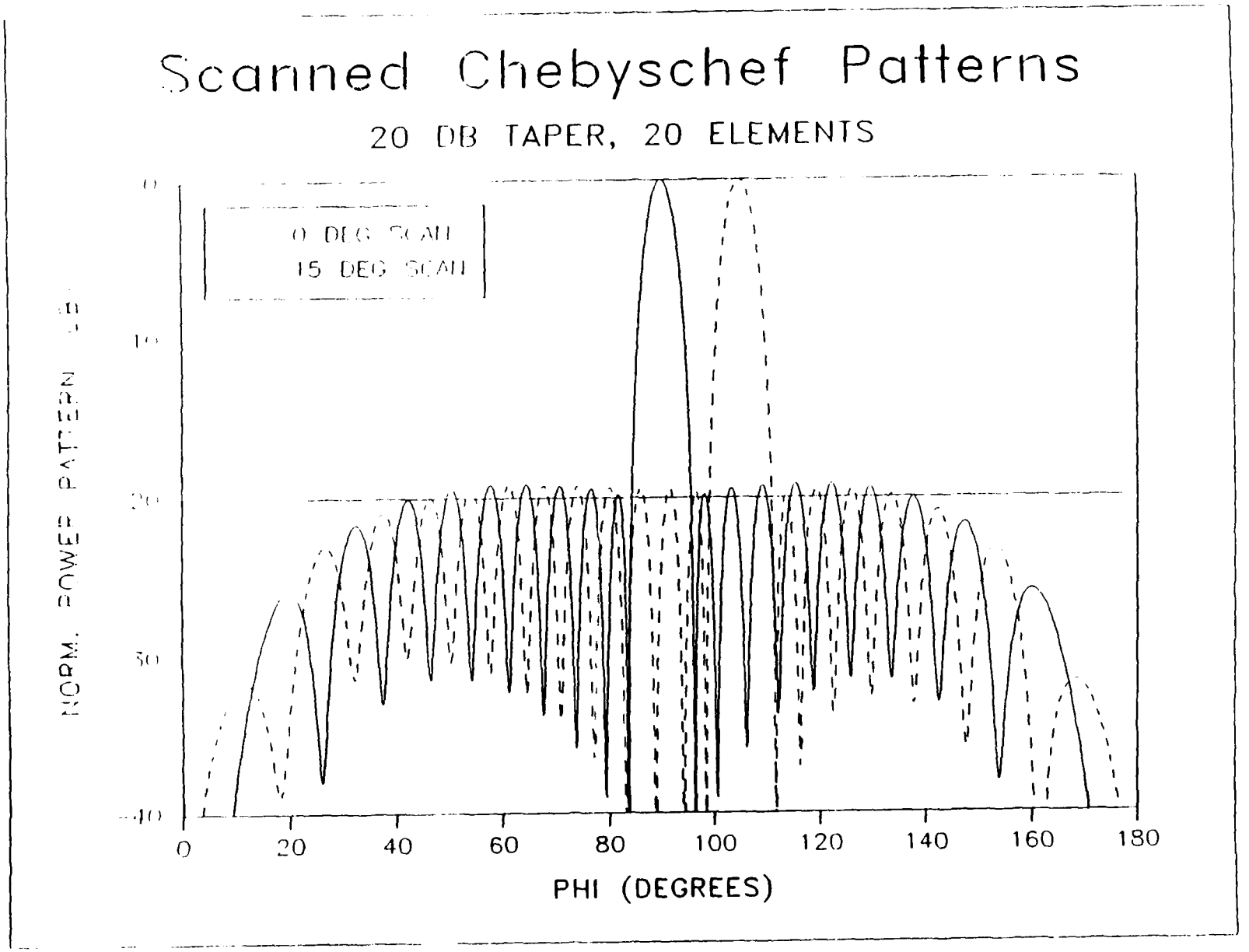
Scanned Chebyschef Patterns
20 DB TAPER, 20 ELEMENTS
0 DEG SCAN
15 DEG SCAN
NORM. POWER PATTERN (dB)
0
-10
-20
-30
-40
0
20
40
60
80
100
120
140
160
180
PHI (DEGREES)

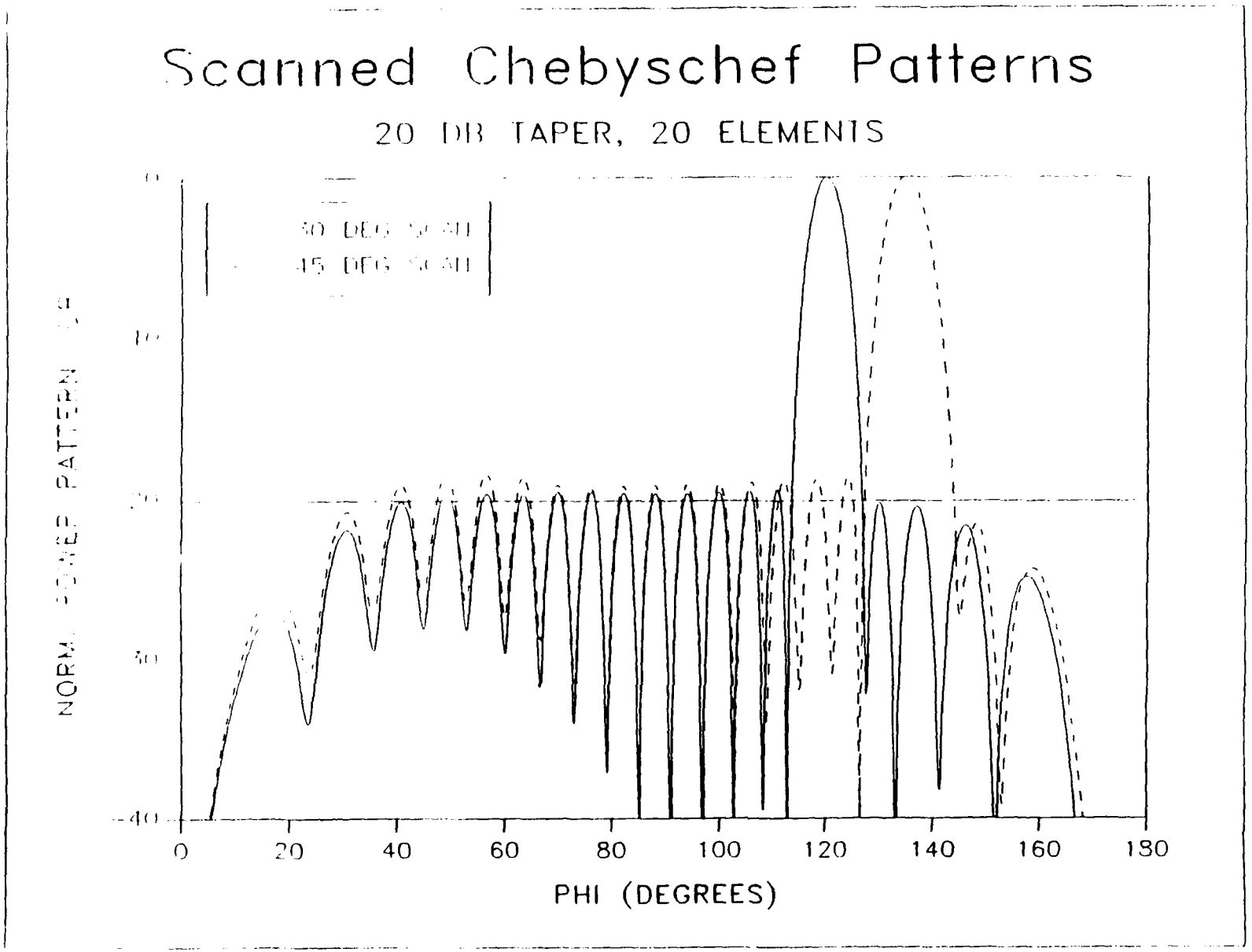
Scanned Chebyschef Patterns
20 DB TAPER, 20 ELEMENTS
30 DEG SCAN
45 DEG SCAN
NORM. POWER PATTERN (dB)
0
-20
-40
0
20
40
60
80
100
120
140
160
180
PHI (DEGREES)

Scanned Chebyschef Patterns

30 DB TAPER, 20 ELEMENTS

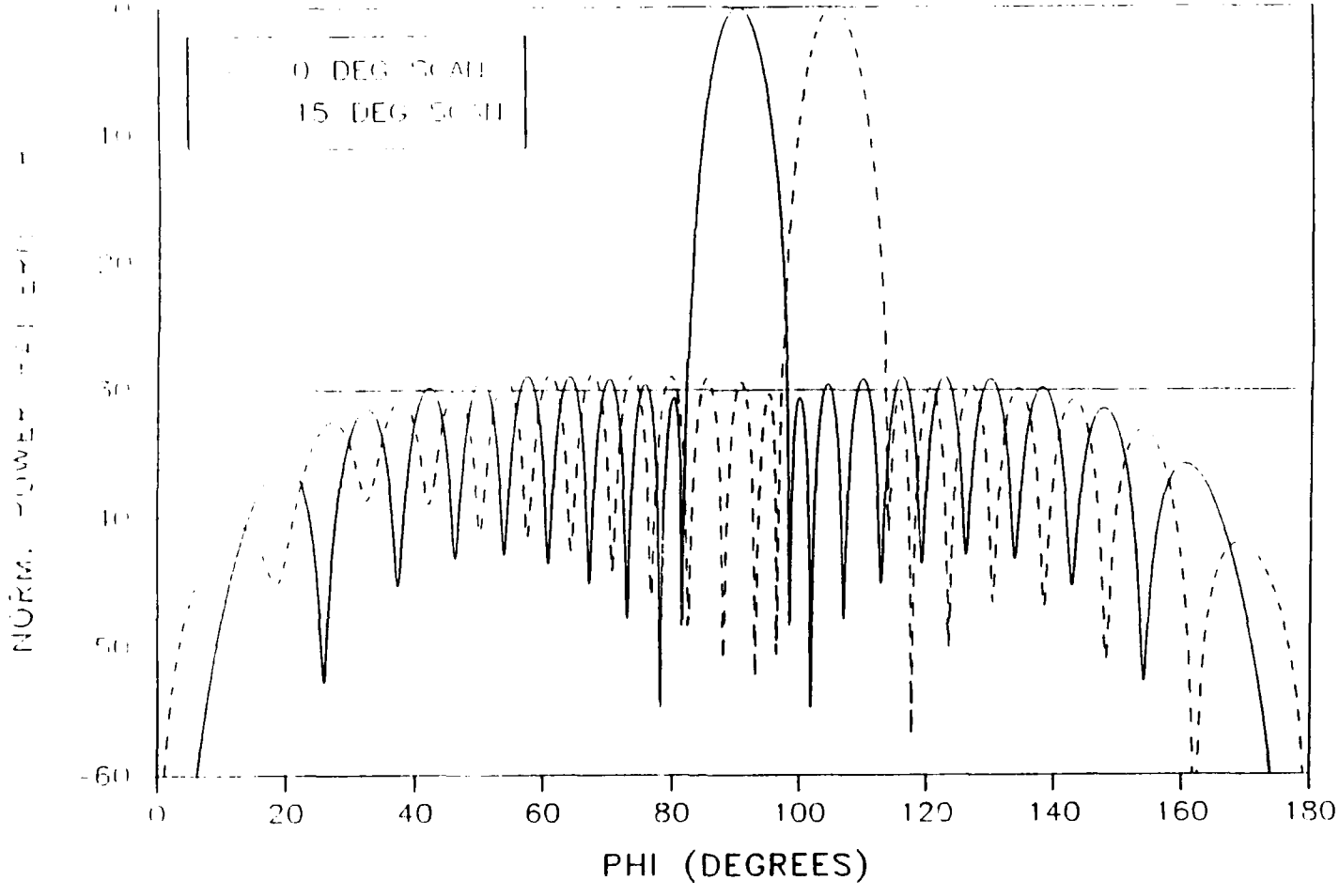

Scanned Chebyschef Patterns

30 DB TAPER, 20 ELEMENTS

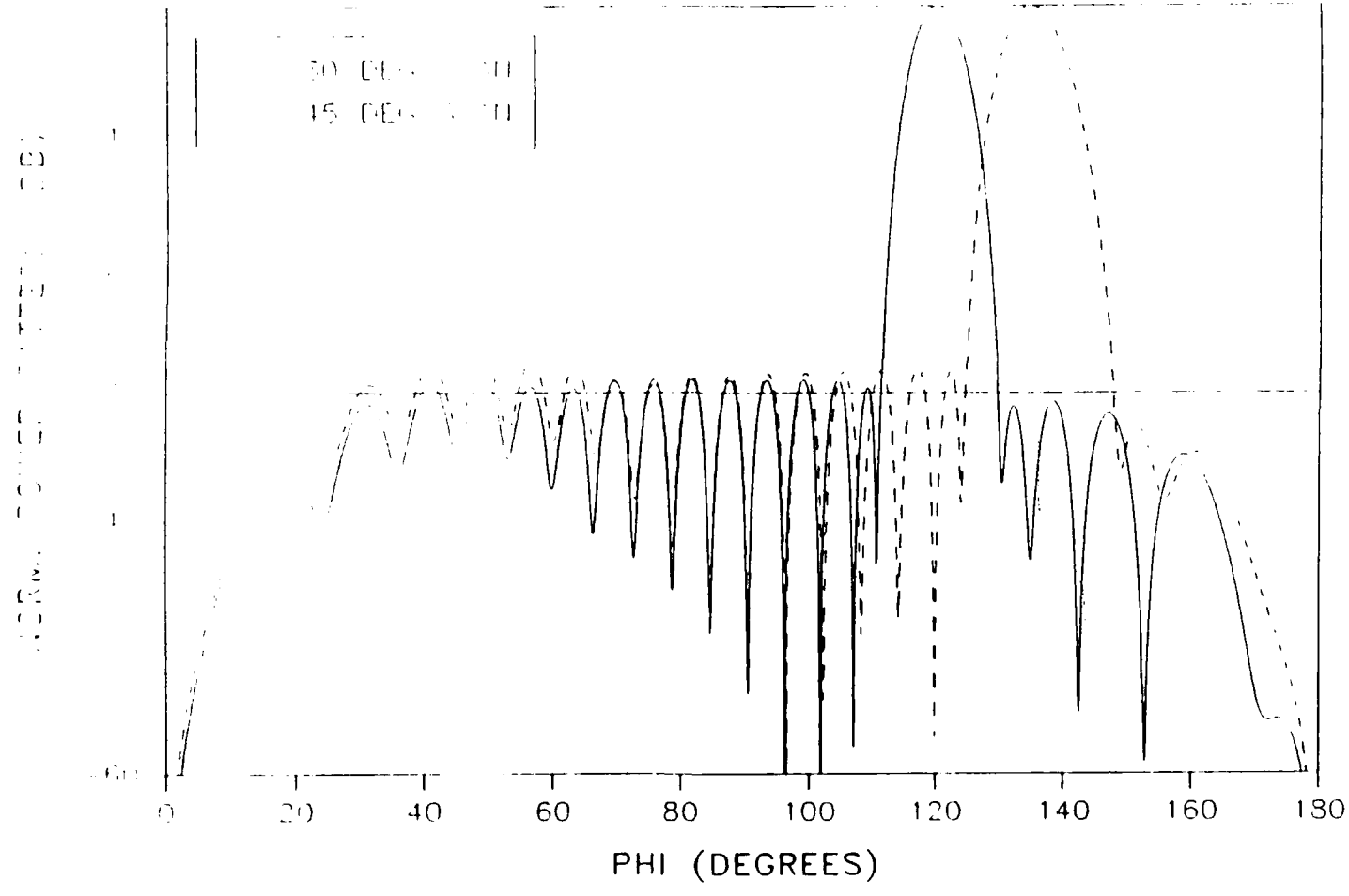

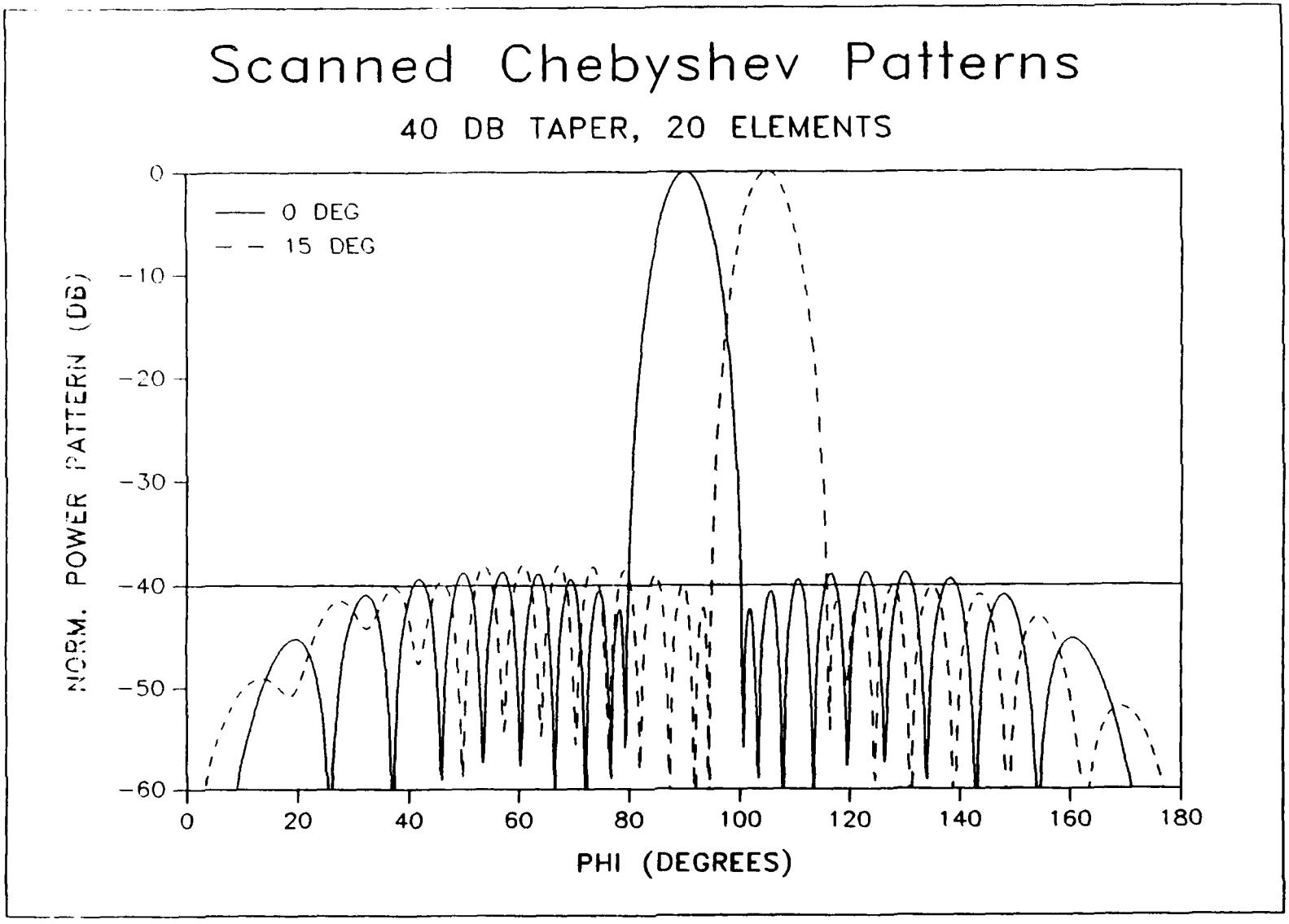
Scanned Chebyshev Patterns
40 DB TAPER, 20 ELEMENTS
0 DEG
15 DEG
NORM. POWER PATTERN (DB)
0
-10
-20
-30
-40
-50
-60
0
20
40
60
80
100
120
140
160
180
PHI (DEGREES)

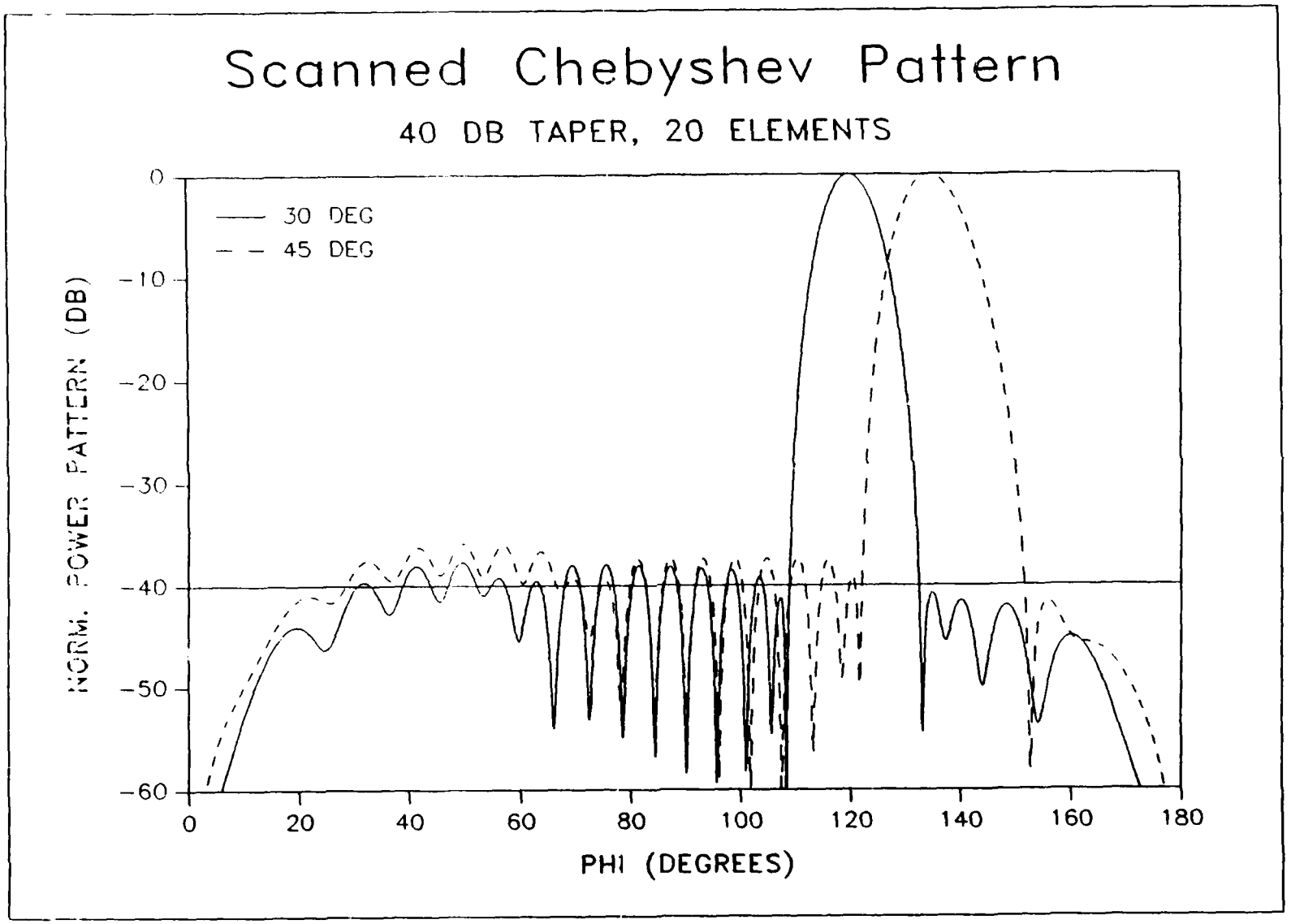
Scanned Chebyshev Pattern
40 DB TAPER, 20 ELEMENTS
30 DEG
45 DEG
NORM. POWER PATTERN (DB)
0
-10
-20
-30
-40
-50
-60
0
20
40
60
80
100
120
140
160
180
PHI (DEGREES)

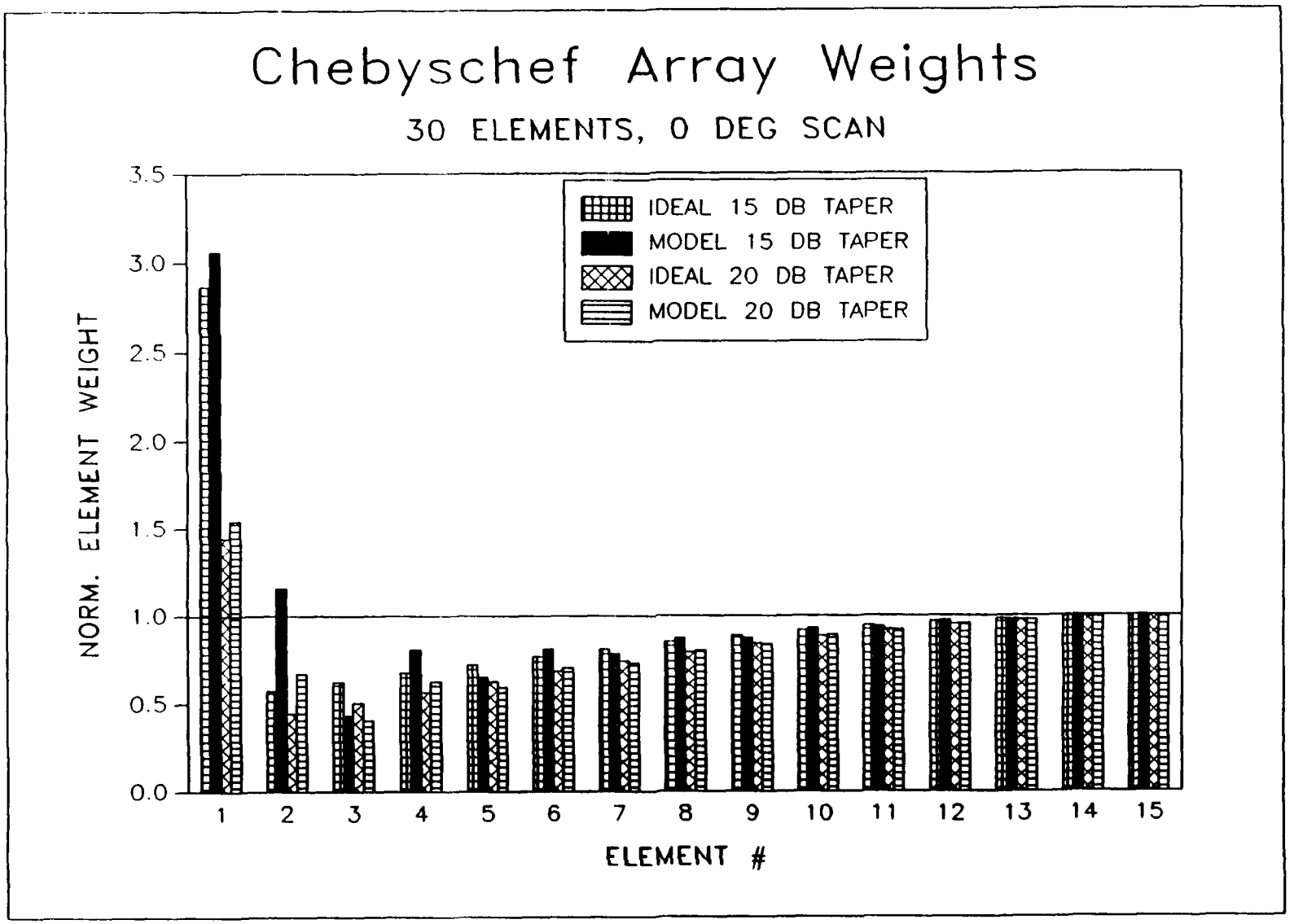
Chebyschef Array Weights
30 ELEMENTS, 0 DEG SCAN
IDEAL 15 DB TAPER
MODEL 15 DB TAPER
IDEAL 20 DB TAPER
MODEL 20 DB TAPER
NORM. ELEMENT WEIGHT
3.5
3.0
2.5
2.0
1.5
1.0
0.5
0.0
1
2
3
4
5
6
7
8
9
10
11
12
13
14
15
ELEMENT #

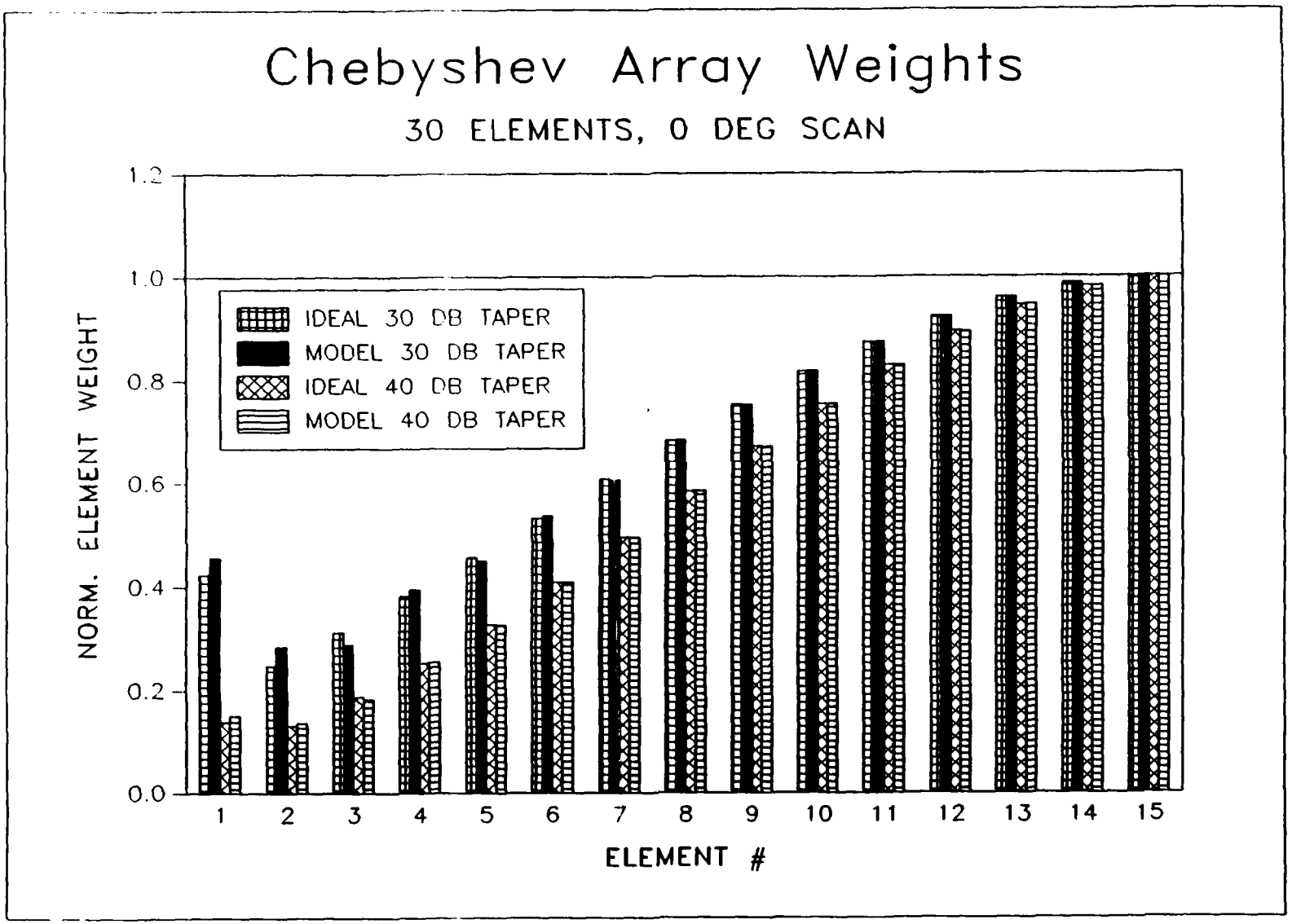
Chebyshev Array Weights
30 ELEMENTS, 0 DEG SCAN
NORM. ELEMENT WEIGHT
1.2
1.0
0.8
0.6
0.4
0.2
0.0
IDEAL 30 DB TAPER
MODEL 30 DB TAPER
IDEAL 40 DB TAPER
MODEL 40 DB TAPER
1
2
3
4
5
6
7
8
9
10
11
12
13
14
15
ELEMENT #

Scanned Chebyschef Patterns

15 DB TAPER, 30 ELEMENTS

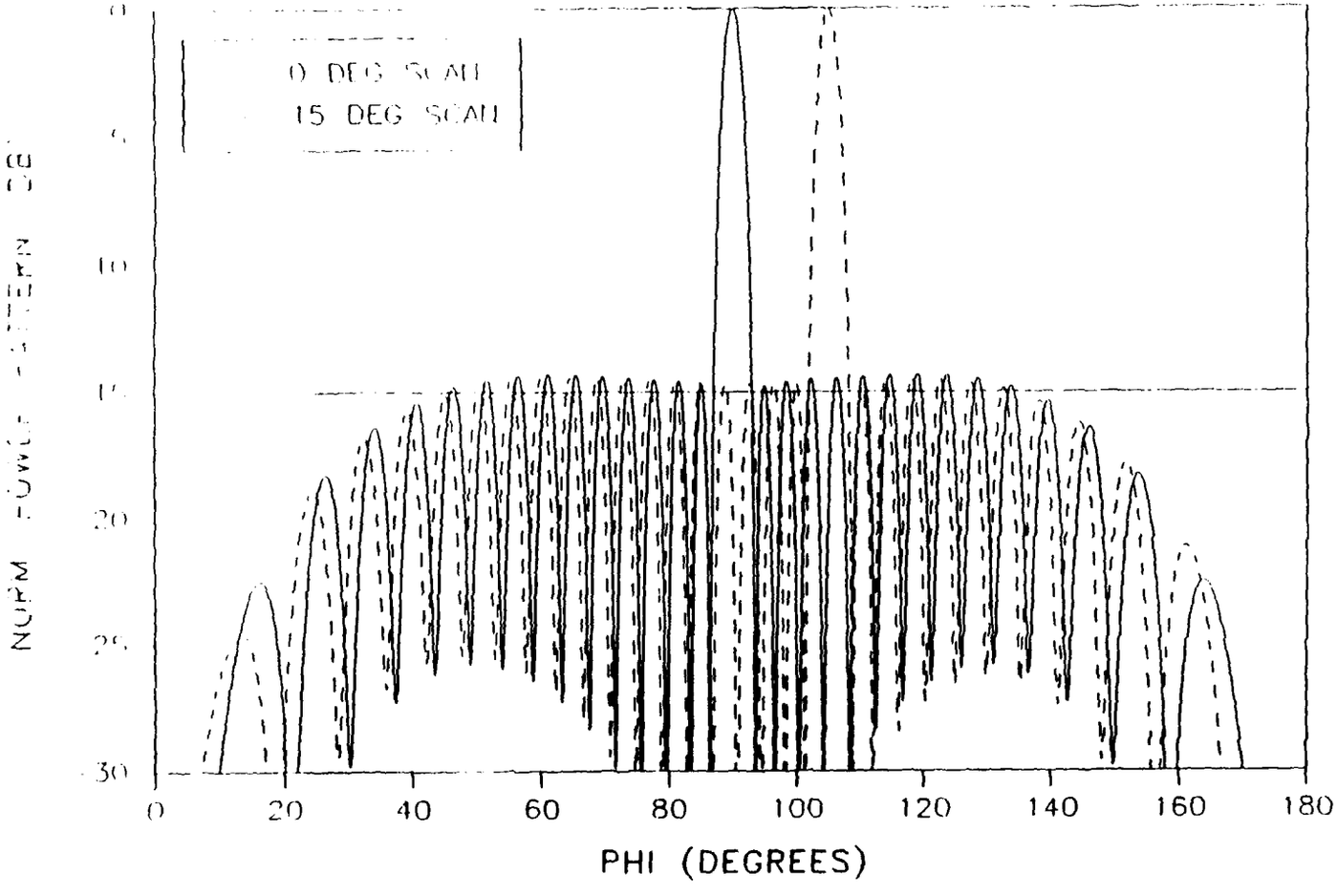

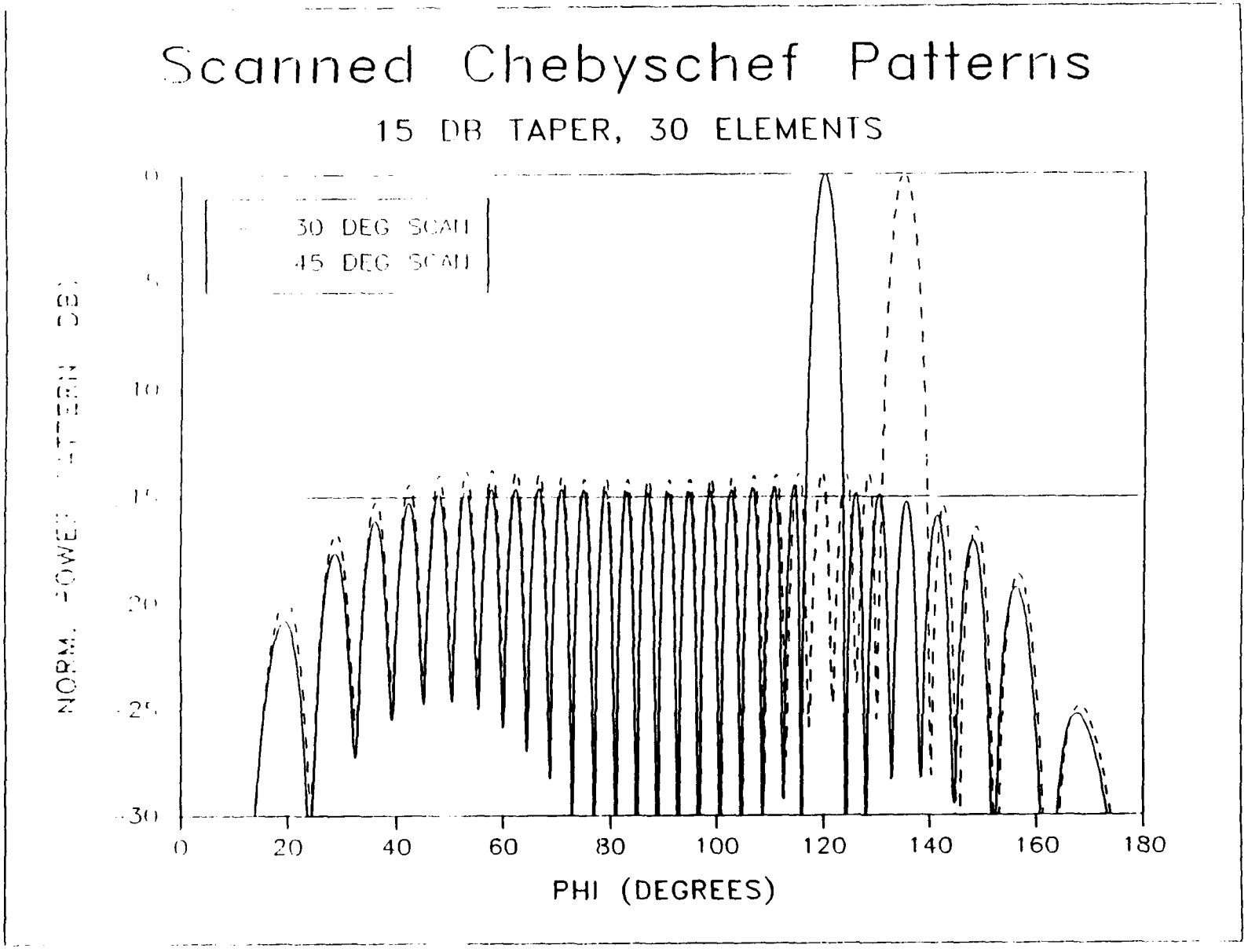
Scanned Chebyschef Patterns
15 DB TAPER, 30 ELEMENTS
30 DEG SCAN
45 DEG SCAN
NORM. POWER PATTERN (DB)
0
-10
-30
0
20
40
60
80
100
120
140
160
180
PHI (DEGREES)

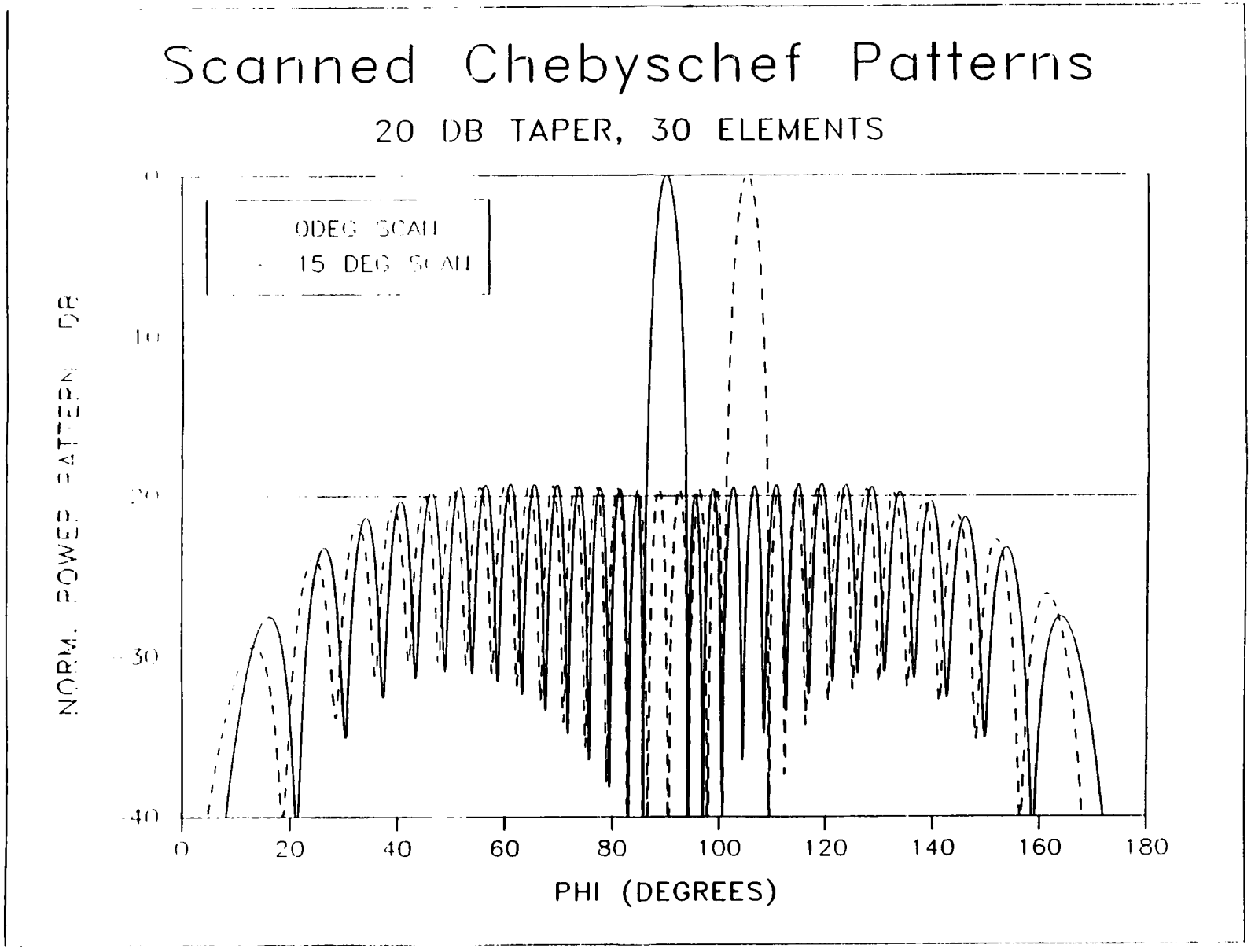
Scanned Chebyschef Patterns
20 DB TAPER, 30 ELEMENTS
0DEG SCAN
15 DEG SCAN
NORM. POWER PATTERN DB
0
-10
-20
-30
-40
0
20
40
60
80
100
120
140
160
180
PHI (DEGREES)

Scanned Chebyschef Patterns

20 DB TAPER, 30 ELEMENTS

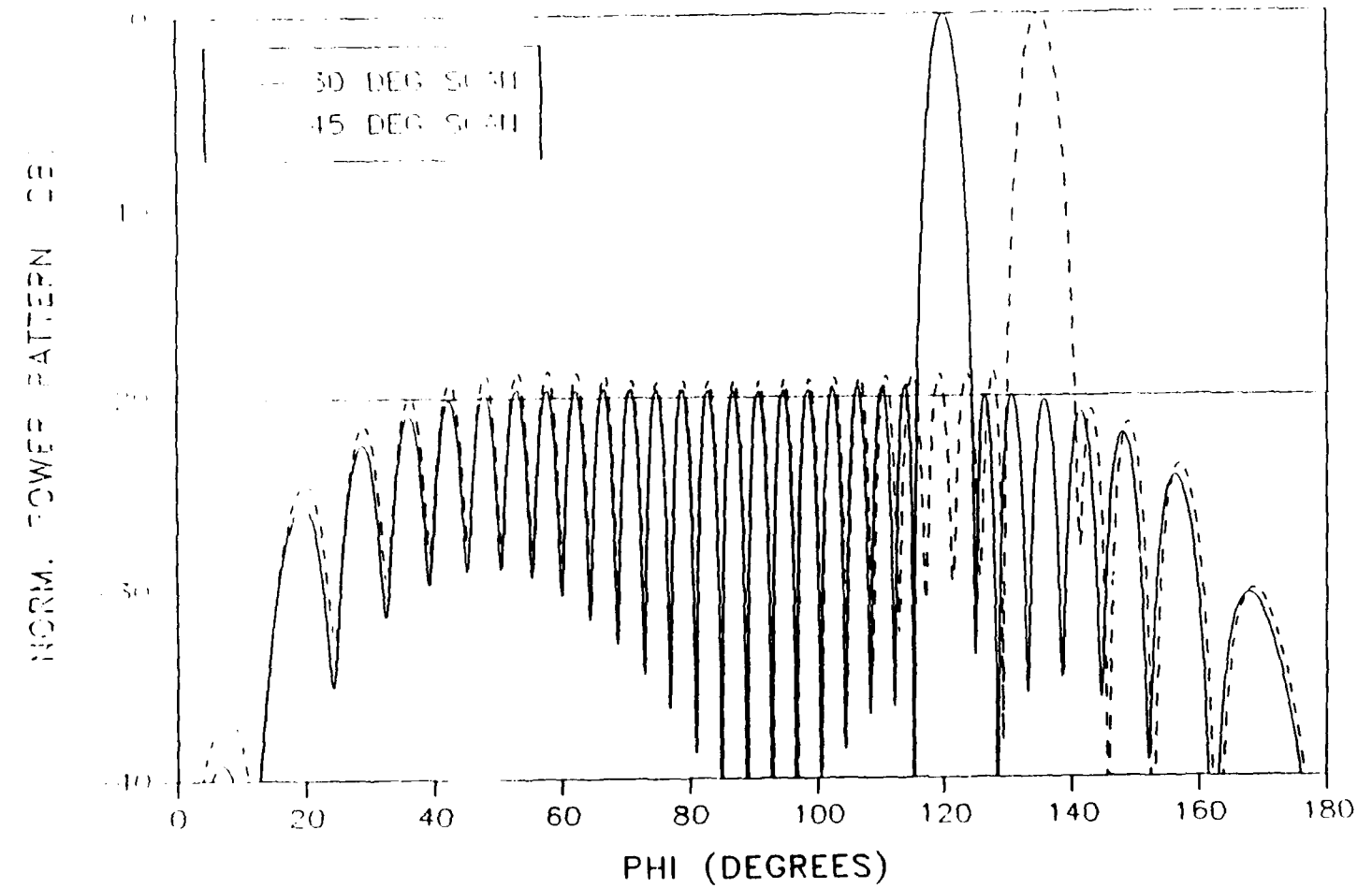

Scanned Chebyschef Patterns

30 DB TAPER, 30 ELEMENTS

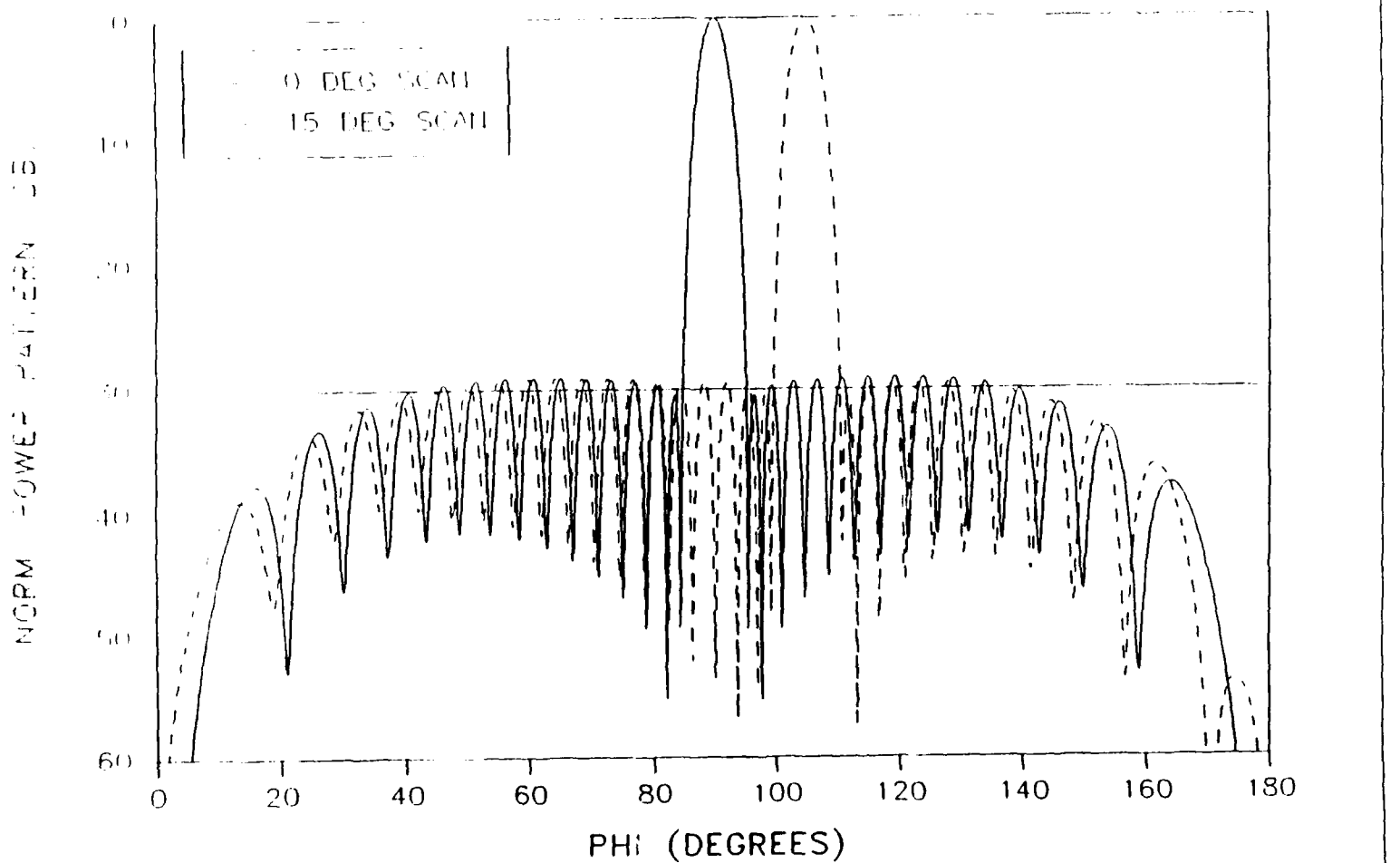

Scanned Chebyschef Patterns

30 DB TAPER, 30 ELEMENTS

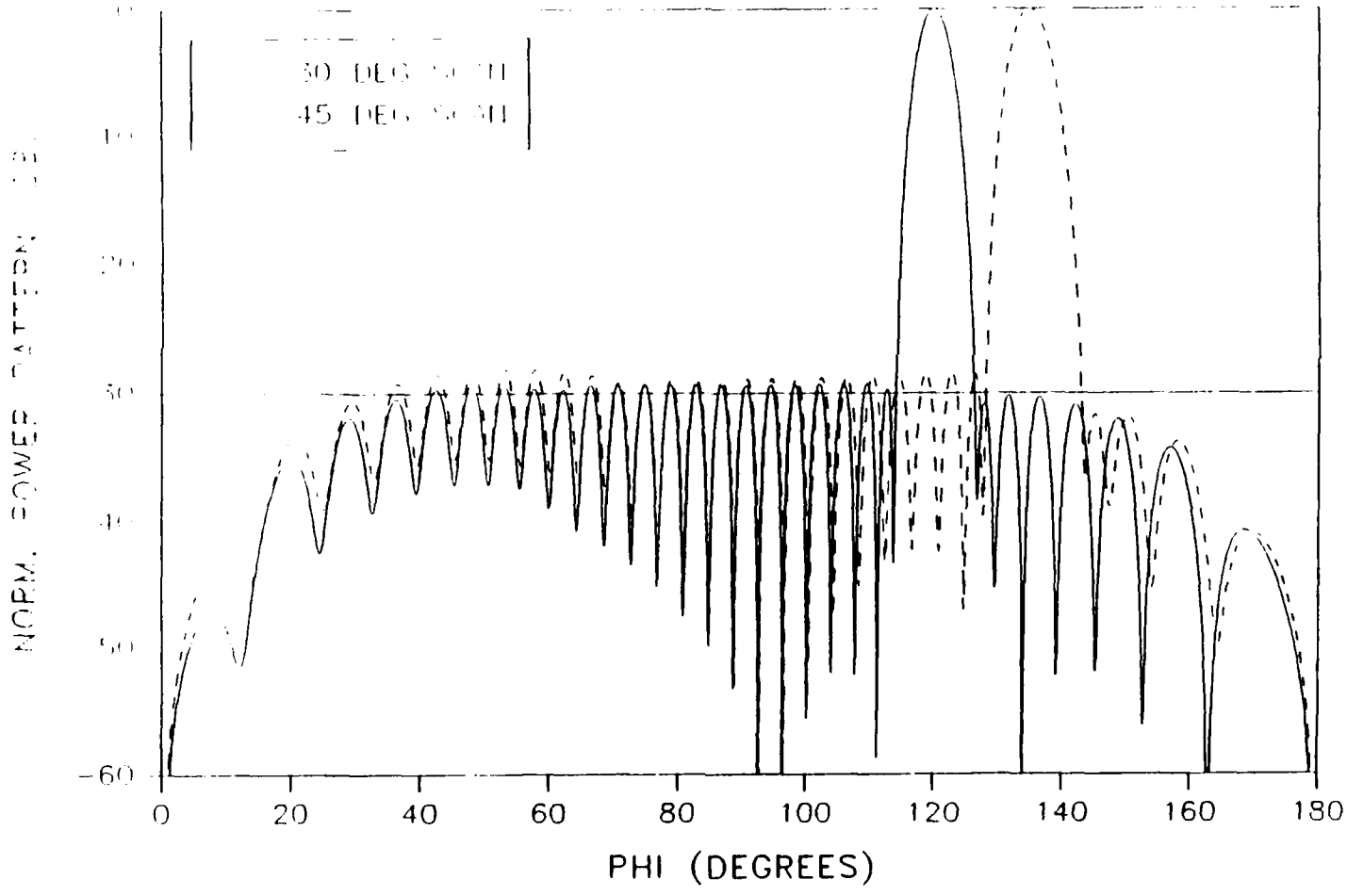

Scanned Chebyschef Patterns

40 DB TAPER, 30 ELEMENTS

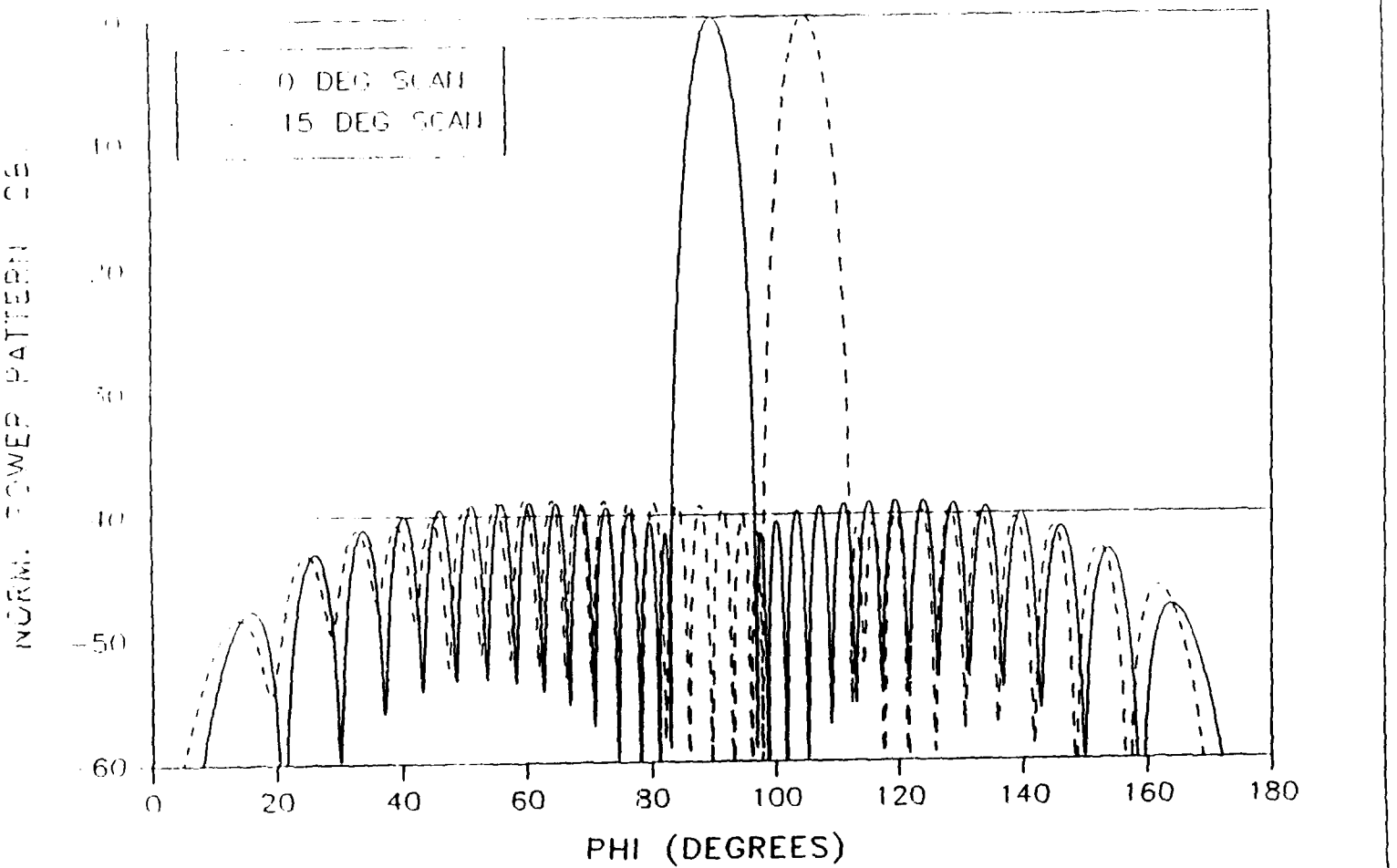

Scanned Chebyschef Patterns

40 DB TAPER, 30 ELEMENTS

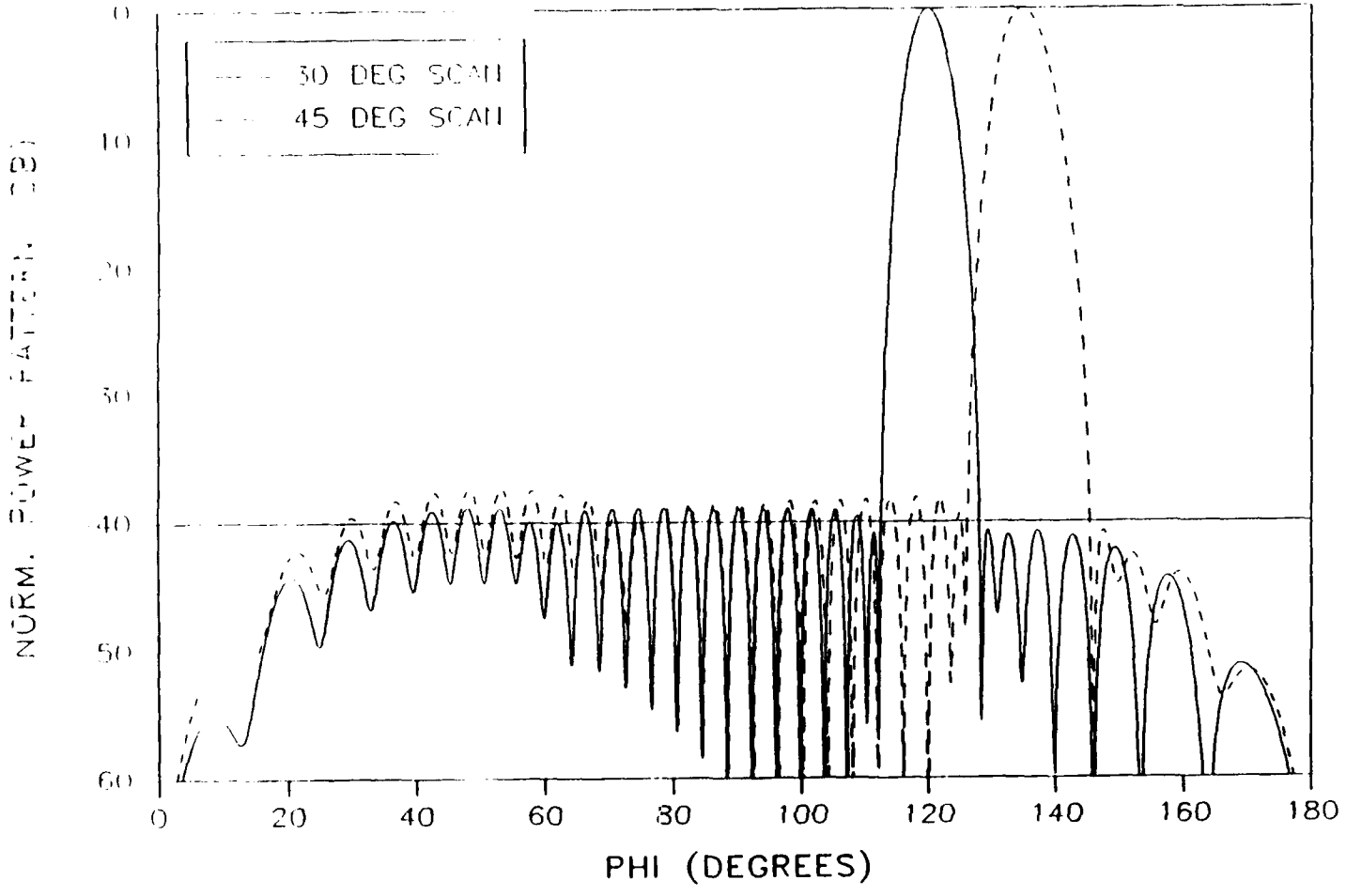

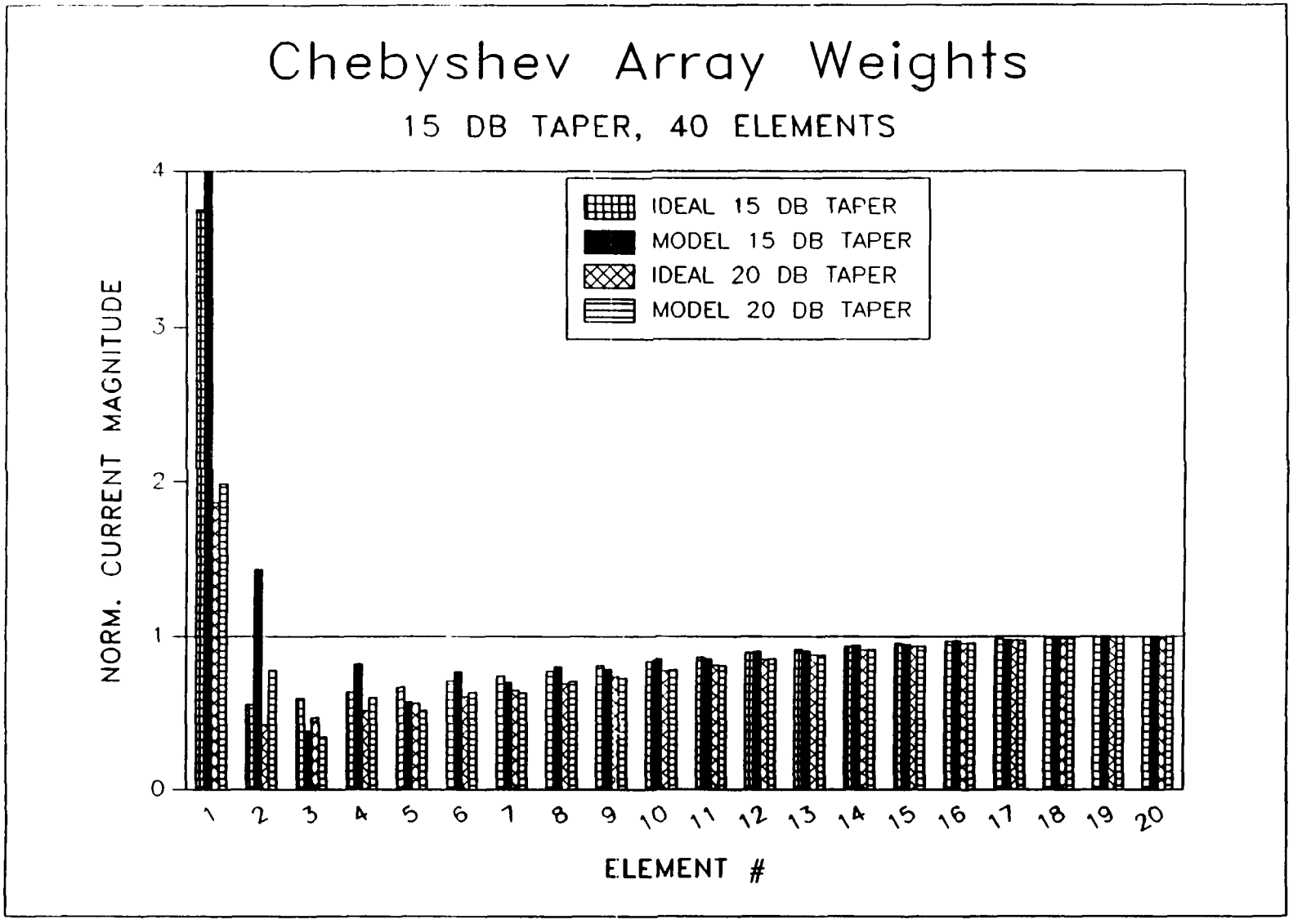
Chebyshev Array Weights
15 DB TAPER, 40 ELEMENTS
IDEAL 15 DB TAPER
MODEL 15 DB TAPER
IDEAL 20 DB TAPER
MODEL 20 DB TAPER
NORM. CURRENT MAGNITUDE
0
1
2
3
4
1 2 3 4 5 6 7 8 9 10 11 12 13 14 15 16 17 18 19 20
ELEMENT #

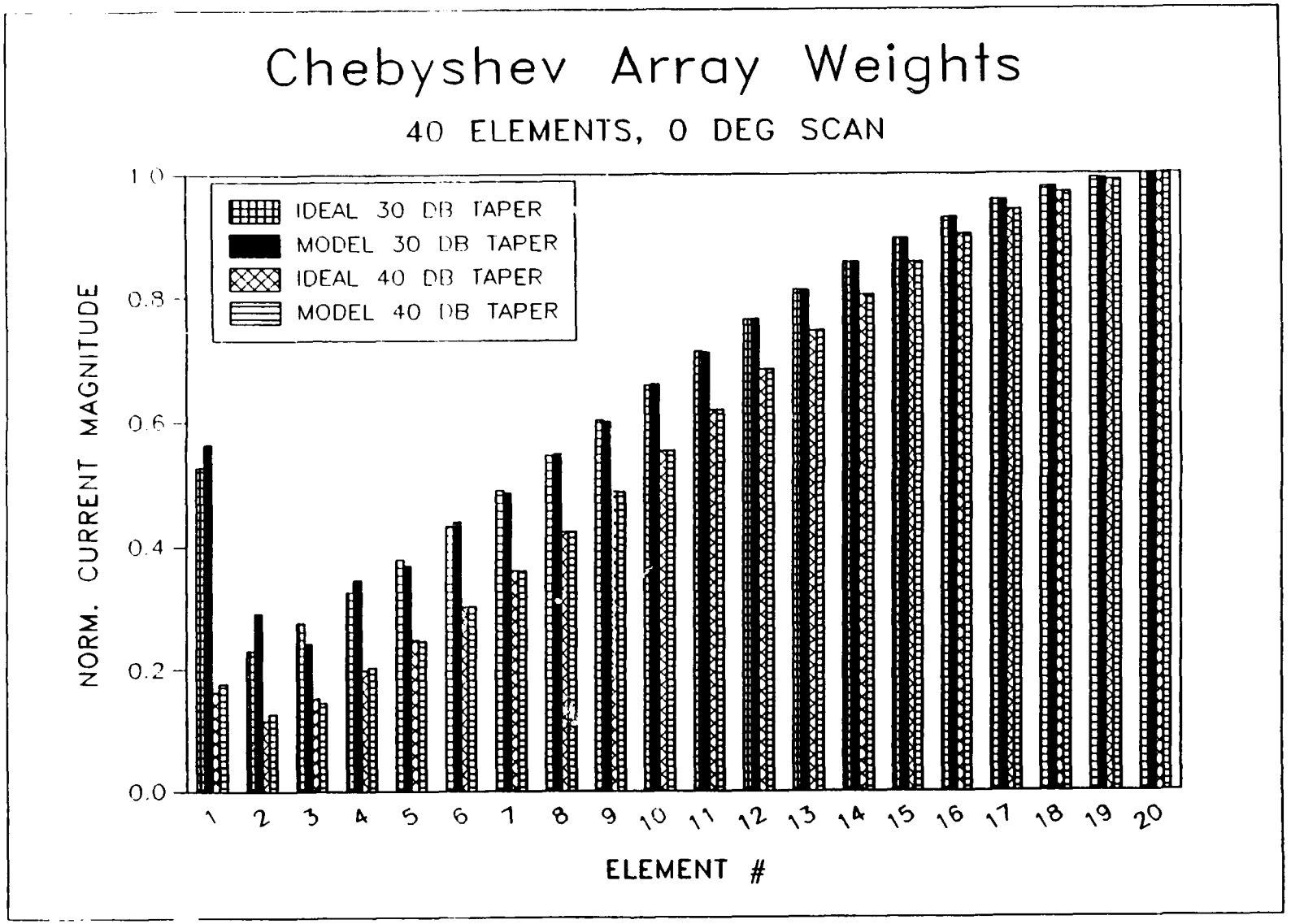
Chebyshev Array Weights
40 ELEMENTS, 0 DEG SCAN
IDEAL 30 DB TAPER
MODEL 30 DB TAPER
IDEAL 40 DB TAPER
MODEL 40 DB TAPER
NORM. CURRENT MAGNITUDE
1.0
0.8
0.6
0.4
0.2
0.0
1 2 3 4 5 6 7 8 9 10 11 12 13 14 15 16 17 18 19 20
ELEMENT #

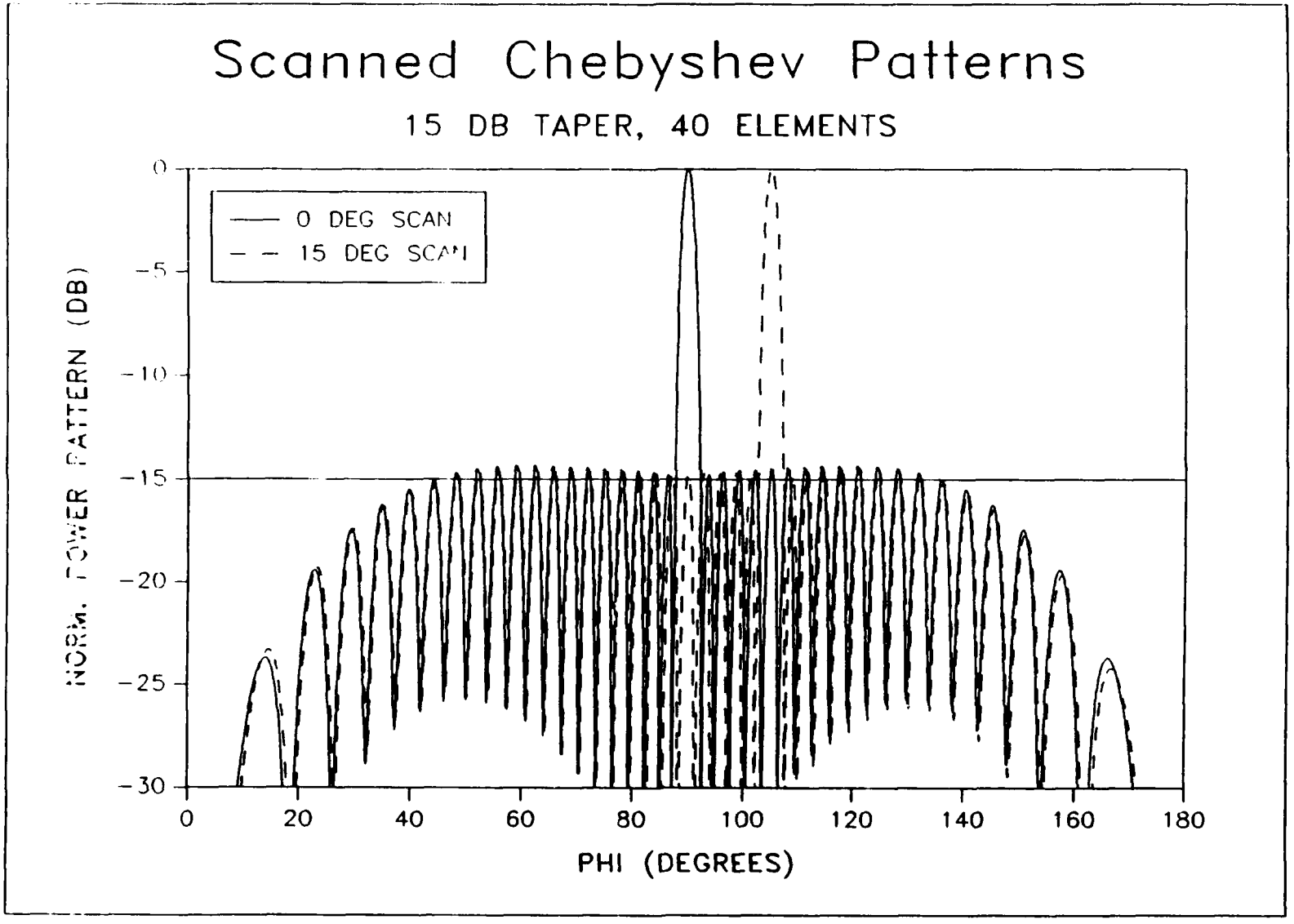
Scanned Chebyshev Patterns
15 DB TAPER, 40 ELEMENTS
0 DEG SCAN
15 DEG SCAN
NORM. POWER PATTERN (DB)
0
-5
-10
-15
-20
-25
-30
0
20
40
60
80
100
120
140
160
180
PHI (DEGREES)

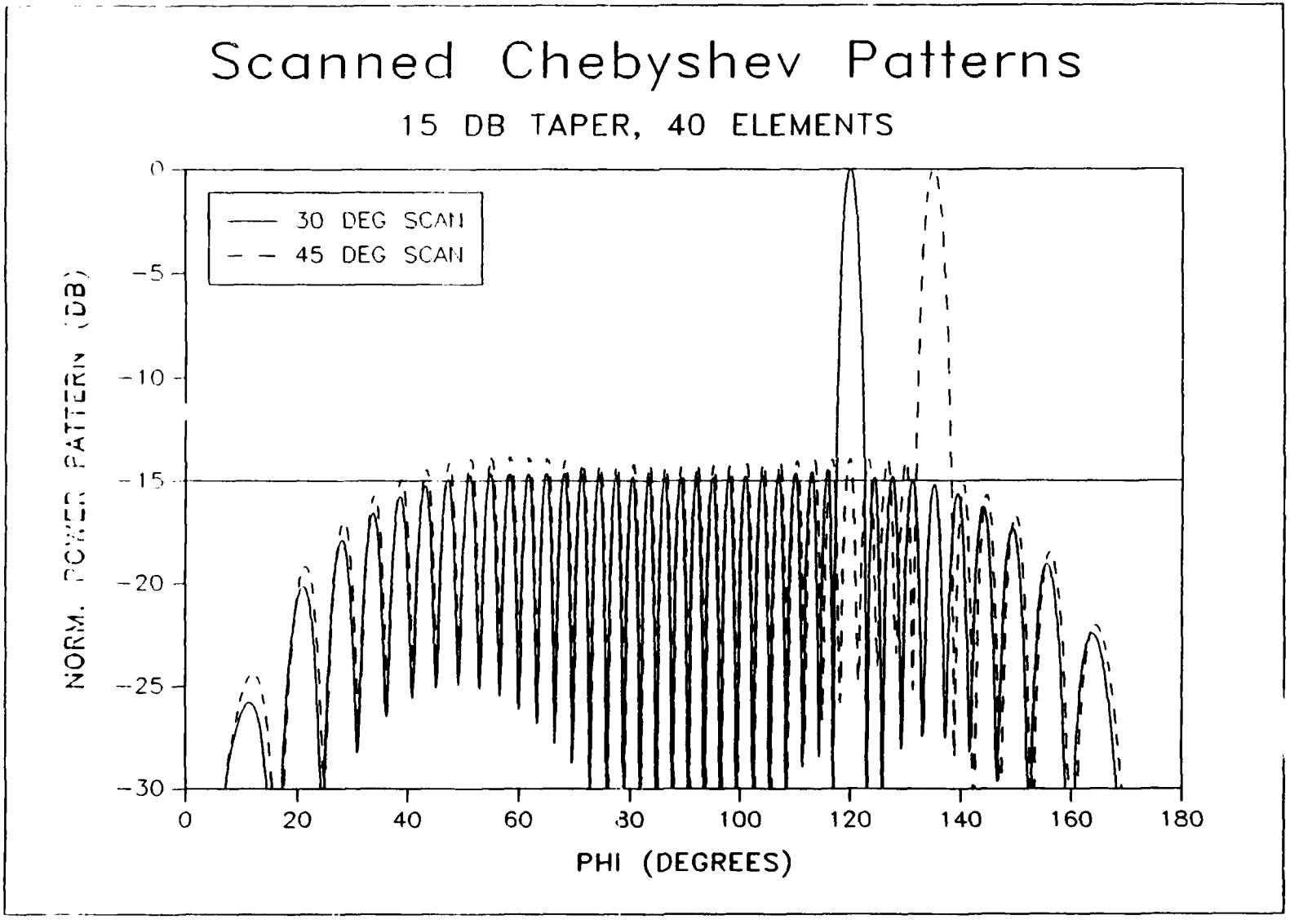
Scanned Chebyshev Patterns
15 DB TAPER, 40 ELEMENTS
30 DEG SCAN
45 DEG SCAN
NORM. POWER PATTERN (DB)
0
-5
-10
-15
-20
-25
-30
0
20
40
60
80
100
120
140
160
180
PHI (DEGREES)

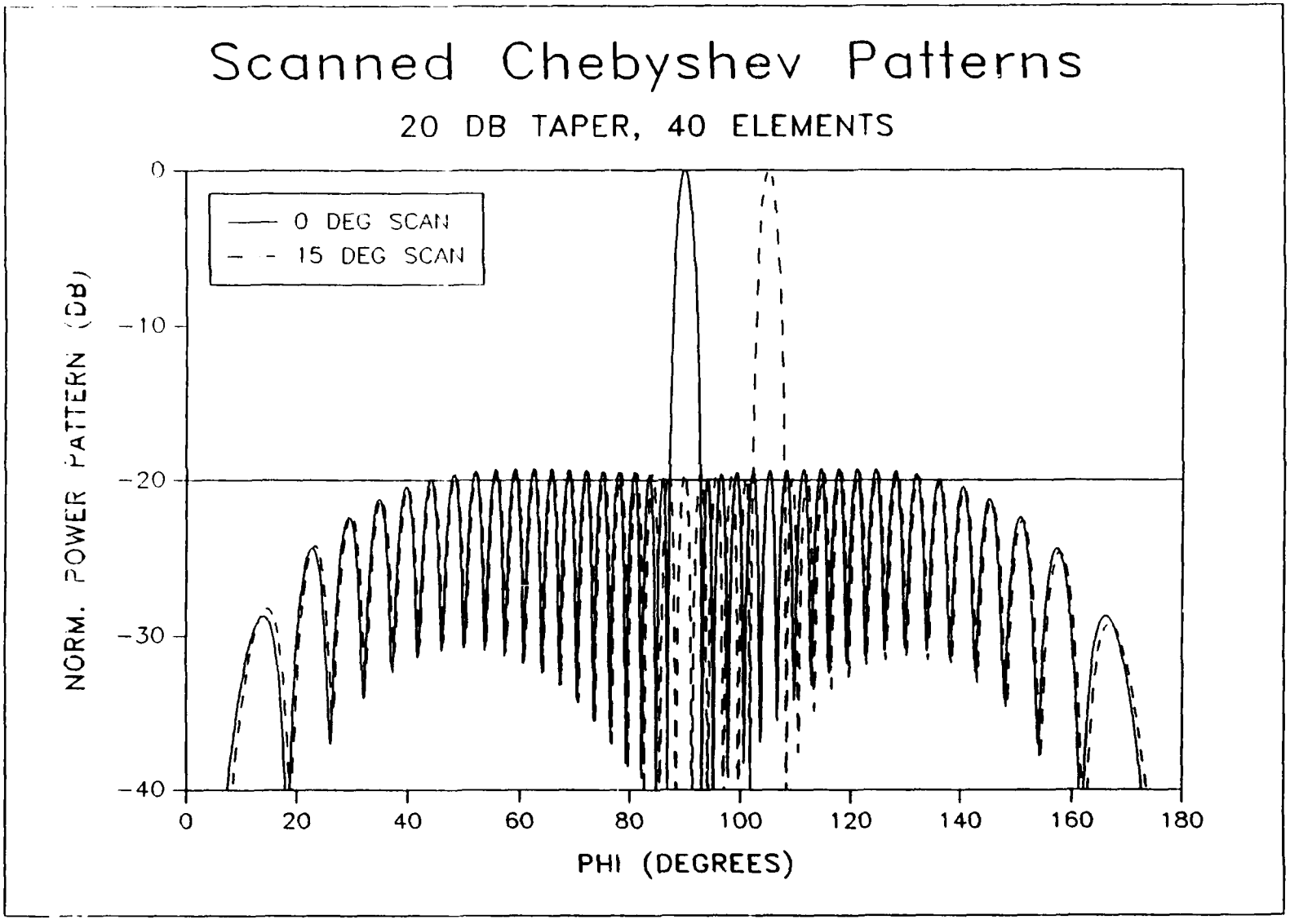
Scanned Chebyshev Patterns
20 DB TAPER, 40 ELEMENTS
0 DEG SCAN
15 DEG SCAN
NORM. POWER PATTERN (DB)
0
-10
-20
-30
-40
0
20
40
60
80
100
120
140
160
180
PHI (DEGREES)

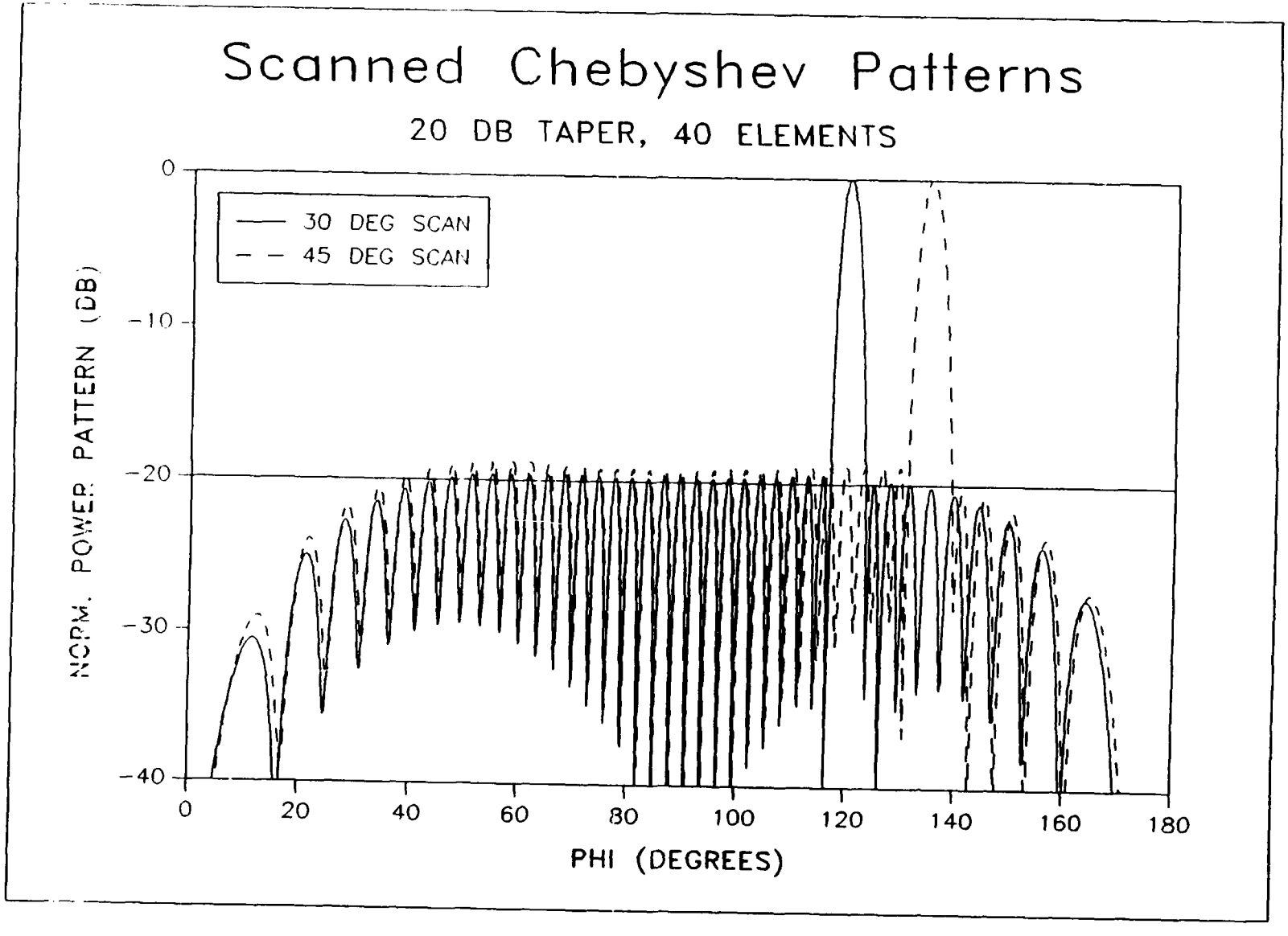
Scanned Chebyshev Patterns
20 DB TAPER, 40 ELEMENTS
30 DEG SCAN
45 DEG SCAN
NORM. POWER PATTERN (DB)
0
-10
-20
-30
-40
0
20
40
60
80
100
120
140
160
180
PHI (DEGREES)

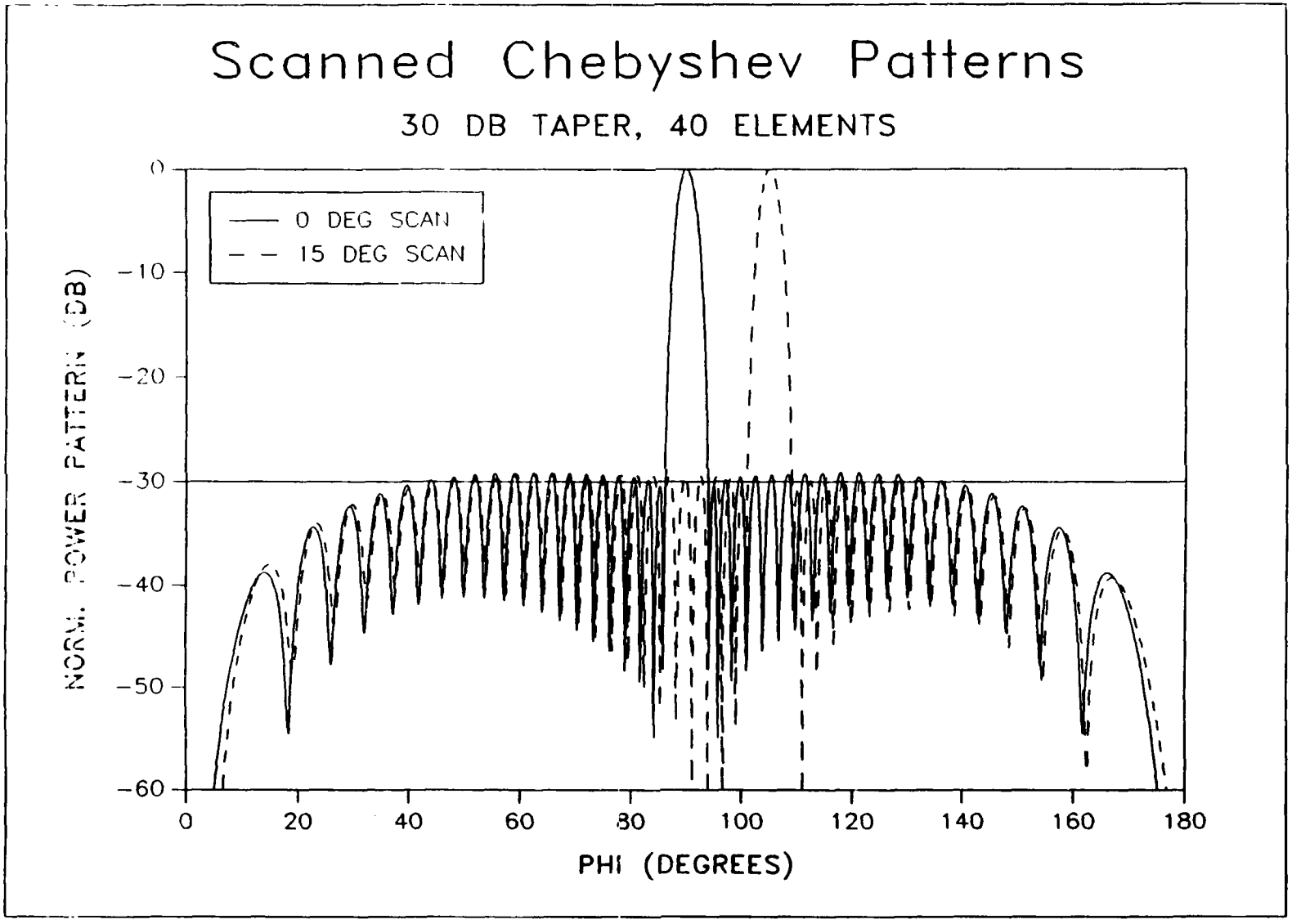
Scanned Chebyshev Patterns
30 DB TAPER, 40 ELEMENTS
0 DEG SCAN
15 DEG SCAN
NORM. POWER PATTERN (DB)
0
-10
-20
-30
-40
-50
-60
0
20
40
60
80
100
120
140
160
180
PHI (DEGREES)

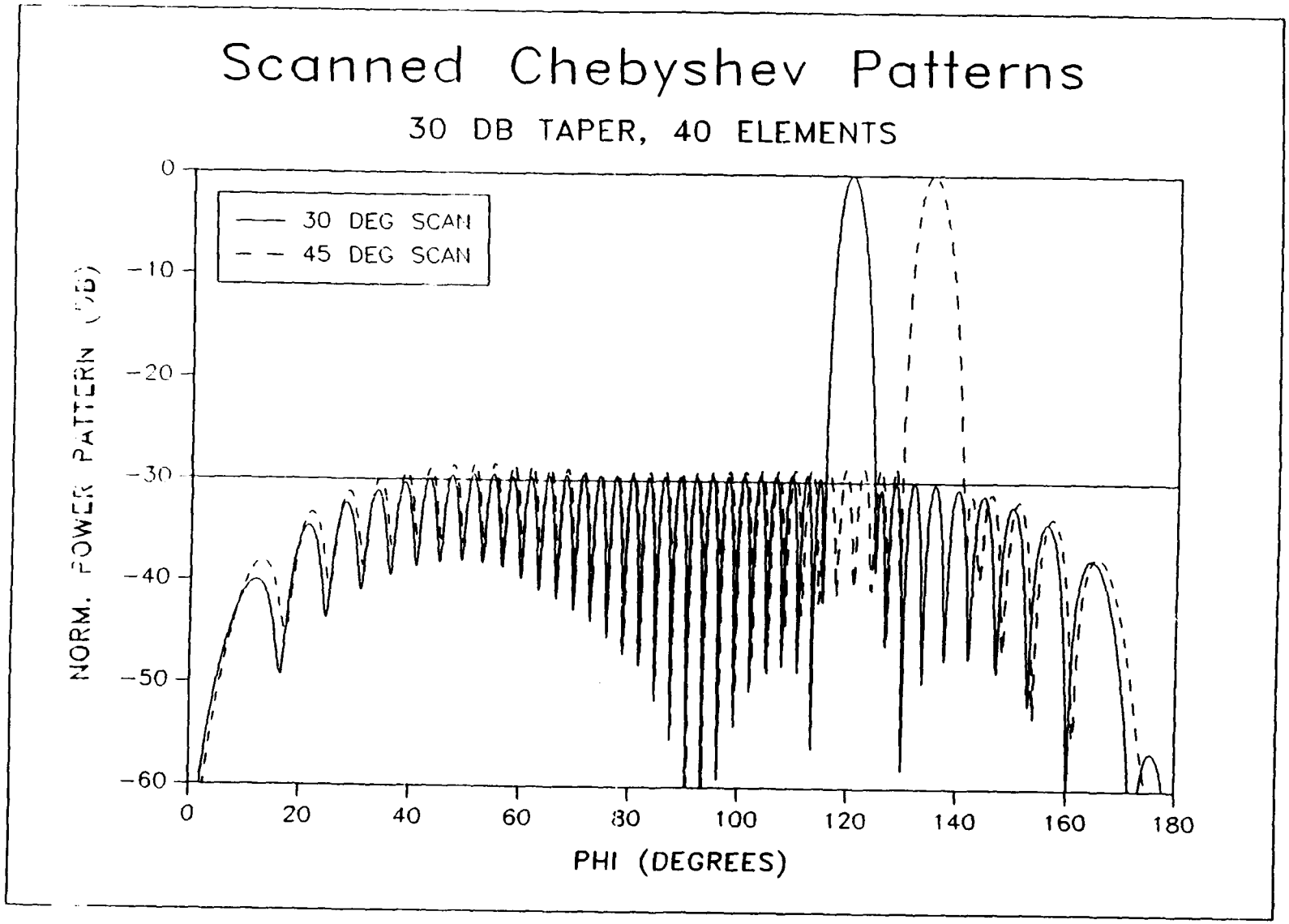
Scanned Chebyshev Patterns
30 DB TAPER, 40 ELEMENTS
30 DEG SCAN
45 DEG SCAN
NORM. POWER PATTERN (DB)
0
-10
-20
-30
-40
-50
-60
0
20
40
60
80
100
120
140
160
180
PHI (DEGREES)

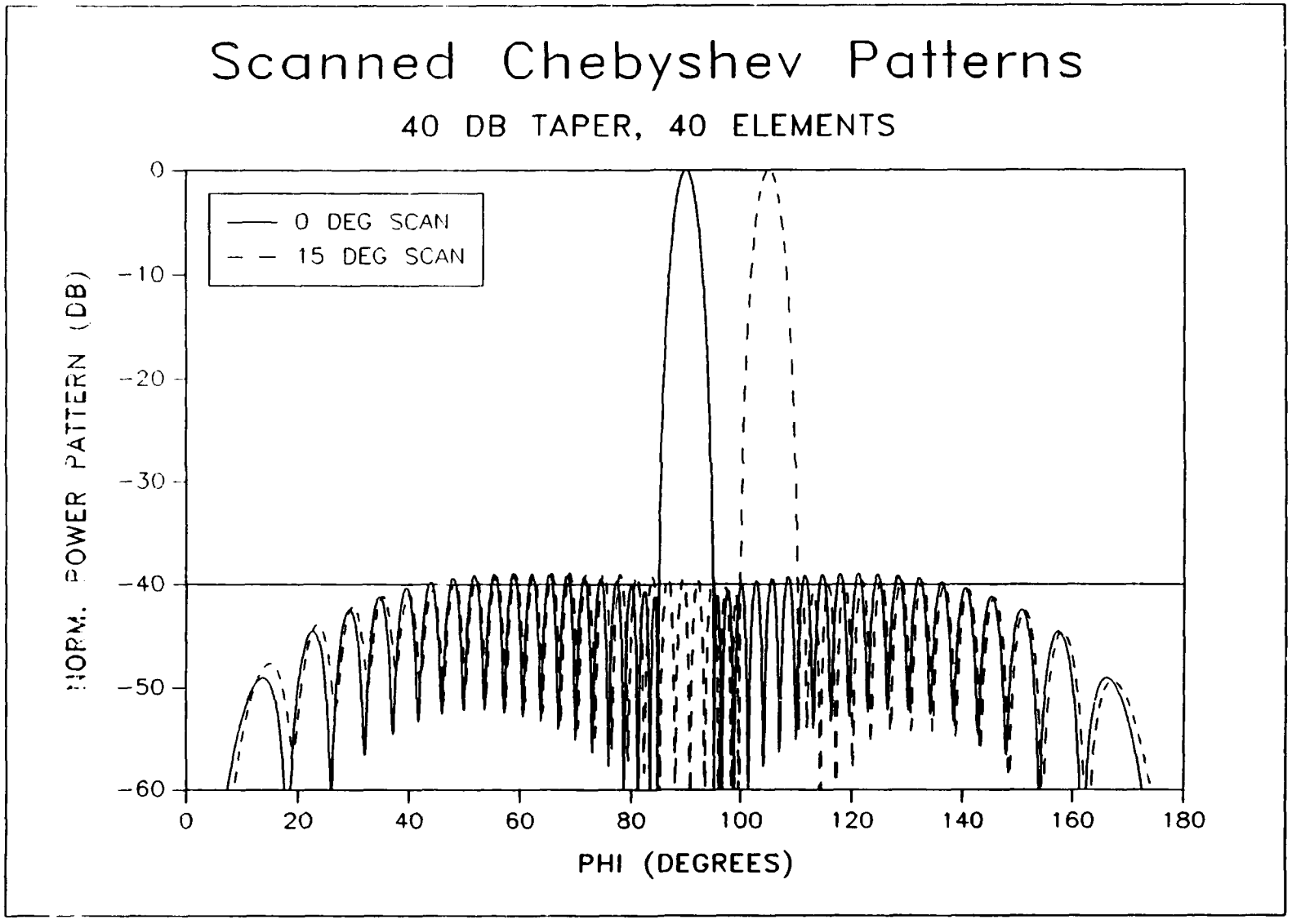
Scanned Chebyshev Patterns
40 DB TAPER, 40 ELEMENTS
0 DEG SCAN
15 DEG SCAN
NORM. POWER PATTERN (DB)
0
-10
-20
-30
-40
-50
-60
0
20
40
60
80
100
120
140
160
180
PHI (DEGREES)

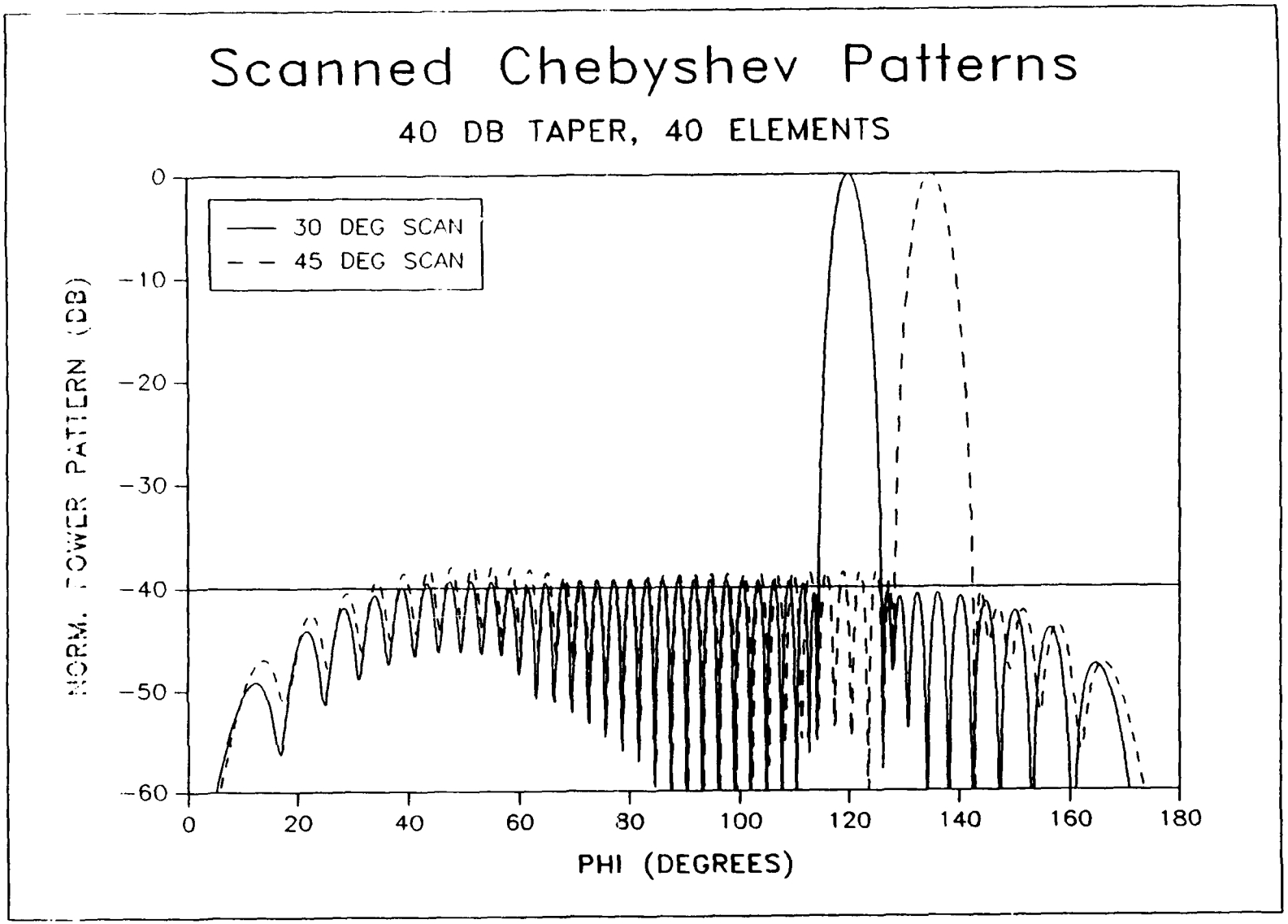
Scanned Chebyshev Patterns
40 DB TAPER, 40 ELEMENTS
30 DEG SCAN
45 DEG SCAN
NORM. POWER PATTERN (DB)
0
-10
-20
-30
-40
-50
-60
0
20
40
60
80
100
120
140
160
180
PHI (DEGREES)

APPENDIX C

COMPENSATION RESULTS: 10 ELEMENT ARRAY

20 ELEMENT ARRAY

40 ELEMENT ARRAY

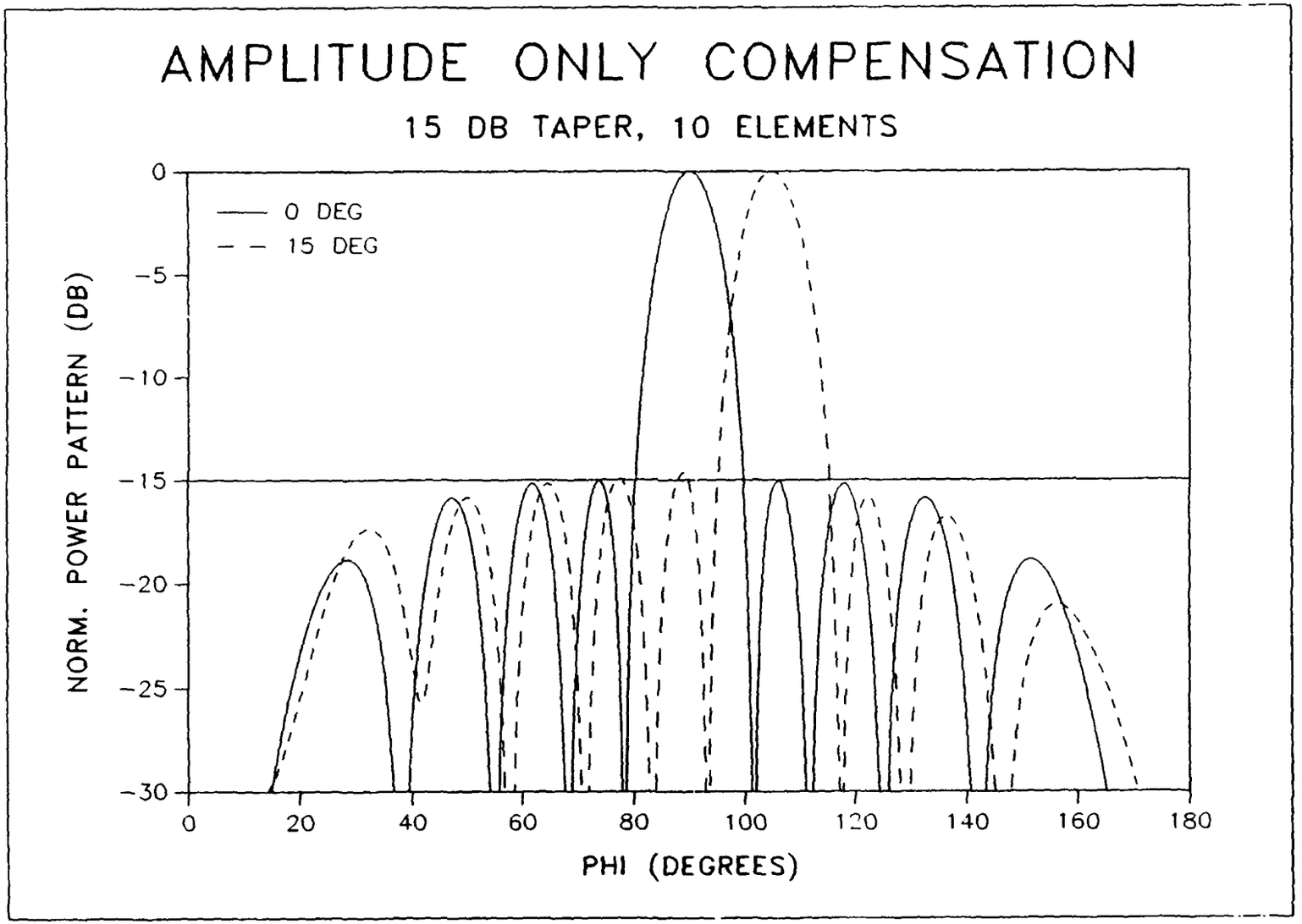
AMPLITUDE ONLY COMPENSATION
15 DB TAPER, 10 ELEMENTS
0 DEG
15 DEG
NORM. POWER PATTERN (DB)
0
-5
-10
-15
-20
-25
-30
0
20
40
60
80
100
120
140
160
180
PHI (DEGREES)

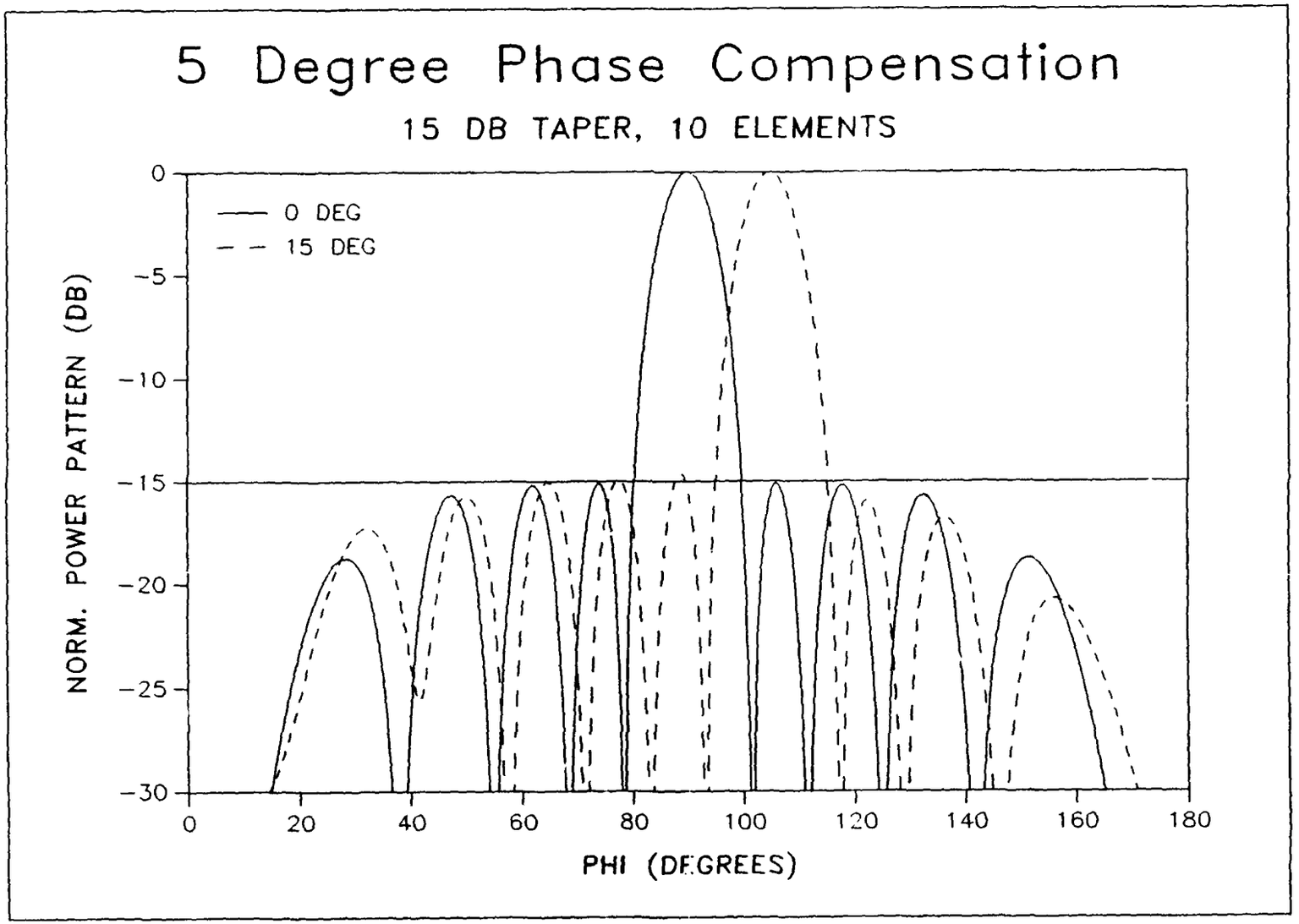
5 Degree Phase Compensation
15 DB TAPER, 10 ELEMENTS
0 DEG
15 DEG
NORM. POWER PATTERN (DB)
0
-5
-10
-15
-20
-25
-30
0
20
40
60
80
100
120
140
160
180
PHI (DEGREES)

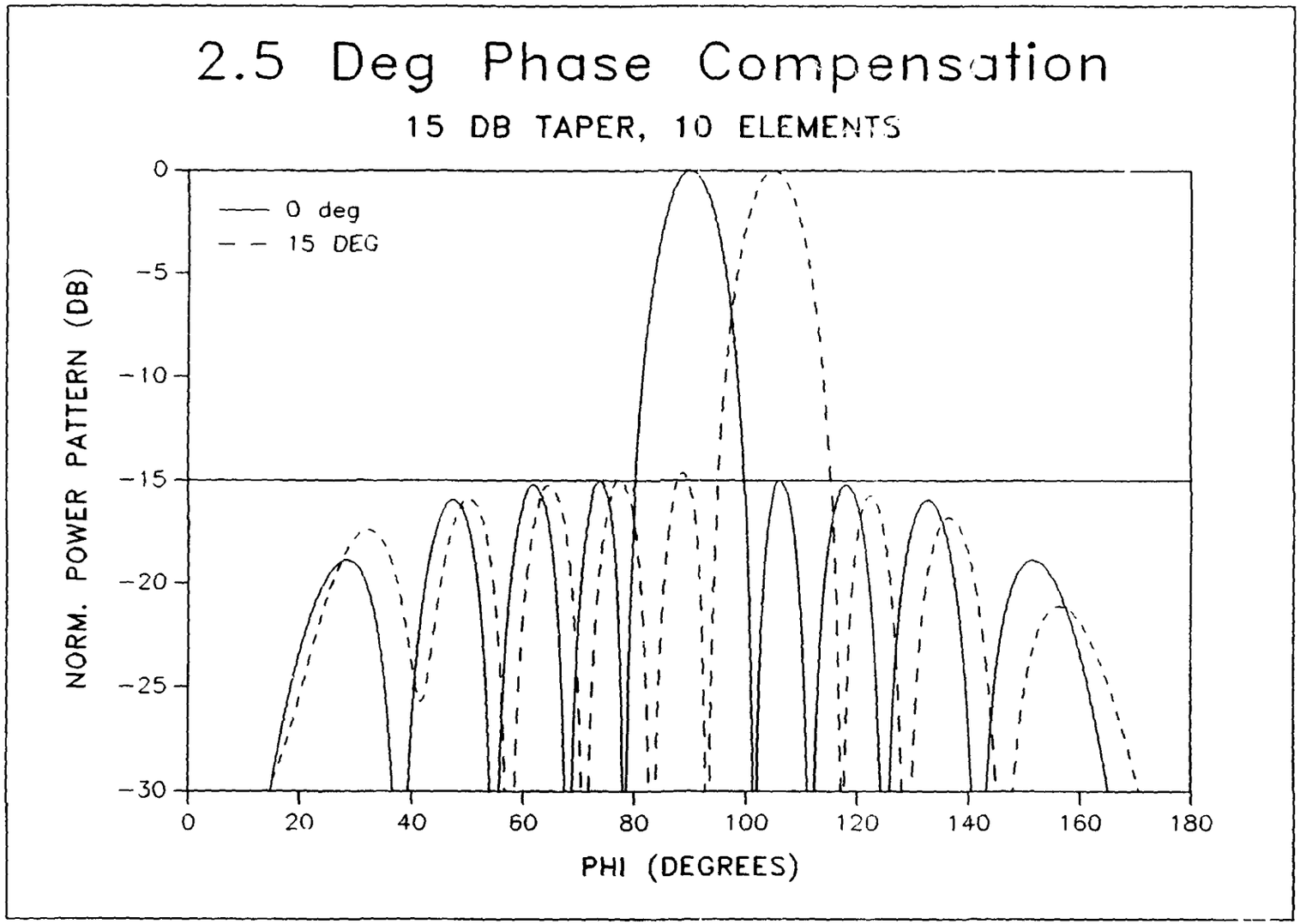
2.5 Deg Phase Compensation
15 DB TAPER, 10 ELEMENTS
0 deg
15 DEG
NORM. POWER PATTERN (DB)
0
-5
-10
-15
-20
-25
-30
0
20
40
60
80
100
120
140
160
180
PHI (DEGREES)

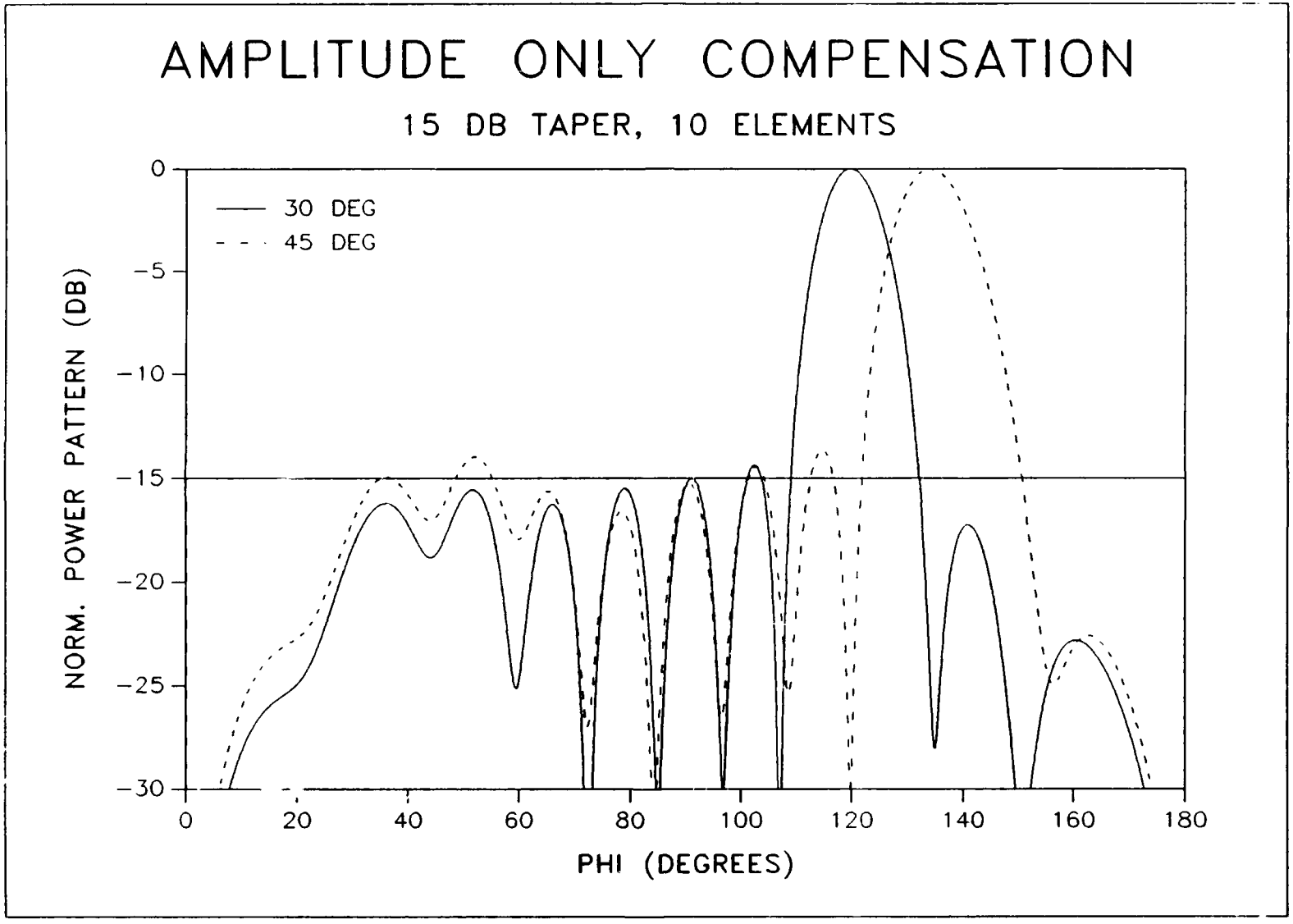
AMPLITUDE ONLY COMPENSATION
15 DB TAPER, 10 ELEMENTS
30 DEG
45 DEG
NORM. POWER PATTERN (DB)
0
-5
-10
-15
-20
-25
-30
0
20
40
60
80
100
120
140
160
180
PHI (DEGREES)

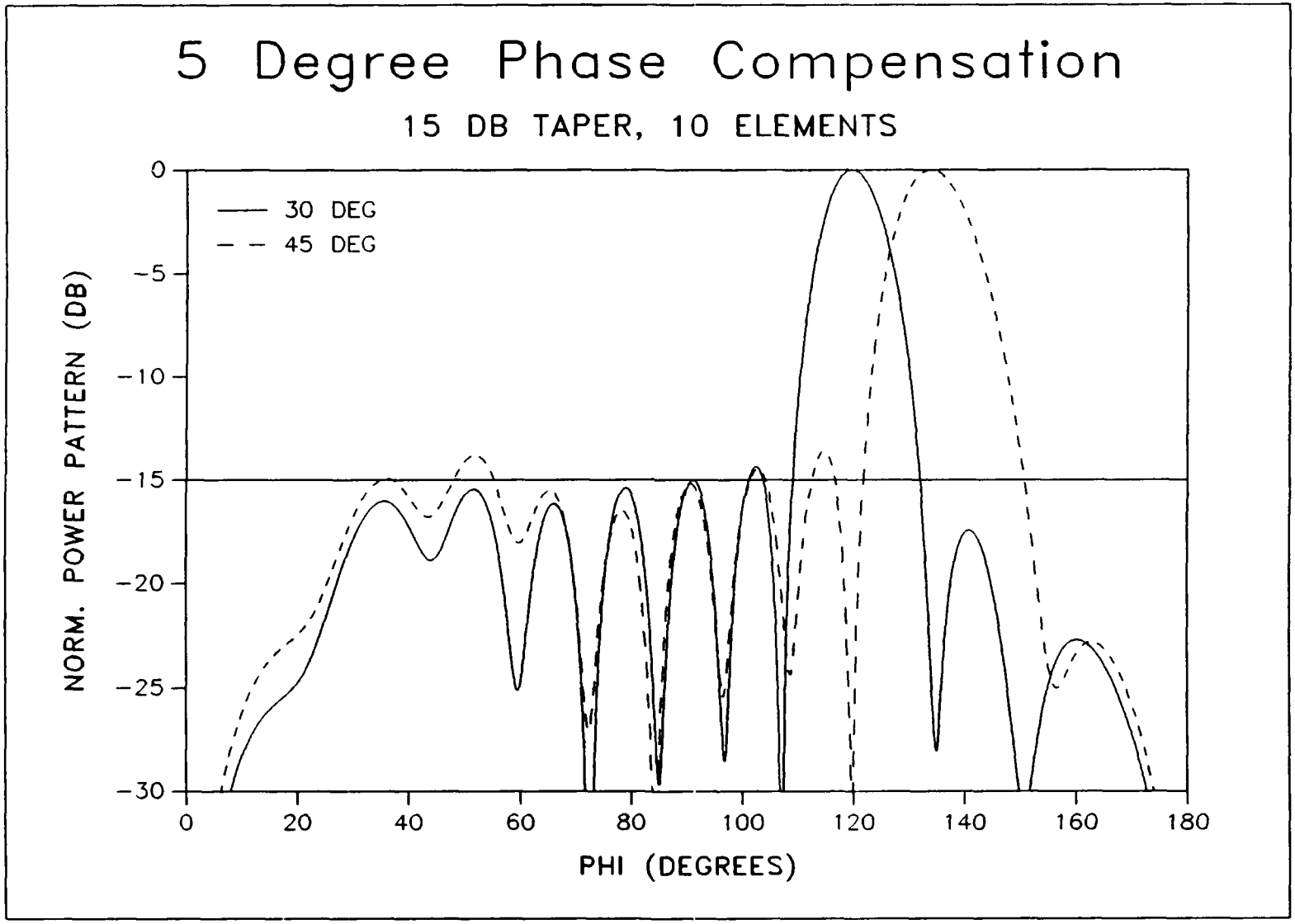
5 Degree Phase Compensation
15 DB TAPER, 10 ELEMENTS
30 DEG
45 DEG
NORM. POWER PATTERN (DB)
0
-5
-10
-15
-20
-25
-30
0
20
40
60
80
100
120
140
160
180
PHI (DEGREES)

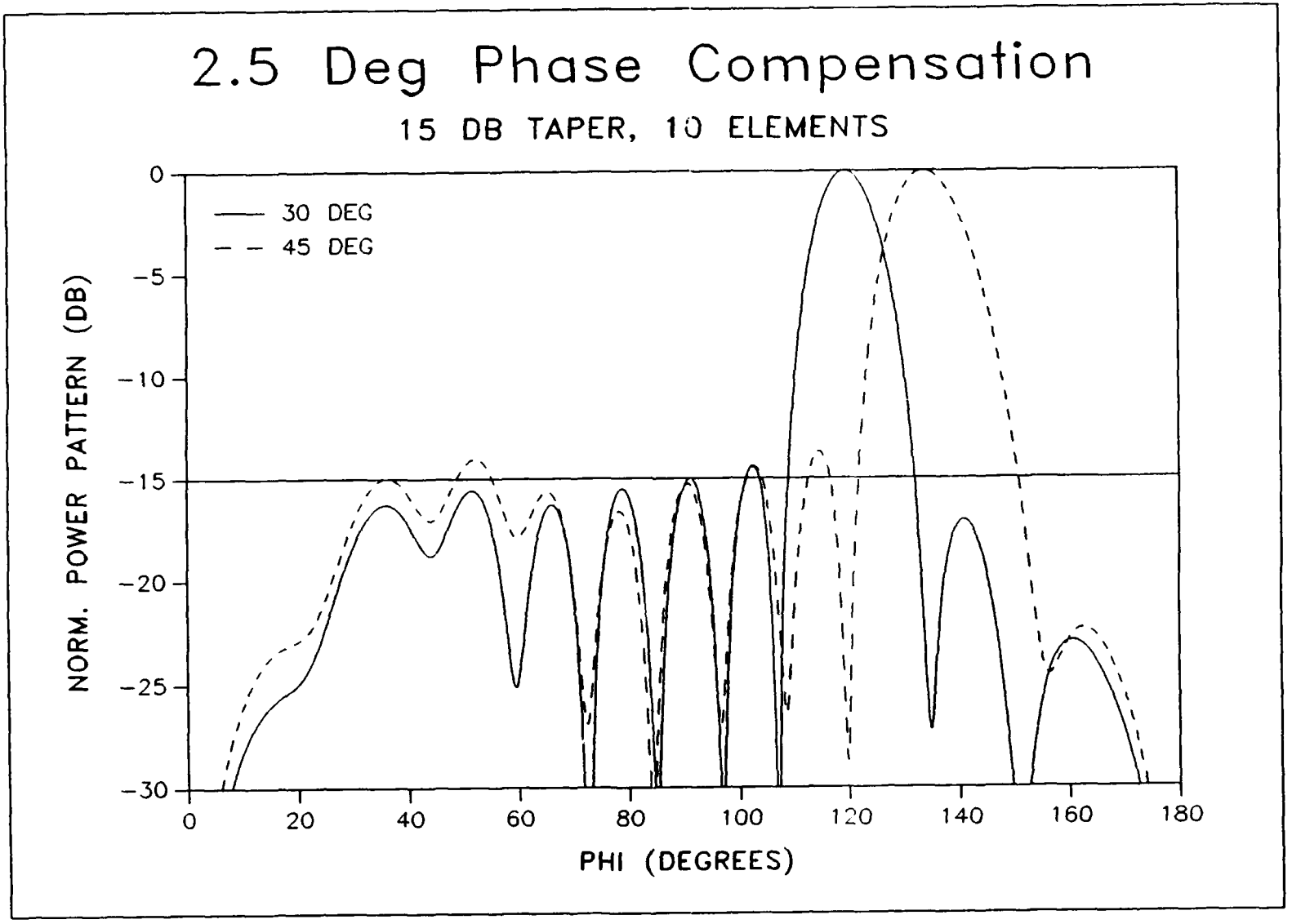
2.5 Deg Phase Compensation
15 DB TAPER, 10 ELEMENTS
30 DEG
45 DEG
NORM. POWER PATTERN (DB)
0
-5
-10
-15
-20
-25
-30
0
20
40
60
80
100
120
140
160
180
PHI (DEGREES)

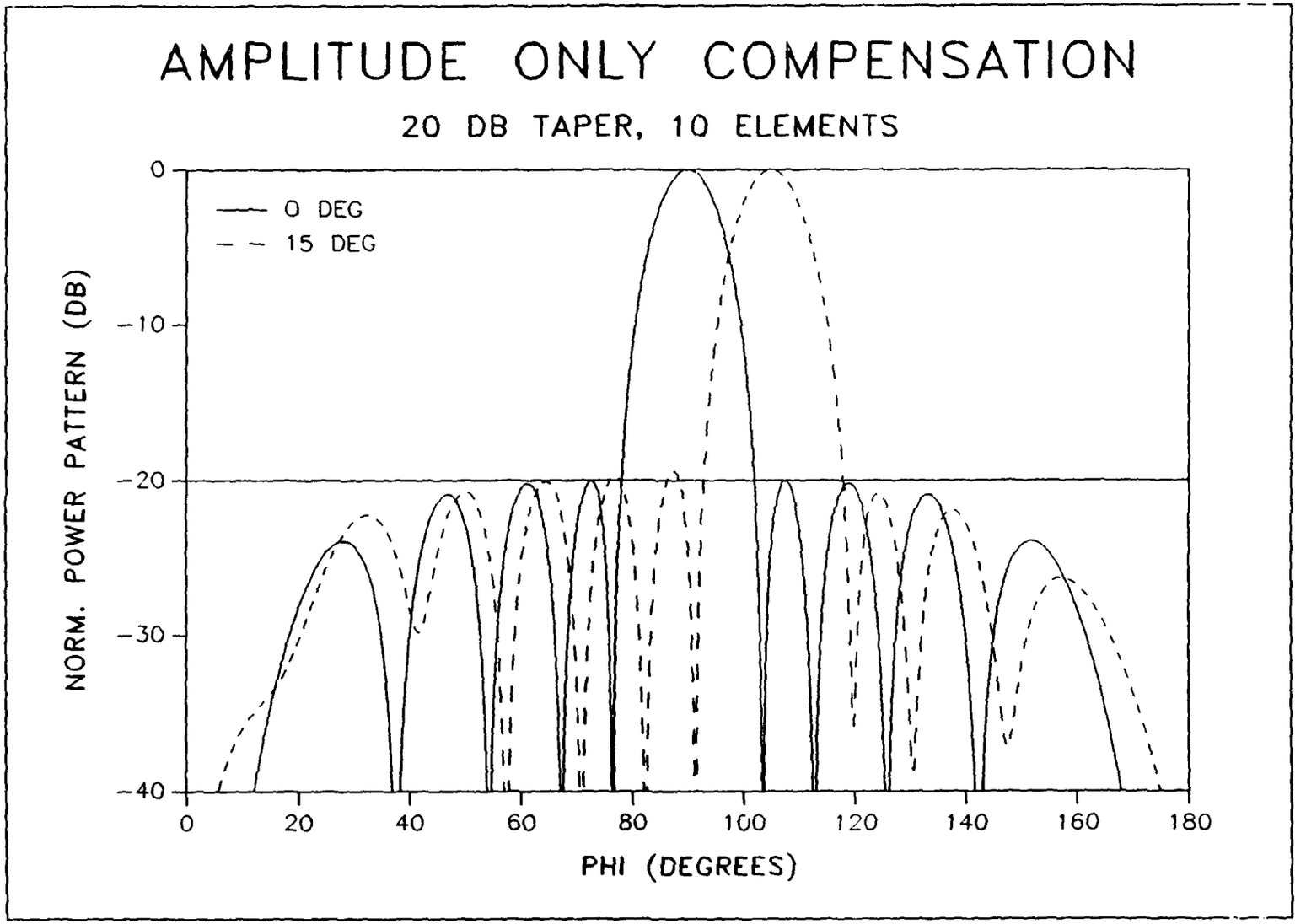
AMPLITUDE ONLY COMPENSATION
20 DB TAPER, 10 ELEMENTS
0 DEG
15 DEG
NORM. POWER PATTERN (DB)
0
-10
-20
-30
-40
0
20
40
60
80
100
120
140
160
180
PHI (DEGREES)

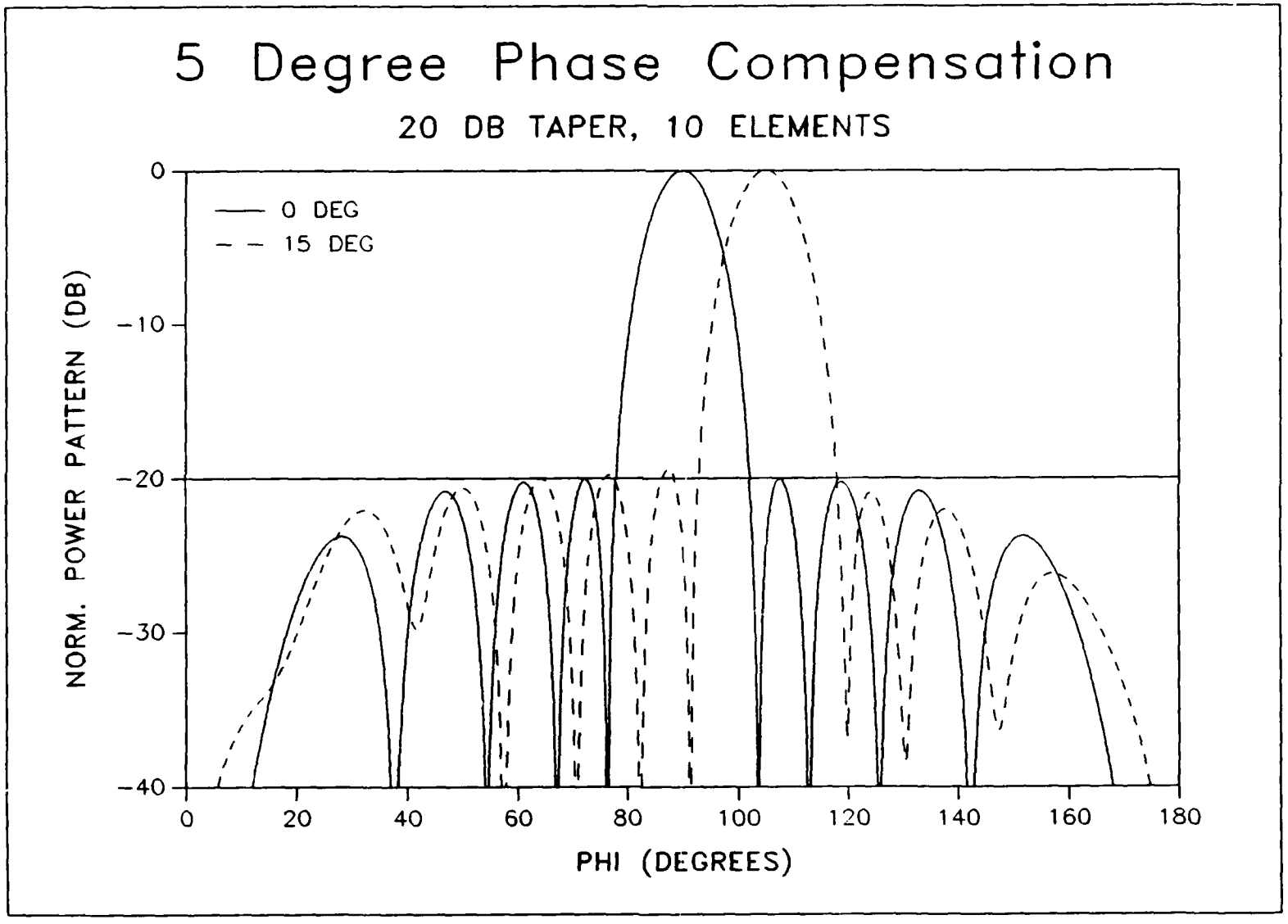
5 Degree Phase Compensation
20 DB TAPER, 10 ELEMENTS
0 DEG
15 DEG
NORM. POWER PATTERN (DB)
0
-10
-20
-30
-40
0
20
40
60
80
100
120
140
160
180
PHI (DEGREES)

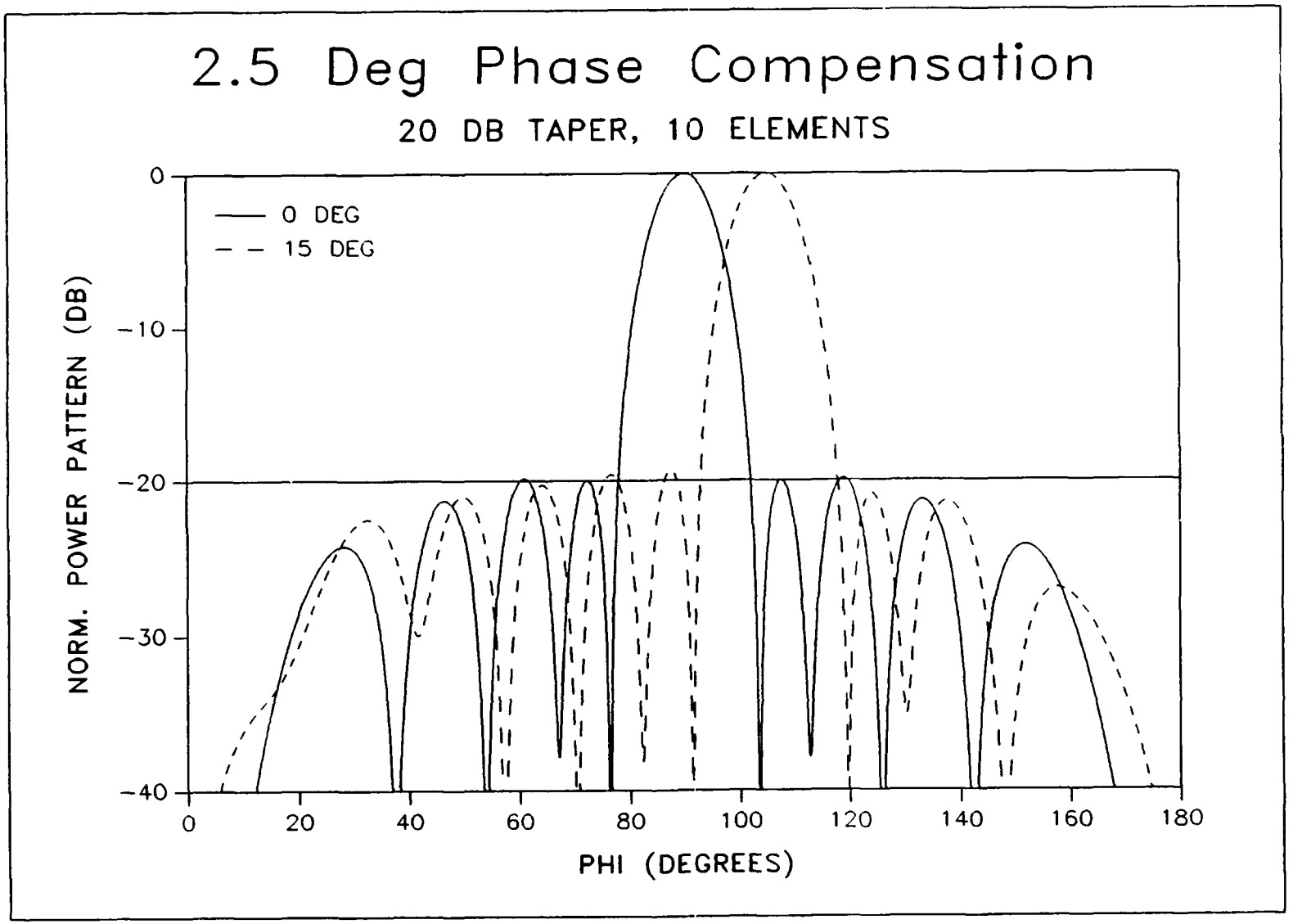
2.5 Deg Phase Compensation
20 DB TAPER, 10 ELEMENTS
0 DEG
15 DEG
NORM. POWER PATTERN (DB)
0
-10
-20
-30
-40
0
20
40
60
80
100
120
140
160
180
PHI (DEGREES)

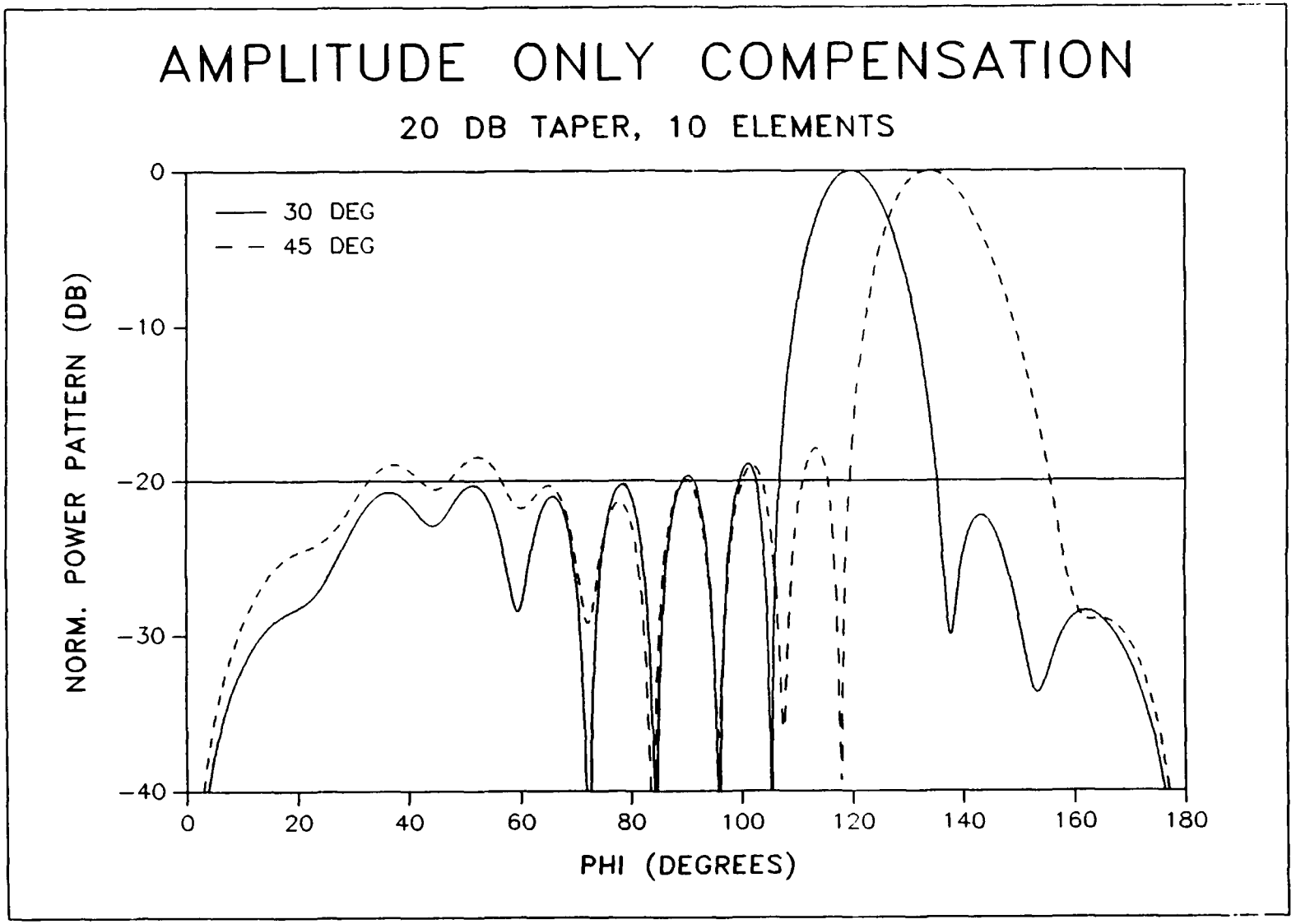
AMPLITUDE ONLY COMPENSATION
20 DB TAPER, 10 ELEMENTS
30 DEG
45 DEG
NORM. POWER PATTERN (DB)
0
-10
-20
-30
-40
0
20
40
60
80
100
120
140
160
180
PHI (DEGREES)

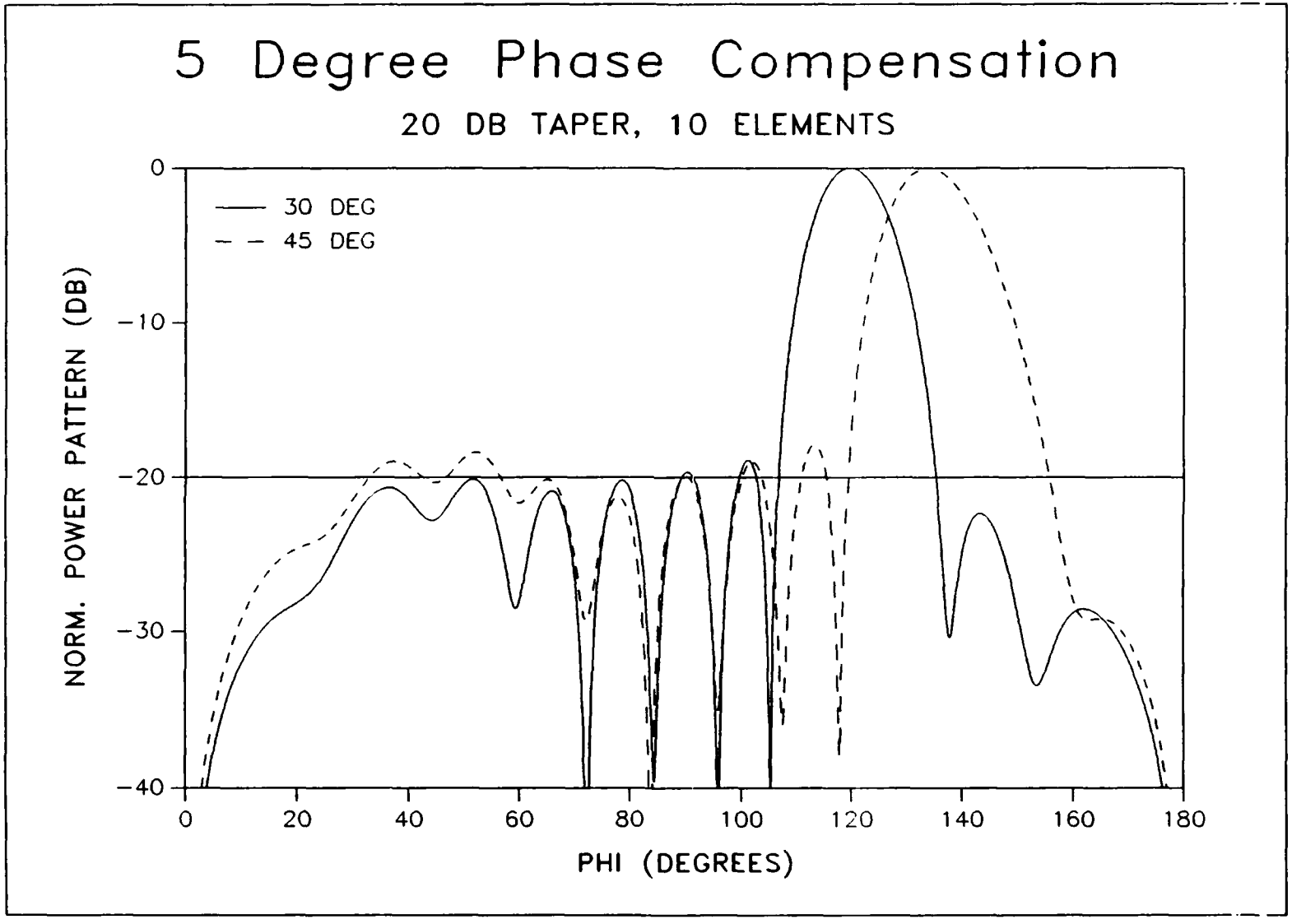
5 Degree Phase Compensation
20 DB TAPER, 10 ELEMENTS
30 DEG
45 DEG
NORM. POWER PATTERN (DB)
0
-10
-20
-30
-40
0
20
40
60
80
100
120
140
160
180
PHI (DEGREES)

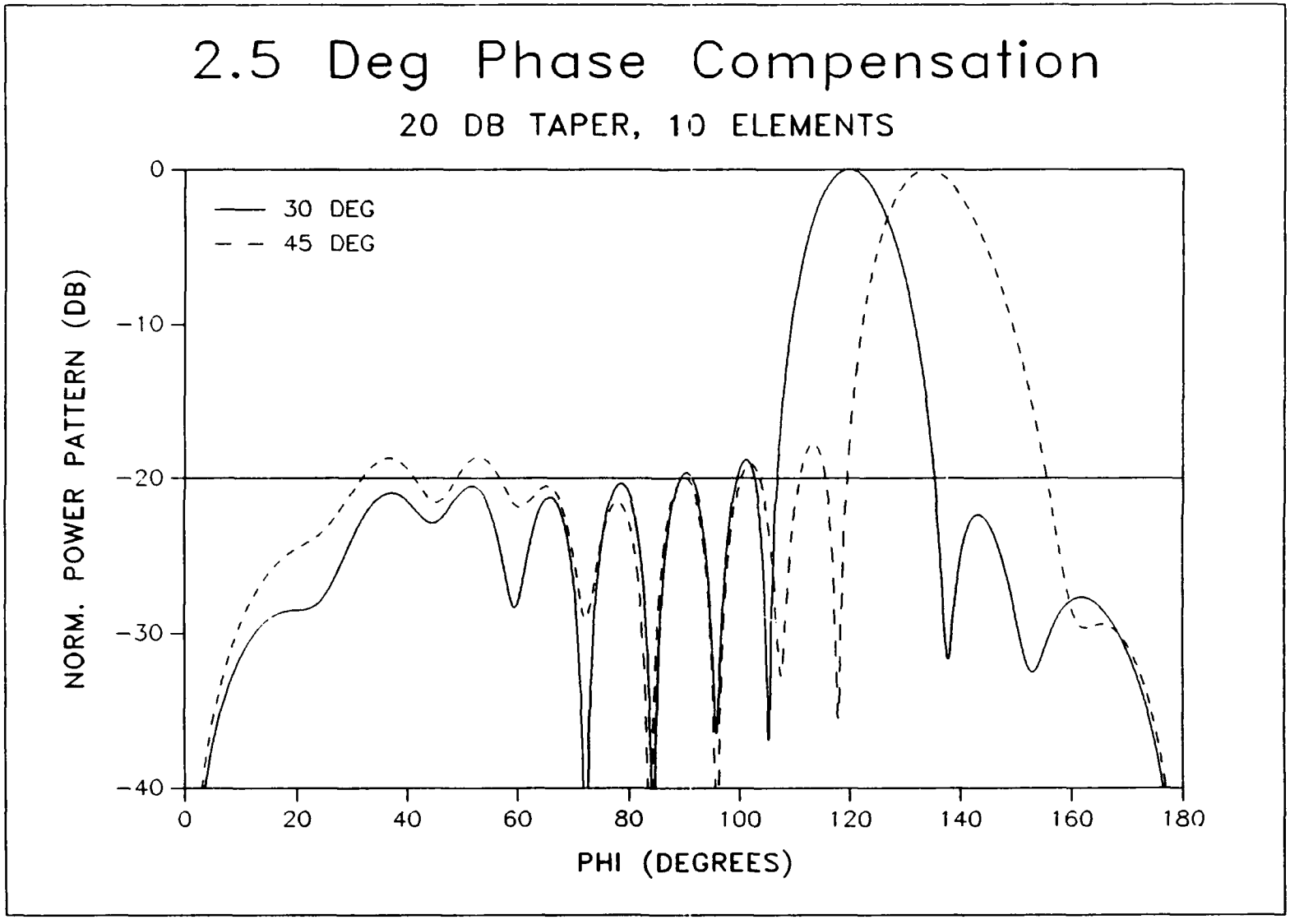
2.5 Deg Phase Compensation
20 DB TAPER, 10 ELEMENTS
30 DEG
45 DEG
NORM. POWER PATTERN (DB)
0
-10
-20
-30
-40
0
20
40
60
80
100
120
140
160
180
PHI (DEGREES)

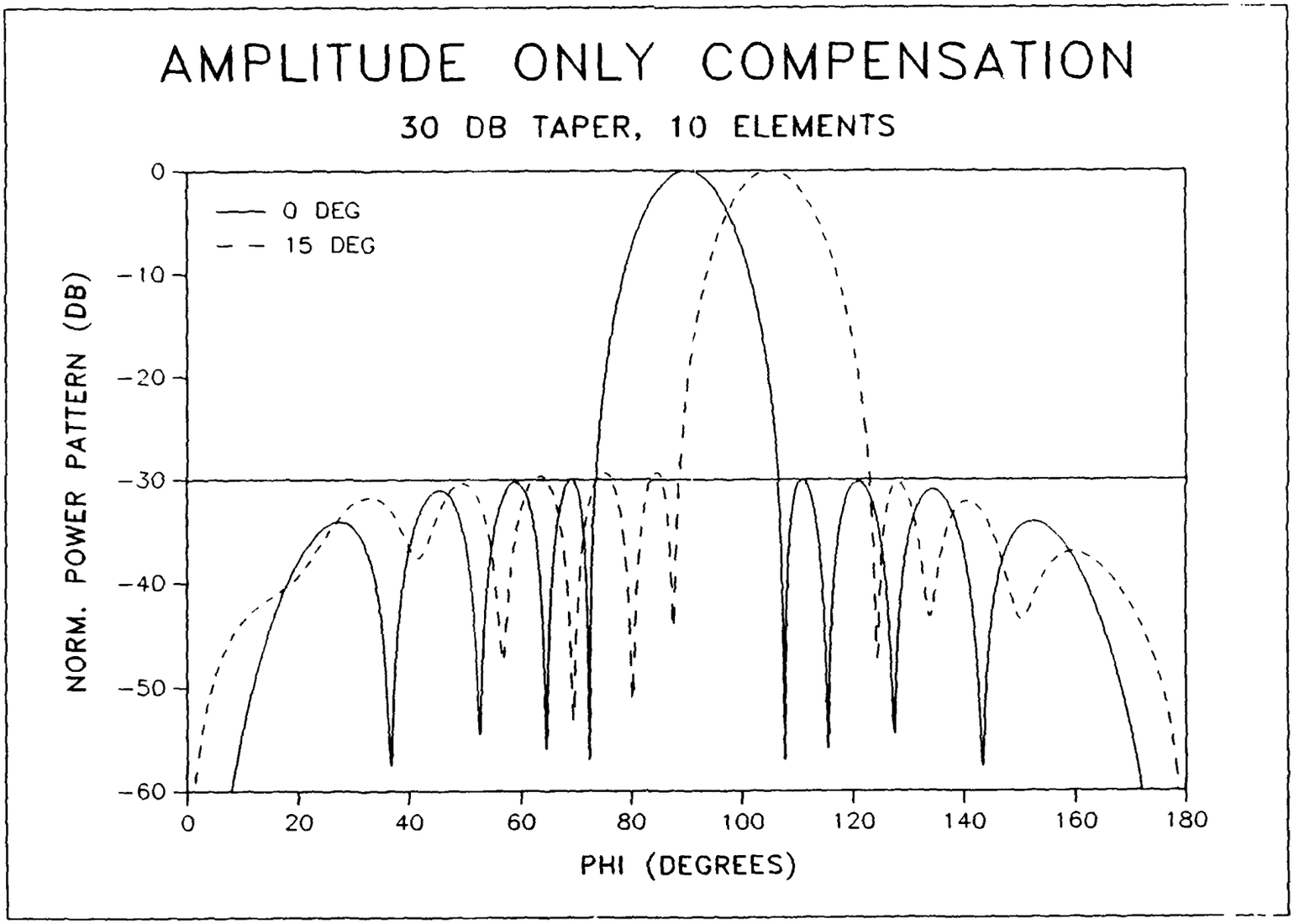
AMPLITUDE ONLY COMPENSATION
30 DB TAPER, 10 ELEMENTS
0 DEG
15 DEG
NORM. POWER PATTERN (DB)
0
-10
-20
-30
-40
-50
-60
0
20
40
60
80
100
120
140
160
180
PHI (DEGREES)

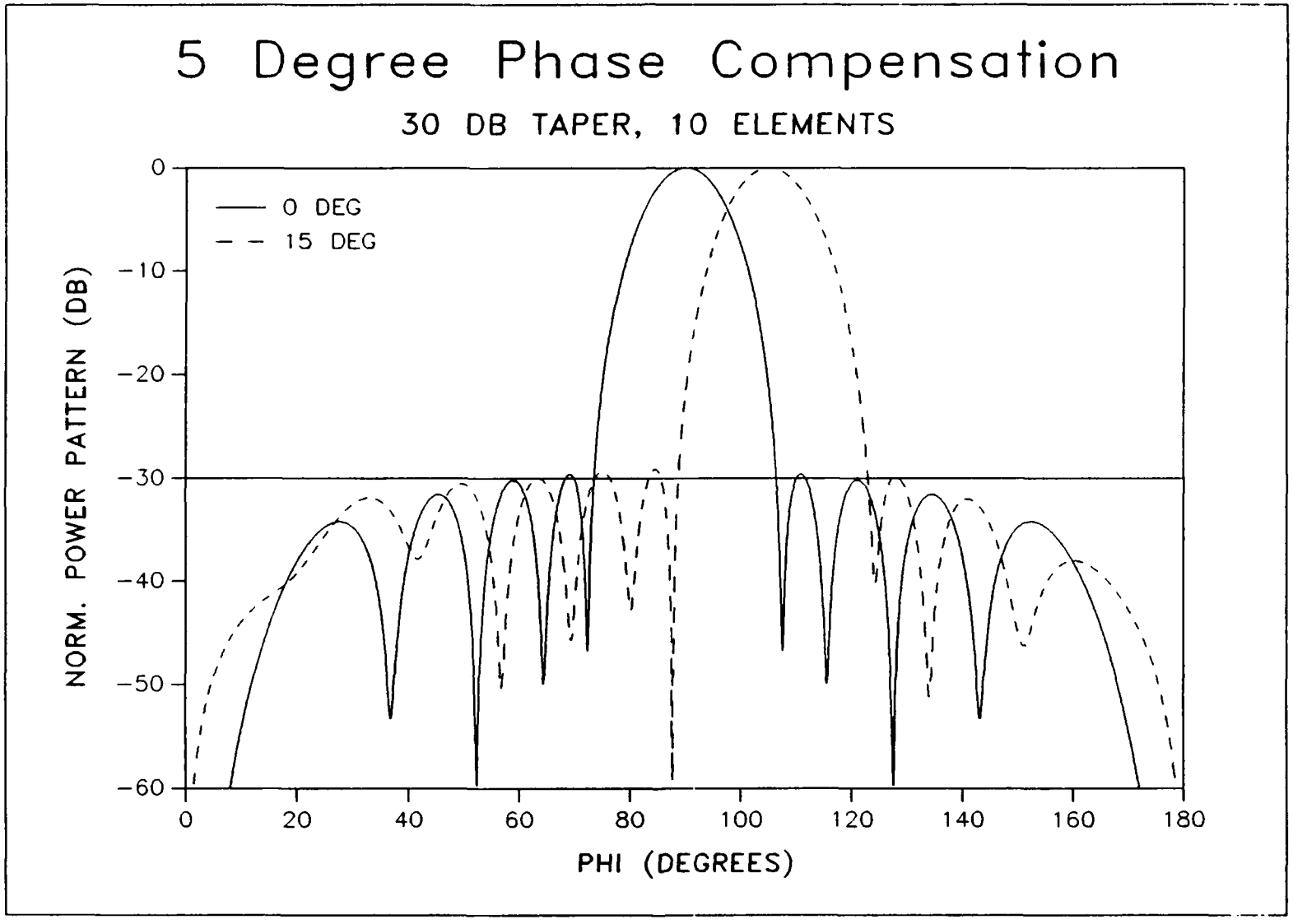
5 Degree Phase Compensation
30 DB TAPER, 10 ELEMENTS
0 DEG
15 DEG
NORM. POWER PATTERN (DB)
0
-10
-20
-30
-40
-50
-60
0
20
40
60
80
100
120
140
160
180
PHI (DEGREES)

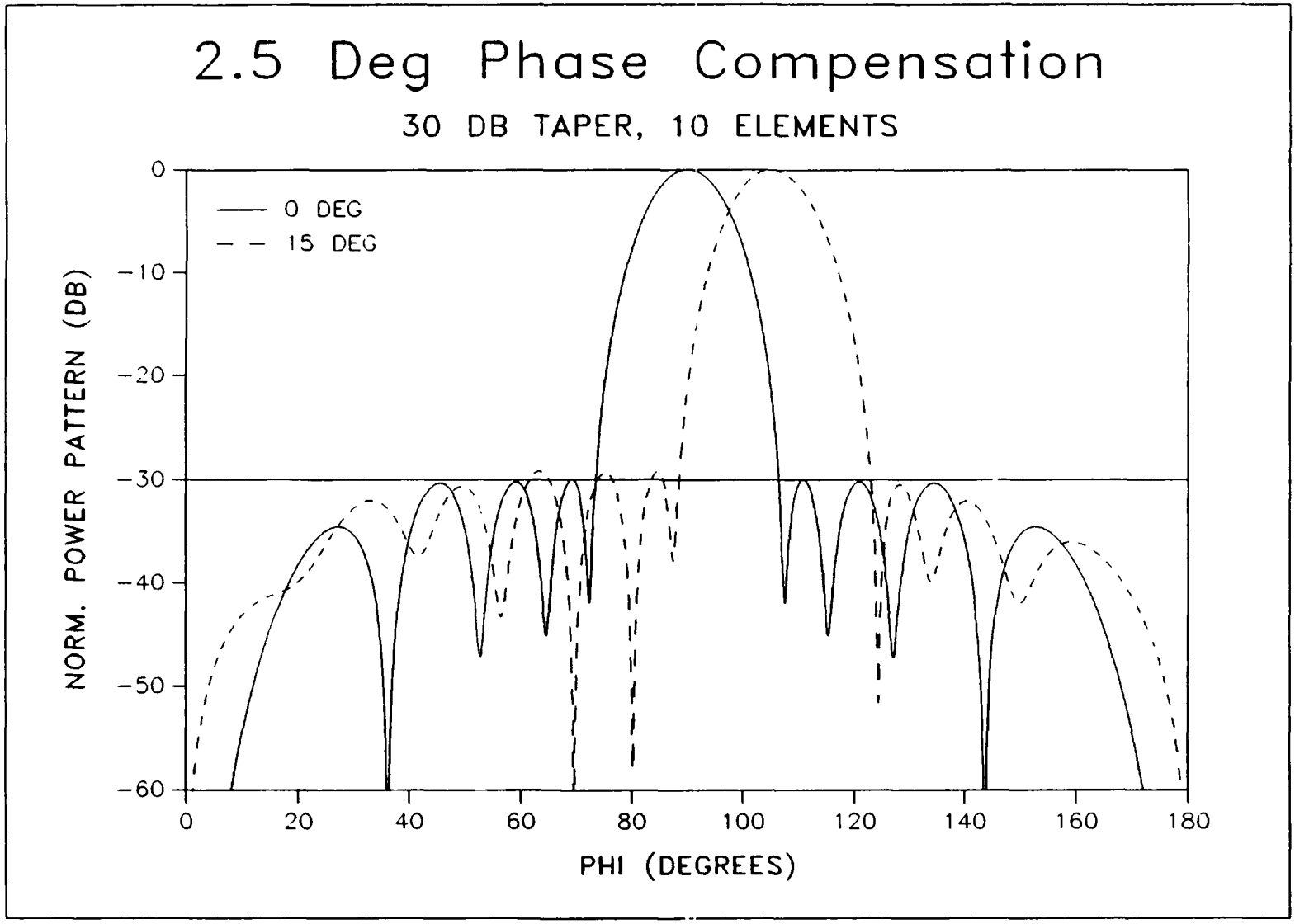
2.5 Deg Phase Compensation
30 DB TAPER, 10 ELEMENTS
0 DEG
15 DEG
NORM. POWER PATTERN (DB)
0
-10
-20
-30
-40
-50
-60
0
20
40
60
80
100
120
140
160
180
PHI (DEGREES)

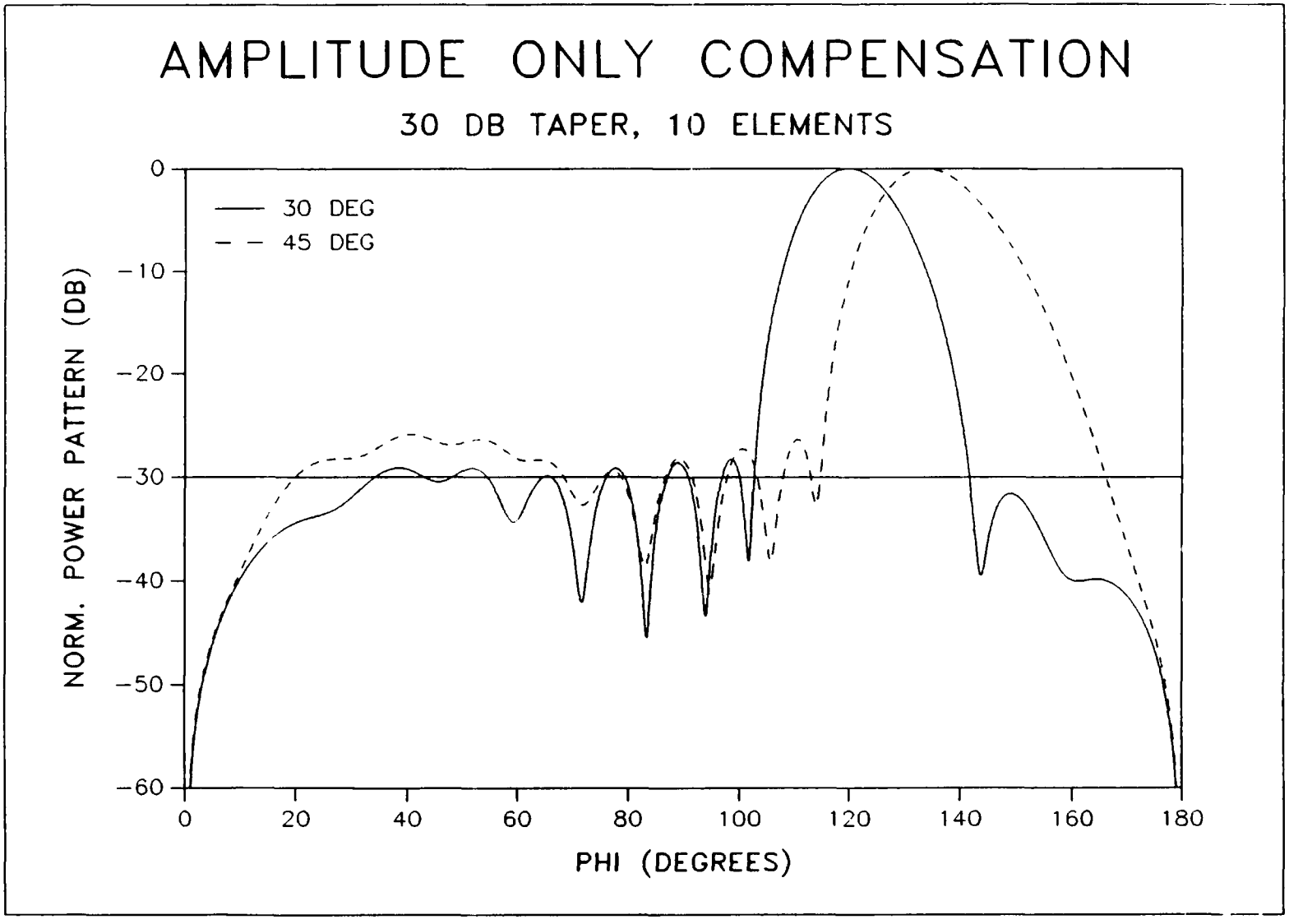
AMPLITUDE ONLY COMPENSATION
30 DB TAPER, 10 ELEMENTS
30 DEG
45 DEG
NORM. POWER PATTERN (DB)
0
-10
-20
-30
-40
-50
-60
0
20
40
60
80
100
120
140
160
180
PHI (DEGREES)

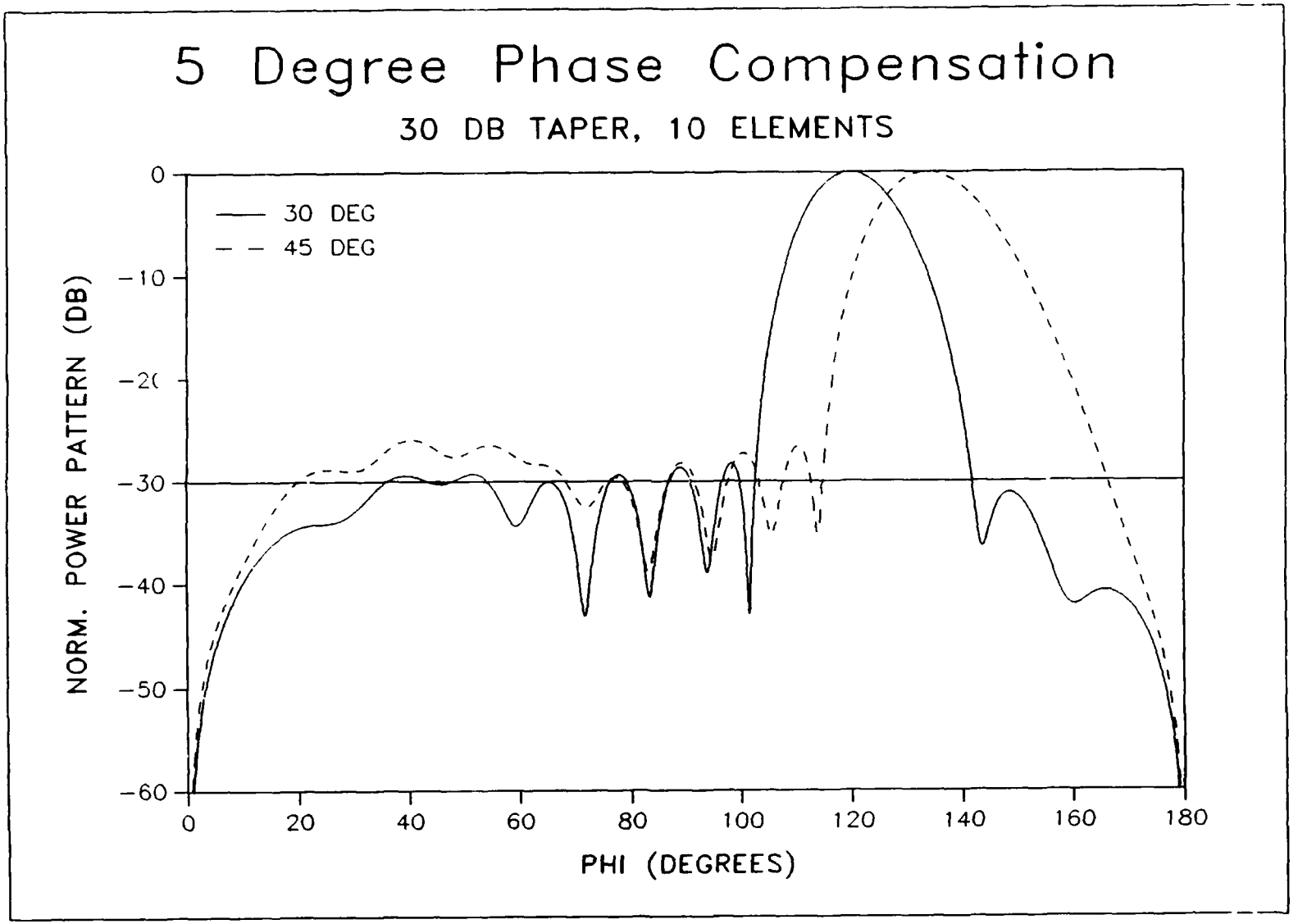
5 Degree Phase Compensation
30 DB TAPER, 10 ELEMENTS
30 DEG
45 DEG
NORM. POWER PATTERN (DB)
0
-10
-20
-30
-40
-50
-60
0
20
40
60
80
100
120
140
160
180
PHI (DEGREES)

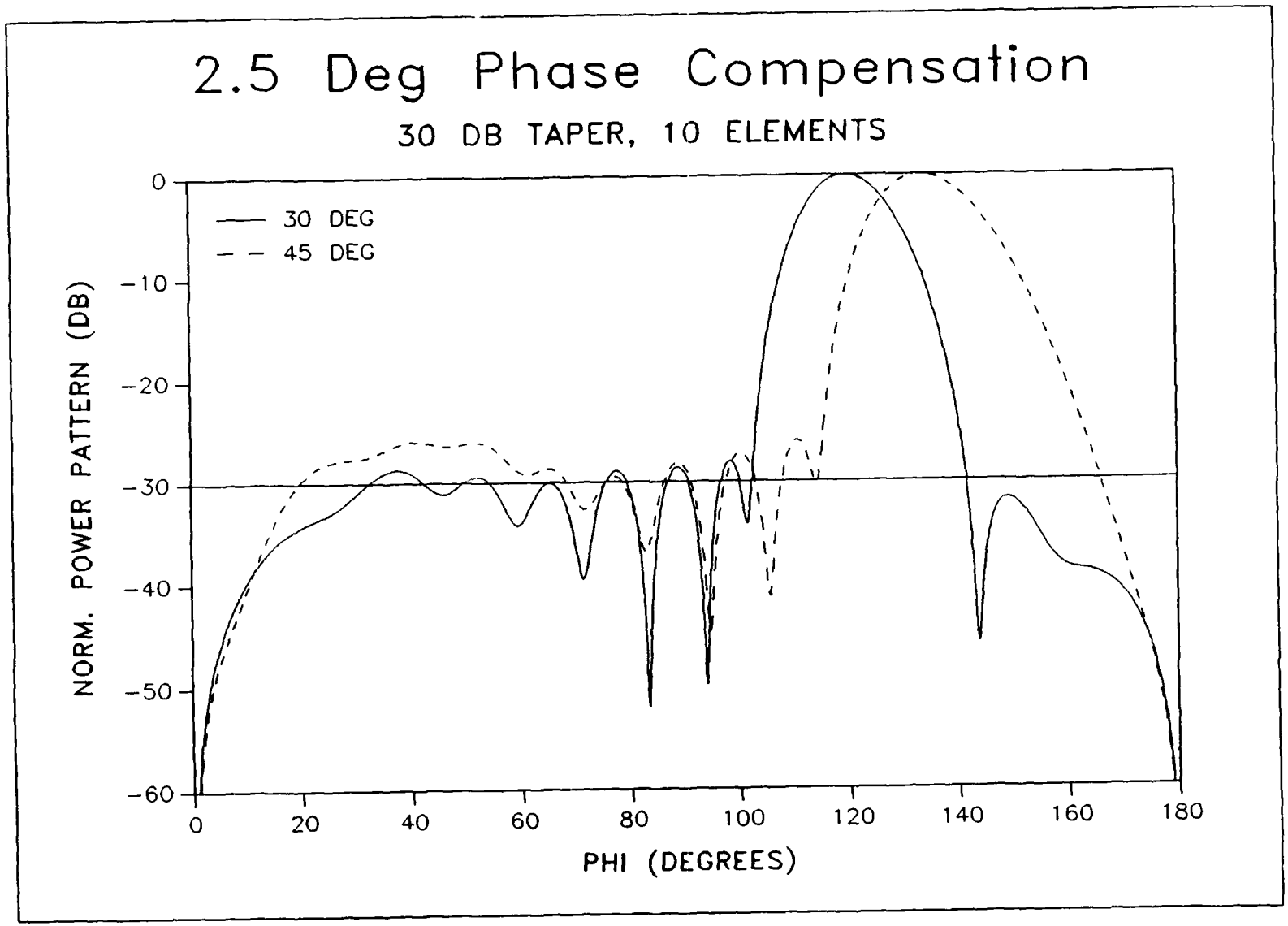
2.5 Deg Phase Compensation
30 DB TAPER, 10 ELEMENTS
30 DEG
45 DEG
NORM. POWER PATTERN (DB)
0
-10
-20
-30
-40
-50
-60
0
20
40
60
80
100
120
140
160
180
PHI (DEGREES)

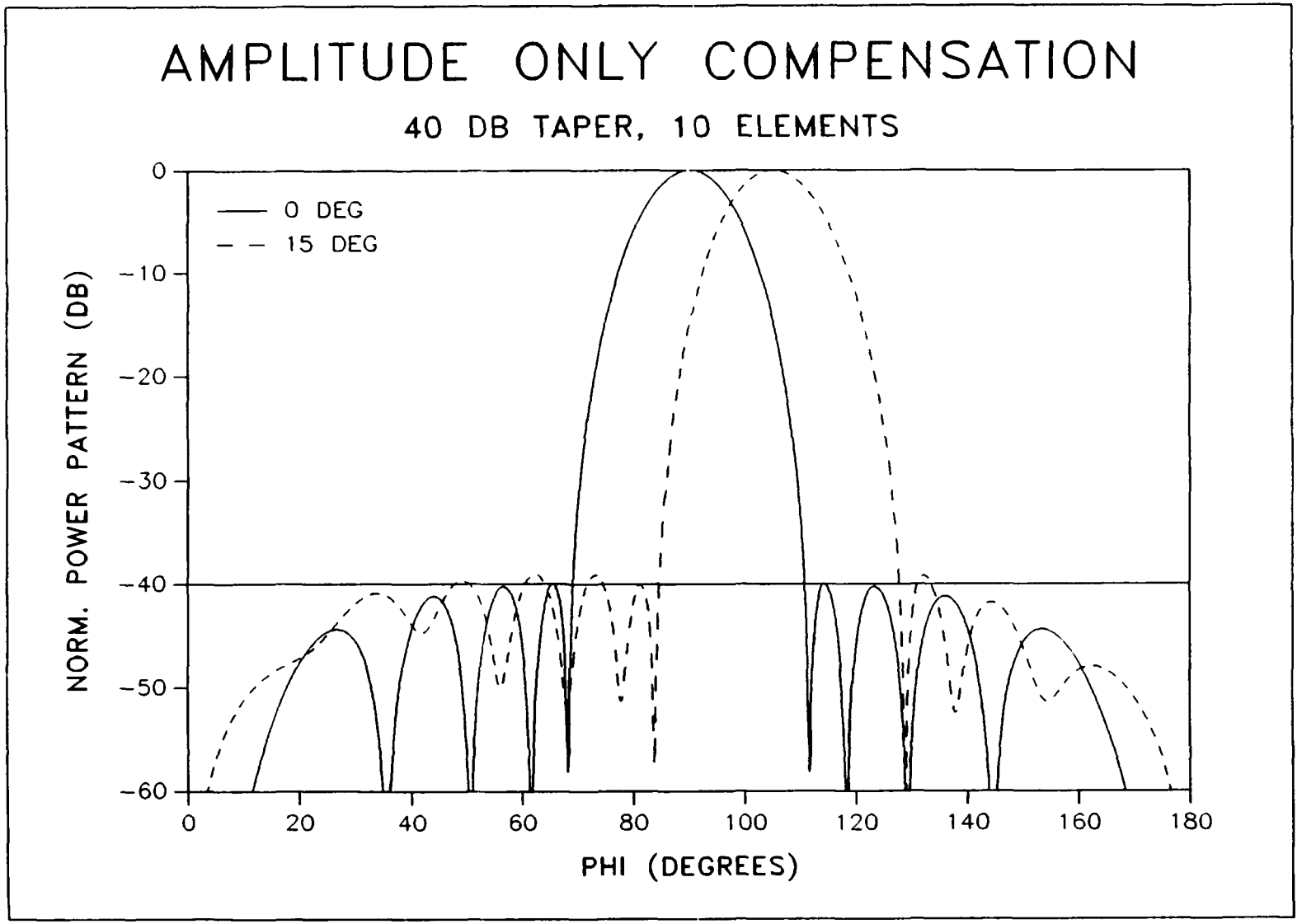
AMPLITUDE ONLY COMPENSATION
40 DB TAPER, 10 ELEMENTS
0 DEG
15 DEG
NORM. POWER PATTERN (DB)
0
-10
-20
-30
-40
-50
-60
0
20
40
60
80
100
120
140
160
180
PHI (DEGREES)

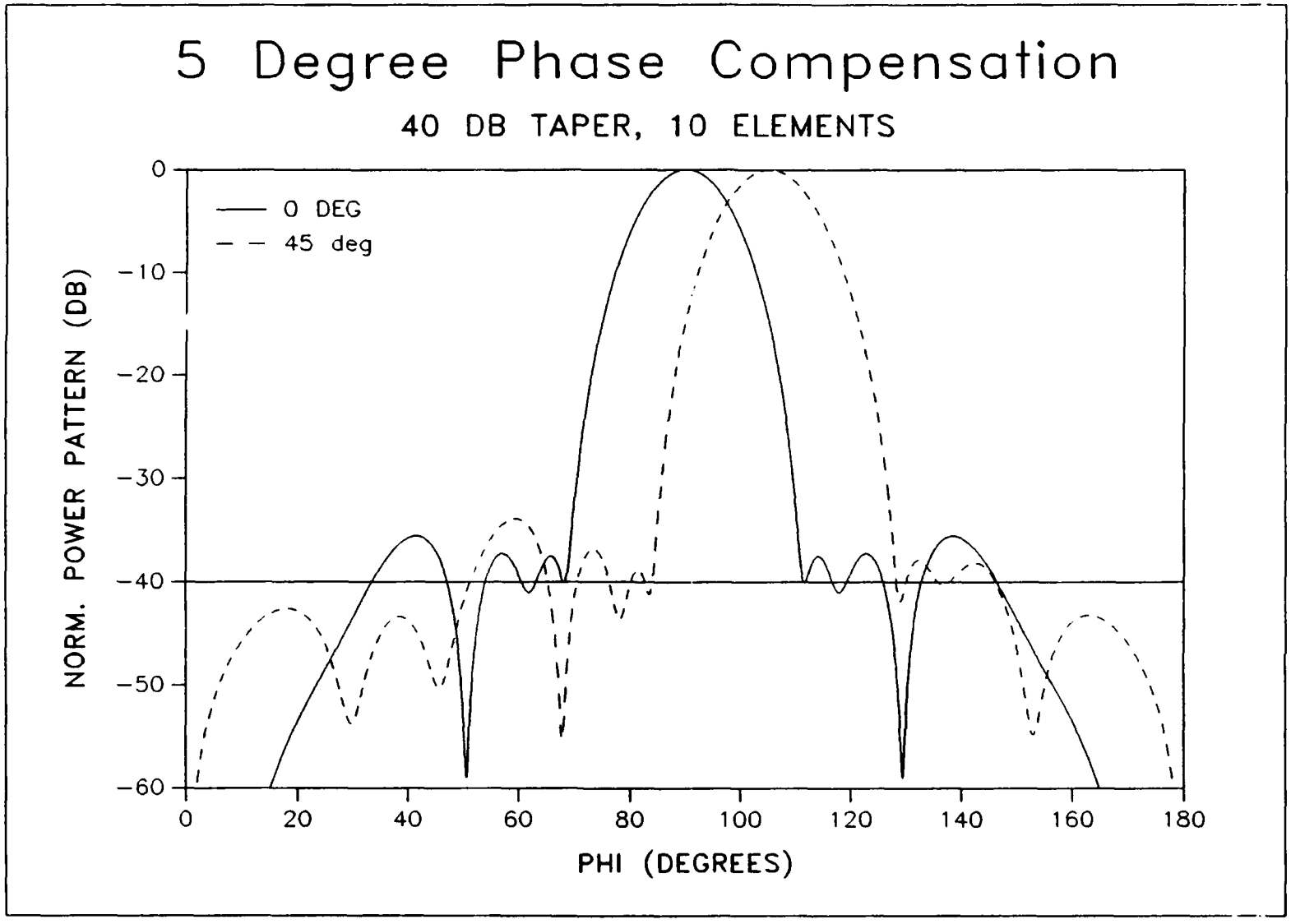
5 Degree Phase Compensation
40 DB TAPER, 10 ELEMENTS
0 DEG
45 deg
NORM. POWER PATTERN (DB)
0
-10
-20
-30
-40
-50
-60
0
20
40
60
80
100
120
140
160
180
PHI (DEGREES)

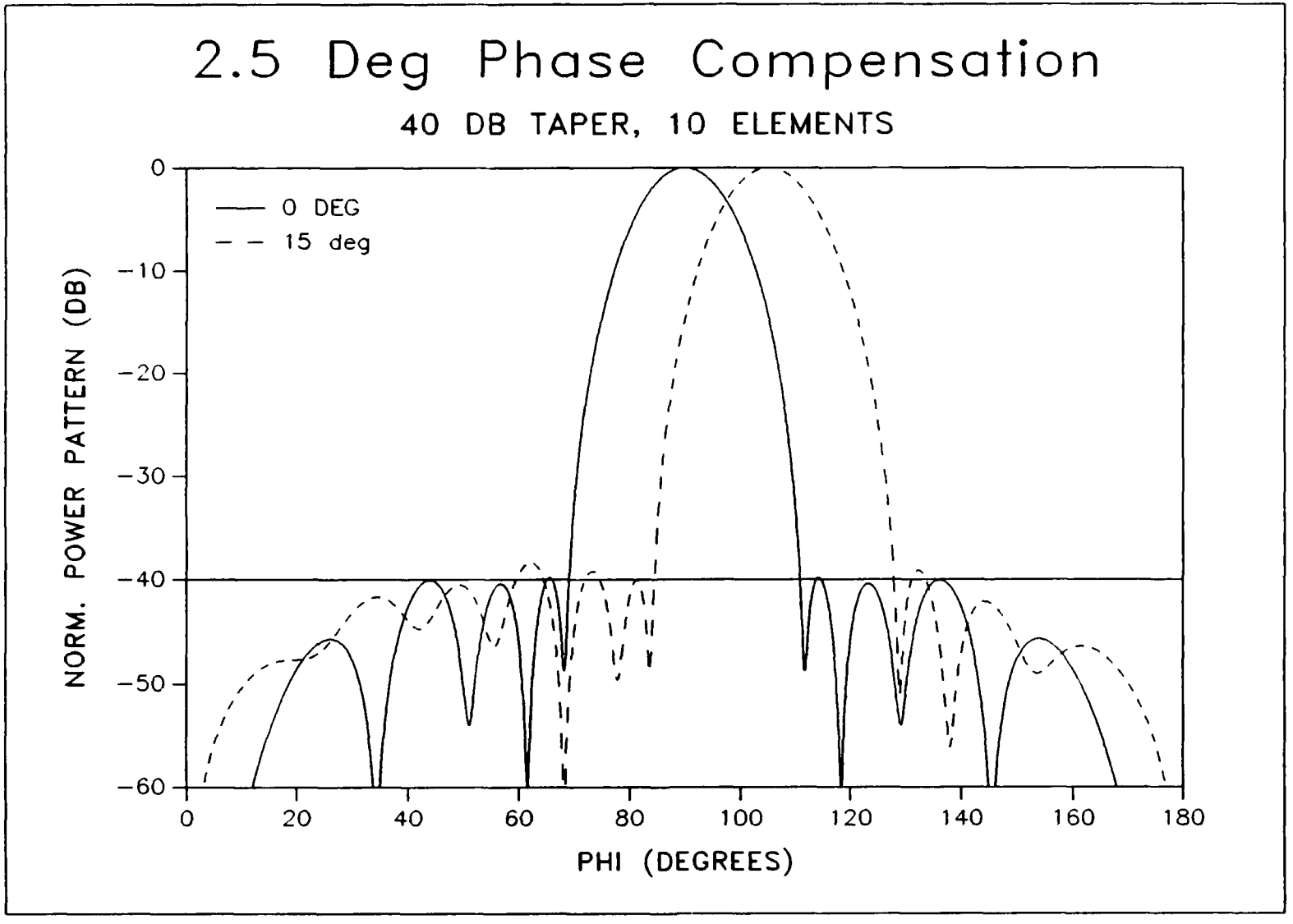
2.5 Deg Phase Compensation
40 DB TAPER, 10 ELEMENTS
0 DEG
15 deg
NORM. POWER PATTERN (DB)
0
-10
-20
-30
-40
-50
-60
0
20
40
60
80
100
120
140
160
180
PHI (DEGREES)

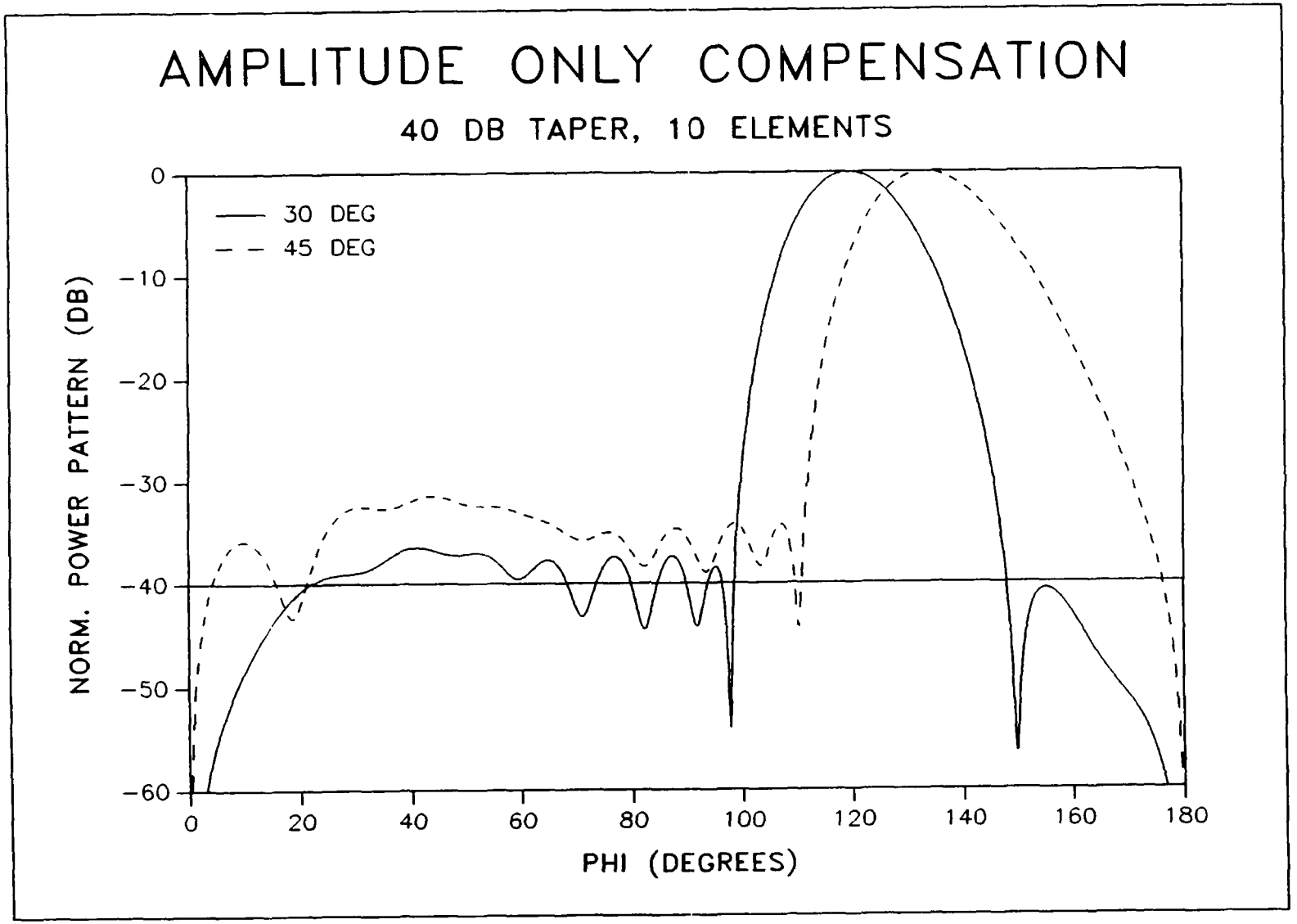
AMPLITUDE ONLY COMPENSATION
40 DB TAPER, 10 ELEMENTS
30 DEG
45 DEG
NORM. POWER PATTERN (DB)
0
-10
-20
-30
-40
-50
-60
0
20
40
60
80
100
120
140
160
180
PHI (DEGREES)

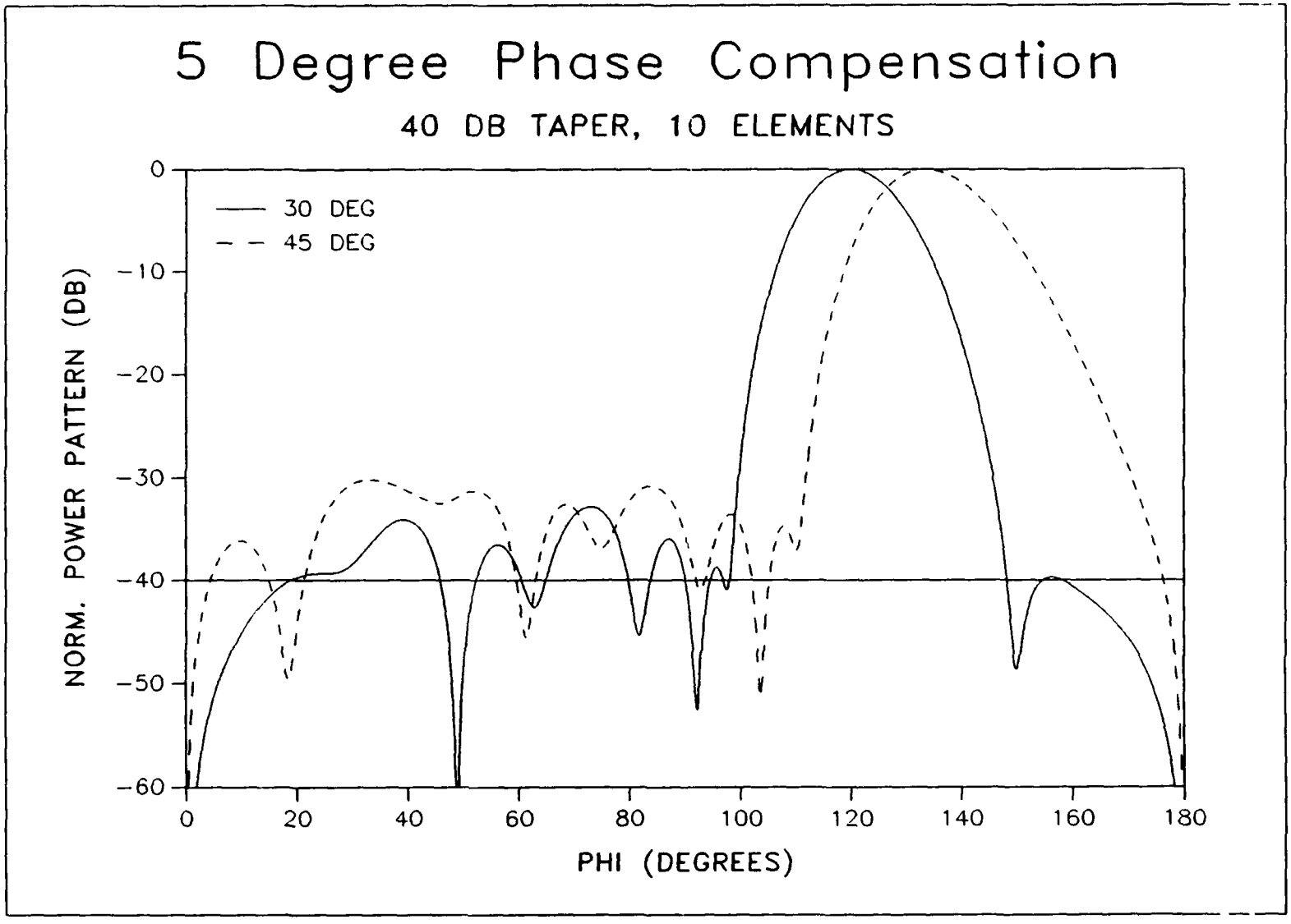
5 Degree Phase Compensation
40 DB TAPER, 10 ELEMENTS
30 DEG
45 DEG
NORM. POWER PATTERN (DB)
0
-10
-20
-30
-40
-50
-60
0
20
40
60
80
100
120
140
160
180
PHI (DEGREES)

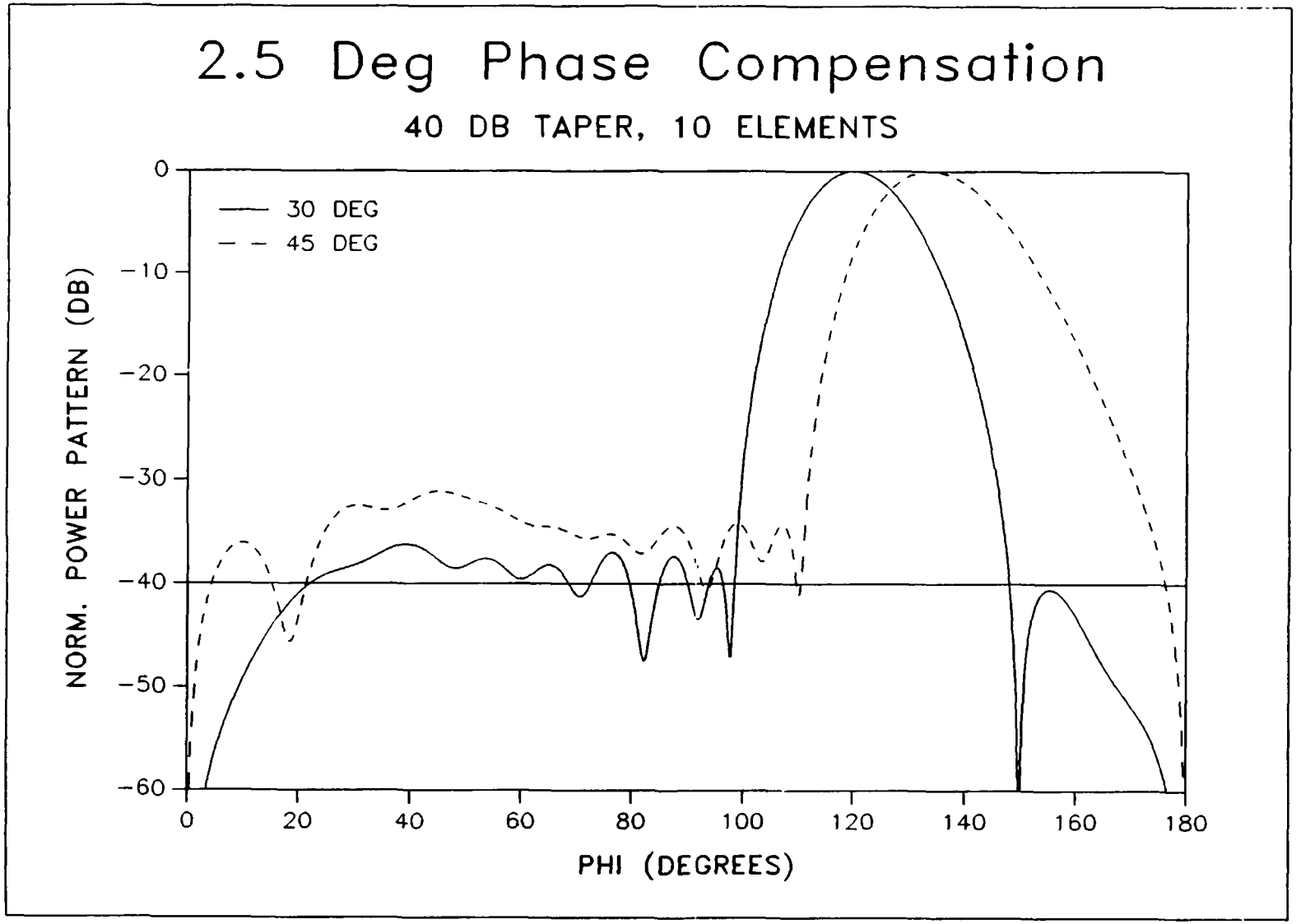
2.5 Deg Phase Compensation
40 DB TAPER, 10 ELEMENTS
30 DEG
45 DEG
NORM. POWER PATTERN (DB)
0
-10
-20
-30
-40
-50
-60
0
20
40
60
80
100
120
140
160
180
PHI (DEGREES)

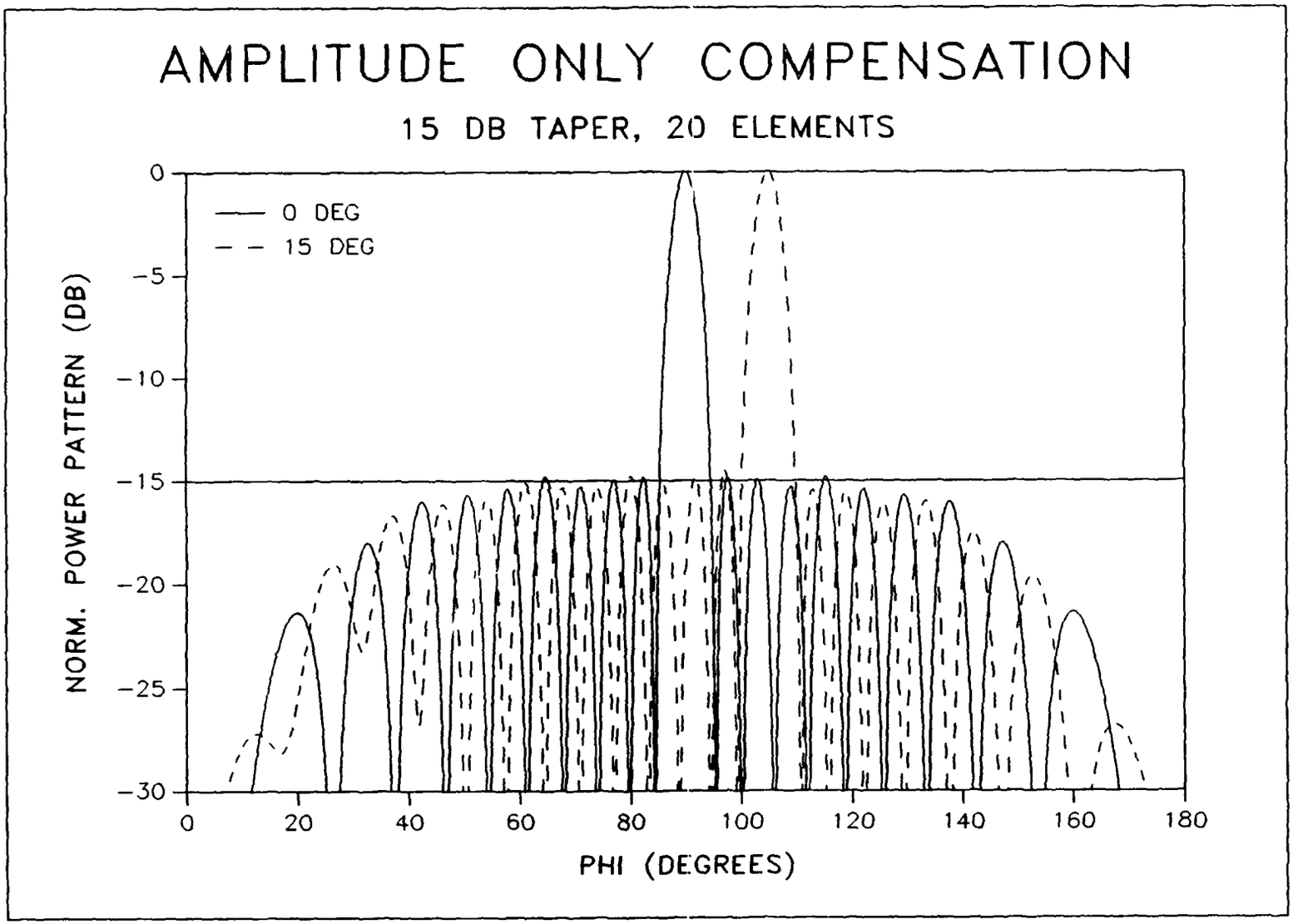
AMPLITUDE ONLY COMPENSATION
15 DB TAPER, 20 ELEMENTS
0 DEG
15 DEG
NORM. POWER PATTERN (DB)
0
-5
-10
-15
-20
-25
-30
0
20
40
60
80
100
120
140
160
180
PHI (DEGREES)

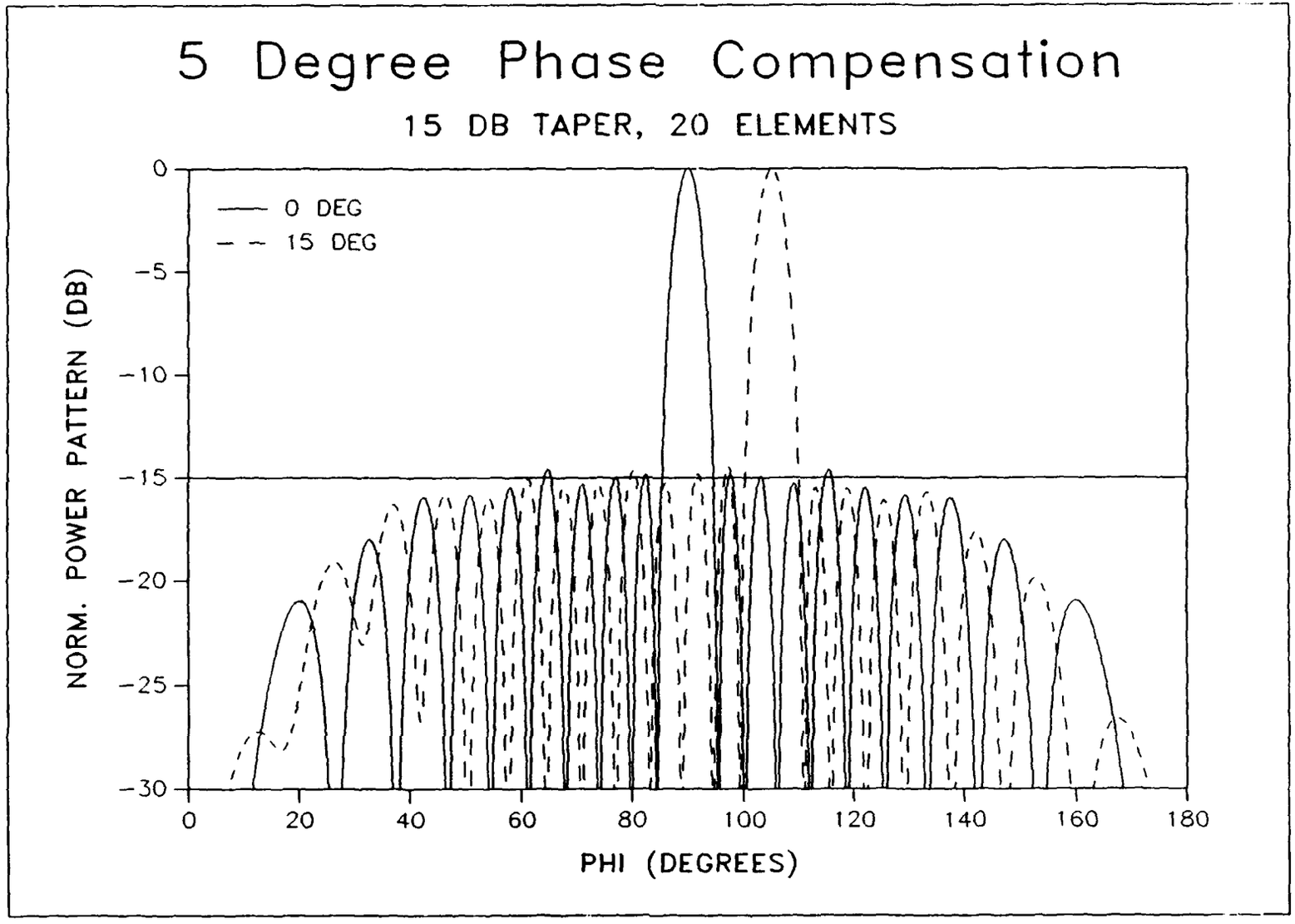
5 Degree Phase Compensation
15 DB TAPER, 20 ELEMENTS
0 DEG
15 DEG
NORM. POWER PATTERN (DB)
0
-5
-10
-15
-20
-25
-30
0
20
40
60
80
100
120
140
160
180
PHI (DEGREES)

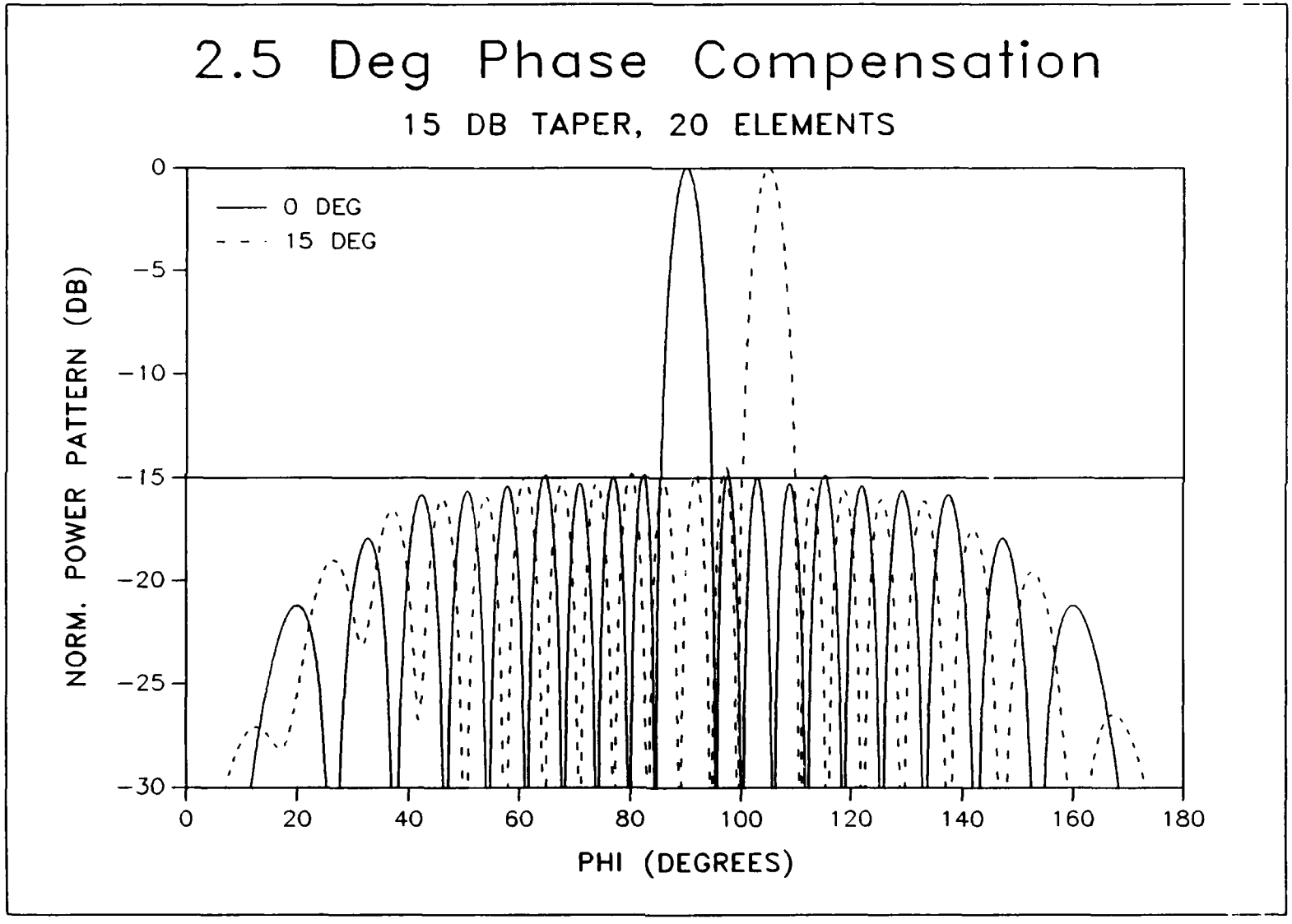
2.5 Deg Phase Compensation
15 DB TAPER, 20 ELEMENTS
0 DEG
15 DEG
NORM. POWER PATTERN (DB)
0
-5
-10
-15
-20
-25
-30
0
20
40
60
80
100
120
140
160
180
PHI (DEGREES)

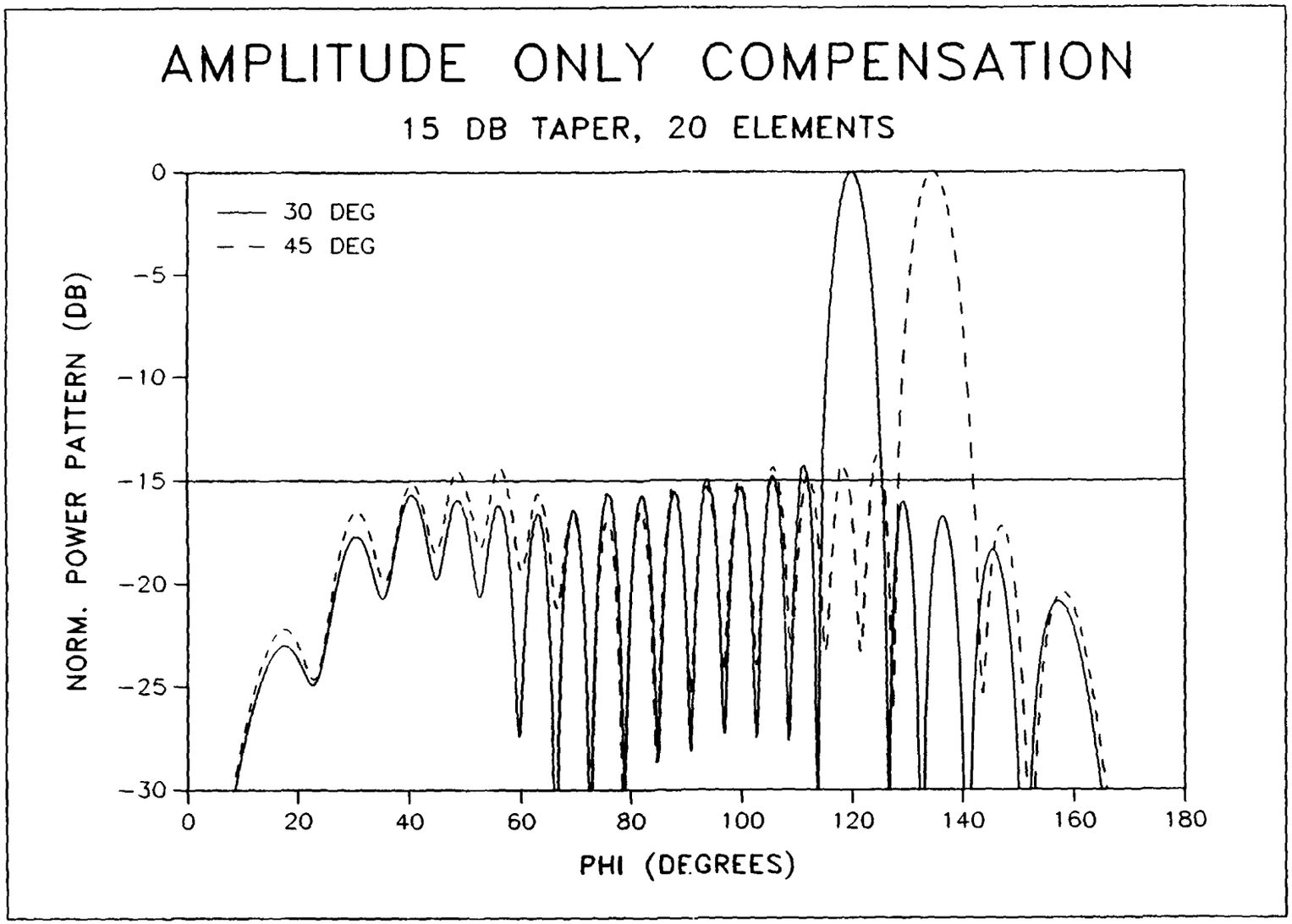
AMPLITUDE ONLY COMPENSATION
15 DB TAPER, 20 ELEMENTS
30 DEG
45 DEG
NORM. POWER PATTERN (DB)
0
-5
-10
-15
-20
-25
-30
0
20
40
60
80
100
120
140
160
180
PHI (DEGREES)

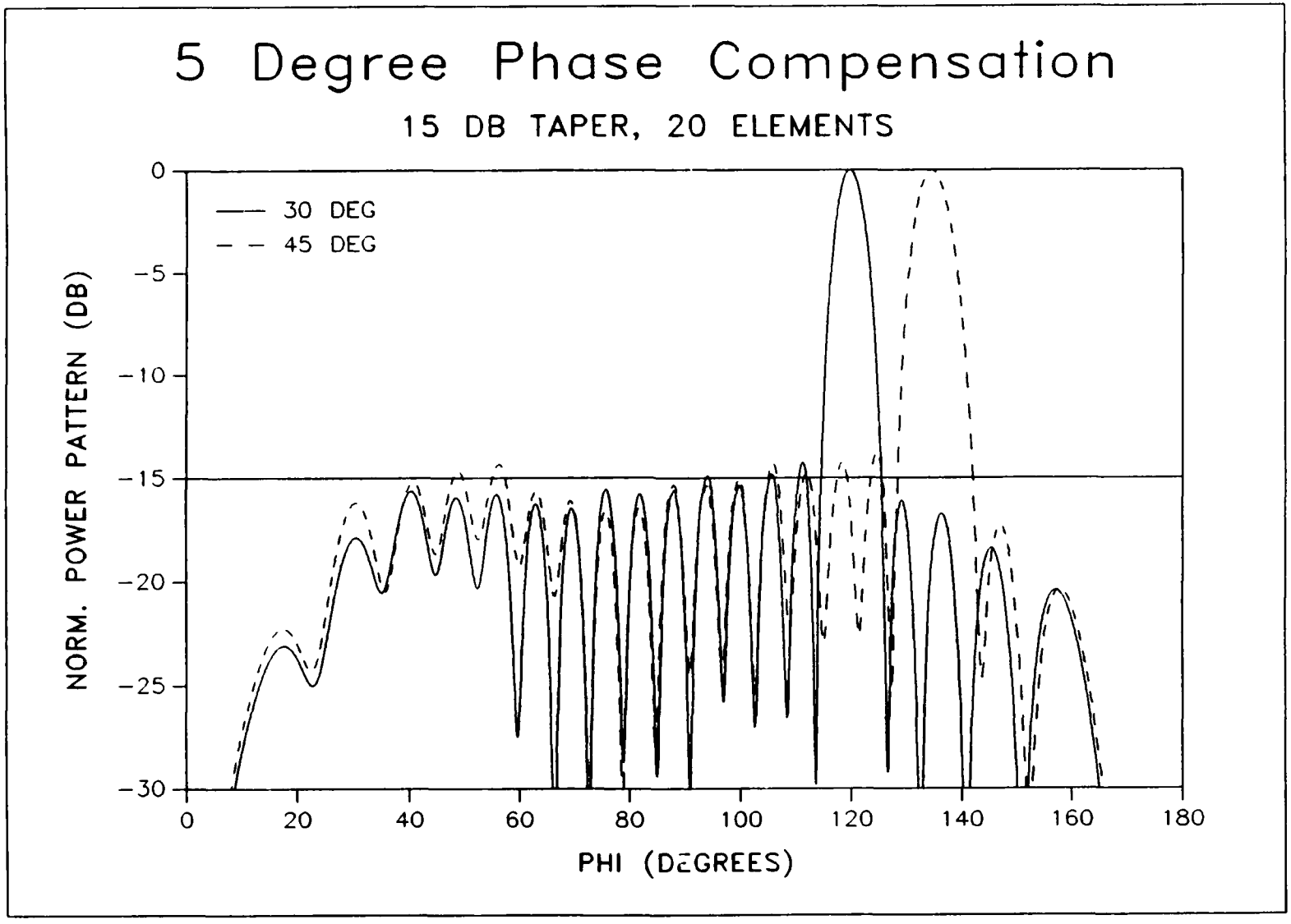
5 Degree Phase Compensation
15 DB TAPER, 20 ELEMENTS
30 DEG
45 DEG
NORM. POWER PATTERN (DB)
0
-5
-10
-15
-20
-25
-30
0
20
40
60
80
100
120
140
160
180
PHI (DEGREES)

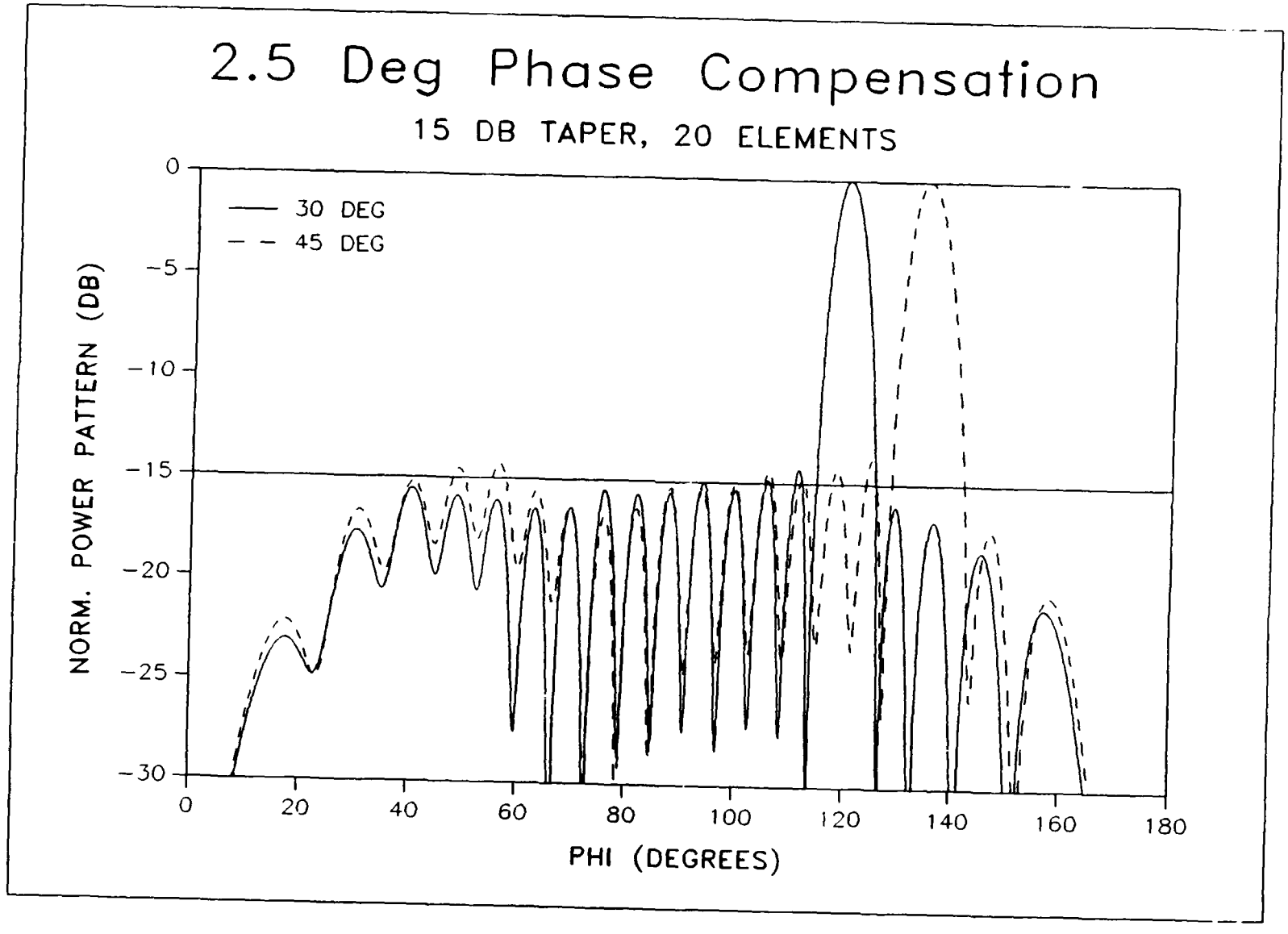
2.5 Deg Phase Compensation
15 DB TAPER, 20 ELEMENTS
30 DEG
45 DEG
NORM. POWER PATTERN (DB)
0
-5
-10
-15
-20
-25
-30
0
20
40
60
80
100
120
140
160
180
PHI (DEGREES)

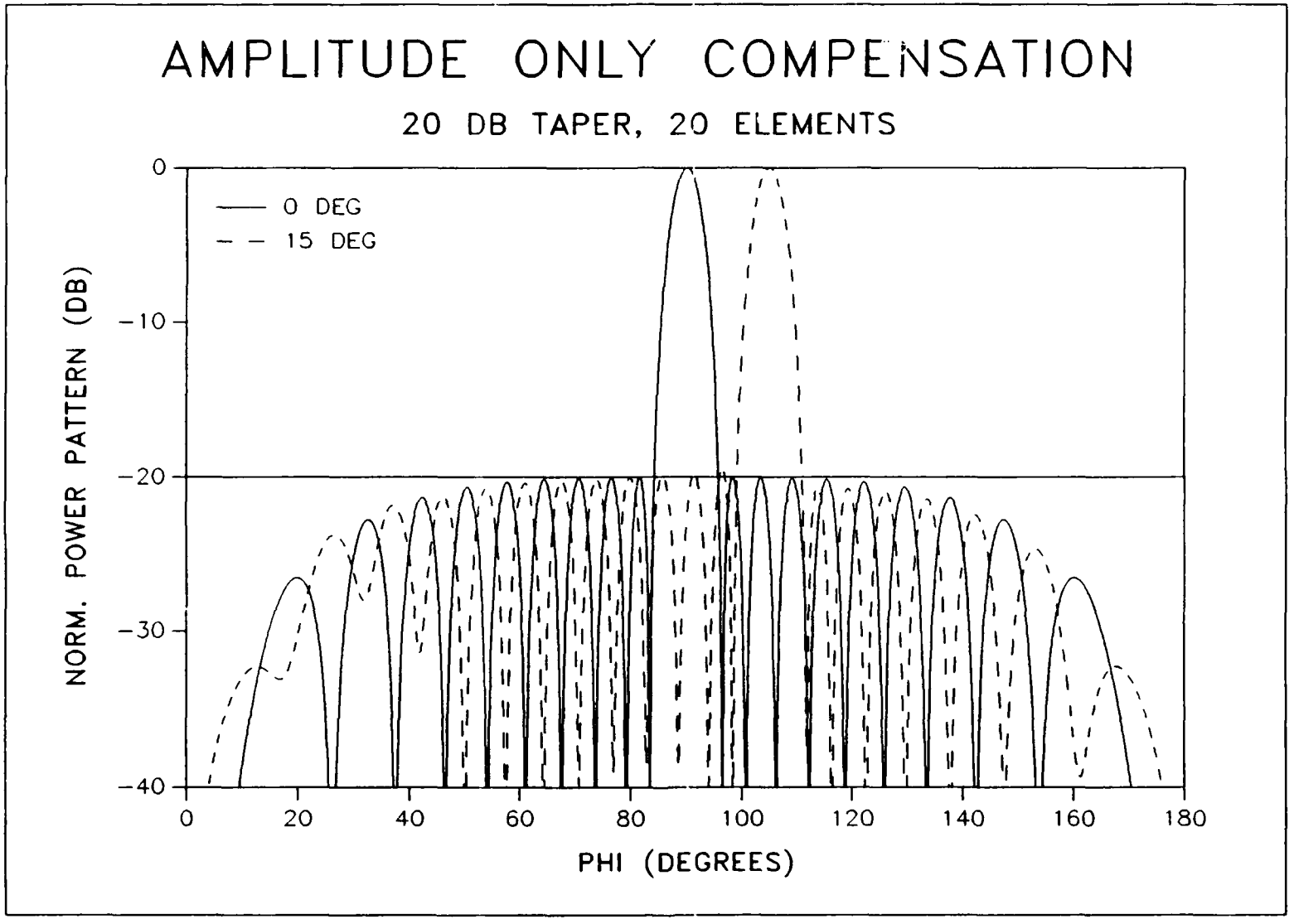
AMPLITUDE ONLY COMPENSATION
20 DB TAPER, 20 ELEMENTS
0 DEG
15 DEG
NORM. POWER PATTERN (DB)
0
-10
-20
-30
-40
0
20
40
60
80
100
120
140
160
180
PHI (DEGREES)

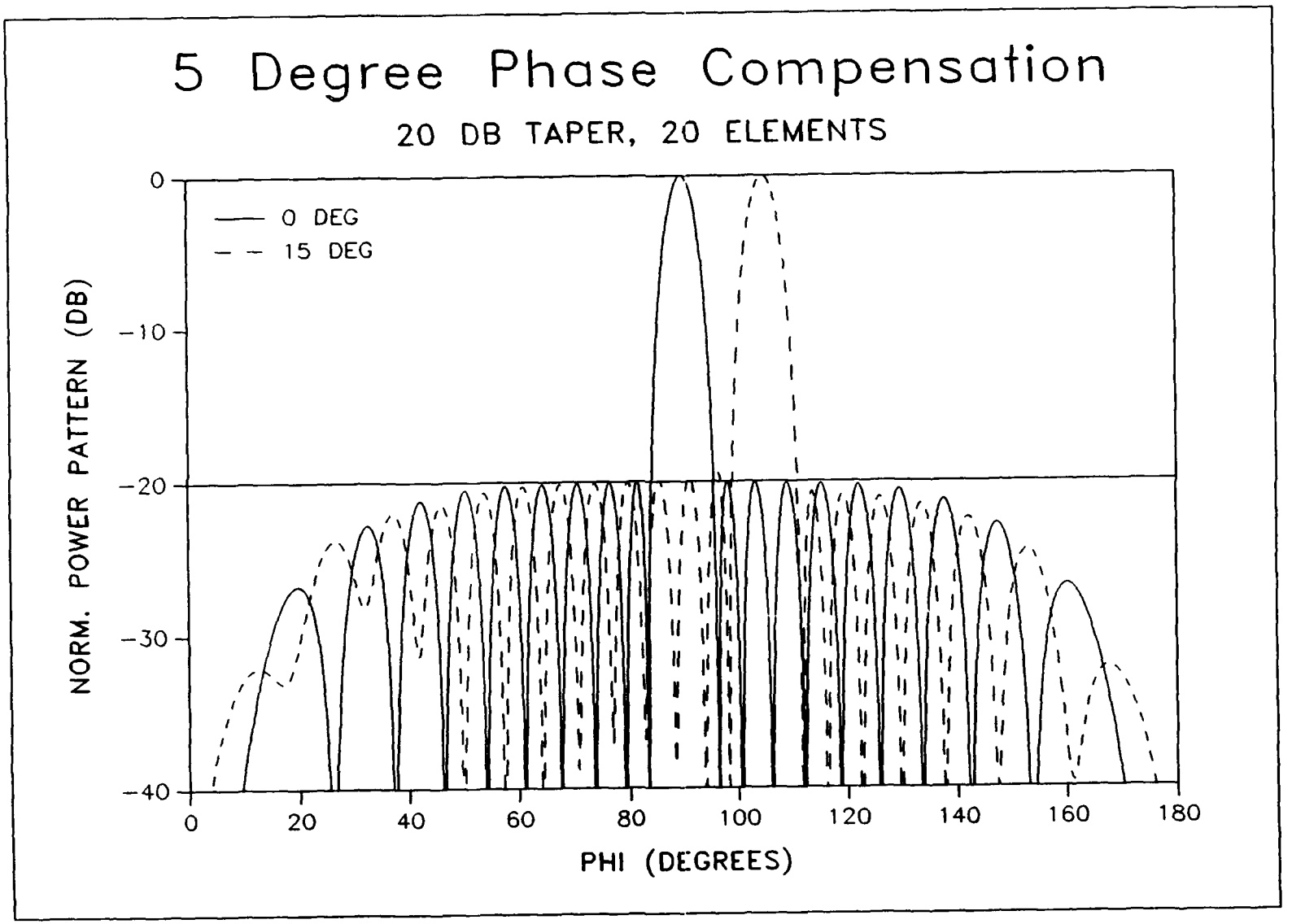
5 Degree Phase Compensation
20 DB TAPER, 20 ELEMENTS
0 DEG
15 DEG
NORM. POWER PATTERN (DB)
0
-10
-20
-30
-40
0
20
40
60
80
100
120
140
160
180
PHI (DEGREES)

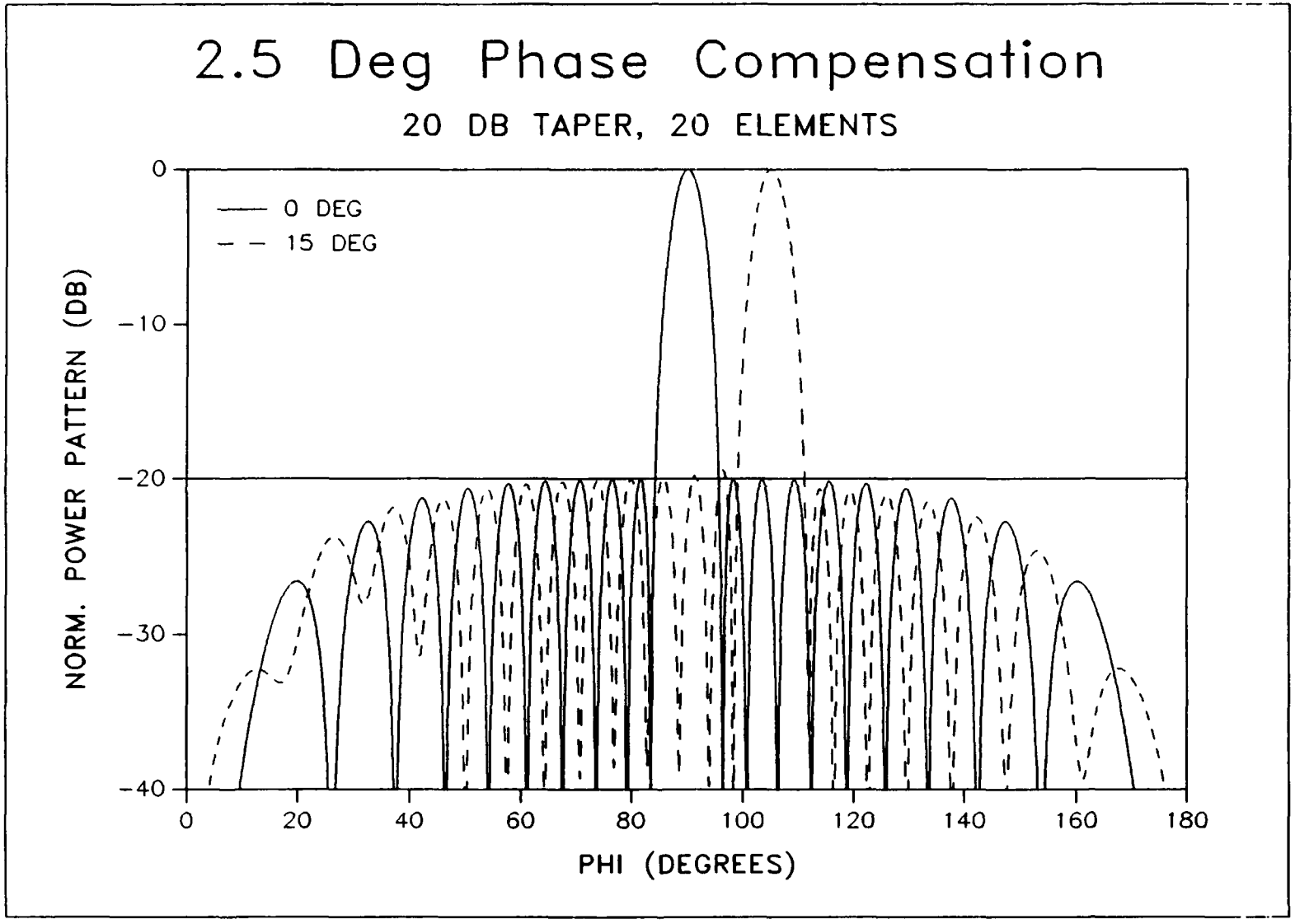
2.5 Deg Phase Compensation
20 DB TAPER, 20 ELEMENTS
0 DEG
15 DEG
NORM. POWER PATTERN (DB)
0
-10
-20
-30
-40
0
20
40
60
80
100
120
140
160
180
PHI (DEGREES)

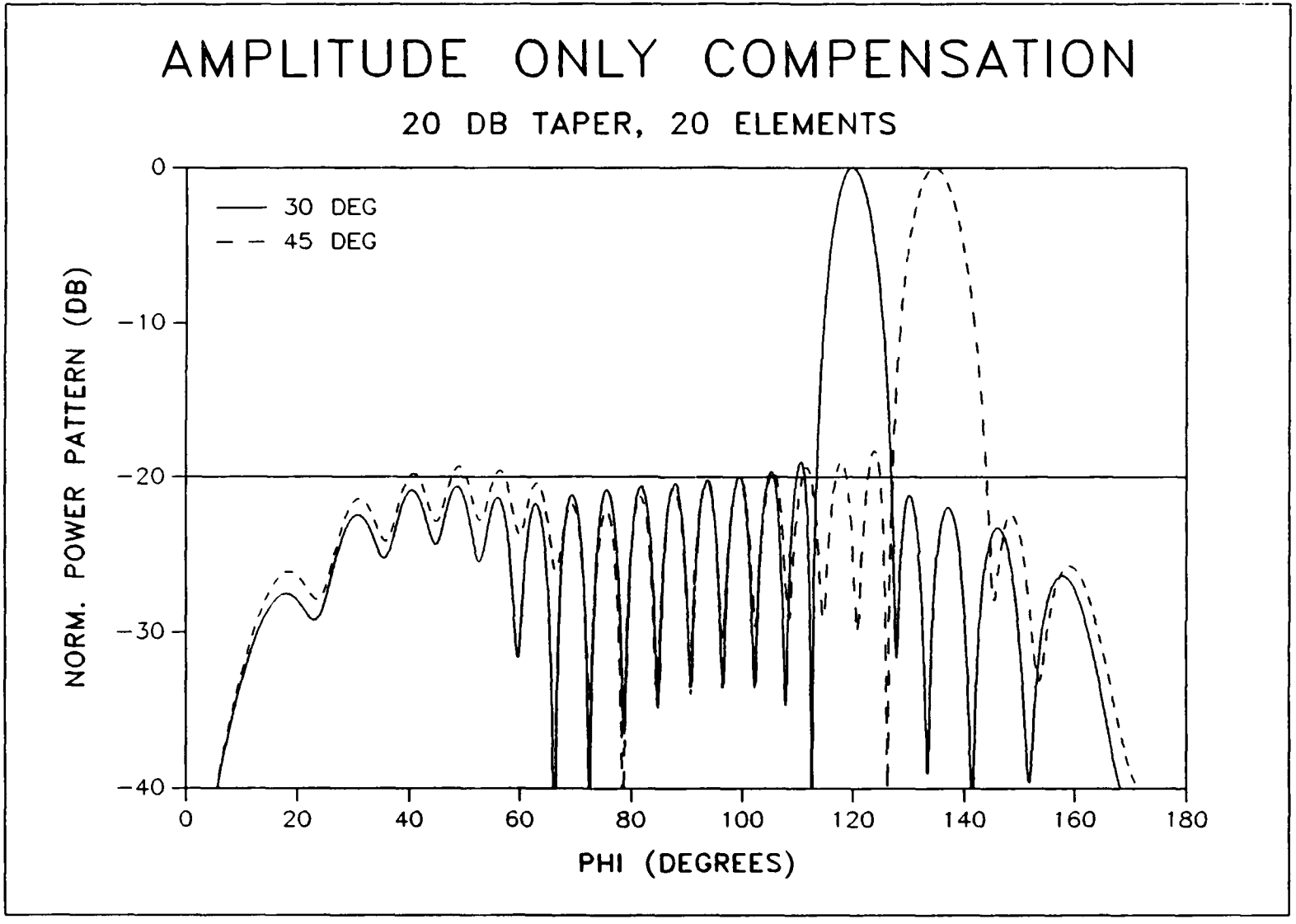
AMPLITUDE ONLY COMPENSATION
20 DB TAPER, 20 ELEMENTS
30 DEG
45 DEG
NORM. POWER PATTERN (DB)
0
-10
-20
-30
-40
0
20
40
60
80
100
120
140
160
180
PHI (DEGREES)

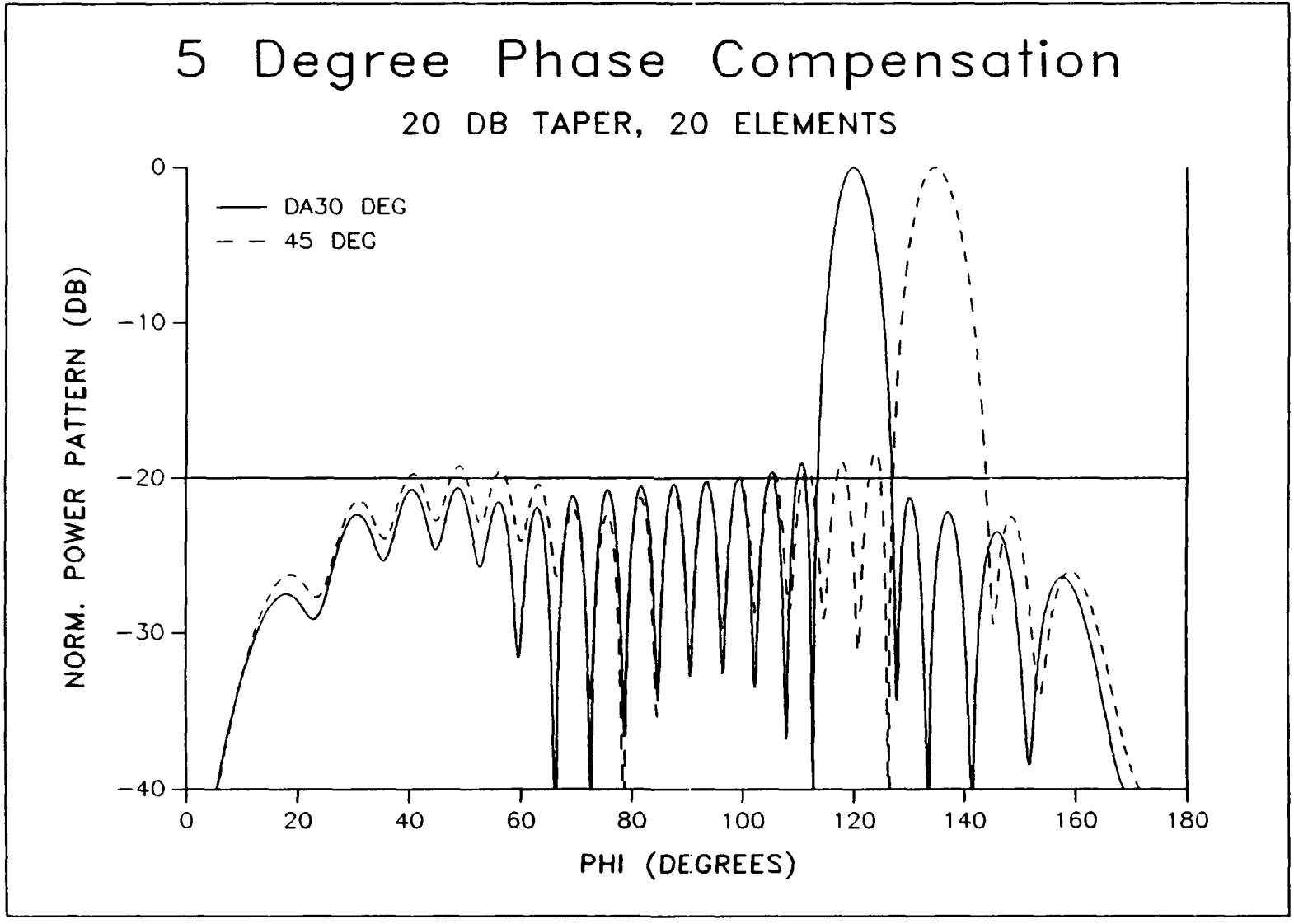
5 Degree Phase Compensation
20 DB TAPER, 20 ELEMENTS
DA30 DEG
45 DEG
NORM. POWER PATTERN (DB)
0
-10
-20
-30
-40
0
20
40
60
80
100
120
140
160
180
PHI (DEGREES)

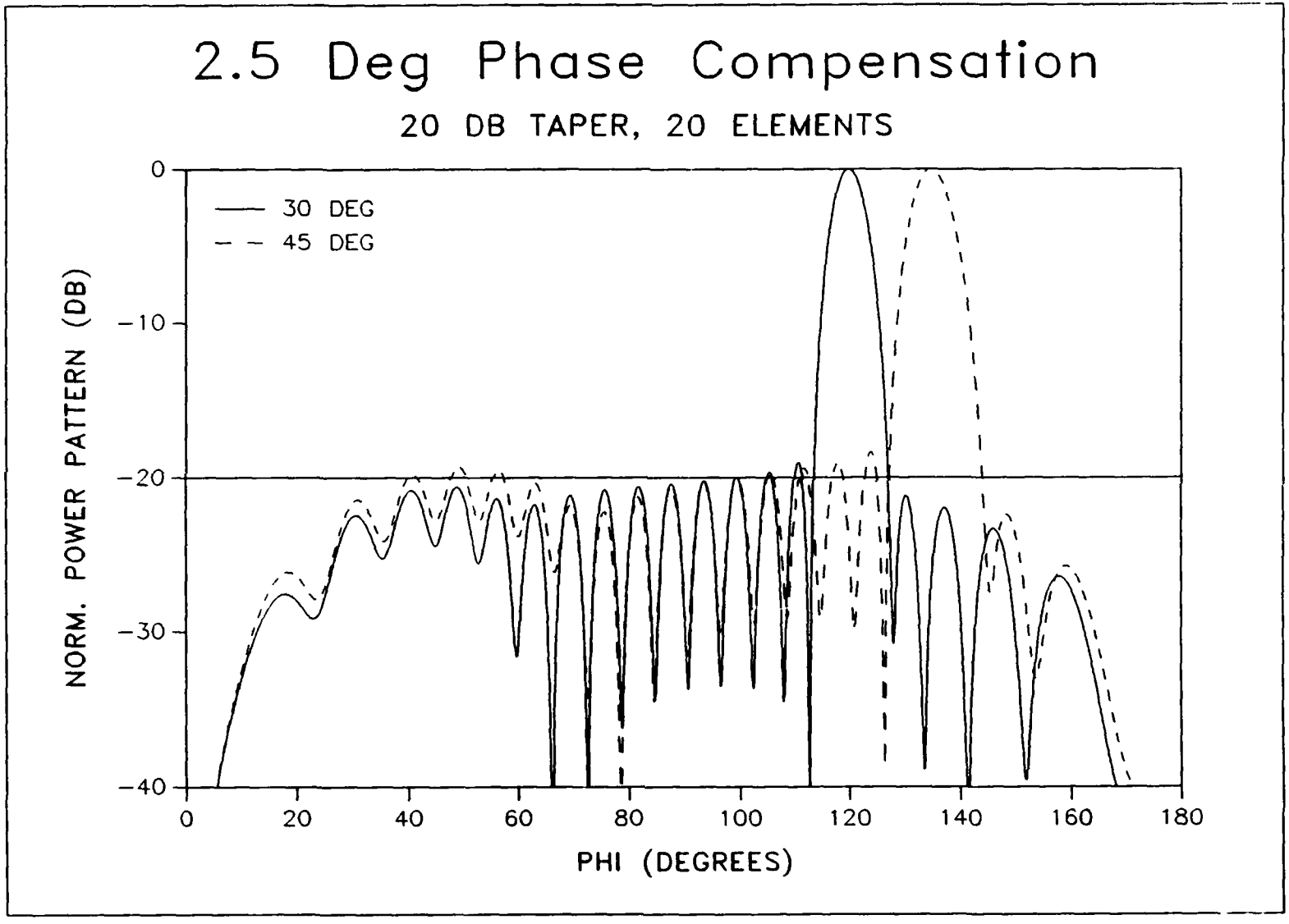
2.5 Deg Phase Compensation
20 DB TAPER, 20 ELEMENTS
30 DEG
45 DEG
NORM. POWER PATTERN (DB)
0
-10
-20
-30
-40
0
20
40
60
80
100
120
140
160
180
PHI (DEGREES)

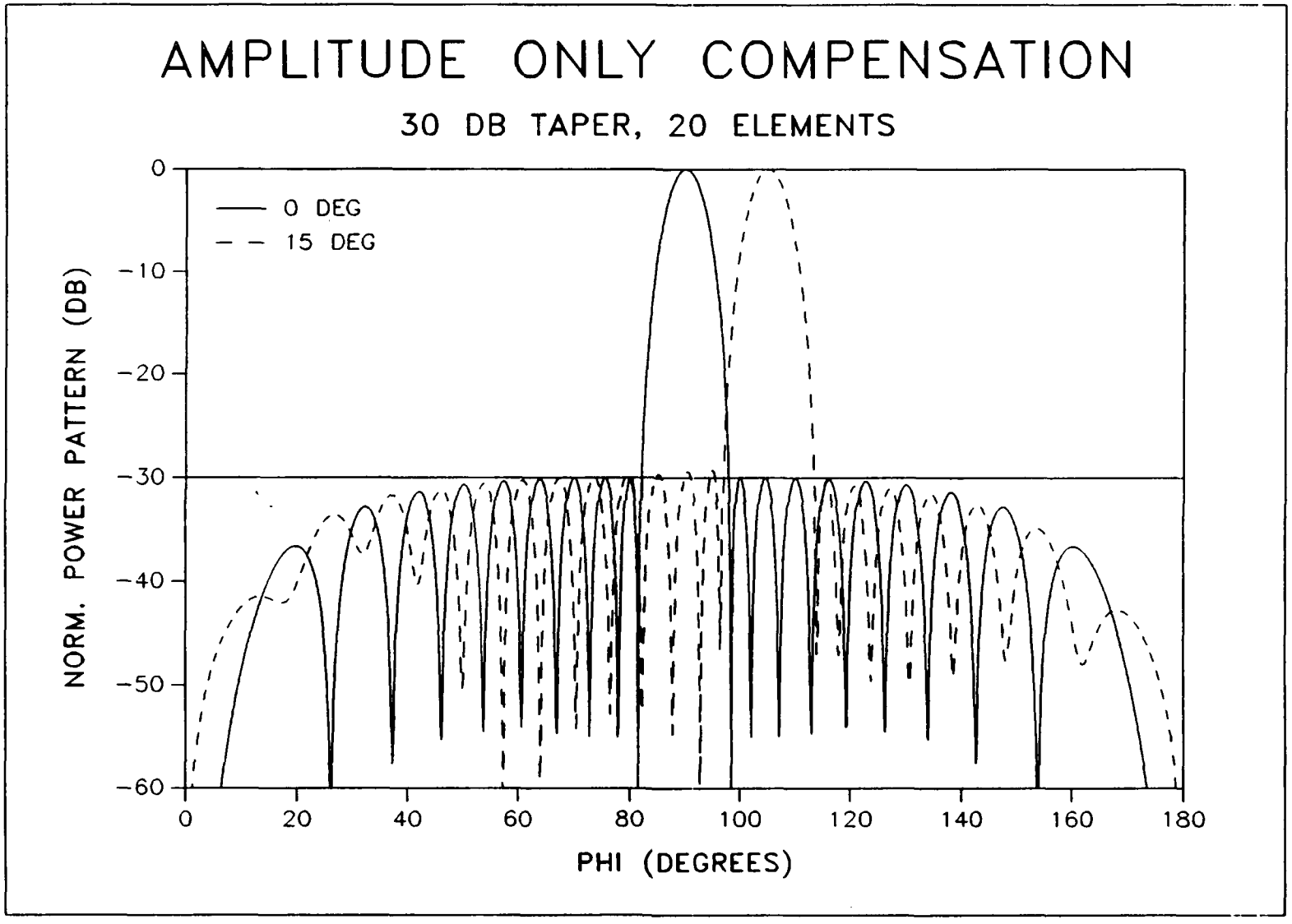
AMPLITUDE ONLY COMPENSATION
30 DB TAPER, 20 ELEMENTS
0 DEG
15 DEG
NORM. POWER PATTERN (DB)
0
-10
-20
-30
-40
-50
-60
0
20
40
60
80
100
120
140
160
180
PHI (DEGREES)

5 Degree Phase Compensation

30 DB TAPER, 20 ELEMENTS

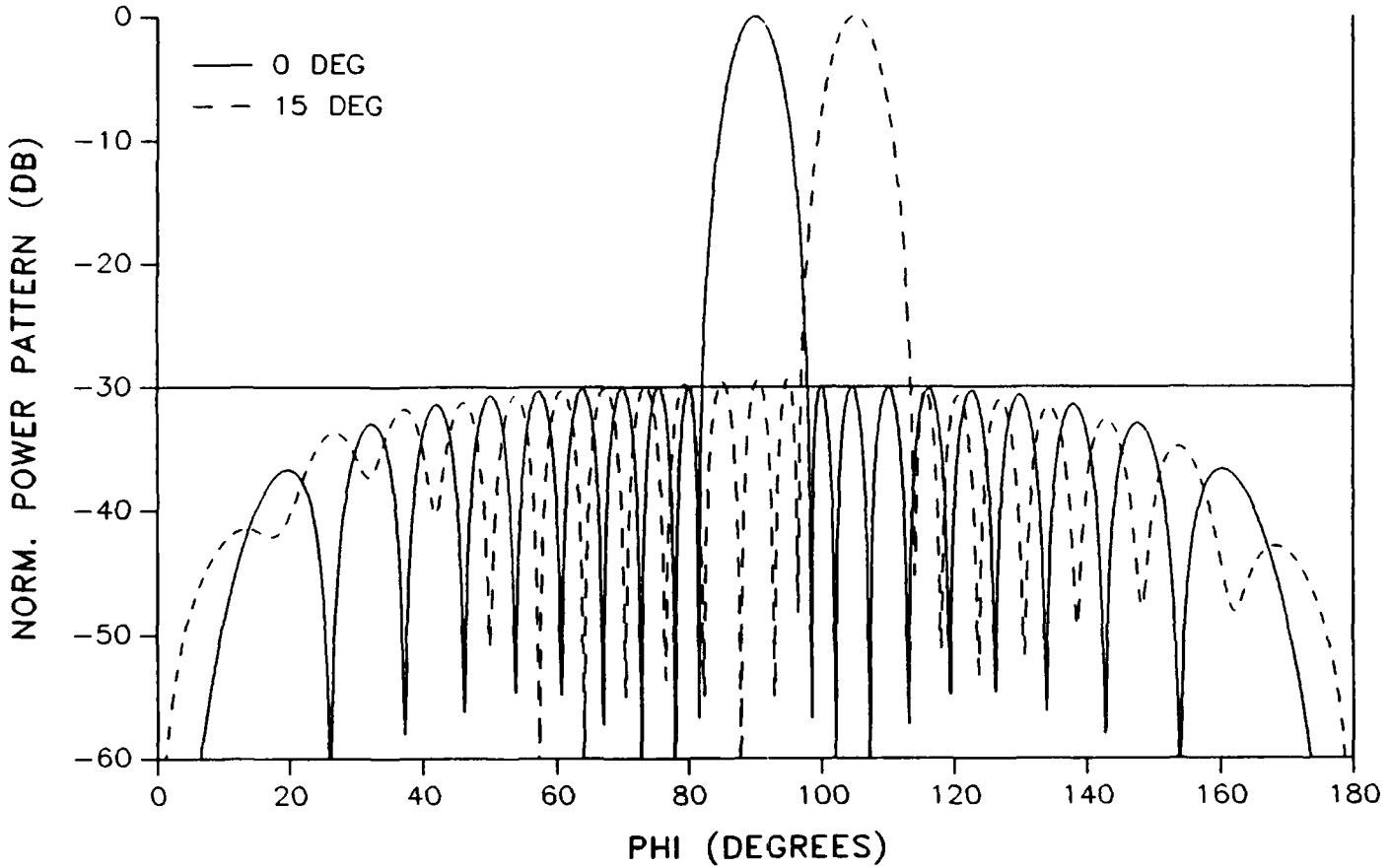

2.5 Deg Phase Compensation

30 DB TAPER, 20 ELEMENTS

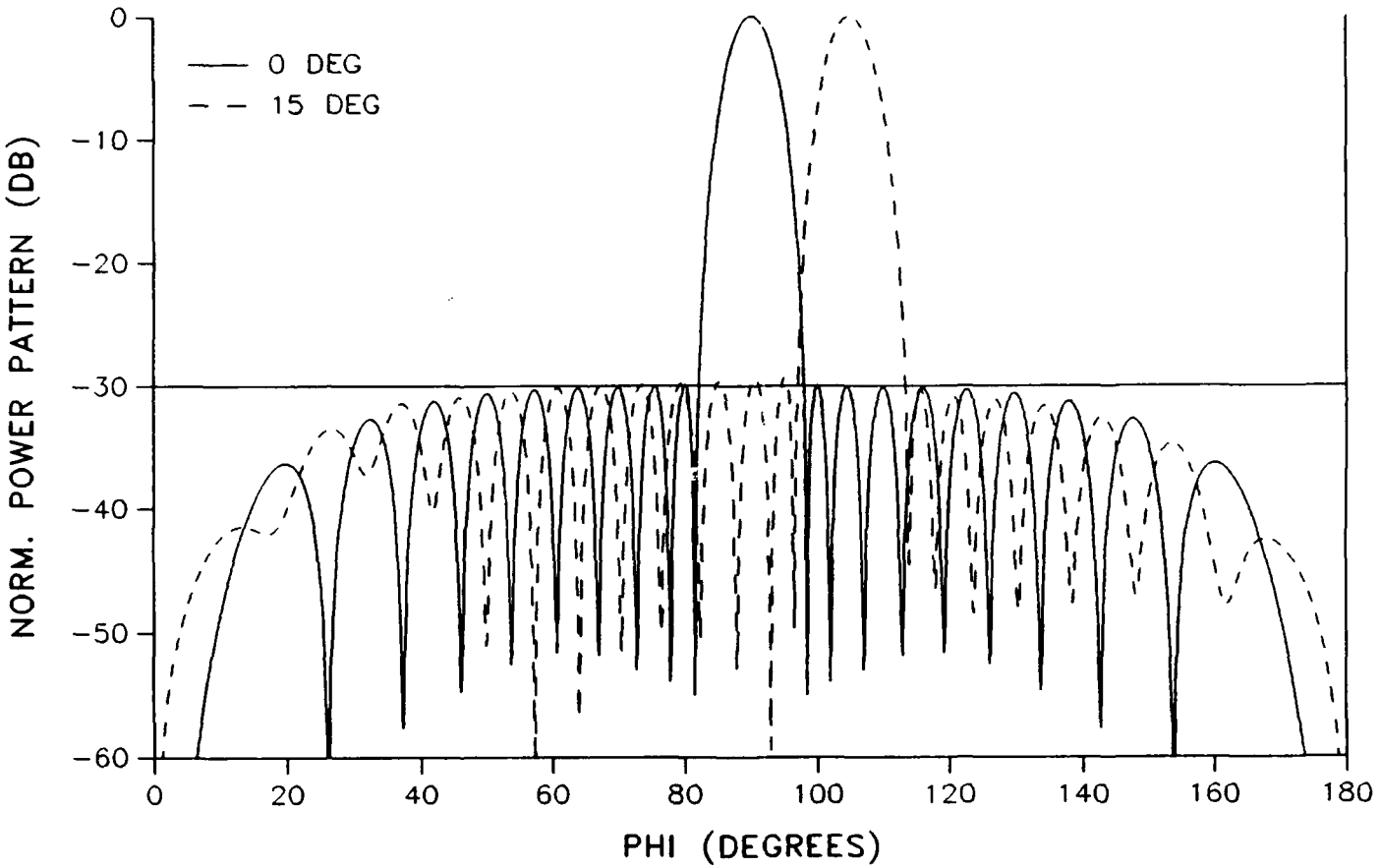

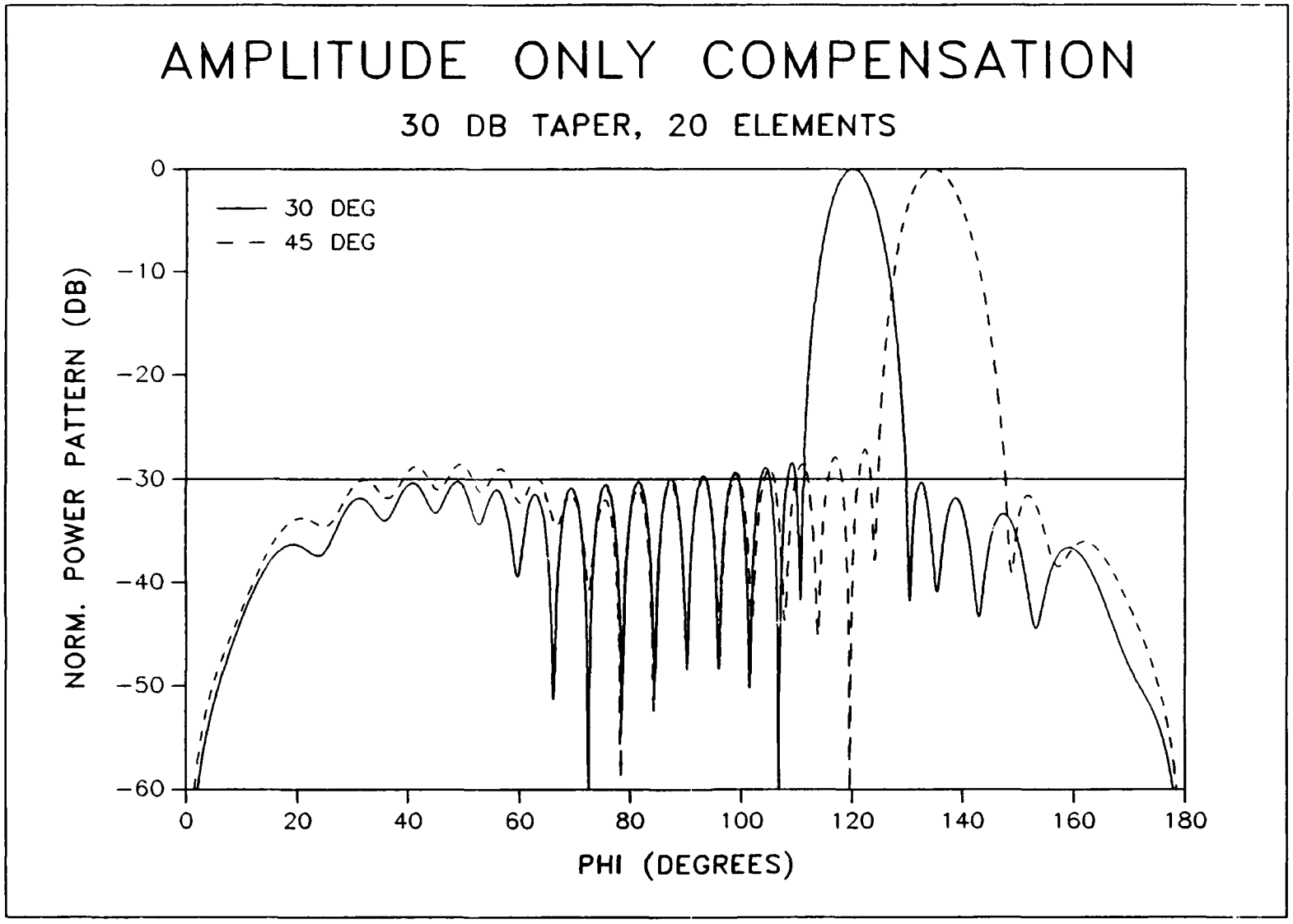
AMPLITUDE ONLY COMPENSATION
30 DB TAPER, 20 ELEMENTS
30 DEG
45 DEG
NORM. POWER PATTERN (DB)
0
-10
-20
-30
-40
-50
-60
0
20
40
60
80
100
120
140
160
180
PHI (DEGREES)

5 Degree Phase Compensation

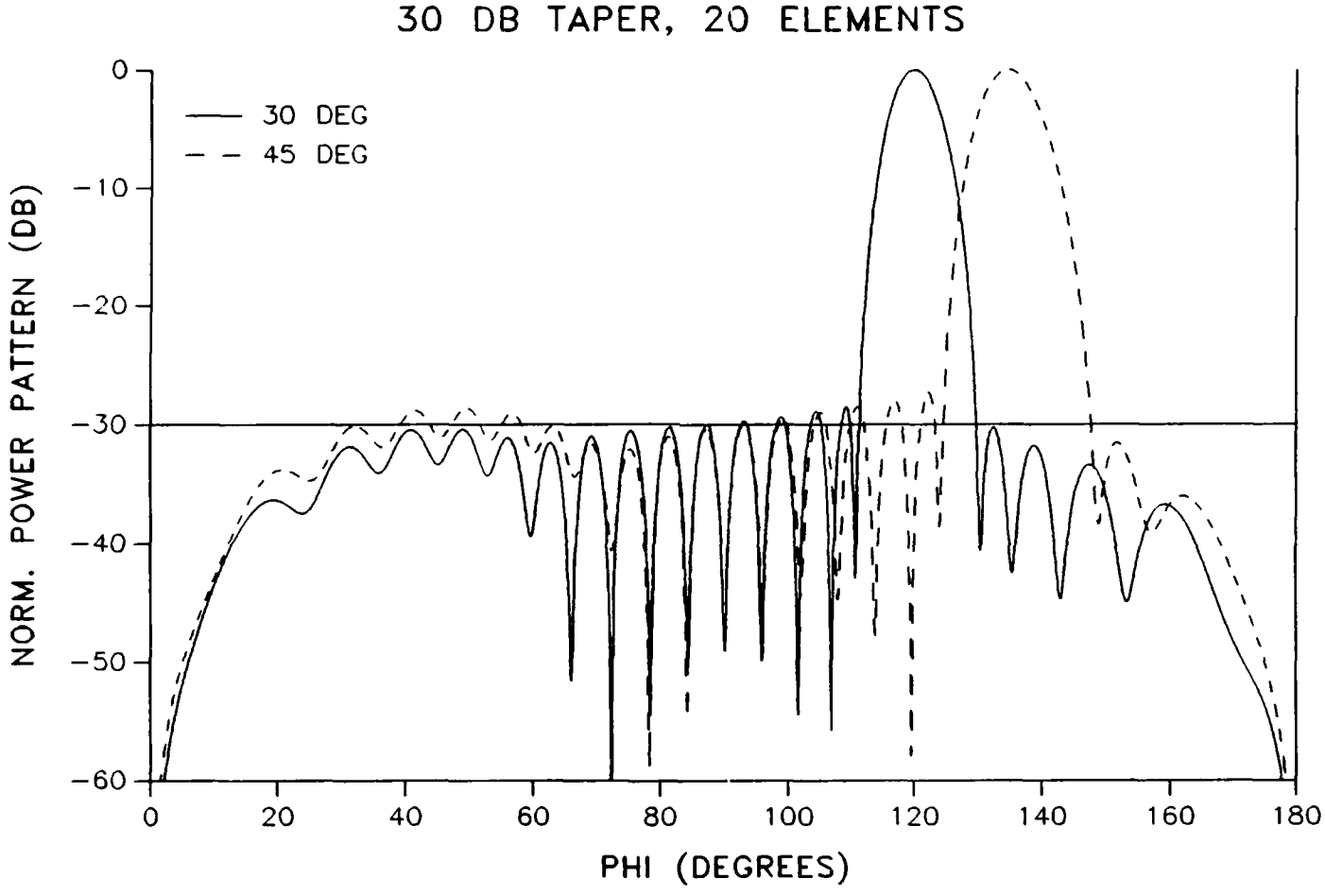

2.5 Deg Phase Compensation

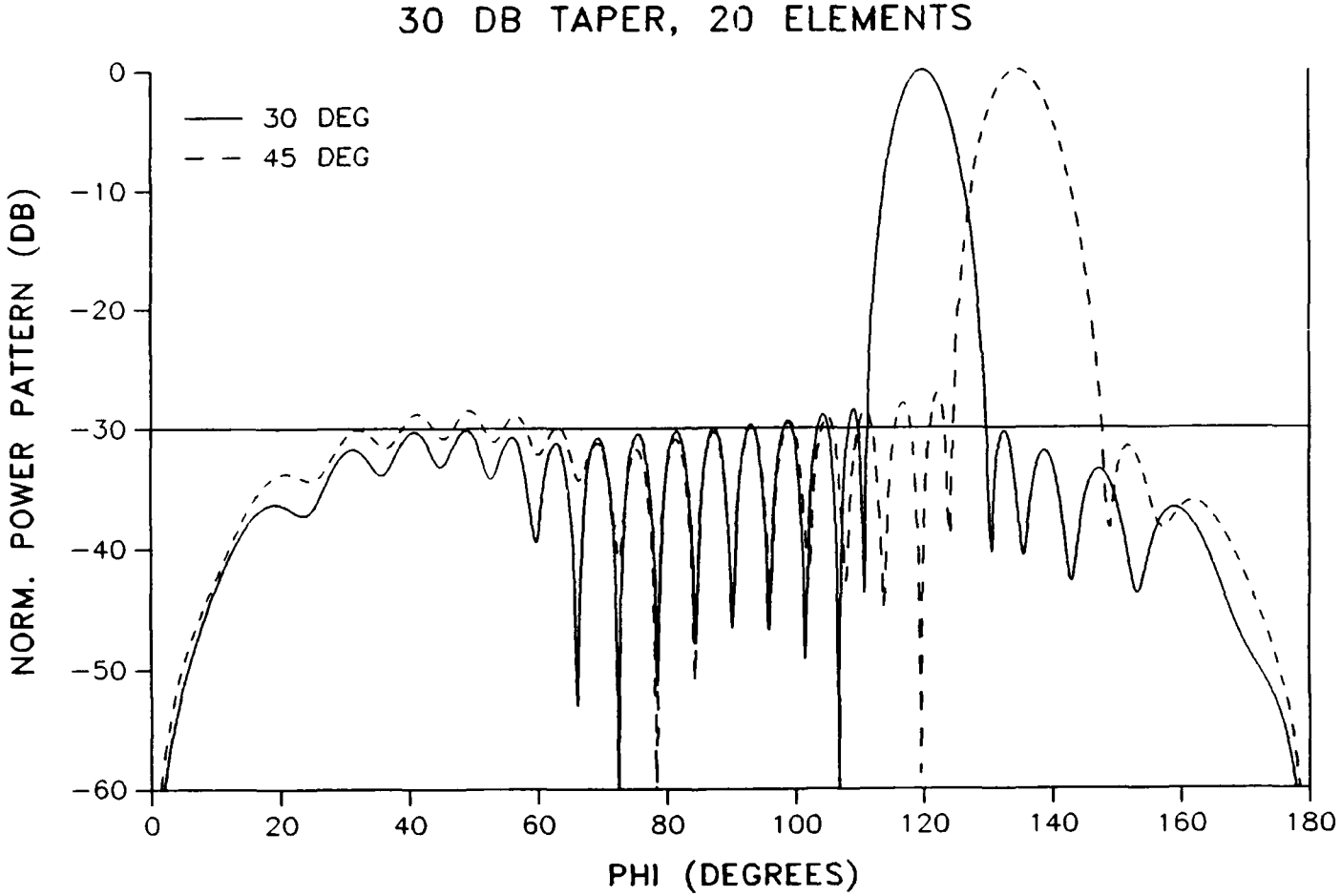

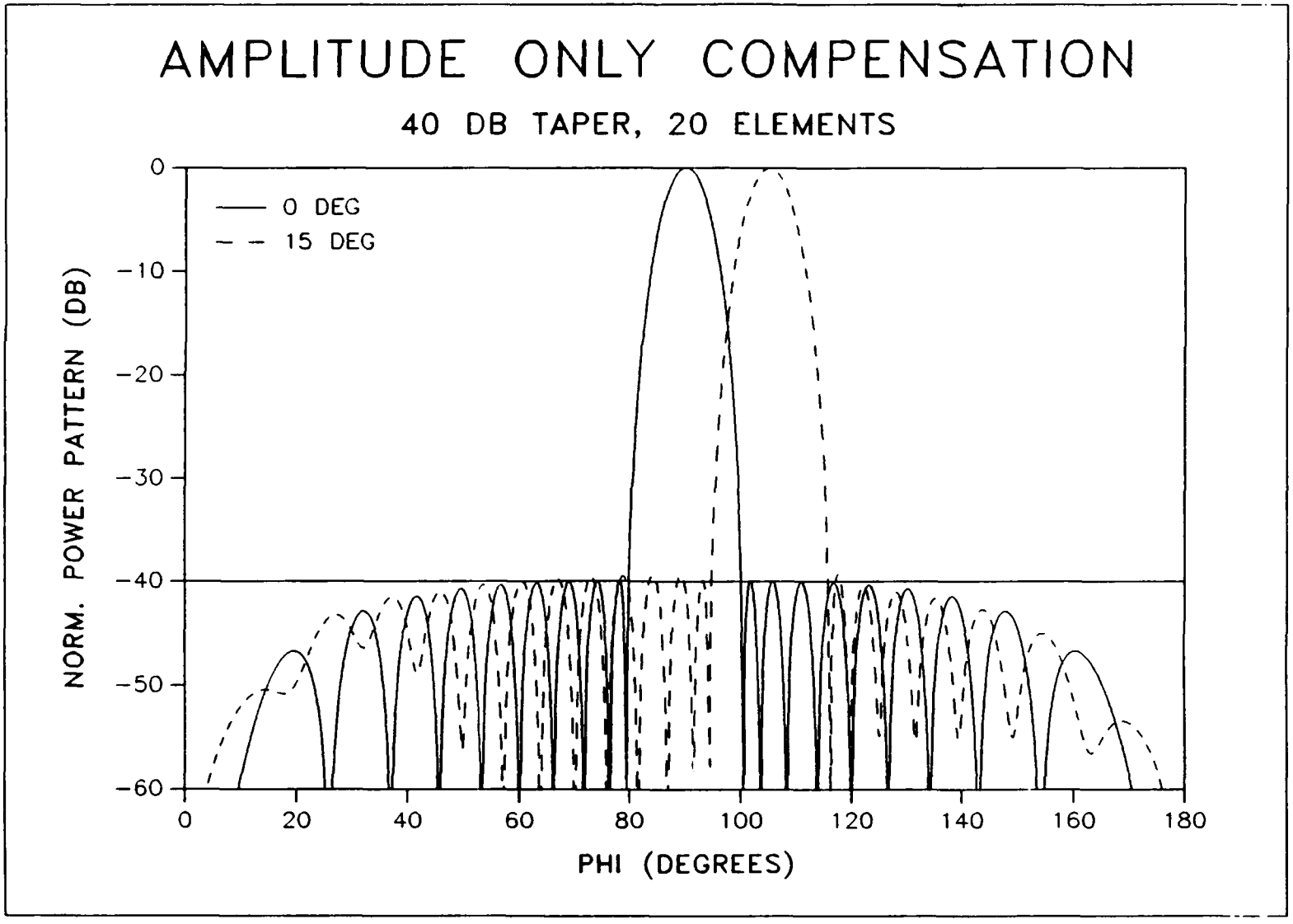
AMPLITUDE ONLY COMPENSATION
40 DB TAPER, 20 ELEMENTS
0 DEG
15 DEG
NORM. POWER PATTERN (DB)
0
-10
-20
-30
-40
-50
-60
0
20
40
60
80
100
120
140
160
180
PHI (DEGREES)

5 Degree Phase Compensation

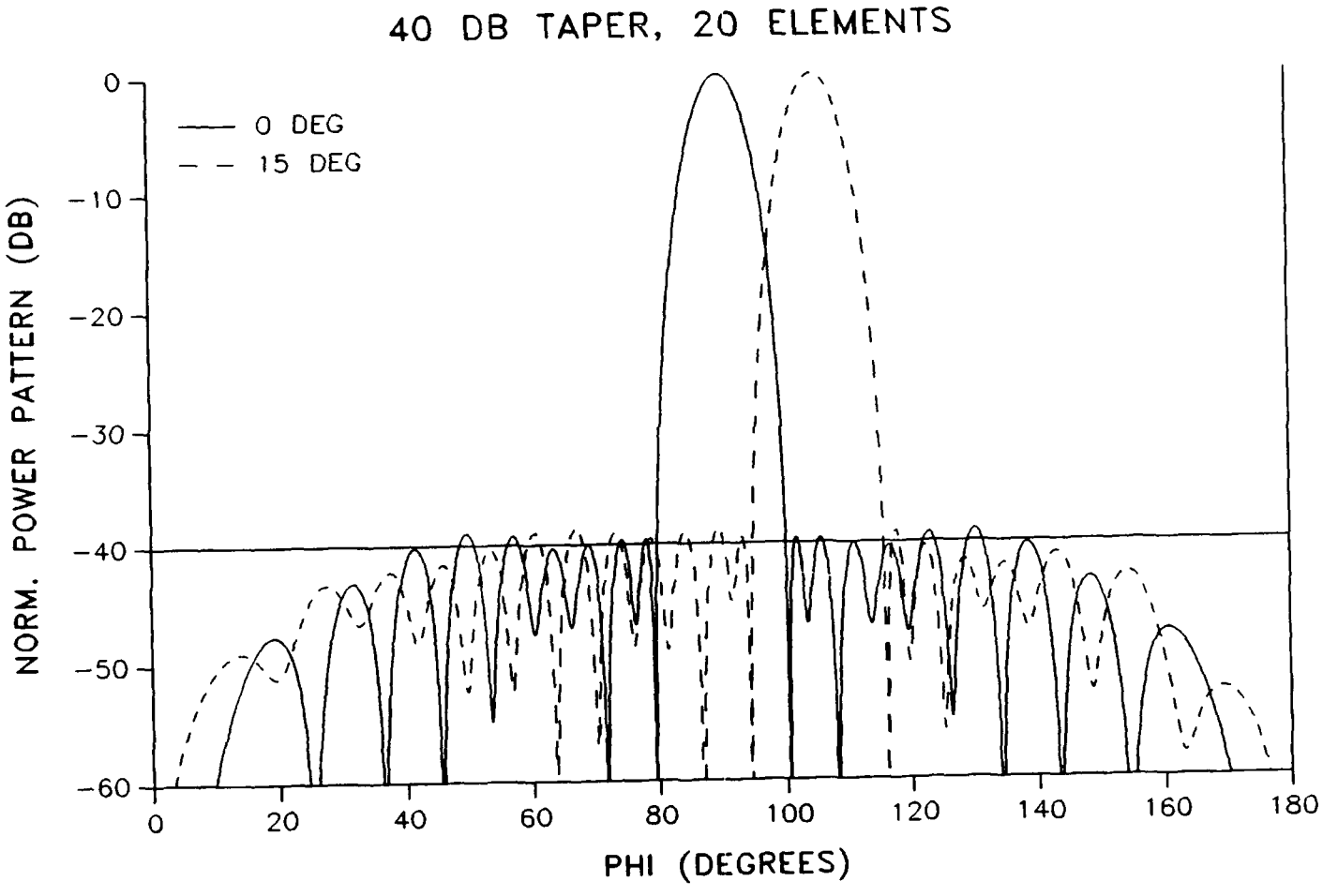

2.5 Deg Phase Compensation

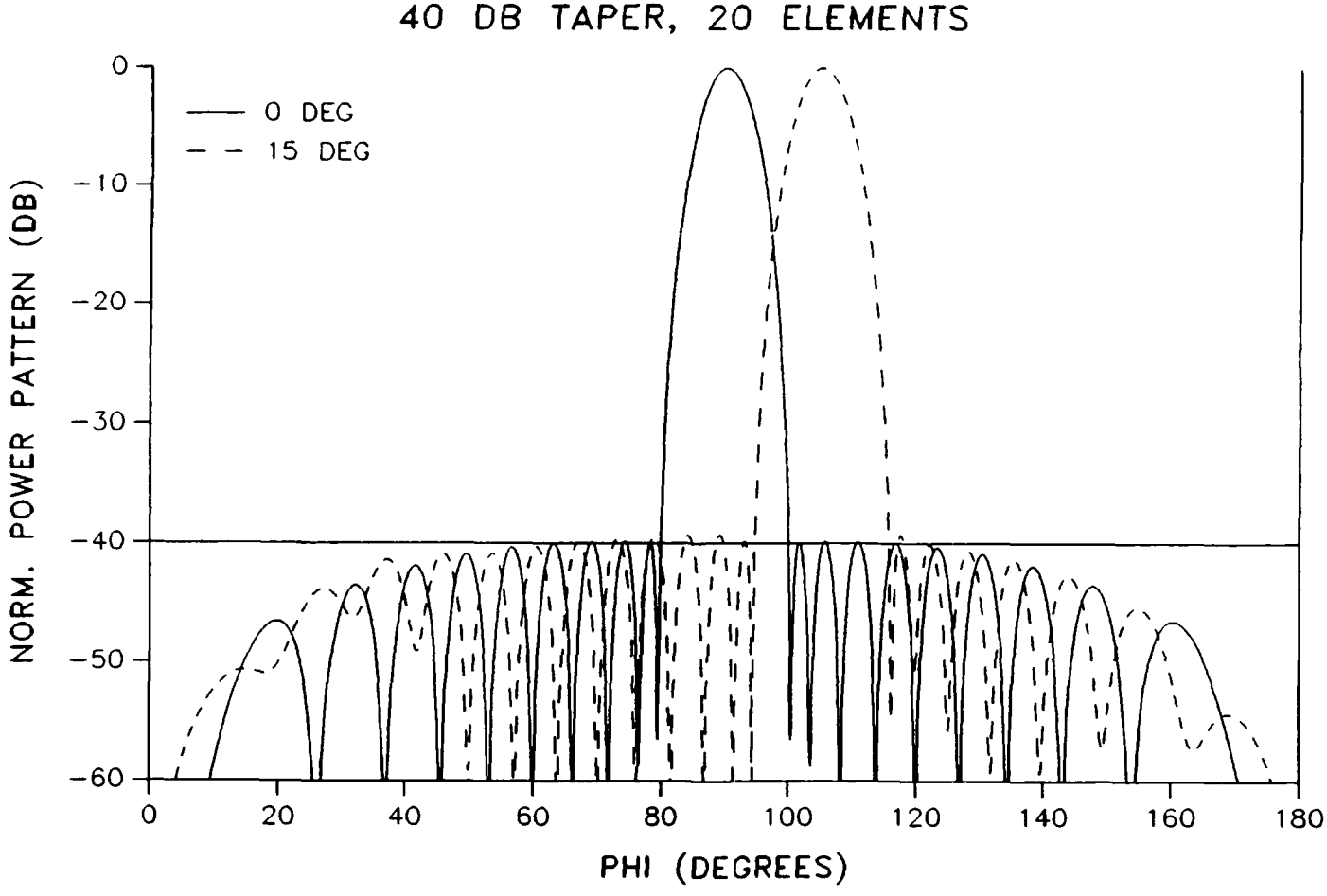

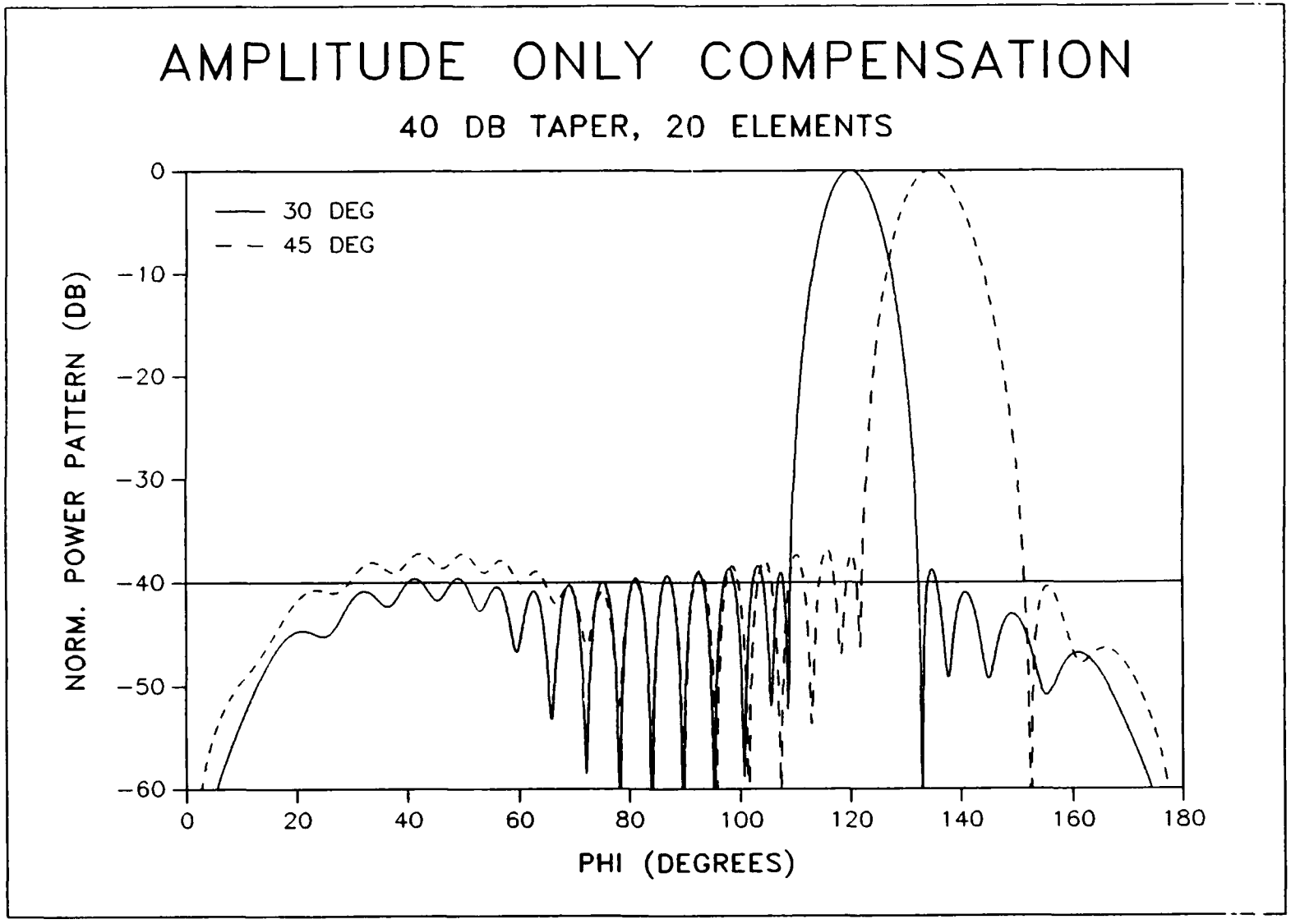
AMPLITUDE ONLY COMPENSATION
40 DB TAPER, 20 ELEMENTS
30 DEG
45 DEG
NORM. POWER PATTERN (DB)
0
-10
-20
-30
-40
-50
-60
0
20
40
60
80
100
120
140
160
180
PHI (DEGREES)

5 Degree Phase Compensation

40 DB TAPER, 20 ELEMENTS

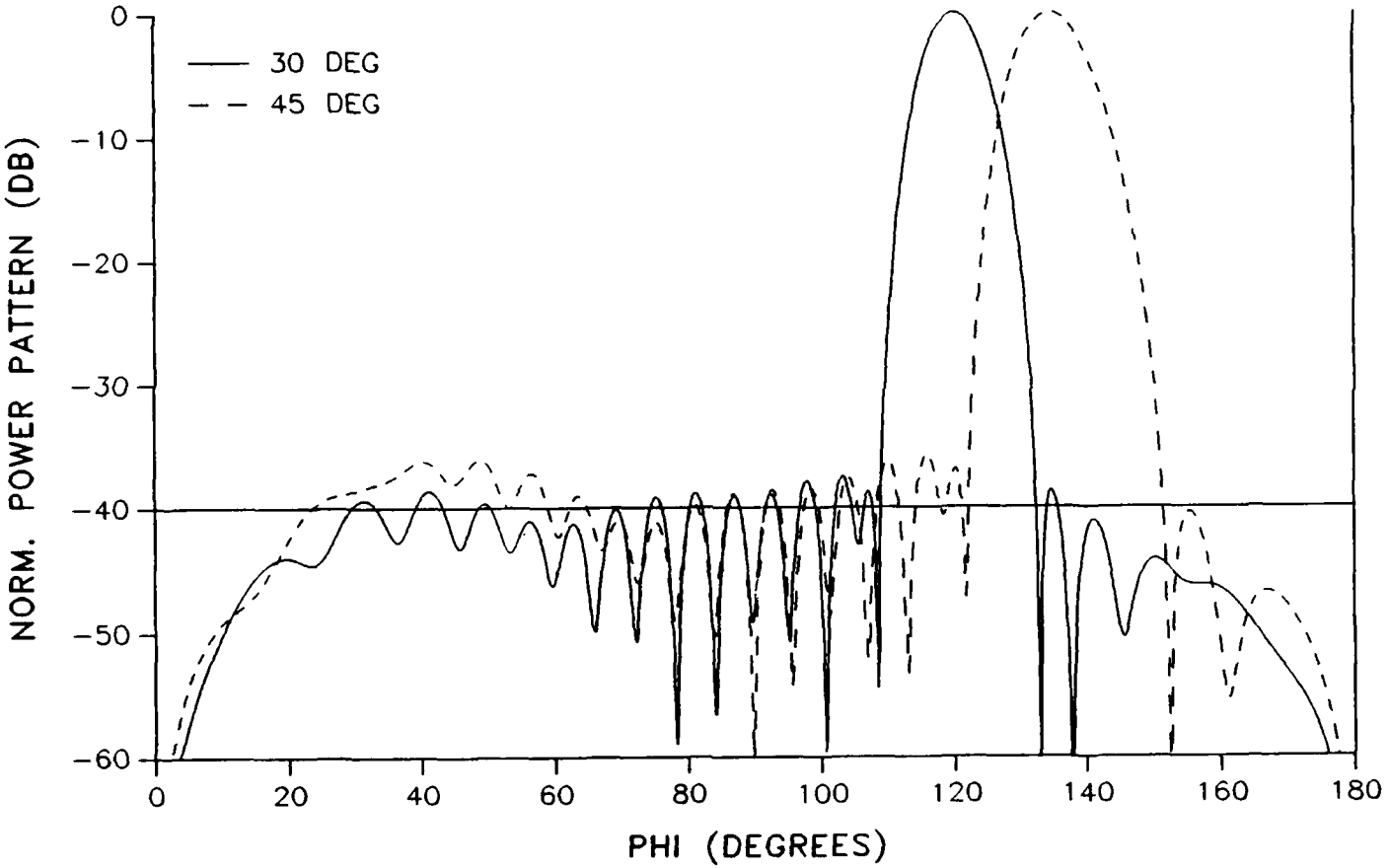

2.5 Deg Phase Compensation

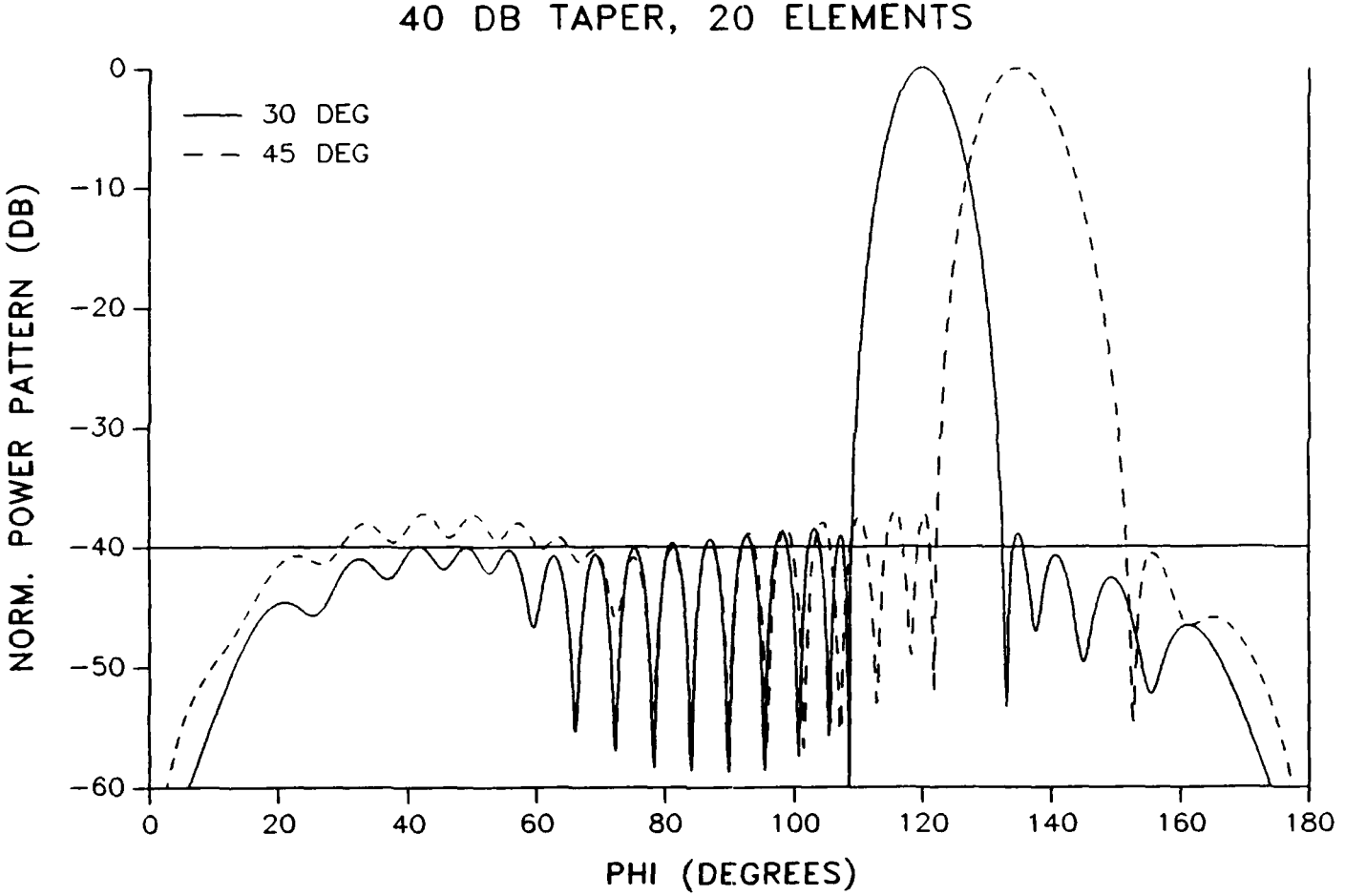

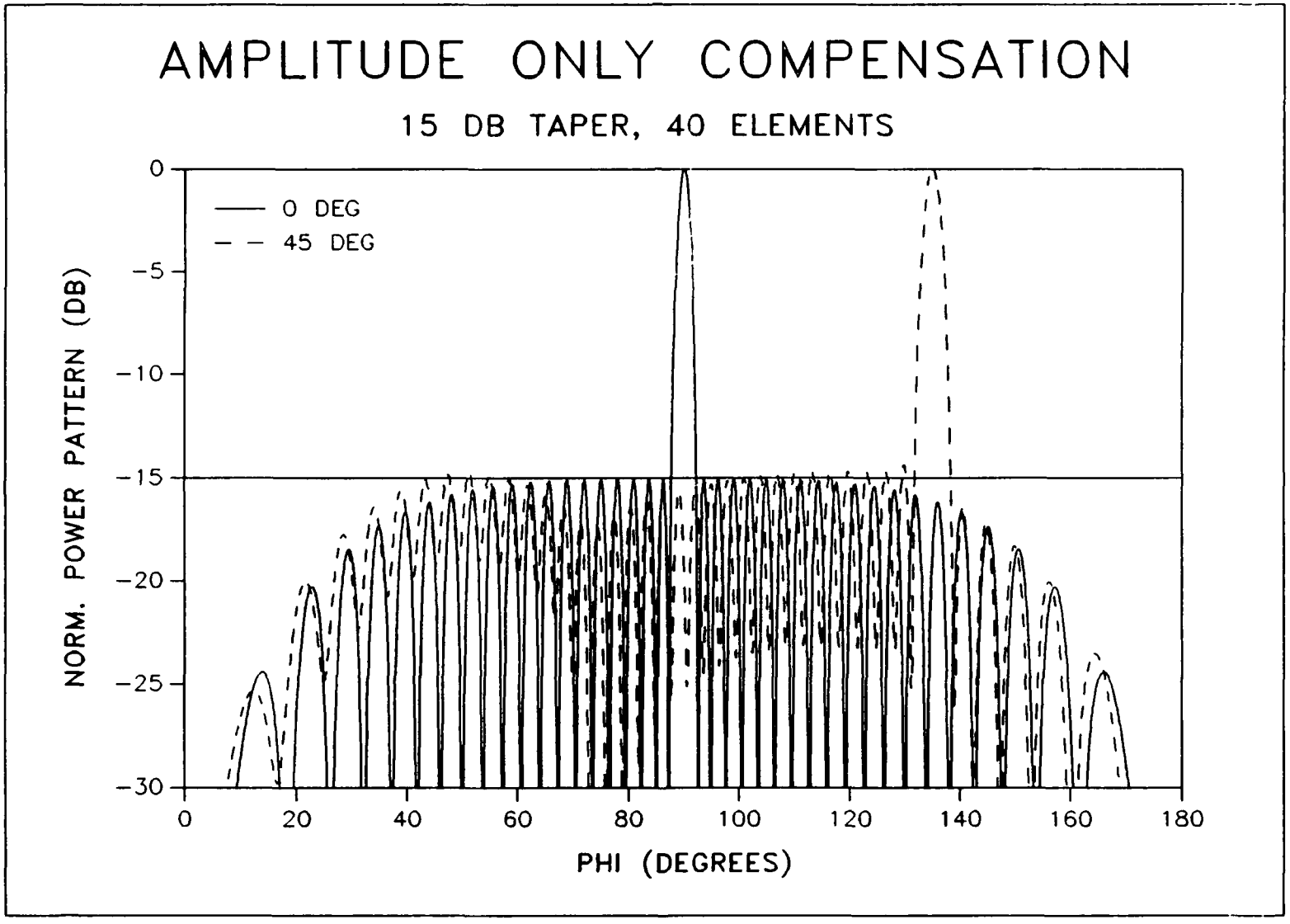
AMPLITUDE ONLY COMPENSATION
15 DB TAPER, 40 ELEMENTS
0 DEG
45 DEG
NORM. POWER PATTERN (DB)
0
-5
-10
-15
-20
-25
-30
0
20
40
60
80
100
120
140
160
180
PHI (DEGREES)

5 Degree Phase Compensation

15 DB TAPER, 40 ELEMENTS

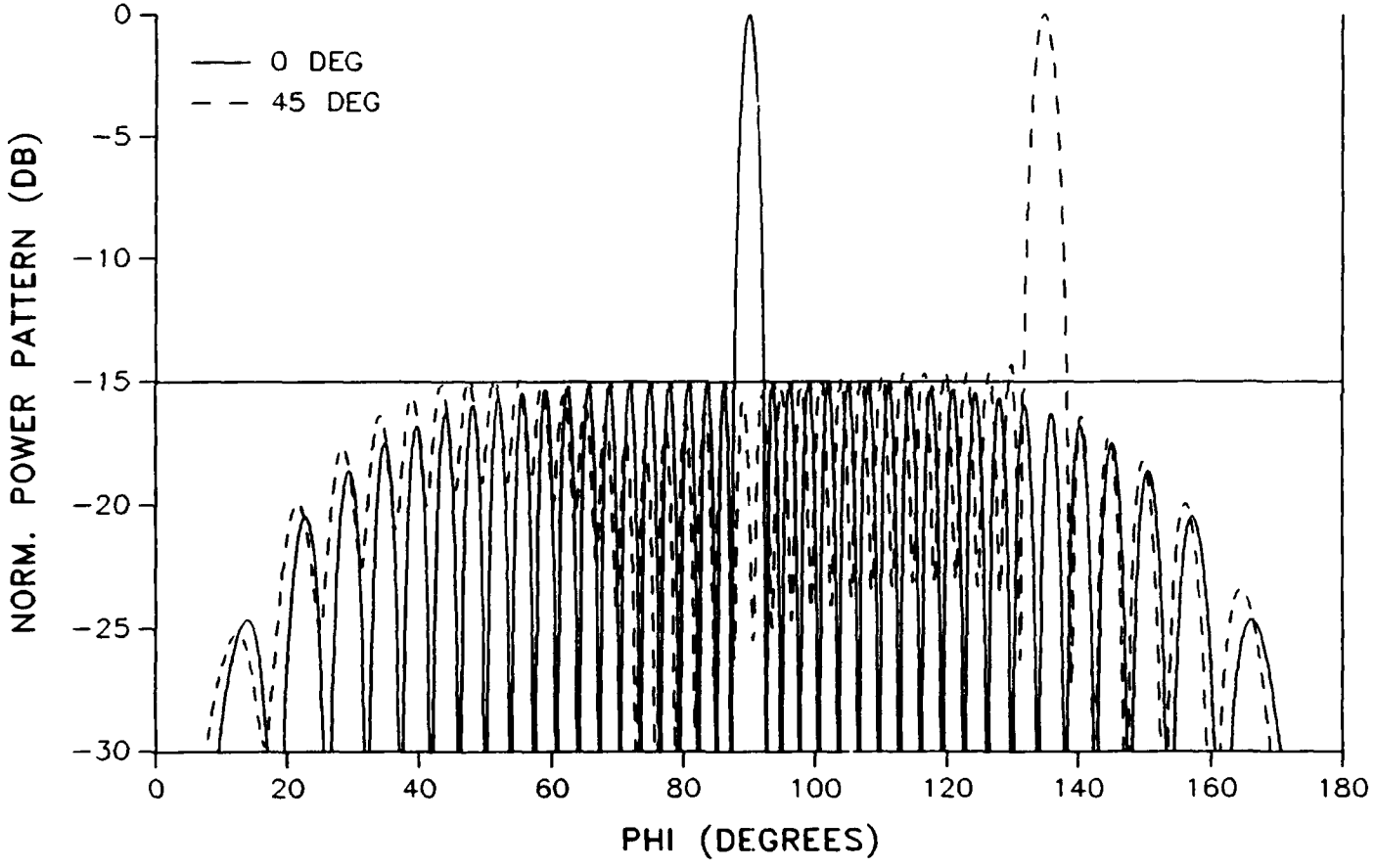

2.5 Deg Phase Compensation

15 DB TAPER, 40 ELEMENTS

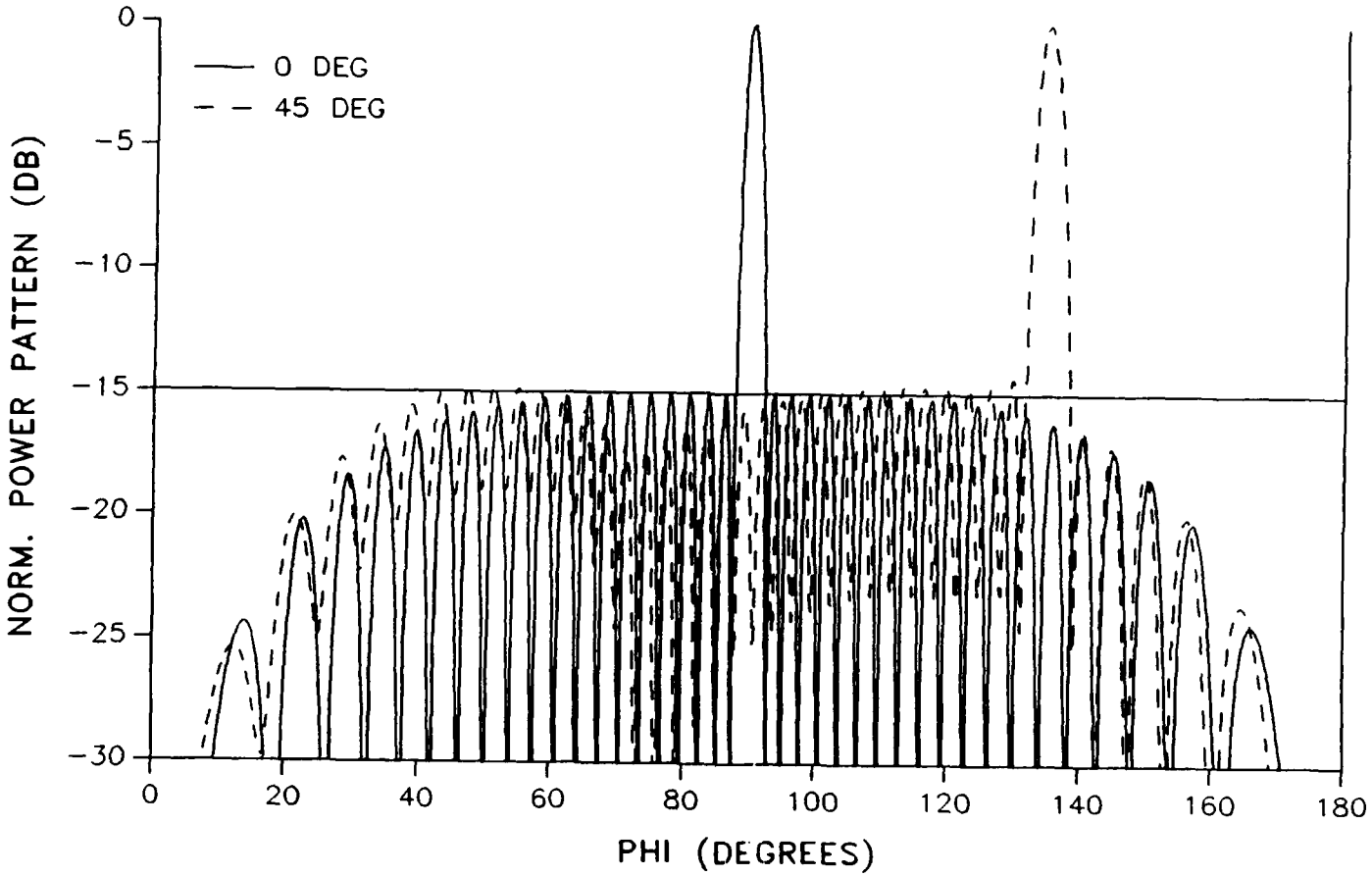

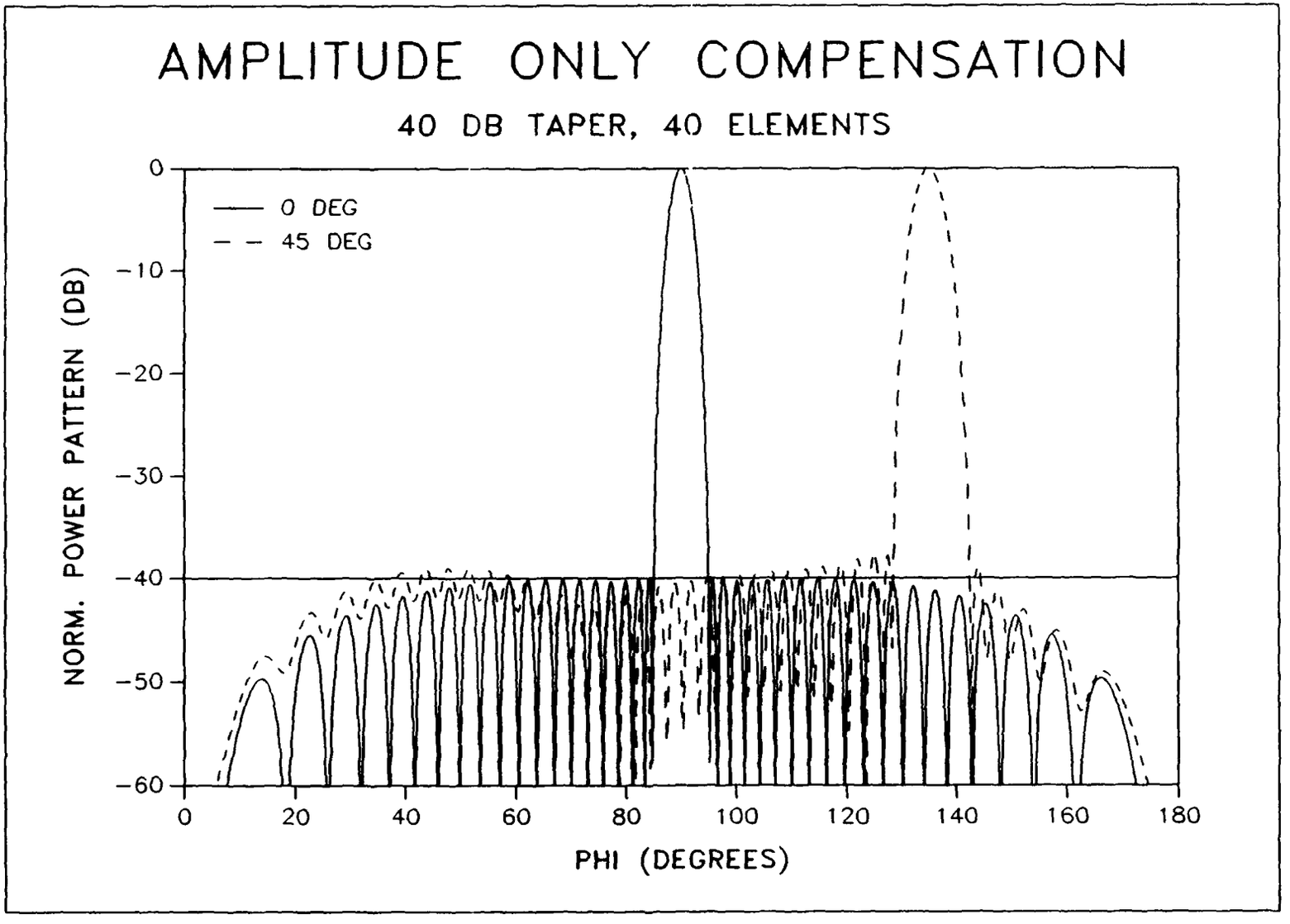
AMPLITUDE ONLY COMPENSATION
40 DB TAPER, 40 ELEMENTS
0 DEG
45 DEG
NORM. POWER PATTERN (DB)
0
-10
-20
-30
-40
-50
-60
0
20
40
60
80
100
120
140
160
180
PHI (DEGREES)

5 Degree Phase Compensation

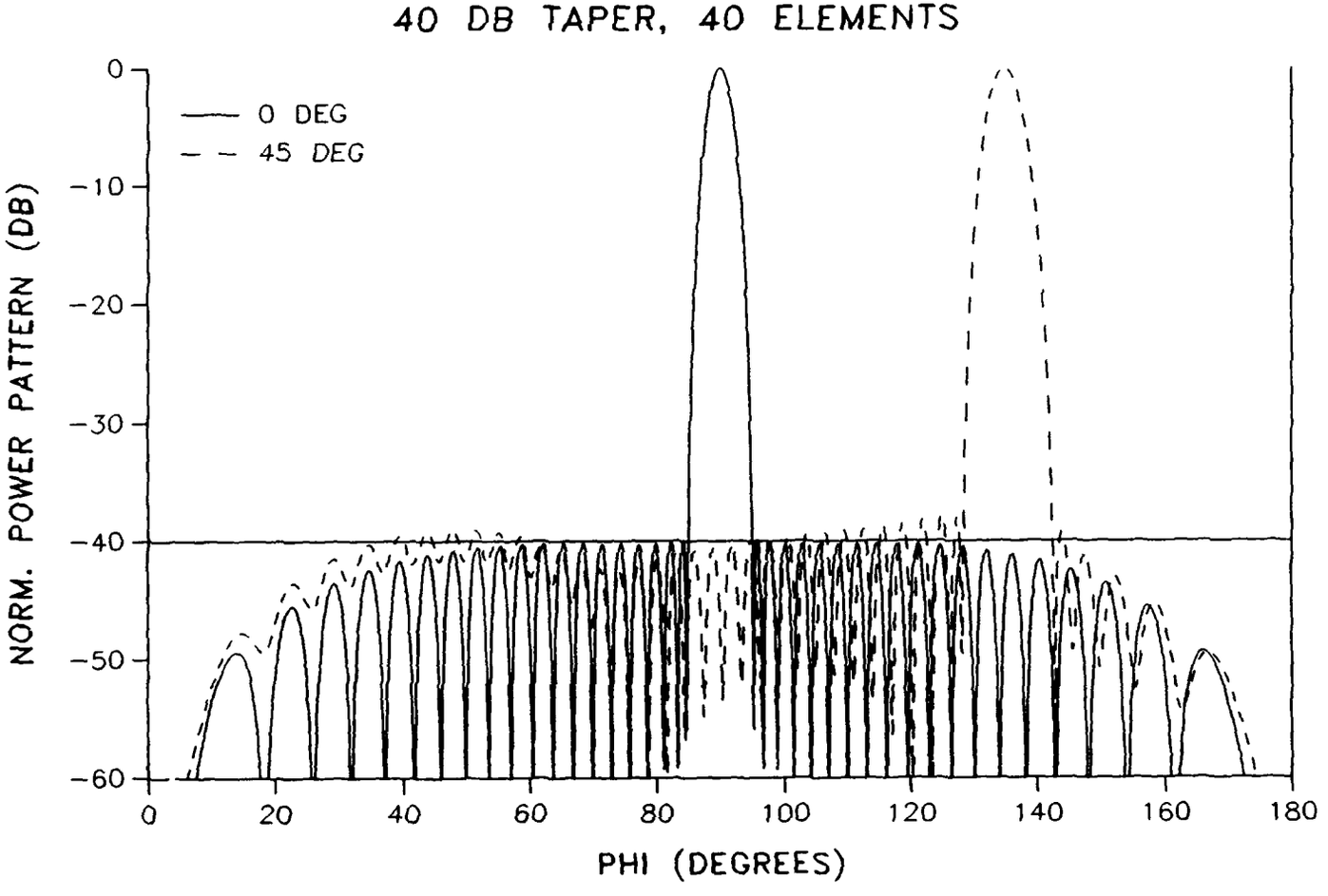

2.5 Deg Phase Compensation

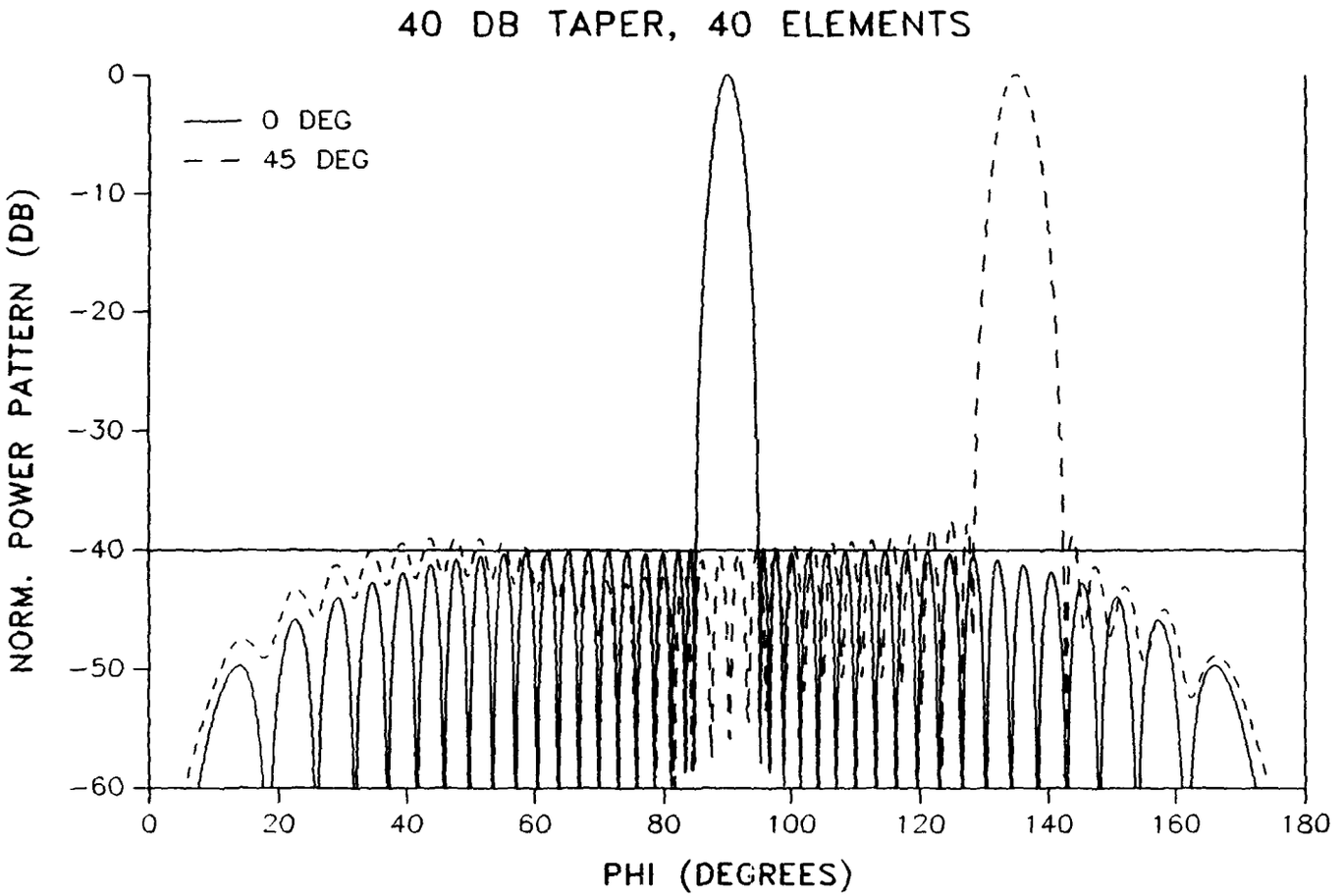

BIBLIOGRAPHY

1. Barbiere, D., "A Method for Calculating the Current Distribution of Tschebyscheff Arrays", Proceedings of Institute of Radio Engineers, ppg 78-82 (January 1952).

2. Brown, Lawrence B. and Sharp, Glenn A., "Tschebyscheff Antenna Distribution, Beamwidth and Gain Tables", Navord Report 4629 (NOLC Report 383), Naval Ordnance Laboratory Corona (February 1958).

3. Carter, P.S., Hansell, C.W. and Lindenblad, N.E. "Development of Directive Transmitting Antennas by RCS Communications, Inc.", Proceedings of the Institute of Radio Engineers, 19:1773 (1931).

4. Chang, V. W. H. and King, R. W. P., "On Two Arbitrarilly Located Identical Parallel Antennas", IEEE Transactions on Antennas and Propagation, Vol AP-16 NO.3:309-317 (May 1968).

5. Collin, Robert E. and Zucker, Francis J., Antenna Theory Part 1, McGraw-Hill Inc, New York (1969).

6. Deford, John F. and Gandhi, Om P. "Mutual Coupling and Side Lobe Tapers in Phase Only Antenna Synthesis for Linear and Planar Arrays," IEEE Transactions for Antennas and Propagation, Vol. 36, No. 11:1624-29 (November 1988).

7. Diamond, B. L. and Allen, J. L., "Mutual Coupling In Array Antennas", Technical Report 424 (October 1966), MIT Lincoln Laboratory.

8. Dolph, C.L., "A Current Distribution for Broadside Arrays which Optimizes the Relationship between Beamwidth and Side Lobe Level", Proceedings of the Institute of Radio Engineers, 34:335-48, (1946).

9. Elliot, Robert S., Antenna Theory and Design, Prentice-Hall, Inc., Englewood Cliffs, N.J. (1981).

10. Elliot, Robert S., "An Approximation to Chebyshev Distributions", IEEE Transactions on Antennas and Propagation, AP-11:707-9, (1963).

11. Hansen, R.C. Microwave Scanning Antennas, Vol. 2, Academic Press, New York (1966).

12. Harrington, Roger F., Field Computation by Moment Methods, Robert E. Krieger Publishing Co, Malabar, Florida (1968).

13. Herd, J. "Array Element Pattern Correction in a Digital Beamforming Array: An Experimental Study", Proceedings of the URSI National Radio Science Meeting, Canada (1985).

14. King, R.W.P., Theory of Linear Antennas, Harvard University Press, Cambridge, Mass., (1956).

15. King, R.W.P., Mack, Richard B. and Sandler, Sheldon S., Arrays of Cylindrical Dipoles, Cambridge University Press, London (1968).

16. King, R. W. P., Sandler, B. H. and Sandler, S. S., "Tables for Curtain Arrays", Cruft Laboratory Scientific Report 4 (Series 3) (1964), Harvard University.

17. Lee, K. M. and Chu, R. S. "Analysis of Mutual Coupling Between a Finite Phased Array of Dipoles and its Feed Network", IEEE Transactions on Antennas and Propagation, Vol 36, No. 12:1681-99 (December 1988).

18. Mack, Richard B., "A Study of Circular Arrays" Technical Report Nos. 381-386, Cruft Laboratory, Harvard University (1963).

19. Mack, Richard B. and Mack Evelyn W., "Tables of E(h,z), C(h,z), S(h,z)", Technical Report 331 (November 1960), Cruft Laboratory, Harvard University.

20. Moore, J. and Pizer, R., Moment Methods in Electromagnetics: Techniques and Applications, Research Studies Press Ltd., London, England (1984).

21. Richmond, J.H., "Radiation and Scattering by Thin-Wire Structures in the Complex Frequency Domain"{, TR-2902-10, Ohio State University Electroscience Laboratory, Columbus, Ohio (May 1974).

22. Richmond, J.H., "Computer Program for Thin-Wire Structures in a Homogeneous Conducting Medium", TR-2902-12, Ohio State University Electroscience Laboratory, Columbus, Ohio (August 1973).

23. Steyskal, Hans "Digital Beamforming Antennas, an Introduction", Microwave Journal, pg 107-22 (January 1987).

24. Stutzman, Warren L. and Thiele, Gary A., Antenna Theory and Design, John-Wiley and Sons, New York (1981).

VITA

Captain Robert A. Girard [redacted] He graduated from high school in Rochester, Michigan, in 1975 and attended Carnegie-Mellon University from which he received the degree of Bachelor of Science in Electrical Engineering in May 1979. Upon graduation, he received a commission in the USAF through the ROTC Program. He was in residence at the School of Engineering from June 1979 to December 1980. He is currently serving as a Special Program Manager for Detachment 3, Air Force Flight Test Center, Henderson, Nevada.

[redacted]

UNCLASSIFIED

SECURITY CLASSIFICATION OF THIS PAGE

REPORT DOCUMENTATION PAGE

1a REPORT SECURITY CLASSIFICATION UNCLASSIFIED	1b RESTRICTIVE MARKINGS
2a SECURITY CLASSIFICATION AUTHORITY	3 DISTRIBUTION/AVAILABILITY OF REPORT APPROVED FOR PUBLIC RELEASE: DISTRIBUTION UNLIMITED.
2b DECLASSIFICATION/DOWNGRADING SCHEDULE	
4 PERFORMING ORGANIZATION REPORT NUMBER(S) AFIT/GE/ENG/89M-4	5. MONITORING ORGANIZATION REPORT NUMBER(S)
6a. NAME OF PERFORMING ORGANIZATION SCHOOL OF ENGINEERING 6b. OFFICE SYMBOL (If applicable) AFIT/ENG	7a. NAME OF MONITORING ORGANIZATION
6c. ADDRESS (City, State and ZIP Code) AIR FORCE INSTITUTE OF TECHNOLOGY WRIGHT PATTERSON AFB, OH 45433-6583	7b. ADDRESS (City, State and ZIP Code)
8a. NAME OF FUNDING/SPONSORING ORGANIZATION ROME AIR DEVELOPMENT CTR ELECTROMAGNETIC SCIENCES 8b. OFFICE SYMBOL (If applicable) DIV RADC/EEAA	9. PROCUREMENT INSTRUMENT IDENTIFICATION NUMBER
8c. ADDRESS (City, State and ZIP Code) RADC/EEAA HANSCOM AFB, MA 01731-5000	10. SOURCE OF FUNDING NOS. PROGRAM ELEMENT NO. / PROJECT NO. / TASK NO. / WORK UNIT NO.
11 TITLE (Include Security Classification) SEE BOX 19	
12 PERSONAL AUTHOR(S) ROBERT A GIERARD, CAPT, USAF	
13a. TYPE OF REPORT MS THESIS 13b. TIME COVERED FROM _____ TO _____	14. DATE OF REPORT (Yr., Mo., Day) MARCH, 1989 15. PAGE COUNT 228
16 SUPPLEMENTARY NOTATION	

17 COSATI CODES			18. SUBJECT TERMS (Continue on reverse if necessary and identify by block number)
FIELD	GROUP	SUB. GR.	ANTENNA RADIATION PATTERNS, COUPLED ANTENNAS, LINEAR ARRAYS, DIPOLE ANTENNAS, CHEBYSHEV FUNCTIONS
09	01		
20	03		

19 ABSTRACT (Continue on reverse if necessary and identify by block number)

TITLE: THE EFFECTS OF MUTUAL COUPLING ON THE SIDE LOBE PERFORMANCE OF CHEBYSHEV ARRAYS, VOL. 1

THESIS CHAIRMAN: DR ANDREW J TERZUOLI
ASSISTANT PROFESSOR OF ELECTRICAL ENGINEERING

20 DISTRIBUTION/AVAILABILITY OF ABSTRACT UNCLASSIFIED/UNLIMITED ☒ SAME AS RPT. ☐ DTIC USERS ☐	21. ABSTRACT SECURITY CLASSIFICATION UNCLASSIFIED
22a NAME OF RESPONSIBLE INDIVIDUAL DR A J TERZUOLI	22b. TELEPHONE NUMBER (Include Area Code) (513)255-6913 22c. OFFICE SYMBOL AFIT/ENG

DD FORM 1473, 83 APR EDITION OF 1 JAN 73 IS OBSOLETE

UNCLASSIFIED

SECURITY CLASSIFICATION OF THIS PAGE

This computer analysis assessed the impact of mutual coupling on the side lobe performance of Chebyshev linear arrays as a function of array size, scan condition, and the severity of Chebyshev taper. Array elements were horizontal parallel dipoles over a ground plane. Three simple compensation schemes to account for coupling were also investigated.

A fortran computer program, based upon King-Middleton's modified, zero-order, two-term theory for cylindrical dipoles, was written to calculate the generalized admittance matrix for the linear array, dipole current distributions and the far-field H-plane patterns in the presence of coupling. It is sufficiently general to allow the user to specify; the number of dipoles, dipole length and radius, dipole spacing, height aboveground plane, frequency, and complex generator voltages driving the array. The results relate side lobe degradation (growth) to array size, scan condition and desired chebyshev side lobe level.

Additional programs were written to reverse the matrix solution, and solve for generator voltages, which after coupling, produce a base current distribution with a Chebyshev taper. Three simple compensation schemes then used approximations of the compensated (complex) voltages to drive the array. The effectiveness of these compensation schemes are discussed. The results of this study indicate that linear arrays greater than 20 elements can probably ignore coupling for side lobe considerations, and amplitude only compensation schemes significantly improve side lobe performance under all but the severest scan conditions (45 deg) and Chebyshev tapers (-40 db) considered.